KN-based Lead-free Ferroelectric Materials for SONAR applications

Samuel Jack Parry

Submitted in accordance with the requirements for the degree of
Doctor of Philosophy

The University of Leeds
Functional Materials
School of Chemical and Process Engineering

March 2019

The candidate confirms that the work submitted is his own and that appropriate credit has been given where reference has been made to the work of others.

Acknowledgements

I would like to thank my supervisor Prof. Andrew J. Bell for his valuable guidance and assistance throughout the PhD.

I would like to acknowledge EPSRC and Thales for providing the funding for the research. A special thanks to Alan Elliott who helped in the early stages and provided me with the opportunity to visit Paris and discuss the future of lead-free piezoelectric research with our French colleagues.

A big thank you to everybody who made my summer placement in Templecombe informative, comfortable and rewarding both in research and in personal development. This includes but is not limited to Laura Stoica, Phil O'Gara, Chris Kavanagh, Chris Page, Andrew Mathieson, Bo Tyson, Andrew Bond, Dan Rowe, Hannah Rose and Jack Stevenson.

At Leeds I would like to thank Rob Simpson for his technical support and Faith Bamiduro for his help in the XRD lab. I would also like to thank everybody in the functional materials group, thank you to Anton, Tom, Stephen, Richard, Chloe, Danielle and Yang. It would not have been the same without you.

A special mention to Stephen and Laura for the feedback and proofreading.

Thank you to everybody in the Bike Gang and at Burley RUFC for keeping me entertained through the years. As well as all the CPR players and supporters.

Finally a massive thank you to my family, especially my parents for all the help, support and advice throughout the process and to anybody else I missed.

Diolch yn fawr pawb.

Abstract

$(Ba_{0.85}Ca_{0.15})(Ti_{0.90}Zr_{0.10})O_3$ ceramic was synthesised using the mixed oxide method. The full piezoelectric matrix of the device was characterised and the material was machined and used in two types of transducer device. The receive sensitivity and transmit voltage response of the device was then measured.

The synthesis of pure $KNbO_3$ by the mixed oxide method was optimised to reduce potassium loss. Solid solutions of $(1-x)KNbO_3$-$xCaZrO_3$, $(1-x)KNbO_3$-$xLiNbO_3$ and $(1-x-y)KNbO_3$-$xCaZrO_3$-$yLiNbO_3$ were synthesised. The aim was to replicate the mixed of phases found in PZT and BCTZ. Substituting $KNbO_3$ with $CaZrO_3$ induced a rhombohedral phase to appear at room temperature when x=0.03, making a mixed phase of orthorhombic and rhombohedral. $CaZrO_3$ decreased the T_{O-T} and T_{T-C} phase transitions. Substituting $KNbO_3$ with increasing amounts of $LiNbO_3$ initially reduced the T_{O-T} before inducing a secondary phase. $LiNbO_3$ also acted as a sintering aid, which allowed high electric field measurements. The d_{33}* of the solid solution peaked when x=0.07.

Combining both solid solutions the individual effects of each system was repeated. Increasing the fraction of $CaZrO_3$ induced a rhombohedral phase at room temperature and increasing the fraction of $LiNbO_3$ improved the sinterability and overall piezoelectric performance.

Contents

List of Figures

List of Tables

List of Abbreviations

KN – Potassium Niobate ($KNbO_3$)

SONAR – Sound Navigation Ranging

PZT – Lead Zirconate Titanate

BCTZ – Barium Calcium Titanate Zirconate

RoHS – Restriction of Hazardous Substances

REACH - Registration, Evaluation, Authorisation and restriction of Chemicals

MPB – Morphotropic Phase Boundary

PPT – Polymorphic Phase Transition

BLSF – Bismuth Layer-Structured Ferroelectrics

TTB – Tetragonal-Tungsten Bronze structure

AC – Alternating Current

PNRs – Polar Nanoregions

PT – Lead Titanate

PZN-PT – $Pb(Zn_{1/3}Nb_{2/3})O_3$-$PbTiO_3$

PMN-PT – $Pb(Mg_{1/3}Nb_{2/3})O_3$-$PbTiO_3$

PIN-PMN-PT – $Pb(In_{1/2}Nb_{1/2})O_3$-$Pb(Mg_{1/3}Nb_{2/3})O_3$-$PbTiO_3$

NBT – Sodium Bismuth Titanate

KNN – Potassium Sodium Niobate

BNBT – 0.94 Sodium Bismuth Titanate – 0.06 Barium Titanate

KBT – Potassium Bismuth Titanate

LF4 – $(K_{0.48}Na_{0.52})(Nb_{0.86}Ta_{0.10}Sb_{0.04})O_3$

LF4T – Textured LF4

HDPE – High Density Polyethylene

IPA – 2-Isopropanol

XRD – X-Ray Diffraction

PRAP – Piezoelectric Resonance Analysis Program

FEM – Finite Element Modelling

IEEE – Institute of Electrical and Electronics Engineers

DAQ – Data Acquisition Card

TVR – Transmit Voltage Response

FFT – Fast Fourier Transform

WRP – Weighted R Profile

KNCZ – $(1-x)KNbO_3$-$xCaZrO_3$

KNLN – $(1-x)KNbO_3$-$xLiNbO_3$

KNCZLN – $(1-x-y)KNbO_3$-$CaZrO_3$-$LiNbO_3$

EU – European Union

1 Introduction

1.1 Background and Motivation

Piezoelectric materials have a wide range of applications due to their unique ability of converting an electronic signal into a mechanical signal and vice versa. This allows them to be used as actuators, sensors and transducers. Exploitation of the piezoelectric effect has led to innovative devices, from fuel injection systems in engines to SONAR in submarines.

Since the formation of the Restriction of Hazardous Substances (RoHS) and the Registration, Evaluation, Authorisation, and Restriction of Chemicals (REACH) in 2006 and 2007 respectively, there has been an increase in research into lead-free piezoelectric materials (1-3). This research has mainly focused on finding an alternative to the piezoelectric materials market leader, lead zirconate titanate (PZT) by attempting to replicate the morphotropic phase boundary (MPB) it possesses (4, 5).

Although many different lead-free materials have been devised, not one has been able to completely replace PZT. There has also been a lack of translation from research to industry, or from material to device.

1.2 Aims and Objectives

The first aim of this work is to determine the feasibility of a $(Ba,Ca)(Ti,Zr)O_3$ based material being incorporated into a transducer device. This will be done by initially producing large, fully characterised and machined samples of $(Ba,Ca)(Ti,Zr)O_3$, modifying the manufacturing process of a device to reduce high temperature conditions, and then characterising the device.

The second aim is to find, and characterise a novel lead-free piezoelectric material with a higher Curie point than that of $(BaCa)(TiZr)O_3$. This will be done by doping a base material ($KNbO_3$) with dopants that will induce a rhombohedral and tetragonal phase at room temperature.

1.3 Thesis Structure

The thesis is split into 7 chapters. Chapter 1 describes the background and aims of the project. The principles of electroceramics and piezoelectric materials are described in chapter 2. Chapter 3 provides a brief history of piezoelectric materials and a background introduction into lead-free alternatives. The experimental techniques are discussed in chapter 4. This includes the mixed oxide synthesis route of electroceramics and the characterisation techniques used.

Chapter 5 covers the results of the full piezoelectric matrix of $(Ba_{0.85}Ca_{0.15})(Ti_{0.90}Zr_{0.10})O_3$ and the manufacturing and characterisation of two types of lead-free transducer. The search for a novel lead-free piezoelectric material and the characterisation of the materials made is described in chapter 6.

There is then a summary of the main conclusions of this work and a discussion of potential further work in the field.

2. Introduction to the structure and electrical properties of electroceramics.

This chapter covers the principles of the crystal structure and the functional properties that arise from specific ordering of atoms, focusing primarily on the perovskite structure. It will define some of the technical terminology that will be used freely throughout the thesis and describe the phenomena of piezoelectricity, ferroelectricity and their origins. Later in the chapter the applications of piezoelectric materials will be discussed.

2.1 Crystalline Definitions

The crystal structure is a way of describing the arrangement of atoms in a material. Understanding the crystal structure of a material is vital to understanding the physical properties that said material can exhibit. Manipulating the crystal structure changes the properties of the material which is the fundamental basis of material science.

2.1.1 Crystal Structure

Crystalline materials consist of atoms in a regular arrangement or pattern and are said to have long range order in 3 dimensions. The repeating array of atoms form a lattice and points that have identical environments, for example, the same distances between atoms, are known as lattice points. The smallest representation of lattice points is known as a unit cell. The unit cell on any structure can be classified into 1 of 7 crystal systems, cubic, tetragonal, orthorhombic, rhombohedral, hexagonal, monoclinic or triclinic. These crystal systems are described by three unit cell lengths, a, b and c, and the angles between them α, β, and γ. Where the angle between axis a and b is γ, between b and c is α and the angle between a and c is β (Figure 2.1). They can be further split into systems with a body, face, or base centred atom or without a centred atom. This type of classification is known as the Bravais lattice, and all 14 can be seen in Table 2.1.

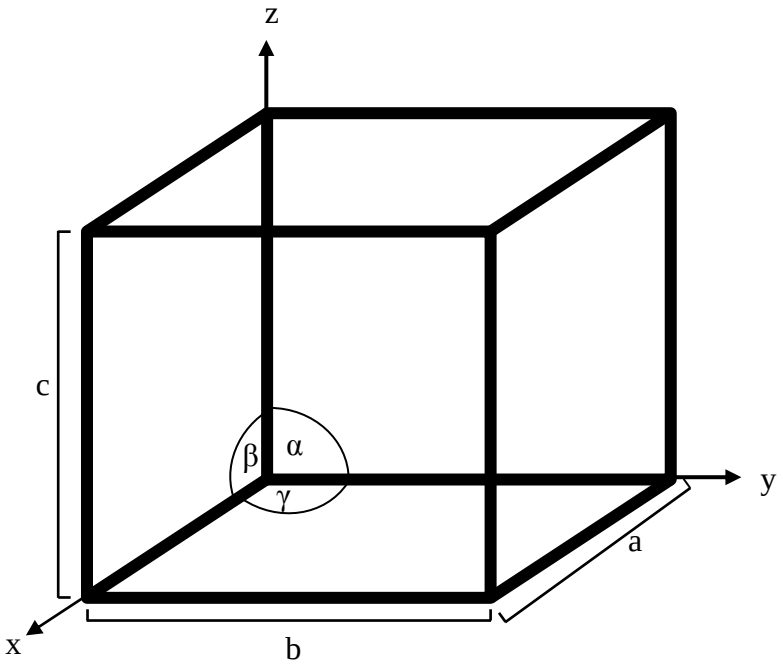

Figure 2.1: A unit cell of length, a, b and c, the angles α, β, and γ between them and the Cartesian axis x,y, and z.

Table 2.1: Table of the 14 Bravais lattice, including crystal system lengths and angles.

Crystal System	Primitive (P)	Body-centred (I)	Face-centred (F)	Base-centred (C)
Cubic a=b=c α=β=γ=90°	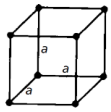	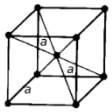	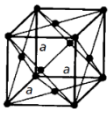	
Tetragonal a=b≠c α=β=γ=90°	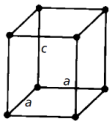	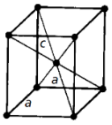		
Orthorhombic a≠b≠c α=β=γ=90°	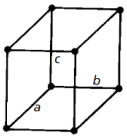	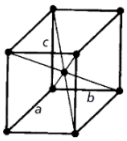	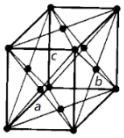	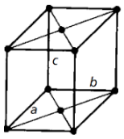
Rhombohedral a=b=c α=β=γ≠90°	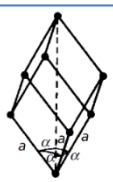			
Hexagonal a=b≠c α=β=90° γ=120°	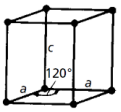			
Monoclinic a≠b≠c α=γ=90° β≠90°	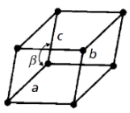			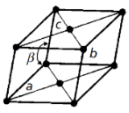
Triclinic a≠b≠c α≠β≠γ≠90°	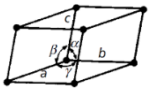			

2.1.2 Symmetry, Space Groups and point groups

Applying point symmetry operations such as mirror, rotation or inversion can allow for a crystalline material to be categorised into 1 of 32 point groups. Adding translation elements such as screw axis or glide to a crystal system allows for an even more detailed description of a crystal's inherent symmetry and further categorises it into 1 of 230 space groups.

Mirror plane symmetry, glide symmetry and rotational symmetry are 2 dimensional and can be easily displayed as seen in Figure 2.2. Inversion axis symmetry is rotation that passes through the centre of symmetry. Whereas screw axis is a form of rotation and translation.

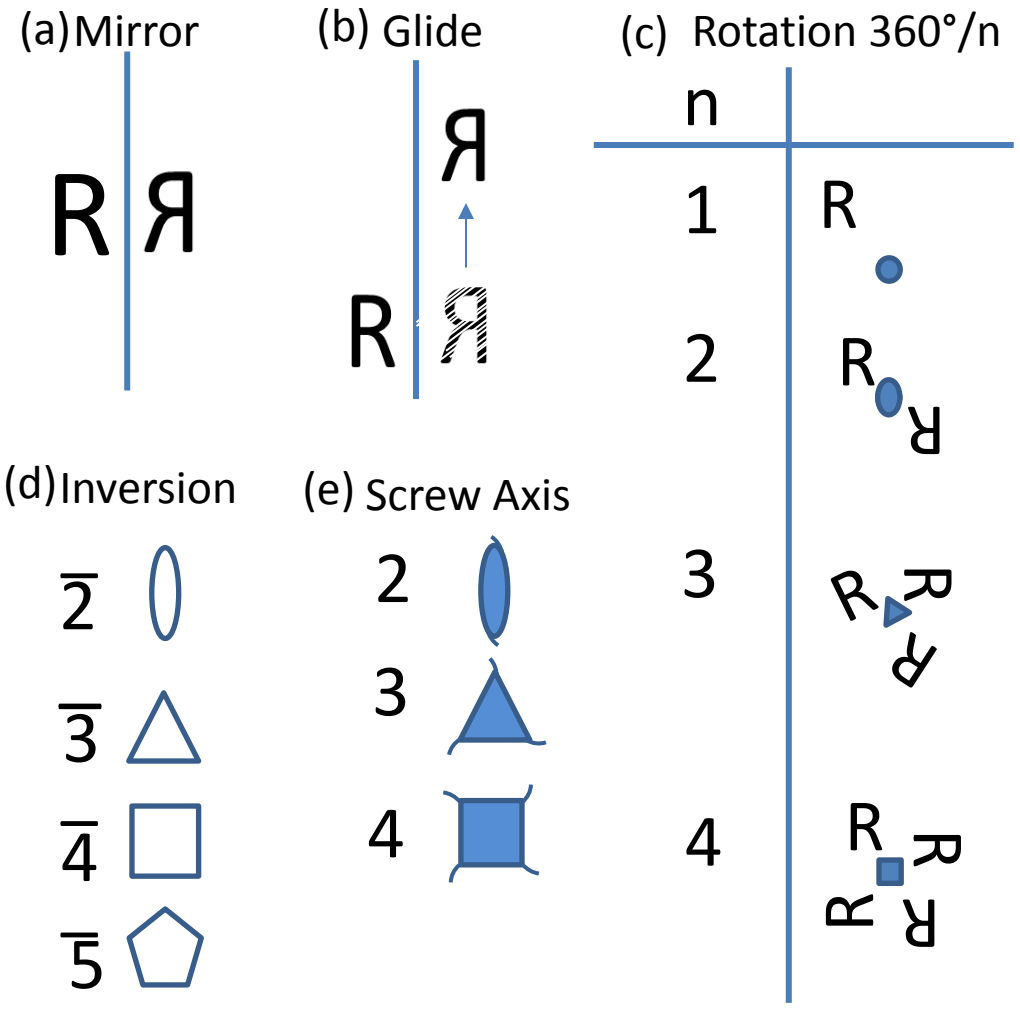

Figure 2.2: Simple representation of (a) Mirror, (b) Glide, (c) Rotation, (d) Inversion and (e) Screw Axis symmetry.

The space group notation used during this thesis is the Hermann-Maugiun notion (6)**.** Where the first letter describes the Bravais lattice type, and the further letters and numbers correspond to symmetry elements. For

example, the space group *R3c* is rhombohedral, the '3' relates to its 3-fold rotation and the 'c' corresponds to a glide plane along the c-axis.

Mirror plane symmetry is given the symbol 'm', glide planes are a mirror with the addition of ½ the direction along the unit cell and are given the symbol 'a', 'b', or 'c' depending on the direction. Rotation symmetry is given an integer 'n' where 360°/n is equal to the degrees of rotation. Screw axis symmetry is represented as two numbers, N_m, where N is the rotation integer and m/N is equal to the fraction of the unit cell translated (e.g. 2_1 is 180° rotation and ½ unit cell translation). Inversion symmetry uses the same nomenclature as rotation, with negative numbers, often seen as -3 or $\bar{3}$ .The space groups have also been numbered 1 to 230 by the International Union of Crystallography with 1 having the least symmetry, the triclinic crystal structure *(P1)* and 230 having the most symmetry, the cubic crystal structure *(Ia-3d)* (7).

Of the 32 point groups 21 have no centre of symmetry and 11 are centrosymmetric. If a crystalline material possess a centre of symmetry all the positive and negative charges in the unit cell cancel each other out, and the material cannot display any piezoelectric properties. The cubic point group *432* is the only non-centrosymmetric point group not to exhibit piezoelectricity. It is the only non-centrosymmetric point group with both a 4-fold and 3-fold axis, as a result of these symmetries coexisting there is no dipole moment (8). Of the 20 group points that can exhibit piezoelectric behaviour, 10 groups are spontaneously polar. Every polar space group is pyroelectric, where they generate a voltage with a change in temperature. Every ferroelectric space group is also pyroelectric (9).

2.1.3 Planes and directions

Lattice point positions are given in terms of its Cartesian axis coordinates, and are numbered in relation to the origin of a unit cell in terms of fractions of lengths along x, y and z. They are represented as three integers known as Miller indices. Planes use round brackets (h,k,l) and directions use square brackets [u,v,w]. The brackets {hkl} and <u,v,w> can be used to describe the equivalent planes or directions respectively. For example {001}, would describe the (001), (010) and the (100) planes as well as the negative equivalents (00 $\bar{1}$), (0 $\bar{1}$ 0) and (00 $\bar{1}$).

In the examples found in Figure 2.3 the direction A is [110], B is [101] and C is [012]. The plane D is (001), E is (010), and F is (002).

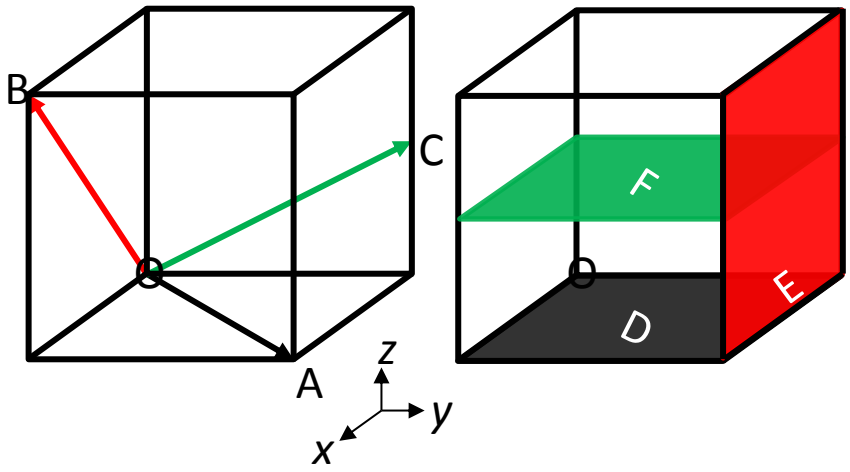

Figure 2.3: A unit cell with the origin marked O (a) directions marked A, B and C and (b) planes marked D, E, and F.

2.1.4 The Perovskite Structure

The mineral perovskite, first discovered by Gustav Rose in 1839, and named after mineralogist Lev Perovski, is a calcium titanium oxide mineral ($CaTiO_3$), and it lends its name to a very important crystal structure (10). Most piezoelectric and ferroelectric materials that are researched and used in applications have the perovskite structure (11).

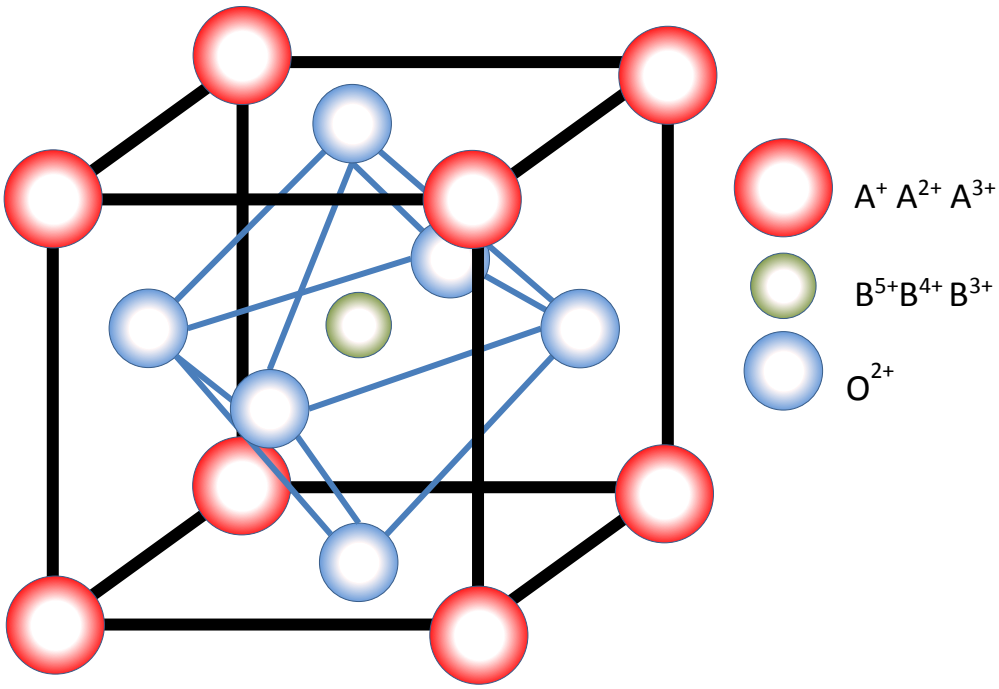

Figure 2.4: Typical perovskite structure, the large A-site cation at the corners, the central smaller B-site cation and the X-site anion acting as an oxygen octahedra at the face centres.

The perovskite structure has the form ABX_3 as seen in Figure 2.4. Where A is a cation found at the corners of the unit cell and is much larger than B, a cation found at the body centre. X is an anion found at the face centres, and is usually an oxygen atom. A and B can be a wide variety of elements, however their positive valences must equal the sum of the negative valences of the X-site (12). When the X-site is occupied by oxygen atoms, the B-site atom and the surrounding 6 oxygen atoms can combine to create an oxygen octahedra. Tilting or distortion of the oxygen octahedra can lead to phase transitions (13).

2.1.5 The Goldschmidt tolerance factor

As mentioned in 2.1.2, in order for a crystalline material (including perovskite) to exhibit piezoelectricity, it must be a non-centrosymmetric structure. The perovskite structure can accommodate a large range of atoms, different atoms and different combinations lead to distortion from the cubic crystalline structure leading to piezoelectricity. This can arise from displacement of the central ion, as well as distortion or tilting of the oxygen octahedra.

Goldschmidt proposed the concept of a perovskite tolerance factor 't' in 1926 seen in Equation 2.1 (14). Where r_A, r_B and r_O are the ionic radii of the respective ions.

$$t = \frac{r_A + r_O}{\sqrt{2}(r_B + r_O)} \qquad \textbf{Equation 2.1}$$

The equation can be used to determine the stability of an ionic paring, where an 'ideal' perovskite structure would have a t≈1, such as $SrTiO_3$. It has been found that difficult to prepare Pb-based samples such as $Pb(Mg_{1/3}Nb_{2/3})O_3$ with a t=0.89, can have enhanced stability when the small Pb^{2+} cation is replaced by a small amount of Ba^{2+}, bringing the tolerance factor closer to 1.00. It has also been found that there is a link between tolerance factor and Curie temperature, with the lower the tolerance factor, the higher the Curie temperature (15). When t≠0.95-1.00, the structure is non-cubic, becoming orthorhombic or rhombohedral when t<0.95 and tetragonal when t>1.00 (16-18).

2.1.6 Phases and Phase Transitions

The ability for the B-site atom to be displaced from its central positon gives rise to piezoelectricity. A piezoelectric perovskite under certain conditions (temperatures, pressures or electric fields) has a displaced B-site atom. In ferroelectric materials, this can happen in ambient conditions as they exhibit a spontaneous displacement of the central atom or 'polarization' below its Curie point (see 2.2.5).

When the B-site atom is displaced from the centre, the shape of the whole perovskite structure changes. This is due to the intra-unit cell atom conditions changing, known as electrostriction. The direction of displacement also has an effect on the shape. Take for example the ferroelectric material, potassium niobate ($KNbO_3$), a material which will be discussed in detail during this thesis. As it cools through the Curie point at 435°C, it changes from cubic to ferroelectric tetragonal. Further cooling to 225°C, and there is a ferroelectric-ferroelectric phase transition from tetragonal to orthorhombic. At -10°C another ferroelectric-ferroelectric transition occurs, from orthorhombic to rhombohedral.

A phase transition that occurs due to a change in temperature is called a polymorphic phase transition (PPT). In Figure 2.5 it can be seen that the change in temperature causes the niobium ion found at the B-site to occupy certain directions, indicated by the polarization arrow. The arrows only represent one direction however the equivalent angles are also valid. For example, in a ferroelectric material, when the structure is tetragonal the atom could occupy anywhere along the arrow under electric field or either extremity when under no field (19, 20).

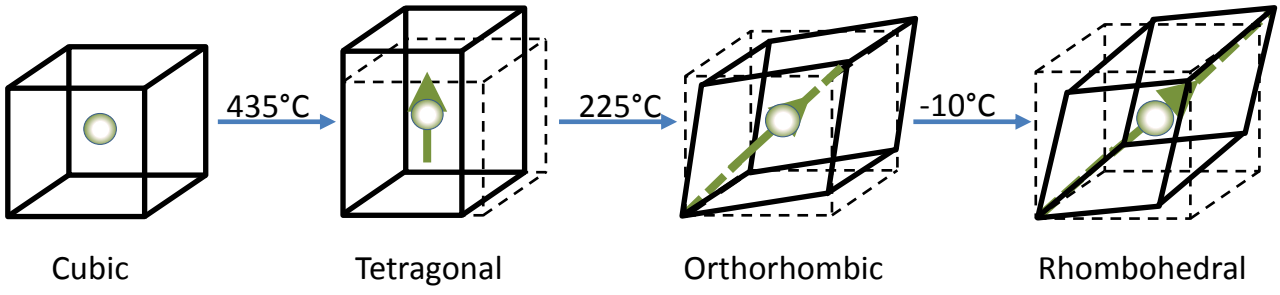

Figure 2.5: Ferroelectric phase transitions of $KNbO_3$ with the directions of polarization indicated.

2.1.7 Solid Solutions and morphotropic phase boundaries

Phase transformations can also occur with changes in composition. Substitution of one or more types of atoms on either A or B-site (or both) can induce a phase change. These systems are called solid solutions, and are the major topic of research amongst the electroceramic community. The composition at which there is a phase transition often has a coexistence of more than one phase. At this point there is often a maximum in the electromechanical properties, and the composition is said to be at the morphotropic phase boundary (MPB) (21).

The morphotropic phase boundary is often observed as a vertical line on a phase diagram. The original definition is a temperature independent phase boundary between differing symmetries (22). In practice however, the term MPB gets used to indicate the presence of more than one phase, whether temperature dependant or not, as well as increased piezoelectric performance (23).

The increase in piezoelectric performance is due to the presence of two phases allowing for an increasing number of polarization directions available for the B-site atom to occupy. For example, a coexistence between a tetragonal phase, which can have 6 directions, and a rhombohedral phase that can have 8 directions, will allow for 14 different polarization directions.

2.1.8 Non Perovskite Ferroelectric materials

Although perovskite piezoelectric materials are the most researched and applied materials, there are several non-perovskite piezoelectric systems. Bismuth layer-structured ferroelectrics (BLSF) have the general formula $Bi_2A_{n-1}B_nO_{3n+3}$ and consist of at least one perovskite unit cell sandwiched between bismuth oxide sheets (Bi_2O_2). The maximum d_{33} coefficient for a BLSF reported is 25pC/N (18). They are characterised by their low dielectric constant, high Curie temperature and large anisotropic electromechanical coupling factors (24).

Another non-perovskite structure with ferroelectric materials is the tetragonal tungsten-bronze structure (TTB). They have the general formula A_xWO_3 and exist in three basic structures, all based on a corner sharing WO_6 octahedra. They generally exhibit relaxor properties (see 2.2.10), have very low piezoelectric d_{33} coefficients and are of interest in high temperature applications owing to their high Curie point (25-27).

2.2 Functional properties of ferroelectrics

Characterising the unique functional properties of piezoelectric and ferroelectric materials is a major part of the research undertaken in this thesis. The origin and relevance of these properties will be described in this section.

2.2.1 Dielectric Properties

Dielectric materials do not conduct electricity, instead, when a dielectric is placed under an electric field the charges in the crystal structure rearrange. The rearrangement of the charges forms a dipole moment, and the material is said to be polarised.

The permittivity of a dielectric is the displacement per unit of electric field. When two parallel plates have an electric field, V, applied to them and a vacuum separating them, there is a charge build up at the surface, Q. This is dependent on the surface area, A, of the plates and the separation distance, d, between them.

$$\boldsymbol{Q = \varepsilon_0 V * \frac{A}{d}} \qquad \textbf{Equation 2.2}$$

The proportionality constant, $\boldsymbol{\varepsilon_0}$ is known as the permittivity of free space which is equal to 8.845×10^{-12} Fm^{-1}. The capacitance, C, of the system is the ratio of charge to voltage.

$$\boldsymbol{C = \frac{Q}{V} = \varepsilon_0 * \frac{A}{d}} \qquad \textbf{Equation 2.3}$$

The electric field, E, between the two plates is the voltage divided by the distance between the plates. Expressing in terms of electric field instead of voltage applied and rearranging, will allow for the surface charge density, σ, to be calculate.

$$\boldsymbol{\sigma = \frac{Q}{A} = \varepsilon_0 E} \qquad \textbf{Equation 2.4}$$

When the gap between the parallel plates is filled with a dielectric material, the capacitance and the surface charge density increases by a factor known as $\boldsymbol{\varepsilon_r}$ which is known as the relative permittivity or dielectric constant. Therefore, the capacitance for a dielectric material is

$$\boldsymbol{C = \varepsilon_0 \varepsilon_r * \frac{A}{d}} \qquad \textbf{Equation 2.5}$$

And the permittivity of the system is

$$\boldsymbol{\varepsilon = \varepsilon_0 \varepsilon_r} \qquad \textbf{Equation 2.6}$$

Polarization, P, is the amount charge distribution is distorted by the electric field and is proportional to the applied electric field.

$$\boldsymbol{P = \frac{\varepsilon_0 \chi}{E}} \qquad \textbf{Equation 2.7}$$

Where χ is the dielectric susceptibility and is related to the relative permittivity of the dielectric material by

$$\boldsymbol{\varepsilon_r = \chi + 1} \qquad \textbf{Equation 2.8}$$

2.2.2 Dielectric loss

In practice a dielectric material is not a complete insulator and there is some charge transport through the system. There is also some energy lost in the material, as polarization switching lags behind the alternating current (AC) field. There are a number of mechanisms which contribute to the polarization. The electronic contribution comes from electron orbitals being distorted by the electric field, the ionic contribution is from the position of the ions changing, and there is also a contribution from molecular orientation and space charge carriers. Each of these mechanisms can be distinguished by the speed with which they can follow an AC field.

The losses are represented by splitting the permittivity into a real, $\boldsymbol{\varepsilon'}$ and imaginary (lossy), $\boldsymbol{\varepsilon''}$ components, making the permittivity complex.

$$\boldsymbol{\varepsilon^* = \varepsilon' - i\varepsilon''} \qquad \textbf{Equation 2.9}$$

The phase difference between the current (I) and the voltage (V) in a pure capacitive circuit is 90°. As the voltage charges, the current becomes zero. In a real dielectric there are some losses, and so the phase difference is less than 90°. In the phasor diagrams (Figure 2.6) it can be seen that the current splits into two components in a lossy capacitor, the component in the direction of the current, I_{cap}, and the component in the direction of the voltage, I_{loss}.

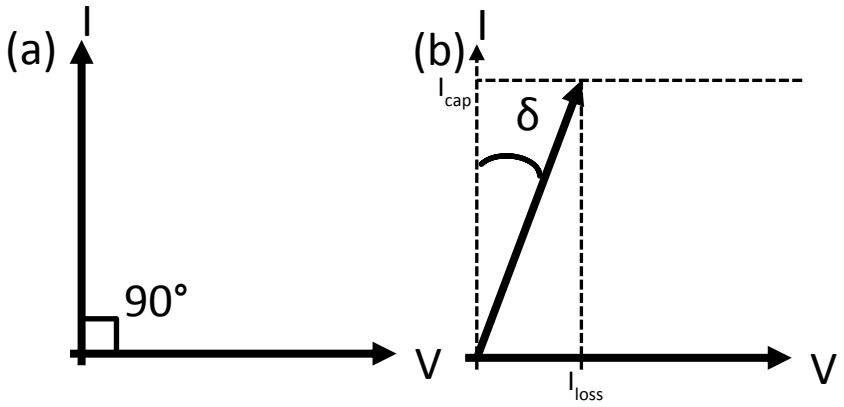

Figure 2.6: Phasor diagram of the phase difference between current and voltage of (a) an ideal capacitor and (b) a lossy capacitor.

$$I_{cap} = Isin(90 - \delta) = Icos(\delta) \qquad \textbf{Equation 2.10}$$

$$I_{loss} = Icos(90 - \delta) = Isin(\delta) \qquad \textbf{Equation 2.11}$$

The loss component is typically expressed as the ratio between the imaginary and real components, and therefore;

$$\frac{I_{cap}}{I_{loss}} = \frac{\varepsilon''}{\varepsilon'} = tan\delta \qquad \textbf{Equation 2.12}$$

2.2.3 Piezoelectric coefficients and modes

When a mechanical stress, T, is applied to a piezoelectric material, the material will generate a polarization, P, this produces an electrical charge, and is known as the direct piezoelectric effect (Equation 2.13). The indirect, or converse effect is the opposite. Under an electric field, the material produces a strain, x (Equation 2.14).

$$P = d_{ij}T \qquad \textbf{Equation 2.13}$$

$$x = d_{ij}E \qquad \textbf{Equation 2.14}$$

Where d is the piezoelectric charge coefficient with units of pm/V or pC/N. It is usually expressed with two subscripts. Under the converse effect, the first relates to the direction of the applied electric field or stress and the second relates to the axis of the resultant strain measured.

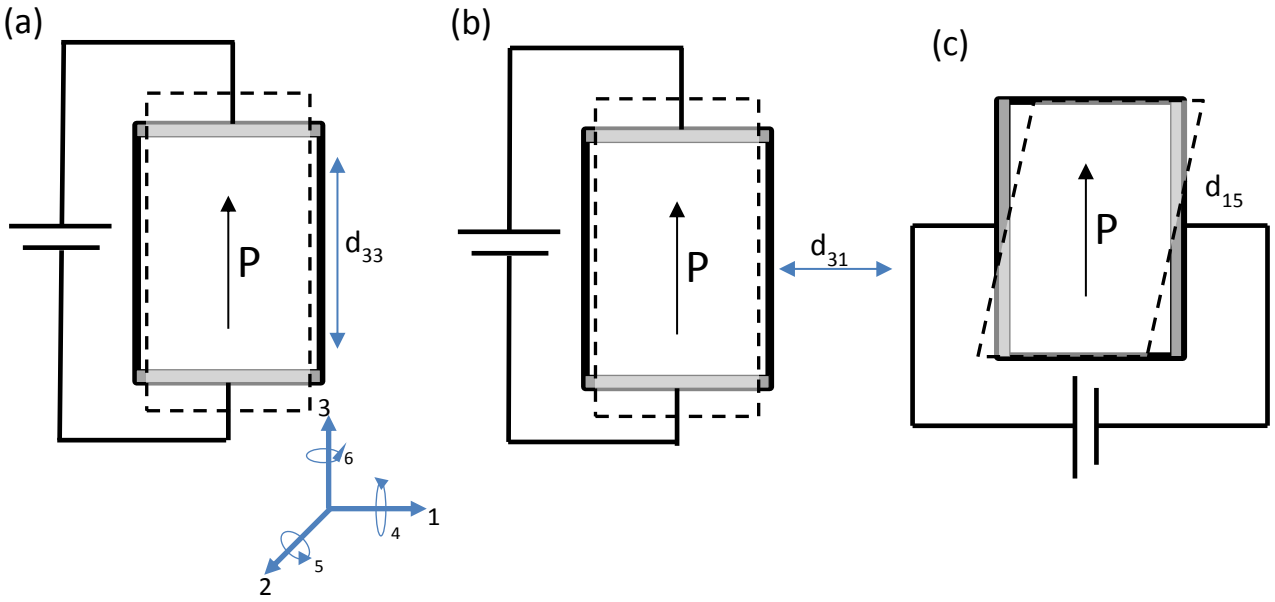

Figure 2.7: The three piezoelectric modes (a) longitudinal, (b) transverse, (c) shear, and the piezoelectric tensor notation.

The longitudinal mode, or d_{33}, is the measure of strain induced by the electric field along the polarization direction. The transverse mode, or d_{31}, is the measure of strain induced perpendicular to the direction of the electric field applied along the polarization direction. The shear mode is the strain measured around the 2-direction as the electric field is applied perpendicular to the polarization (Figure 2.7).

The piezoelectric voltage coefficient, g, is the electric field generated by a piezoelectric material per unit of mechanical stress or, the mechanical strain on the material per unit of electrical displacement.

$$g_{ij} = \frac{d_{ij}}{\varepsilon^T} \qquad \textbf{Equation 2.15}$$

Where ε^T is the permittivity under constant stress. The voltage coefficient also uses directional subscripts following the same rules as the piezoelectric charge coefficient. The units for g are Vm/N. The voltage coefficient is important for assessing the suitability of a material to be used in a sensor.

2.2.4 Electromechanical coupling Factor

The electromechanical coupling factor, k, gauges a piezoelectric material's ability to convert electrical energy to mechanical energy and vice versa.

$$k = \sqrt{\frac{electrical\ energy\ converted\ to\ mechanical\ energy}{input\ electrical\ energy}}$$ **Equation 2.16**

$$k = \sqrt{\frac{mechanical\ energy\ converted\ to\ electrical\ energy}{input\ mechanical\ energy}}$$ **Equation 2.17**

This also uses the subscript notation, k_{ij}. The electromechnical coupling factor and the piezoelectric charge coefficient can be related by the following equation:

$$d_{33} = k_{33}\sqrt{\varepsilon_{33}^{T} S_{33}^{E}}$$ **Equation 2.18**

Where ε_{33}^{T} is the permittivity at a constant stress and S_{33}^{E} is the compliance at constant electric field.

2.2.5 Ferroelectricity

Ferroelectric materials possess a spontaneous polarization that can be in more than one orientation and can be switched between orientations with an electric field. Above a certain temperature called the Curie point (T_C), there is enough energy in the system for the crystal structure that allows ferroelectricity to transition into a paraelectric cubic structure. Cubic structures are centrosymmetric and so the material will have no spontaneous polarization. This is the case for every ferroelectric material although the Curie point does vary.

The Curie point is not to be confused with the Curie Temperature (T_0). T_0 is a material constant determined by extrapolation of 1st-order (discontinuous) phase transitions. In 2nd-order (continuous) phase transitions T_c and T_0 are equal.

2.2.6 Curie-Weiss Law

Above T_C the dielectric permittivity of a material follows the Curie-Weiss Law.

$$\varepsilon_{T<T_C} = \frac{C_c}{T_C - T}$$ **Equation 2.19**

Where C_C is the Curie constant and is material specific (28).

2.2.7 Ferroelectric Domains

Domains are small areas in a ferroelectric material where the polarization direction is the same. They are formed to reduce the free energy of a system as it changes phase structure.

As a paraelectric material cools through the Curie point, it transitions into (for example) a tetragonal ferroelectric structure and the spontaneous polarization is induced. This polarization creates surface charges which is in turn minimised by the formation of 180° ferroelectric domains. When the crystal structure changes, there is also a change in the lattice parameters which results in stress. To minimize the effect of this elastic stress, 90° domains are formed (see Figure 2.8). If the material cooled and became rhombohedral, to reduce charge build up and stress, 109°, 71° and 180° domains would be formed.

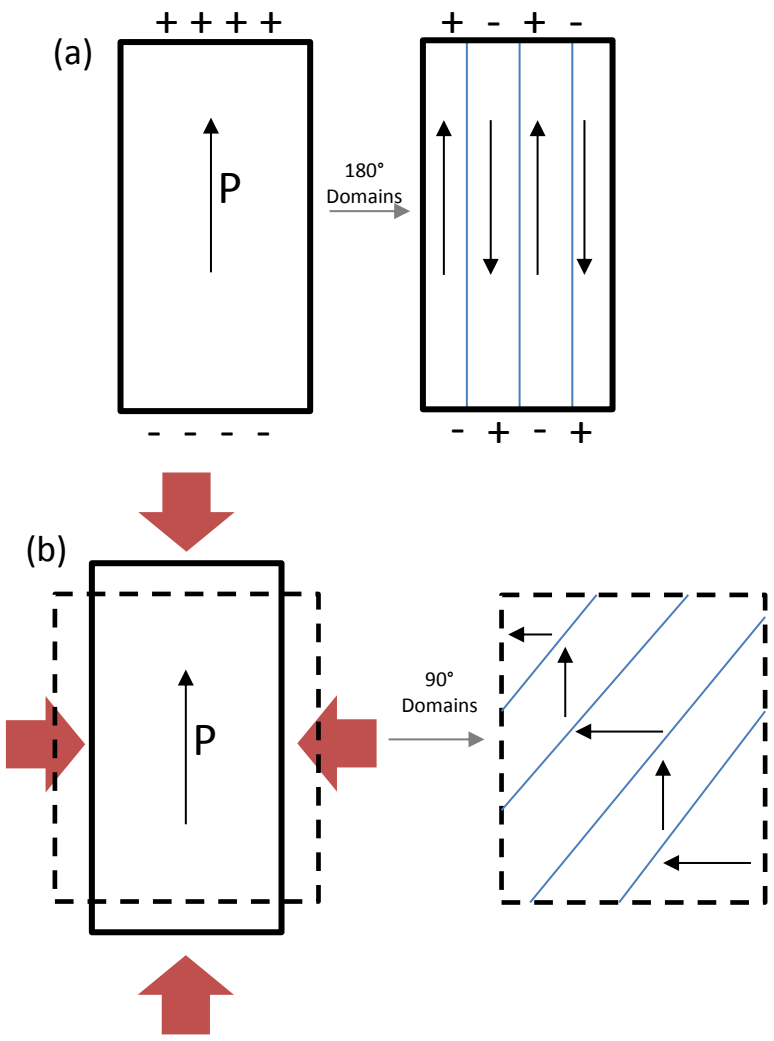

Figure 2.8: Formation of (a) 180° domains and (b) 90° domains in a tetragonal structure.

2.2.8 Poling

In a crystalline ferroelectric, after the formation of domains there is no net polarization present in the material, as the randomly distributed polarization directions cancel each other out. For a crystalline sample to exhibit macroscopic polarization, it must undergo a process known as *poling*. Poling involves placing a material under a constant electric field of sufficient magnitude to rearrange the domains in the structure, providing a remanent polarization. The domains with a polarization direction in the same direction as the poling field grow, and the domains with different polarization directions to the poling field shrink. This occurs due to domain wall motion a schematic can be seen in Figure 2.9.

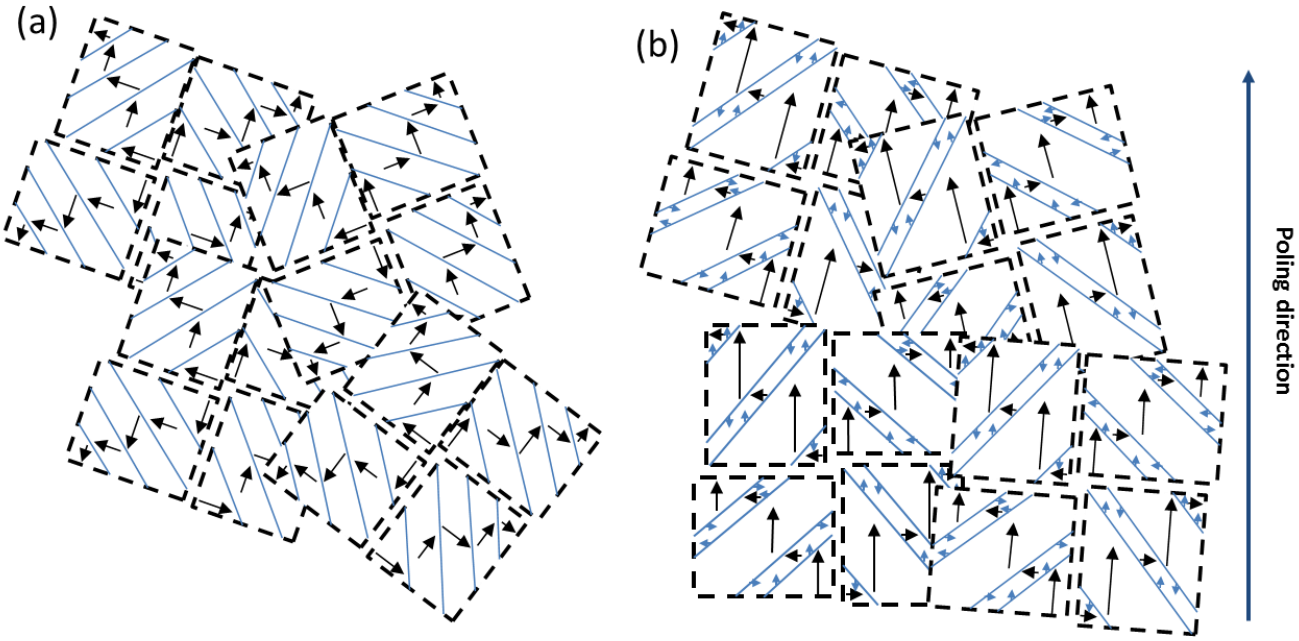

Figure 2.9: Direction of polarization of a (a) un-poled and (b) poled material.

The displacement of the central atom with electric field and the resultant change in shape of the unit cell is the *intrinsic* piezoelectric effect. However, a large part of the piezoelectric effect comes from the *extrinsic* domain wall motion described above (29).

The ideal poling conditions are material specific. The poling voltage is usually 2-3 times the coercive field. Ideally, poling occurs during cooling from above T_C to below, however in practice the T_C is often too high for the high-voltage-breakdown oil that poling occurs in. Poling at phase transition temperatures can result in improved properties when compared to room temperature poling (30).

2.2.9 Ferroelectric Hysteresis

Measuring the polarization as a function of electric field of an un-poled ferroelectric will give rise to a hysteresis loop as seen in Figure 2.10. Prior to an electric field being applied, at the graphs origin, the domains are randomly oriented and the net polarization is zero. As the field is increased, following the direction of the arrows, the domains orientate themselves to align the polarization with the field. At this point the polarization is saturated, P_s. When the applied field is reduced to zero, there is a remanent polarization, P_r. The electric field required to reduce the remanent polarization back to zero is known as the coercive field, E_C. Above the coercive field and the domains reorient themselves to follow the field, now in the opposite direction. The field is reversed again and the loop is complete. P_s is the spontaneous polarization and is calculated by extrapolating along a tangent from the P_{sat} back to zero field. Changing the field strength, the temperature and the frequency of the loop will change its shape.

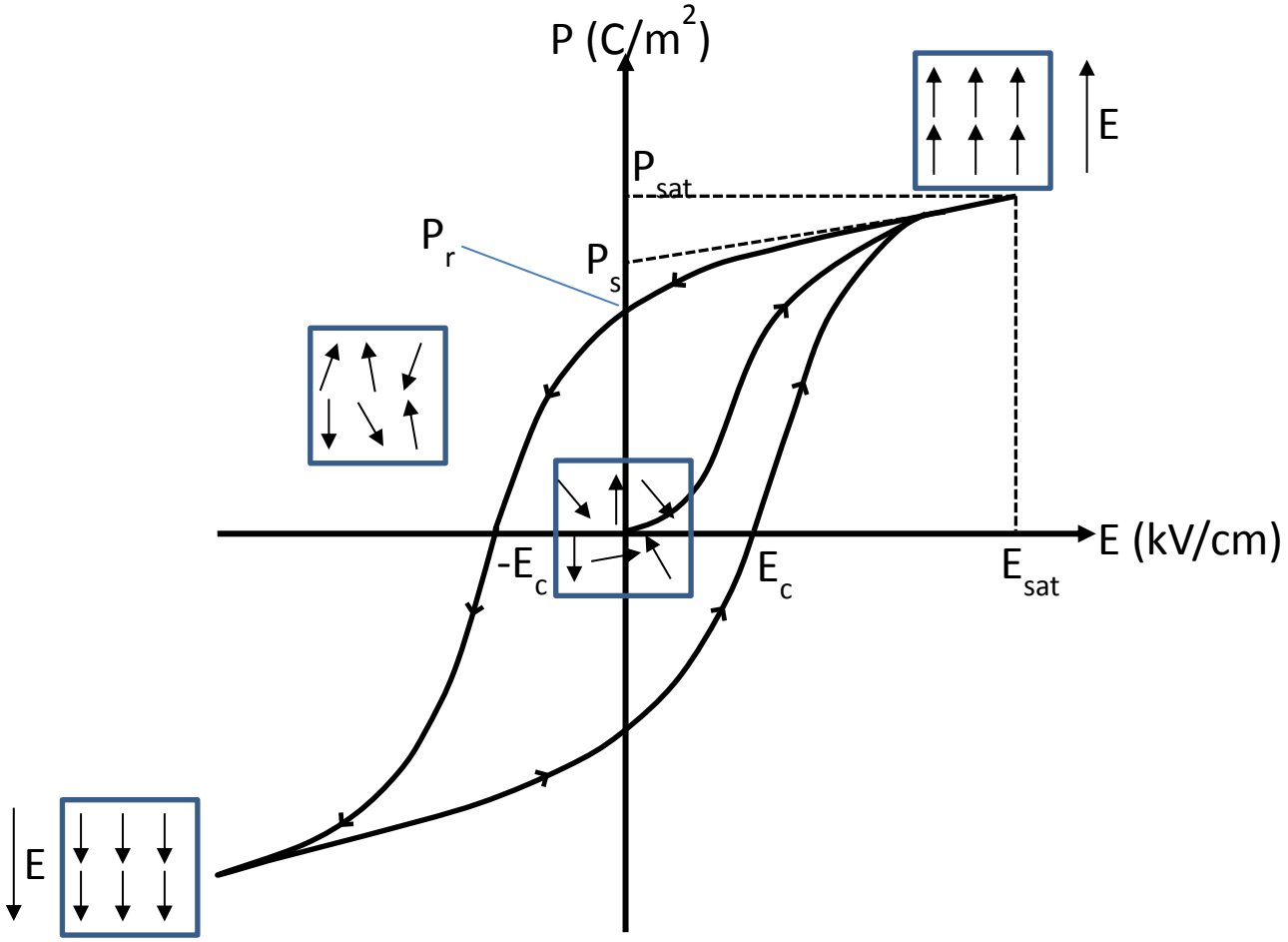

Figure 2.10: Typical polarization-electric field plot for a ferroelectric material, with the domain orientation indicated.

2.2.10 Relaxor Ferroelectrics

Relaxors are a sub category of ferroelectrics, and are categorised by dispersion of the permittivity with frequency and broad phase transitions with temperature (see Figure 2.11). Unlike non-relaxor ferroelectrics, the peak permittivity temperature does not coincide with the Curie point. The 'model' relaxor ferroelectric is lead magnesium niobate, $Pb(Mg_{1/3}Nb_{2/3})O_3$, (PMN) (31).

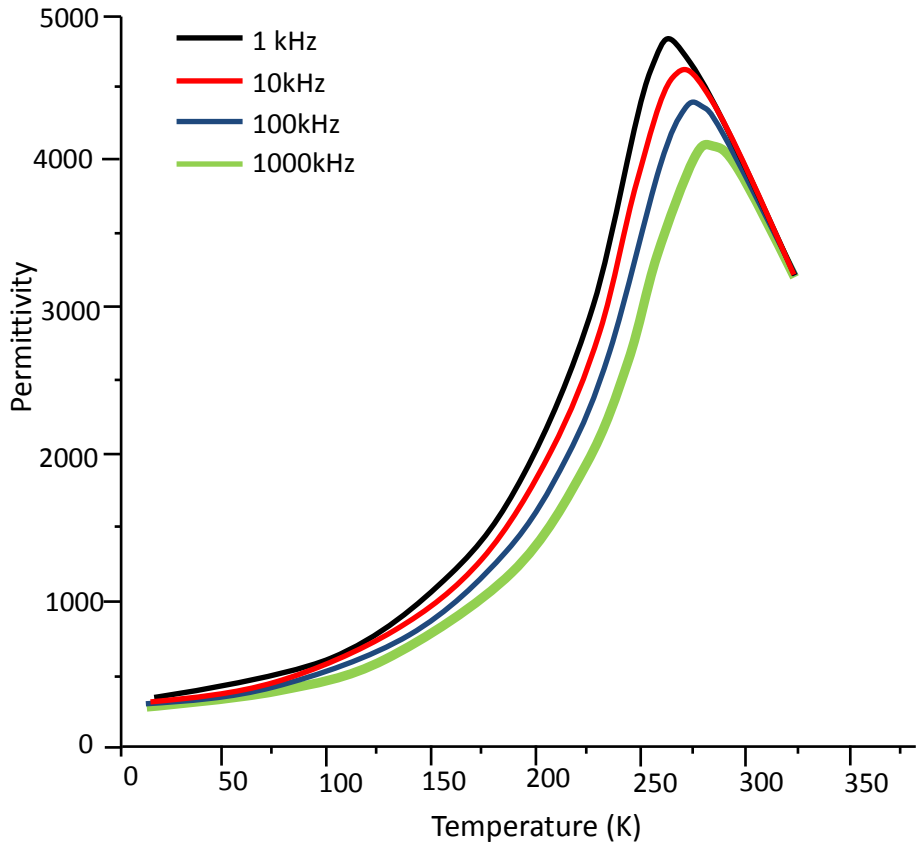

Figure 2.11: Dispersion of permittivity with frequency of a typical PMN sample.

In PMN the B-site is shared by Mg^{2+} and Nb^{5+} cations. This leads to disorder, which has been theorised by Smolensky to produce fluctuations in the Curie point within regions of the sample, thus leading to the diffuse phase transitions (32). Another model of the broadening of relaxor ferroelectric phase transitions, proposed by Cross, is based on an analogy with superparamagnets, now known as the polar region size effect model (33). It describes the mechanism of relaxor behaviour through the formation of polar nano regions (PNRs) below T_C that cause low-symmetry regions within a higher symmetry matrix.

2.2.11 Miscellaneous properties

Density, ρ, is a property used throughout the thesis. It is the mass, m, per unit of volume, V of a sample and is calculated as seen in Equation 2.20.

Equation 2.20 $\boldsymbol{\rho = \frac{m}{V}}$ **Equation 2.20**

The Archimedes principle is an accurate way of obtaining the density of a sample as it gives an accurate volume measurement. However, this volume is usually obtained by submerging the sample in water which cannot be used with potentially soluble samples. Therefore the geometric density is measured. For a round sample, this involves measuring the thickness, t, and diameter, d (or 2r), of the sample and calculating the volume,V, by:

$$\boldsymbol{V = (\pi r^2)\, t} \qquad \textbf{Equation 2.21}$$

Or for a cuboidal sample, multiplying the length, l, width, w, and thickness, t;

$$\boldsymbol{V = l * w * t} \qquad \textbf{Equation 2.22}$$

The geometric volume is then used to calculate the density. The Archimedes principle is more accurate as it can account for any voids or holes within the sample as well as the roughness of the surface or any irregularities, whereas the geometric density does not.

The elastic constant, E, or Young's modulus of a material is the ratio between stress, σ, and strain, ε in a material under uniaxial deformation and us given as;

$$\boldsymbol{E = \frac{\sigma}{\varepsilon}} \qquad \textbf{Equation 2.23}$$

It is the measurement of elasticity or stiffness of a material.

2.3 Applications

Piezoelectric and ferroelectric materials convert electrical energy into mechanical energy and vice versa. This phenomenon can be used in many different applications, the global demand for piezoelectric devices was valued at approximately $21.6 billion in 2015. With the industrial and manufacturing industries having the biggest demand, followed by the automotive industry (34).

A device that converts a mechanical stress into an electrical signal is classed as a sensor and a device that converts an electrical signal into mechanical movement is an actuator. Devices that use piezoelectric materials are known as transducers however, the term is also used to describe a device which uses both conversion from mechanical to electrical and electrical to mechanical energy in one.

Table 2.2: A table of different devices and applications that use the piezoelectric effect.

Device	Applications
Sensor – uses the direct effect	Pressure sensor Engine knock sensor
Actuator – uses the converse effect	Micropositioning Inkjet printing Fuel Injection
Transducer – uses a combination of both effects	SONAR Ultrasound Scanners Parking Sensors
Generator	Spark igniters Energy Harvesting
Resonator – uses materials under resonance	Microbalance Quartz Clock

3. Literature Review

This chapter aims to cover a history of piezoelectric materials from humble Rochelle salt, through the discovery of Barium Titanate, to the foundation of high performance materials such as PZT and single crystal materials. It will then focus on why the discovery of a lead-free alternative to PZT has such significance, and review the literature that has been written since the search began.

3.1. The History of Piezoelectric Materials

3.1.1. Quartz, Rochelle salt, and Early Piezoelectric Materials

The Curie Brothers discovered piezoelectricity in the materials; zinc blende, sodium chlorate, boracite, tourmaline, calamine, topaz, tartaric acid, cane sugar, Rochelle salt and quartz in 1880 (35). Paul Langevin developed the first practical application of the piezoelectric effect making an acoustic wave generator using a quartz crystal based transducer during World War I. Quartz crystal was then replaced by Rochelle Salt in the underwater sound transducers at the beginning of World War II (36).

Quartz is used most commonly today as a crystal oscillator, which allows for a much more accurate clock than a mechanical clock. It is also used in quartz crystal microbalances, where the resonant frequency changing under mechanical load allows for very precise measurements of small masses. Rochelle Salt is no longer used for piezoelectric or ferroelectric applications, but has found its use as a laxative and also as a combustion accelerator in cigarette papers (37).

3.1.2. Barium Titanate

Barium titanate was the first ferroelectric perovskite to be discovered (38). It was independently discovered in three different countries, by Wainer and Salomon in the USA,(39) by Ogawa of Japan (40) and Vul in Russia (41, 42). Its ferroelectricity and high dielectric properties were discovered by Thurnauer and Deaderick at the American Lava Co in 1941 (43). Below -90°C, barium titanate has a rhombohedral structure, between -90°C and 5°C it has an orthorhombic structure, this changes to a tetragonal structure

at 5°C which remains until 120°C, which is the Curie point of barium titanate, at which point it becomes cubic (44).

The first commercial use for barium titanate was in phonograph pickups in 1947 (18). Due to its high dielectric, and low loss characteristics, barium titanate is widely used in multilayer capacitors today (38).

3.1.3. Early Niobate solid solutions

Lead niobate was discovered to be piezoelectric in 1952 (45). It is a member of the tungsten bronze family. It found some uses in non-destructive testing and medical testing, however its high porosity and low mechanical strength properties have prevented it from being further developed as a system (46). After the discovery of lead niobate, several piezoelectric niobate solid solution systems were found (18).

3.1.4. Lead Zirconate Titanate (PZT)

The most important and most popular piezoelectric material was discovered by Shirane, Suzuki and Takeda in 1952 (47). Where they determined the phase diagram, and measured the excellent piezoelectric properties. The electromechanical properties of PZT were first measured by B. Jaffe *et al* in 1954 (48).

PZT is a solid solution of ferroelectric lead titanate ($PbTiO_3$) and anti-ferroelectric lead zirconate ($PbZrO_3$) and has a perovskite structure. By varying the ratio of Zr:Ti atoms, it is possible to change the phase of the material. Zirconium rich compositions (Zr:Ti > 54:46) are rhombohedral, and titanium rich compositions (Zr:Ti < 48:52) are tetragonal (49). A Zr:Ti ratio within these boundaries will comprise of a coexistence of rhombohedral and tetragonal phases, and an enhancement of the piezoelectric properties seen in Figure 3.1 (48) .

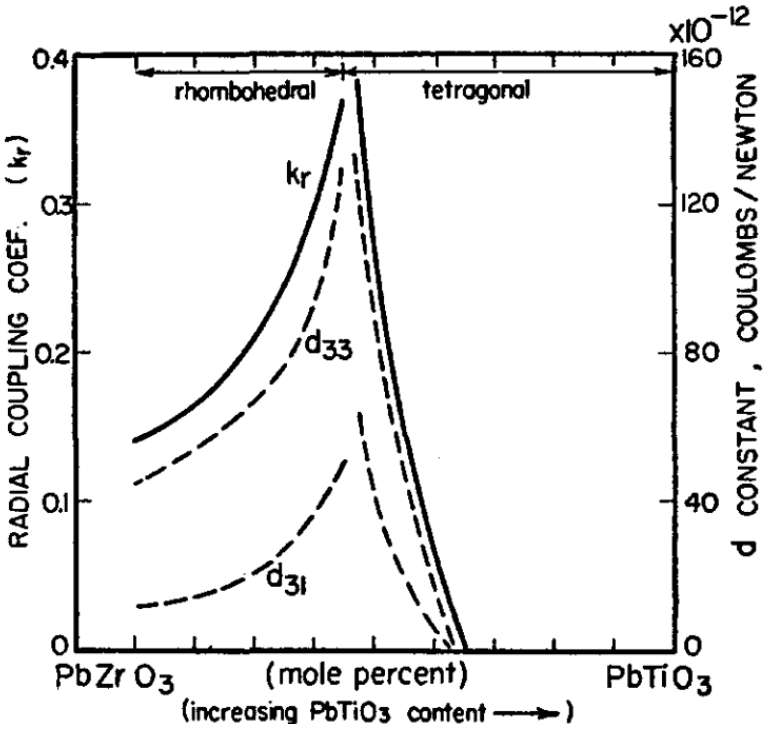

Figure 3.1: Property enhancement of PZT at the MPB.

3.1.4.1 The phase diagram of PZT throughout history

The phase diagram of PZT has changed significantly over the decades since its original conception by Shirane *et al* 1952 (47).

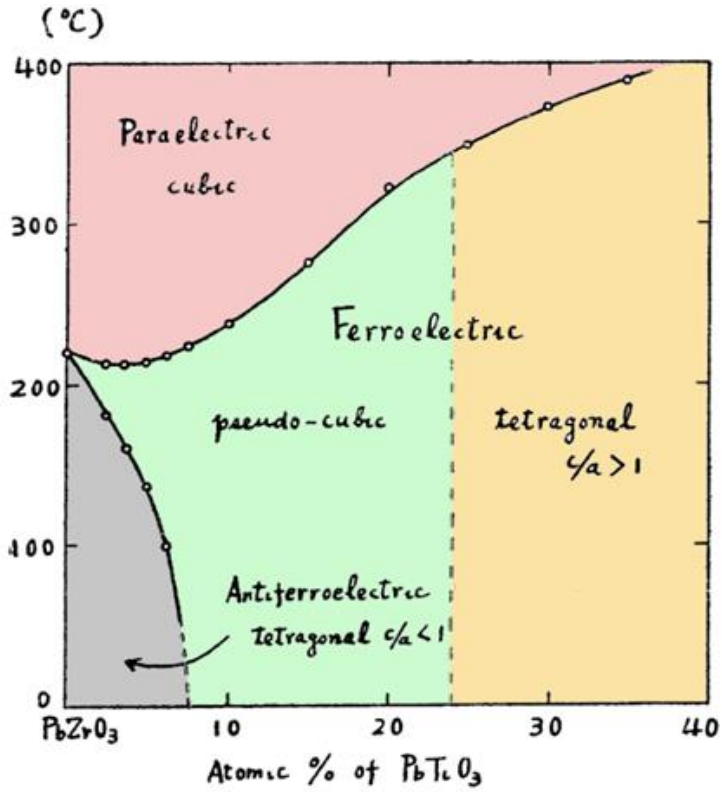

Figure 3.2: Original phase diagram of PZT by G. Shirane et al.

The original phase diagram of PZT by Shirane *et al* in 1952 can be seen in Figure 3.2. The phase diagram does not include the 48:52 MPB that is found in the later phase diagrams, however it does include a pseudocubic ferroelectric to tetragonal ferroelectric phase boundary that is not present in later phase diagrams. An antiferroelectric temperature dependant phase boundary is found below ~8 atomic percent $PbTiO_3$ is included in the phase diagram, and the paraelectric cubic phase can also be seen above ~200°C, with the phase transition temperature increasing with $PbTiO_3$ substitution.

A year later, E. Sawaguchi expanded the phase diagram to include the full solid solution, this can be seen in Figure 3.3 (50). The pseudocubic ferroelectric phase between ~8 and ~25 atomic percent of $PbTiO_3$ was identified as a rhombohedral phase and the phase boundary to the tetragonal phase was moved to ~45 atomic percent of $PbTiO_3$, seen as a near perfectly vertical line. The antiferroelectric phase was also split into two.

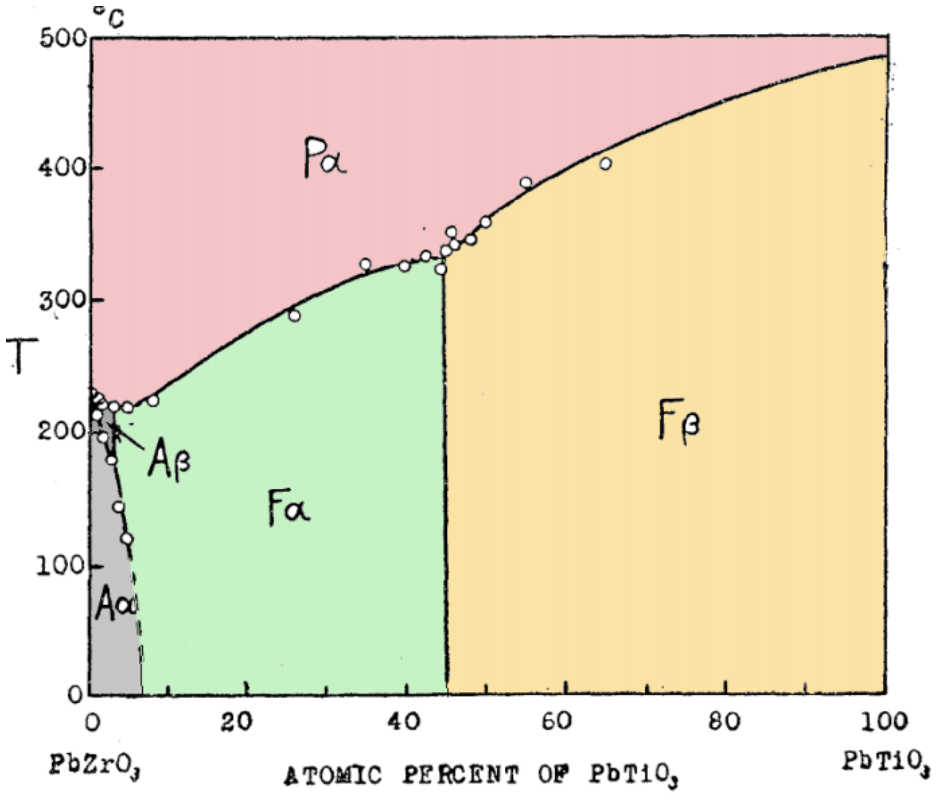

Figure 3.3: The adapted phase diagram of PZT by E. Sawaguchi.

By 1971 the resolution of the phase diagram had improved (Figure 3.4) (18). The rhombohedral phase was split into high temperature and low temperature phases, as a difference in the octahedral tilt was observed at these different temperatures. The near perfectly vertical MPB found in the E. Sawaguchi phase diagram was tilted slightly to accommodate the variation in properties over the different Zr:Ti ratios. The tetragonal antiferroelectric phase was decreased in size.

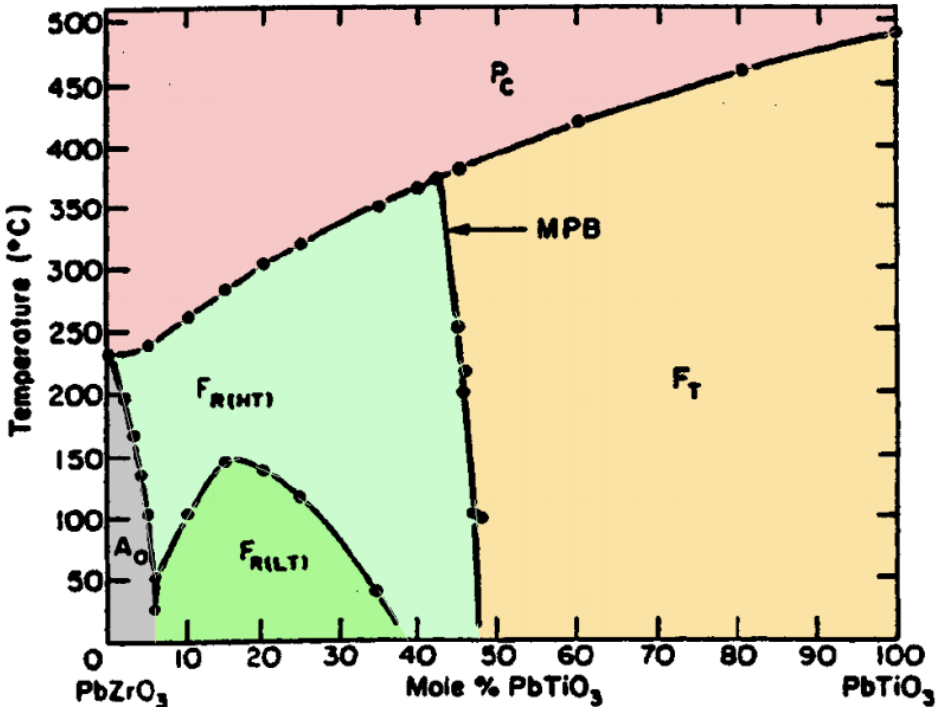

Figure 3.4: The phase diagram of PZT adapted further by B. Jaffe et al.

This phase diagram was widely accepted by the ceramic community until a monoclinic phase was observed by B.Noheda *et al* in 1999 (Figure 3.5) (51). The monoclinic phase was found using high resolution synchrotron x-ray powder diffraction, and can be seen at the 'MPB' between the rhombohedral and tetragonal phases. The observation of a monoclinic phase found at the MPB of PZT lead to the development of a different model to describe why the piezoelectric properties peak at the 'MPB' (21).

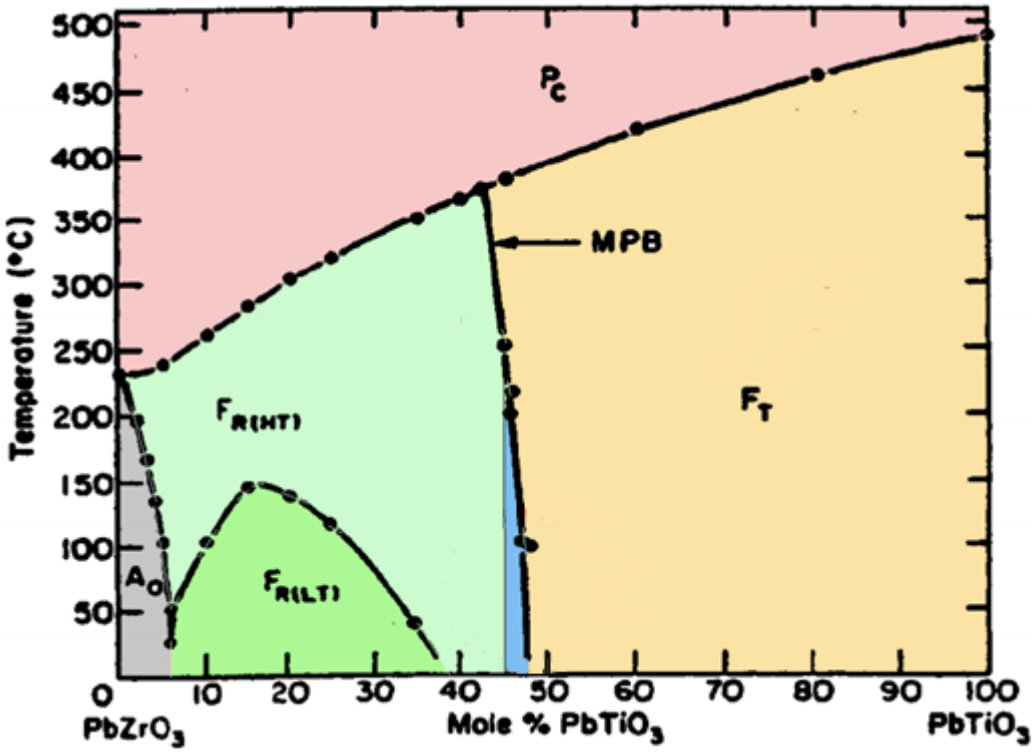

Figure 3.5: The phase diagram displaying the monoclinic phase found in PZT by B. Noheda et al.

It was proposed by A.M Glazer *et al* that there was no morphotropic phase boundary at all, and that in fact both the rhombohedral and tetragonal phases are monoclinic and exhibit different ranges of disorder (52). Figure 3.6 shows how this would appear as a phase diagram.

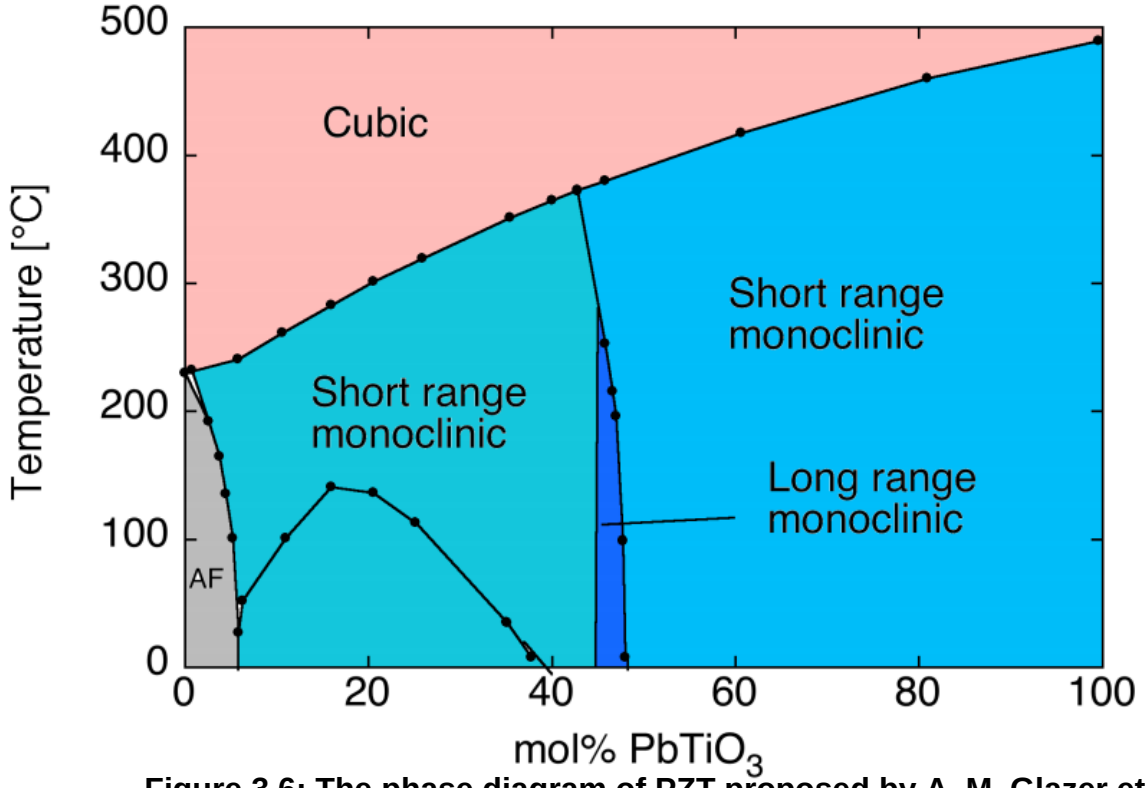

Figure 3.6: The phase diagram of PZT proposed by A. M. Glazer et al.

Finally the most recent phase diagram of PZT was developed by R. Eitel and C. A. Randall in 2007 can be seen in Figure 3.7(53). It splits the monoclinic phase observed by B.Noheda *et al* in two and also introduces a further monoclinic phase between the rhombohedral ferroelectric phase and the orthorhombic antiferroelectric phase.

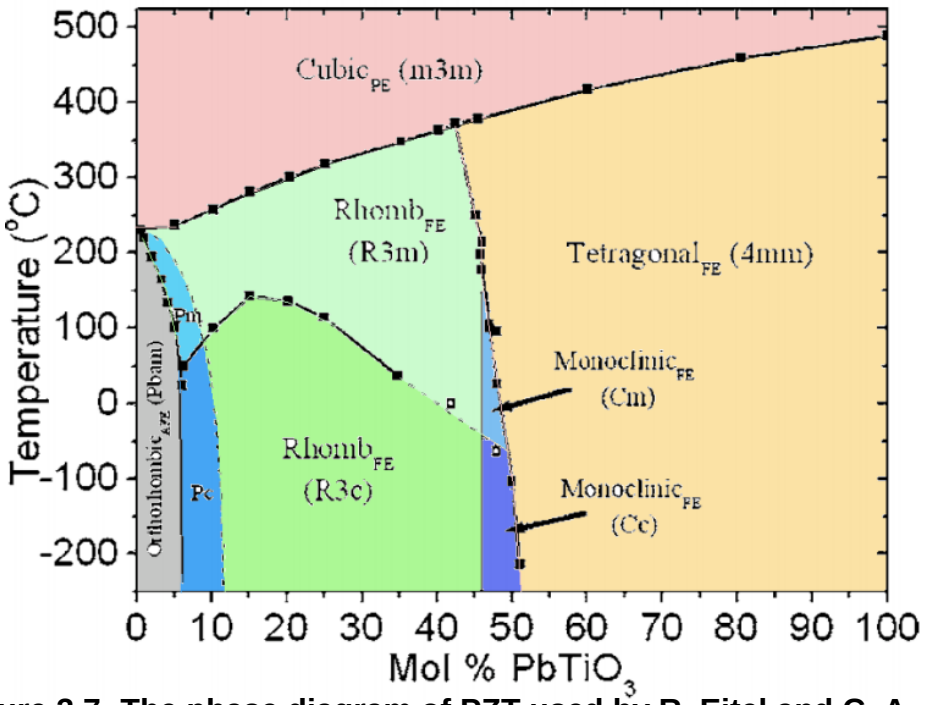

Figure 3.7: The phase diagram of PZT used by R. Eitel and C. A. Randall.

3.1.4.2 PZT Conclusion

The difference in phase diagrams through the years can not only be attributed to improved characterization techniques, but also a development of the understanding of the MPB as a concept. Different models have been used through the decades, leading to different conclusions. The differences are a testament to the scientific process and a reminder that conclusions drawn are not absolute.

In many ways the discovery of PZT has been as much of a hindrance to piezoelectric material research as much as it has been an asset. The existence of such an excellent material will have led to complacency in both research and industry, because there was less of a demand to find alternative materials. There is no doubt that PZT led to a decrease in the intensity of research and development in piezoelectric materials which was only reversed by the discovery of notable single crystal materials, and fairly recent sanctions imposed by the European Union on the use of lead.

3.1.5. Single Crystal Materials

Relaxor lead titanate (PT)-based single crystal have much higher properties than that of PZT. The first PT-based single crystal was grown in 1981 by flux method by Nomura *et al* (54), and was reported to have an extremely high piezoelectric constant and coupling factor in the (001) direction. The solid solution was of $Pb(Zn_{1/3}Nb_{2/3})O_3$-$PbTiO_3$ (PZN-PT). Later, Shrout *et al* grew a single crystal of $Pb(Mg_{1/3}Nb_{2/3})O_3$-$PbTiO_3$ (PMN-PT) also by flux method (55). These successfully grown single crystals sparked a wide interest in the ceramics industry due to their high properties, and several research groups and companies were formed to further research this technique and materials (56). The Shanghai Institute of Ceramics in China and the Rockwell Science Centre in Stanford University, USA, are just two of several groups who went on to grow very large single crystals or PMN-PT by the Bridgman method as opposed to Flux Growth.

Although PZN-PT and PMN-PT (first generation single crystals) have many desirable properties, they also have a low coercive field (2.5kV/cm) and a low Curie point of ~130°C. These properties can be a detriment where the application involves a high excitation signal or elevated temperatures (57). As a result the ternary system of $Pb(In_{1/2}Nb_{1/2})O_3$-$Pb(Mg_{1/3}Nb_{2/3})O_3$--$PbTiO_3$ (PIN-PMN-PT) was developed which had an elevated coercive field and an increased Curie temperature due to the addition of lead indium niobate (58). This system became known as second generation single crystals.

The effect of MnO_2 addition to PIN-PMN-PT was investigate by Zhang *et al,* the idea behind this was to induce the 'hardening' effect that occurs when manganese is added to PZT. The results were a success, and the addition of manganese to the system improved the mechanical quality factor (59). This system became known as the third generation single crystals.

It has been postulated that single crystals of PZT would have better piezoelectric properties than their polycrystalline counterpart. However, the growth of PZT single crystals has been attempted by numerous groups, with limited success (60).

3.1.6. European Union Lead Restrictions and Exemptions

Since the formation of the Restriction of Hazardous Substances (RoHS) and the Registration, Evaluation, Authorisation, and Restriction of Chemicals (REACH) in 2006 and 2007 respectively, there has been an increase in research into lead-free piezoelectric materials (2, 3, 61). The sanctions limit the amount of lead that can be included in a material or product to 0.1% by weight, and also limit the use of lead oxide in processing procedures. The restrictions are in place in order to reduce the environmental impact of lead containing electrical equipment and devices at the end of its lifecycle, as well as to protect the workforce at the processing factories.

As the market leader PZT is around 50% by weight lead, there is a need to find an alternative material. However, since no credible or reliable, lead-free equivalent has been found, piezoelectric materials have an exemption to these restrictions (62). This exemption is due to expire in July 2021, having recently been extended for an extra 3 years.

The extension must be applied for each time it expires and is not automatically granted. Questions must be asked to find out if a reliable alternative has been found, and whether this alternative is worse for the environment than PZT. Industry and research institutes must also prove that an alternative is actively being searched for.

The restriction of lead in products and the need to search for an alternative is a major reason why there has recently been a huge increase in piezoelectric materials research, and the main reason behind the project as a whole.

3.2. The Search for a PZT Alternative

In order to find an alternative to PZT it is necessary to understand why PZT is such a versatile and successful material. The coexistence of a rhombohedral phase and a tetragonal phase is believed to be the origin of these excellent piezoelectric properties. The morphotropic phase boundary (MPB) between these two phases results in a material which is much easier to pole due to the different states that the polarization can enter. The MPB is present up to the high temperature of ~350°C, which is the reason that PZT has such high temperature stability. This mechanism for high properties was believed to be the case until the monoclinic phase was found in the same area as the MPB.

L. Bellaiche *et al* provided and explanation for the higher piezoactivity in the region around the MPB after the discovery of the monoclinic phase. They stated that the monoclinic phase acted as a bridge between the rhombohedral and tetragonal phases. This was indicated by “the continuous rotation of the polarization as a function of composition” (63).

In order to replicate the MPB of PZT in a lead-free alternative, research groups dope base materials. This affects the phase transition temperatures of the material, with the aim to bring both the rhombohedral phase and tetragonal phase together to co-exist at the same temperature. Each of the starting materials have their advantages and disadvantages and each will be discussed. The starting base materials are usually either titanate or niobate based and therefore, the literature review below has also been split up into these categories.

.

3.2.1. The Titanates

Promising titanate based lead-free potential alternatives to PZT usually have excellent piezoelectric properties but suffer from very low Curie points or low depolarization temperatures. This means that the material only has a very narrow range gap where it may be considered for use. They also require large electric fields to activate their large strain, and can suffer from significant hysteresis. Many studies have been done to try and reduce the required electric field (64, 65).

3.2.1.1 Barium Titanate - $BaTiO_3$

Barium titanate as mentioned previously has a high dielectric constant, of 1100, but a low d_{33} of 190pCN^{-1}, which makes it an excellent material for capacitors (18, 64, 66). It is also used as a model system for fundamental studies (67-69). For instance, the process of poling was discovered using barium titanate (70, 71). In general, as the grain size of the barium titanate crystal in a sample decreases, the d_{33} increase. Nanoscale particles of barium titanate prepared using microwave sintering and the d_{33} observed reached 350pCN^{-1} (72). Another system, with a nanocrystalline structure has an extremely large permittivity that was measured in the ~10^6 magnitude. (73). Lowering the size of the particles is not the only way to increase the d_{33}, hydrothermally synthesised barium titanate with particle size 1-2µm gave a d_{33} of 460pCN^{-1} (74, 75). Texturing of barium titanate can also improve the d_{33}, [110] grain oriented barium titanate with submicron particles gave a d_{33} of 788pCN^{-1}, indicating that structural engineering of the sample is very important. Wada *et al* made single crystals of barium titanate and found that applying an electric field can cause the phase to transition from tetragonal to monoclinic with 10kV/cm and from tetragonal to rhombohedral with 30kV/cm (76).

Barium titanate is generally used as a dopant for other systems as it has desirable properties but a fundamentally low Curie temperature. However, much has been learnt from this basic perovskite system.

3.2.1.2 Sodium Bismuth Titanate - $Na_{0.5}Bi_{0.5}TiO_3$

Sodium bismuth titanate (NBT) was discovered by Smolenskii *et al* in the 1960s (77). It received little attention as a material until the lead free movement began to gain momentum around 20 years ago. Jones and

Thomas found that NBT was rhombohedral with the space group R3c at room temperature, which became tetragonal with heating and then finally cubic with further heating (78). Pure NBT usually has a d_{33} between 57-64pCN^{-1} (79) but can be as high as 78pCN^{-1} depending on the synthesis process. Although the d_{33} is similar to barium titanate, the Curie temperature is much higher, 325°C (80). However NBT exhibits a low depolarization temperature of 187°C, which has been attributed to the presence of an antiferroelectric phase (81, 82), although some disagree, claiming the phase is not completely antiferroelectric (80).

The high sintering temperature of greater than 1200°C can lead to losses in bismuth which can further lead to high conductivity. Hiruma *et al* found an increased resistivity when excess bismuth is added to reduce losses (80).

3.2.1.2.1 Doped NBT

Herabut and Safari added La_2O_3 to NBT forming $(Na_{0.5},Bi_{0.5})_{(1-1.5x)}La_xTiO_3$. The d_{33} went from 64pCN^{-1} in pure NBT to 92pCN^{-1} with 0.6mol% addition (83). Increasing the amount of lanthanum added further leads to reduced dielectric constant due to the phase changing from rhombohedral to pseudocubic.

Li *et al* added $NaNbO_3$ to NBT forming $[Na_{0.5(1+x)}Bi_{0.5(1-x)}](Ti_{1-x}\text{-}Nb_x)$ with the soft additive Nb^{5+} entering the B site and the hard additive Na^+ on the A site. The d_{33} increased with an increase in $NaNbO_3$ up to 2mol% where it reached a maximum of 88pCN^{-1}. However the dielectric constant continued to increase past 2mol% (84).

Kounga *et al* found a coexistence of phases between ferroelectric rhombohedral phase and an antiferroelectric tetragonal phase when 6-7mol% potassium sodium niobate (KNN) was added to NBT (85). Conversely, when 2-3mol% NBT is added to pure KNN, an orthorhombic-tetragonal phase coexistence is formed. This material was measured to have a d_{33} of 195pCN^{-1} and an electrocoupling of 43% (86).

Naga *et al* added $BiFeO_3$ to NBT (87). The T_C increased from 325°C to 340°C and the k_p went from 16.8% to 33.6%. There was no coexistence of phases, only a single rhombohedral phase was present.

A solid solution of NBT-x$Ba(Ti,Zr)O_3$ was made by Peng *et al* (88). The d_{33} increased until reaching a maximum of 147pCN^{-1} at 9mol%. The T_C decreased linearly with an increase in BTZ, however after 9mol% it began to rise again. It was unclear why.

A study of different substituted levels of K^+, Na^+ and Li^+ in $Bi(Na,K,Li)TiO_3$ was performed by Lin *et al.* They found that the more K^+ in the material the larger the piezoelectric constant which reached a peak of $143pCN^{-1}$ (89).

3.2.1.2.2 NBT –$xBaTiO_3$

Takenaka *et al* found an MPB when 6mol% of $BaTiO_3$ is added to NBT (90). This formed the bases of a whole new family of lead-free systems, NBT-BT6 or BNBT. Adding 6mol% of $BaTiO_3$ to NBT causes the d_{33} to rise from $64pCN^{-1}$ to $129pCN^{-1}$ (91). Wang *et al* and Li *et al* also noticed higher piezoelectric properties around the MPB (92, 93). Daniels *et al* found that an electric field can induce a phase transition from rhombohedral to tetragonal in BNBT (61). BNBT also has a high bending strength of 200MPa, which is x2-3 times better than PZT (79).

BNBT doped with cerium oxide has improved piezoelectric properties (94, 95). Ce^{3+} has a radius of 1.18Å and therefore occupies the A site, where as Ce^{4+} has a radius of 0.94Å and occupies the B site. Adding lanthanum to BNBT results in the La^{3+} ion entering the A site space, due to the radius and its valence. This results in aberrance of the crystal structure, which benefits reorientation of domains and also lowers grain growth (91). Adding 0.5mol% of both lanthanum and cerium to BNBT improves the d_{33} from $129pCN^{-1}$ to $162pCN^{-1}$ and the dielectric constant from 626 to 831(94).

Manganese addition to BNBT causes the T_C to drop rapidly, but at 0.56mol%, the piezoelectric constant reaches a maximum of $160pCN^{-1}$. This is due to an increase in tetragonality and the smaller cation leading to a slack lattice which enhances 90° domain motion (96).

3.2.1.2.3 NBT-KBT

Potassium bismuth titanate, $K_{0.5}Bi_{0.5}TiO_3$ (KBT) was also discovered by Smolenskii *et al* in the 1960s (77). It is tetragonal at room temperature, depolarizes at 270°C, and has a T_C of 370°C. It is difficult to produce dense samples of KBT due to potassium loss, this also makes it hard to pole. Hiruma *et al* used excess bismuth as a sintering aid and formed a material with a d_{33} of $101pCN^{-1}$ (97). Adding barium titanate to KBT can also improve the density. When up to 10mol% barium titanate is added to KBT, a dense, textured material, with a d_{33} of $85pCN^{-1}$ can be formed (98)

A solid solution of NBT-KBT was made by Elkechai *et al* in 1996 (99). An MPB between the rhombohedral NBT and the tetragonal KBT was found

between 16-20mol% KBT. This MPB was also found by Sasaki *et al* (100). The d_{33} values at the MPB range from 140-192pCN^{-1} and the T_C ranges from 280-300°C. An issue with this system is that although the T_C is high, the depolarization temperature is 140°C (99, 101). The highly volatile nature of the K^+,Na^+ and Bi^+ ions makes sintering conditions very important (102). Zhang *et al* reported that a 40°C change in sintering temperature could be the difference between a d_{33} of 155pCN^{-1} and 192pCN^{-1}.

3.2.1.2.4 NBT-KBT-BT

The ternary system $(Na_{0.5}Bi_{0.5})TiO_3$-$(K_{0.5}Bi_{0.5})TiO_3$-$BaTiO_3$ was made by Li *et al* in the ratio (1-3x)NBT-2xKBT-xBT (103). The dielectric constant increases with x until reaching a maximum d_{33} of 150pCN^{-1} at x=0.035. The material $0.90(Na_{0.5}Bi_{0.5})TiO_3$-$0.05(K_{0.5}Bi_{0.5})TiO_3$-$0.05BaTiO_3$ or NBT-KBT-BT5,is currently being used as a driving element in a cymbal actuator and is just as effective as PZT (104).

3.2.1.3 Barium Calcium Titanate Zirconate (Ba,Ca)(Ti,Zr)O_3

Barium calcium titanate zirconate (BCTZ) lead-free systems have some of the highest d_{33} measurements of any lead-free polycrystalline materials. W. Liu and X. Ren made (1-x)Ba($Ti_{0.8}Zr_{0.2}$)O_3-x($Ba_{0.7}Ca_{0.3}$)TiO_3 and measured a high d_{33} of 620pCN^{-1}. They found that the material had a triple point of a cubic paraelectric phase, a ferroelectric rhombohedral and a ferroelectric tetragonal phases (see Figure 3.8) (105). The high d_{33} was attributed to the composition at room temperature being very close to that of the tricritical point which was found at 32% BCT, and 57°C. The authors predicted that a single crystal of BCTZ would have a d_{33} 3-4 times larger between 1500-2000pCN^{-1} (105) The major problem with this system is that the Curie point is very low. The T_C being well below the manufacturing temperatures used for most devices would lead to the need for in-situ poling which is undesirable for manufacturers. However the composition at 50% BCT had a very low coercive field E_C of 0.14kV/mm and an optimised poling regime by Praveen *et al* found that a sample can be poled at 0.42kV/mm which is a relatively low poling voltage, however these were made by the sol-gel process (106).

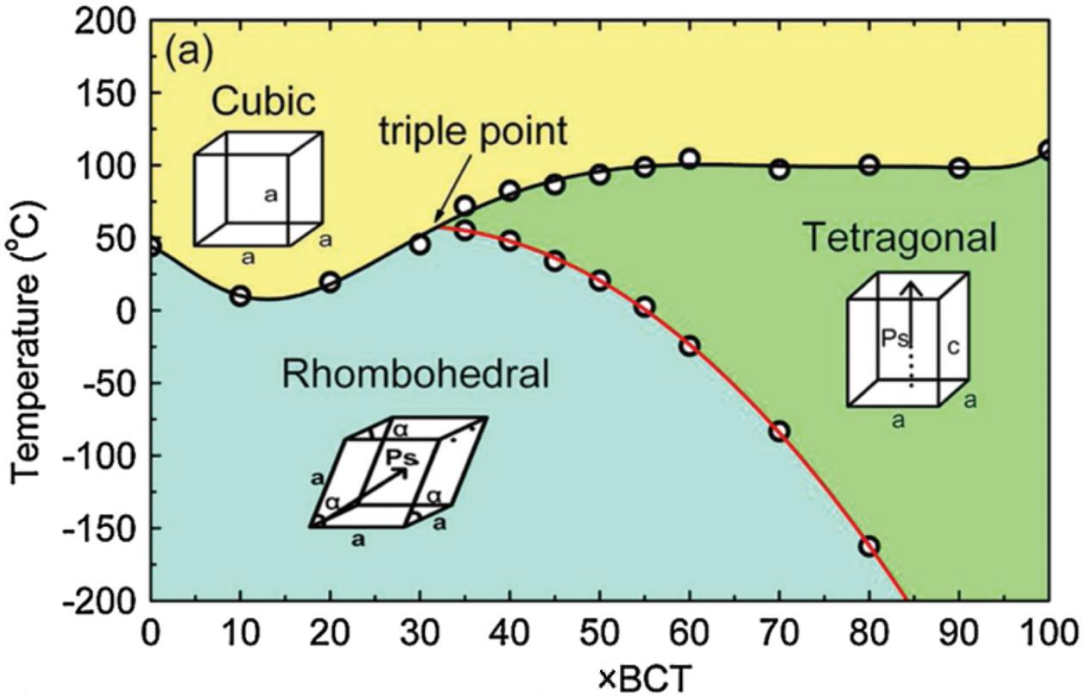

Figure 3.8: Phase diagram of (1-x)Ba($Ti_{0.8}Zr_{0.2}$)O_3-x($Ba_{0.7}Ca_{0.3}$)TiO_3.

3.2.2. The Niobates

Most of the research concerning niobate based materials use $(K_{0.5}Na_{0.5})NbO_3$ as the starting material. Before the literature can be reviewed, it is necessary to understand the end members of this solid solution.

3.2.2.1 Potassium Niobate – $KNbO_3$

Potassium niobate was discovered to be piezoelectric by Matthias in the 1951 (107).The phase transitions of potassium niobate are isomorphous to that of barium titanate. It has a Curie temperature of 435°C, below this temperature it is tetragonal until 225°C, between 225°C and -10°C the material is orthorhombic and a temperature further below this results in the material becoming rhombohedral (108). Due to the volatility of potassium in the material, it can be difficult to produce a pure sample (18). It is possible to produce single crystals of potassium niobate which have interesting piezoelectric coefficients along certain directions of the crystal (109).

3.2.2.2 Sodium Niobate – $NaNbO_3$

Sodium Niobate is an antiferroelectric material and therefore does not exhibit a piezoelectric behaviour. It has an orthorhombic crystal structure at room temperature and becomes tetragonal at 370°C. Further increasing the temperature, it becomes cubic at 670°C (110). Pure sodium niobate has more than 7 polymorphs across the whole temperature range (111).

3.2.2.3 Potassium Sodium Niobate – $(K_xNa_{1-x})NbO_3$

The phase diagram of the solid solution of $KNbO_3$ and $NaNbO_3$ was first studied by G. Shirane *et al* in 1954 (112). The phase diagram of the system can be seen in Figure 3.9 (18). The solid solution shows ferroelectricity, and keeps the phase transition sequence of pure $KNbO_3$, up to 90% $NaNbO_3$ (5). The phase transition temperature of the rhombohedral and orthorhombic phases change throughout the system.

Although potassium sodium niobate (KNN) can mean any solid solution within the phase diagram found in Figure 3.9, unless otherwise stated, the solution that 'KNN' will refer to from here on will be $(K_{0.5}Na_{0.5})NbO_3$. Due to the presence of two different orthorhombic phases at this composition, the piezoelectric response of the system is at its maximum, and therefore it is thought to be a good base composition to begin with.

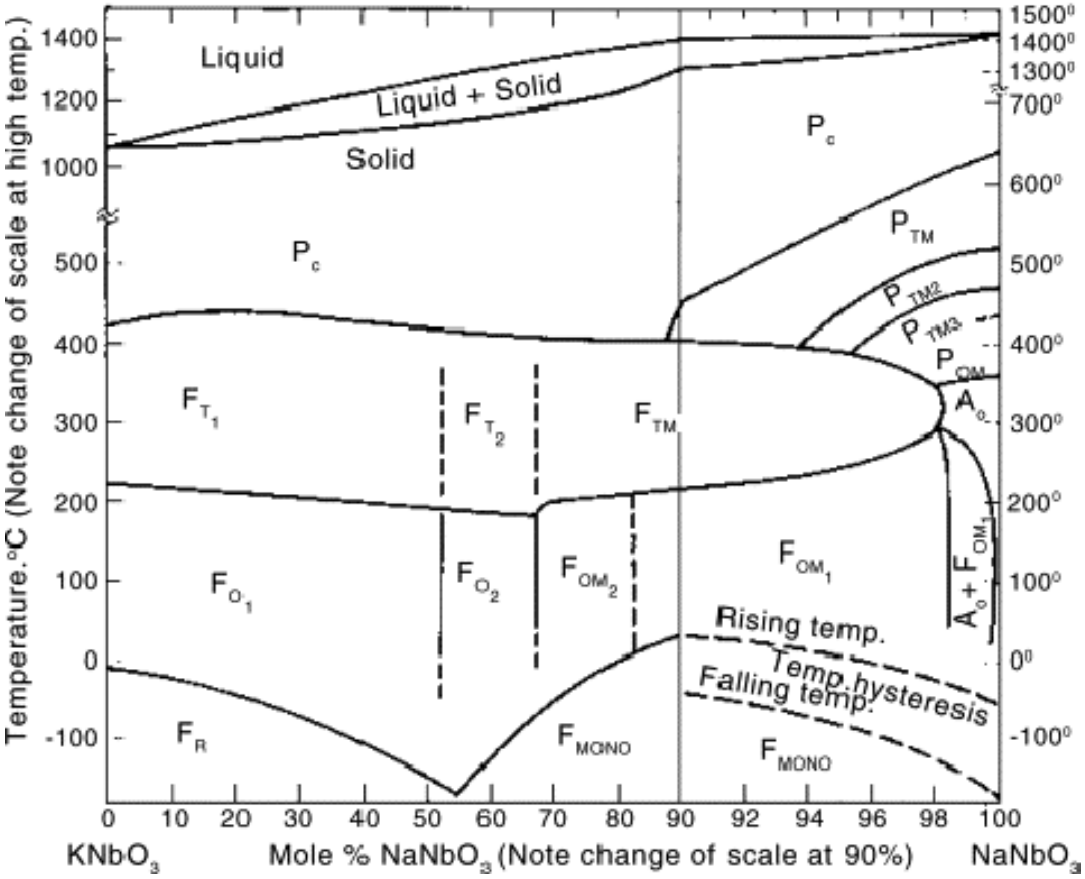

Figure 3.9: Phase diagram of $(K_xNa_{1-x})NbO_3$.

This composition has a Curie point of 420°C. Cooling below this temperature the system is tetragonal (P4mm) until 200°C and then orthorhombic (Amm2) all the way until the temperature reaches -120°C (113). However the primary cell of KNN at room temperature is *monoclinic* with the parameters $a_m=c_m>b_m$. Tellier *et al* did find a small difference between a_m and c_m (0.002Å) with a β angle slightly above 90°. This small difference cannot be seen as a second peak using standard XRD techniques. There has also been a triclinic phase reported in particles with a size of 130nm (114).

The high Curie point makes it a very good candidate for PZT replacement as it has a Curie point even greater than that of PZT. As mentioned previously the volatility of potassium, and also sodium, is one large disadvantage of KNN. The ions are prone to leaving the sample during sintering which can result in lower density and can lead to secondary niobium-rich phases (115). The theoretical density of KNN is 4.62g/cm^3 (116).

KNN based materials came to headline the lead free piezoelectric community after a paper by Saito *et al* was published in Nature in 2004 (117). Saito *et al* optimized lithium, tantalum and antimony additions in KNN and formed $(K_{0.48}Na_{0.52})(Nb_{0.86}Ta_{0.1}Sb_{0.04})O_3$ more affectionately known as LF4. This polycrystalline material has a d_{33} of 300pCN^{-1} and a T_C of 253°C. LF4 was then enhanced by texturing using a reactive grain growth method which grew <001> oriented crystals and had a d_{33} of 416pCN^{-1} and was named LF4T. The high d_{33} in LF4 and LF4T was attributed to the presence of an MPB, which was later discovered by the same group to be a PPT near room temperature (118).

One benefit of using KNN based lead free materials is that they have an inherent compatibility with nickel electrodes, which can help reduce costs (119, 120).

The sintering conditions of KNN are very important and can make it hard to reproduce the same results. Sintering aids can be used to help reduce the sintering temperature, which is important as $KNbO_3$ loses phase stability after 1040°C (121). Different sintering aids give different results and will be discussed in 3.2.2.3.3. Kari *et al* found large dielectric losses in single crystals of $KNbO_3$ which was believed to be due to vacancies left behind by K^+ ions leaving the sample (122). E. Wiesendanger reported that high temperature annealing, above T_C post sintering can reduce losses (123). Another way of reducing the amount of K^+ lost is to include excess alkali carbonates (124, 125). It has also been discovered that reducing the size of the starting reagent powders (126), and the calcined powders (127), can reduce loss of K^+ and Na^+ ions.

Doping KNN changes the phase transition temperatures, a fact which is exploited by research groups as they aim to bring the phase transitions to the operating temperature of the end device, or more generally room temperature. Many different systems and dopants will be discussed however, a very good summary was written by Wu *et al* in (128). To bring the rhombohedral-orthorhombic phase transition (T_{O-R}) up to room temperature, the dopants used are $AZrO_3$ where (A=Ba^{2+}, Sr^{2+} or Ca^{2+}) or $BiBO_3$ where (B=Sc^{3+}, Al^{3+}, Fe^{3+}, or Co^{3+}). To bring the orthorhombic-tetragonal phase transition (T_{O-T}) down to room temperature, the dopants used are $LiCO_3$ where (C=Nb^{5+}, Ta^{5+}, or Sb^{5+}), $Bi_{0.5}D_{0.5}TiO_3$ where (D= Na^+, Li^+ or K^+) or $ETiO_3$ where (E=Ba^{2+}, Sr^{2+} or Ca^{2+}). Dopants that shift T_{O-T} can get a d_{33} as high as 300pCN^{-1}, but most are between 200-250pCN^{-1}. The big

difference in d_{33} is believed to be the ratio of the orthorhombic and tetragonal phases in the sample, but may also be sintering related (129).

Most dopants reduce the T_C of KNN, except for lithium dopants which can increase the T_C up to 500°C (130, 131). It is because of this effect that lithium doped KNN has been studied intently.

3.2.2.3.1 KNN-based Binary Systems

KNN-xLiNbO$_3$

Guo *et al* found a coexistence of an orthorhombic and tetragonal phase at room temperature when 6mol% $LiNbO_3$ was added to KNN. The improved d_{33} of 235pCN^{-1} and coupling factor 44% were believed to be due to this coexistence. However after measuring the Raman-active vibrations it was determined that the KNN-$LiNbO_3$ solid solution was a single orthorhombic phase, and that the NbO_6 octahedra tilting and the formation of a KLN secondary phase showed the appearance of a tetragonal phase (132). Wang et al found that excess K^+ in this system reduced the sintering temperature to below 950°C (133). They made (1-x)($Na_{0.535}K_{0.48}$)NbO_3-x$LiNbO_3$ between x=0.058 and 0.09 and obtained a d_{33} of 280pCN^{-1} and a k_p of 48.3% at x=0.08. This d_{33} however was reduced 15% when the sample was heated up to 100°C, showing that there is a lack of thermal stability in the solid solution. Temperature stability was also a problem when Hollenstein *et al* made lithium doped KNN (134). The d_{31} and k_p factor fell 30% after one heating cycle at 140°C. The temperature stability of the sample can be improved by reducing the T_{O-T} to well below room temperature, or by texturing (135, 136).

KNN-xLiTaO$_3$

Hollenstein *et al* doped KNN with $LiTaO_3$ and measured a d_{33} of over 300pCN^{-1} and a k_p of 52% (137). Guo *et al* found a coexistence of orthorhombic and tetragonal phases when x was between 5-6mol% (138). They measured a d_{33} of 200pCN^{-1} and a k_p of 36%. Saito *et al* measured a d_{33} of 230pCN^{-1} and a k_p of 50% for the same system. Wang *et al* found that the addition of Li and Ta lead to compositional inhomogeneity which may be the cause of the large differences in the properties for the same system in the examples above (139). This inhomogeneity can be reduced by prereacting the tantalum and niobium to form [(1-x)Nb-x$Ta]_2O_5$. Silver was

also added to the system and further improved the d_{33} to 252pCN^{-1}, whilst also increasing the T_C to 438°C (140).

KNN-xLiSbO$_3$

Yang *et al* found that as the amount of $LiSbO_3$ is increased in KNN, the d_{33} and k_p increase and the T_C decreases. This is the case until the d_{33} reaches a maximum, and then further addition reduces the piezoelectric properties (141). When 5mol% $LiSbO_3$ is added to the T_{O-T} shifts to near room temperature (35°C), and the d_{33} can be between 250-265pCN^{-1} (142). Zhang *et al* found the maximum properties when x=0.052, forming a sample with 95% theoretical density. The electromechnical coupling factors of this composition were k_p 27%, k_{33} 62%, and k_{31} 30%. The piezoelectric coefficients were d_{33} of 265pCN^{-1} and a d_{31} of -116pCN^{-1} (143).

When the K:Na ratio is varied and $LiSbO_3$ is added to $(K_{0.48}Na_{0.52})NbO_3$ a coexistence of orthorhombic and tetragonal was found between 0.04≤x≤0.06. At 5mol% the properties were d_{33} 270pCN^{-1}, k_p 27.2%, ε_r 1412, tanδ 2.8%, P_r 25.7μC/cm^2, E_c 11.1kV/cm, the T_{O-T} was 35°C and the T_C was 364°C (144). Further changing the ratio, but keeping the $LiSbO_3$ at 5mol% in the system $0.95(K_xNa_{1-x})NbO_3$-$0.05LiSbO_3$ it can be seen that the dielectric and piezoelectric properties strongly depend on potassium content. At x=0.40 the properties were d_{33} 280pCN^{-1}, k_p 49.4%, ε_r 1463, tanδ 2.3%, P_r 30.8μC/cm^2, E_c 14.0kV/cm, the T_{O-T} becomes 25°C and the T_C remains 364°C (145). Zhang *et al* measured the temperature stability of $LiSbO_3$ doped KNN and found that the d_{33}* was 355pCN^{-1} at room temperature, became 250pCN^{-1} at 50°C (146).

Saito *et al* formed a ternary system of KNN-LiTaO3-LiSbO3 and measured a d_{33} of 373pCN^{-1} (117).

KNN-xCaTiO$_3$

The T_{O-T} was reported to be reduced to below room temperature after 1wt% $CaTiO_3$ was added to KNN, the d_{33} of 210pCN^{-1} was stable between -50°C and 200°C (136, 147). Park *et al* found a coexistence of orthorhombic and tetragonal phase at x=0.05 with a d_{33} of 241pCN^{-1}, a k_p of 41% and the T_C measured was 306°C (148).

KNN-xBaTiO$_3$

Wang *et al* added 6mol% of $BaTiO_3$ to KNN and measured a d_{33} of 150pCN^{-1}, a k_p of 34% and the T_C remained at 279°C. This change in properties was attributed to an orthorhombic-tetragonal phase coexistence (147).

The addition of both $CaTiO_3$ and $BaTiO_3$ to KNN broadens the T_C peak when the permittivity is measured as a function of temperature, and continues to broaden the more dopant that is added. This indicates that there is a diffuse phase transition from tetragonal to cubic and from ferroelectric to relaxor (148).

KNN-xAgNbO$_3$

Lei *et al* added $AgNbO_3$ to KNN between $0 \leq x \leq 0.4$. At $x=0.2$ the d_{33} was measured to be 186pCN^{-1}. This was without any significant change to the T_{O-T} which stayed at 170°C (149).

KNN-AZrO$_3$ (A= Ba, Ca, Sr)

R. Wang *et al* studied the effects of A-site ion substitution on the phase transition temperatures, doping KNN with $xAZrO_3$ (A=Sr, Ba or Ca; $0 \leq x \leq 0.25$) (150). Each A-site dopant had the same effect on the phase structure as it was added. Below $x \leq 0.06$ the phase structure (at room temperature) was orthorhombic, between $0.08 \leq x \leq 0.10$ the samples were rhombohedral, and for $x \geq 0.15$ the phase structure was cubic. With increasing x, the T_C and T_{O-T} decreased, whilst T_{R-O} increased. T_{O-T} and T_{R-O} showed little A-site dependence, whilst the T_C showed much larger A-site dependence. There was a large difference in T_C between the dopants, with $CaZrO_3$ reducing it the least.

KNN + alkaline earth ions

The effect of low amounts (0.5%) of Mg^{2+}, Ca^{2+}, $Sr^{2+,}$ and Ba^{2+} was researched in (151-154). Chang *et al* found adding Ca^{2+} and Sr^{2+} promoted densification, increased electric properties and cell parameters, whilst decreasing the phase transition temperatures. On the other hand Mg^{2+} increased T_C, but lowers the density, cell parameters and considerably decreases the electrical properties. Adding Ba^{2+} decreased density, the phase transition temperatures and the electric properties whilst increasing the cell parameters (155).

Manganese improves the sinterability of KNN (156) and adding 1mol% to tantalum doped KNN decreases the T_{OT} to room temperature without affecting the T_C (157).

3.2.2.3.2 KNN-based Ternary Systems

Jiangang Wu's research group from the Department of Material Science at Sichuan University have researched several complex KNN ternary systems with the aim to make high d_{33} materials whilst maintaining high T_C. They researched $(1-x)(K_{0.4}Na_{0.6})(Nb_{0.965}Sb_{0.035})O_3$-$x(Bi_{0.5}Li_{0.5})ZrO_3$ and found a rhombohedral-tetragonal MPB between $0.025 \leq x \leq 0.035$. With good thermal stability, a composition within these boundaries had a d_{33} of $400pCN^{-1}$ and a T_C of 292°C (158). Another system they looked at was $(0.995-x)(K_{0.48}Na_{0.52})NbO_3$-$0.005BiScO_3$-$xBi_{0.5}(Na_{0.7}K_{0.2}Li_{0.1})ZrO_3$. At x=0.04 the d_{33} was ~$366pCN^{-1}$ the k_p 47%, the T_C remained as high as 335°C and an MPB was present. The high T_C was due to the addition of BLZ. The d_{33} stayed above $319pCN^{-1}$ up to 300°C (159). The final example of a complex system developed at Sichuan University is $0.992(K_{0.46}Na_{0.54})_{0.965}Li_{0.035}(Nb_{1-x}Sb_x)O_3$-$0.008BiScO_3$. A phase coexistence existed between $0.02 \leq x \leq 0.06$. The d_{33} at the MPB was $325pCN^{-1}$, the k_p was 48% and the T_C was 358°C (160).

3.2.2.3.3 KNN Sintering Aids

Sintering aids in KNN as discussed previously, are very important for producing high density materials. A fact that has lead Toyota to patent several sintering aid inclusive processes for producing KNN based materials (161). Sintering aids reduce the sintering temperature by forming a liquid phase within the sample which improves densification by increasing atomic mobility. By lowering the sintering temperature, volatile ions such as K^+, Na^+ or Li^+ are much less likely to leave the system.

Park *et al* used CuO as a sintering aid and decreased the sintering temperature to below 1000°C. This reduced sodium loss and formed a dense microstructure and increased grain size (162). Copper entering the perovskite structure has a hardening effect as it replaces the Nb^{5+} this pins domain walls, increasing the coercive field. Matsubara *et al* and Seo *et al* also found that CuO enhances sinterability (163, 164) Bernard *et al* used germanite as a sintering aid and got to 95.6% of the theoretical density without degrading the properties (165).

Other sintering aids used are $K_4CuNb_8O_{23}$ (166) and $K_{5.4}Cu_{1.3}Ta_{10}O_{29}$ (167) which brought the sintering temperature below 950°C and encouraged

the sample to reach 97.5% of the theoretical density. ZnO, SnO_2 and Sc_2O_3 have all been used with only minor changes to the T_C and T_{O-T} (168, 169).

3.2.2.3.4 Other Processing Methods

Applying heat under the pressing process is known as 'hot pressing'. Hot pressed KNN has reached 99% theoretical density, which compared to traditional air sintering methods that only reach 95% is a vast improvement (170). Spark plasma sintering can also improve dielectric and piezoelectric properties and involves applying a very large electric field over a short time which causes the sample grains to fuse (171).

3.2.3. Lead-free PZT Alternative Conclusion

The academic effort has focused on producing a lead-free material with a similar MPB system to PZT, with the understanding that a phase coexistence has a large effect on improving desirable properties. Titanate based materials can be made that have very large piezoelectric response but have low Curie or depolarization temperatures that reduces the commercial viability of the materials. The most promising titanate based system, BCTZ, has a large d_{33} of 620pCN^{-1} but a very low Curie temperature of 50°C.

Niobate based systems have higher Curie temperatures and can have large piezoelectric responses. However the piezoelectric properties of niobate based systems can suffer from low thermal stability as the 'MPB' often claimed, suffers from the polymorphic phase boundary effects. Some of the most interesting niobate based systems are very complex, but have a good compromise between piezoelectric response and Curie temperature, with a d_{33} of 319pC/N that persists up to 300°C.

The argument could be made that it is not just the coexistence of different phases in PZT that makes the material so useful, but the temperature stability of the phase boundary (and properties) itself. It has been proposed by Zhang *et al* that a better comparison between lead-free materials would be to compare the maximum d_{33} versus the temperature of depolarization (4).

To compare across different systems, the author proposes that the d_{33} should be multiplied by temperature range that said d_{33} persists, starting from room temperature (Equation 3.1).

$$F.O.M = (T_C - T_{ambient}) * d_{33}$$ **Equation 3.1**

Using this system, BCTZ, assuming a constant d_{33} of 620pCN^{-1} until 50°C would be given a figure of merit of 15,500pCN^{-1}K (105). The niobate based system made by X. Cheng *et al* (159) with a d_{33} of 319pCN^{-1} and a T_C of 300°C, would have the figure of merit 87,725pCN^{-1}K. The outcome of which would suggest that the leading lead-free niobate system is 5-6 times better than the leading titanate system.

The research done during this project attempts to prove if a low T_C, lead-free material such as BCTZ can be incorporated into a transducer device. In doing so this bridges the gap between material science and device engineering and should be achieved by altering high-temperature manufacturing steps. A novel $KNbO_3$ based material is then synthesised, which fills a compositional gap found in the literature whilst attempting to reproduce some advantageous properties found in BCTZ and PZT and attempting to keep the T_C relatively high.

4 Experimental techniques

This chapter describes the process used to synthesise the piezoelectric ceramic materials made during the project. It will also explain the techniques used to characterise the products made.

4.1 Sample Synthesis

Mixed oxide synthesis, or the solid state reaction process, is the conventional process used to produce polycrystalline ceramic powders from its constituent metal oxides and carbonates. The process allows for large batches of reagents to react together at high temperatures to produce fine powders of high purity. For example, reacting potassium carbonate (K_2CO_3), and niobium oxide (Nb_2O_5) together at 850°C for 4 hours will produce potassium niobate ($KNbO_3$).

The handling of the oxide/carbonate reactants before and after the heat treatment can heavily affect the product. Steps are taken to control purity, particle size, particle shape and heterogeneity of the powders before and during the process. This allows for consistent starting materials in order to reduce any variation on the densification, microstructure and electrical properties of the product.

The steps used to produce the polycrystalline ceramic powders made by mixed oxide synthesis are described in subsequent sections, however a summarising flow chart can be seen in Figure 4.1.

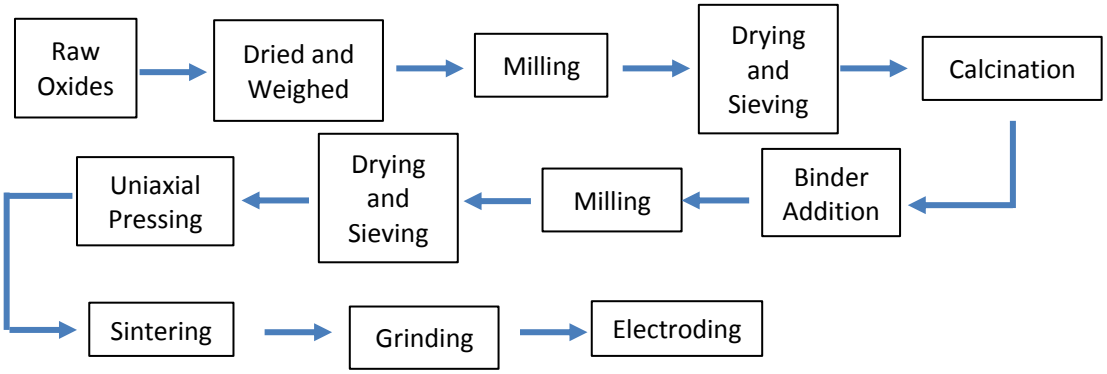

Figure 4.1: Flow chart of mixed oxide processing.

4.1.1 Powder Drying

The oxides and carbonate reagents were dried for 24 hours at 150°C in a conventional drying oven. This was in order to remove any water that

may have been absorbed from the atmosphere into the powder. The oxides and carbonates used in this project can be seen in Table 4.1.

Table 4.1: List of reagents used during the project

Reagent	Molar Mass (g/mol)	Note
K_2CO_3	138.2049	Sigma-Aldrich (99%)
Nb_2O_5	265.8098	Aldrich (99.9%)
$CaCO_3$	100.0869	Sigma-Aldrich (99%)
ZrO_2	123.2228	Aldrich (99%)
$BaCO_3$	197.3359	Alfa Aesar (99%)
TiO_2	79.8688	Aldrich (99.9%)
Li_2CO_3	73.8909	Aldrich (99.9%)

4.1.2 Mass calculations and weighing reagents

The molar mass of the reagent was multiplied by the desired percentage of occupation on a particular site (A-site or B-site) and divided by the molar mass of the product, allowing the mass ratio of reagents to be calculated. This is then multiplied by the number of grams of product required to calculate the mass of reagent needed to be weighed out. This ensured stoichiometry of the reagents.

The dried powder was removed from the oven and weighed out onto plastic boats as quickly and as accurately as possible. This is to reduce the amount of water absorbed. This practice is particularly important when weighing out very hygroscopic powders such as K_2CO_3 and Li_2CO_3 as the masses are less accurate the longer the powder was out of the oven.

The powder was then transferred into a high density polyethylene (HDPE) bottle and the weighing boats cleaned using 2-isopropanol (IPA) (Fisher Scientific, 99.8%) to ensure all of the powder was transferred.

4.1.3 Ball Milling

The ball milling process was used to produce a homogenous mixture of powders of uniform particle size and shape. IPA was added to the mixture of powders until a slurry of double-cream-viscosity was made. Then yttrium-

stabilised zirconium milling media (9.5mm) was added to the bottle until a consistent cascading was heard during rotation on a ball mill.

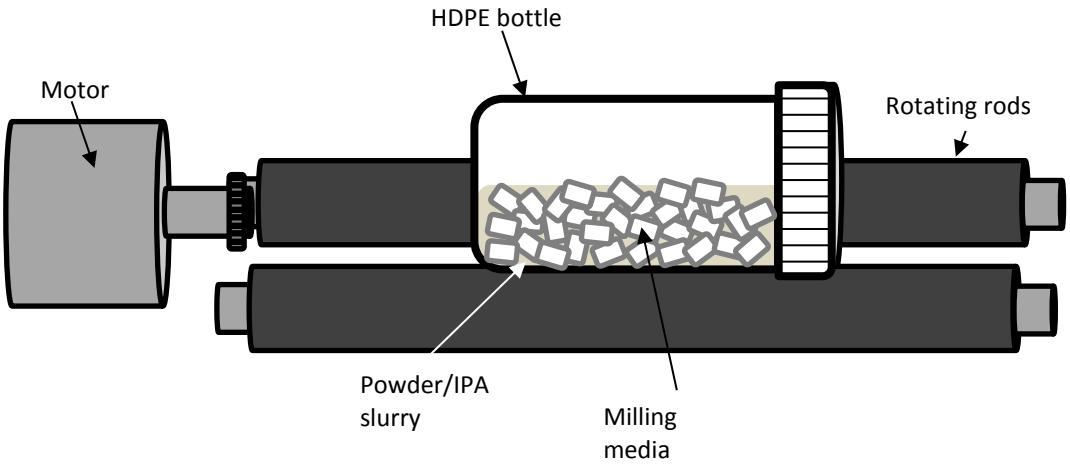

Figure 4.2: Schematic of the ball milling process

Under rotation the milling media breaks down the powder within the slurry and over 24 hours, the different size grains of each of the regents became uniform and a homogenous mixture was produced.

4.1.4 Drying and sieving

After 24 hours the milling media was removed from the slurry using a colander and the slurry is transferred to a metal bowl for drying, the bottle is rinsed with more IPA to ensure as much of the slurry is transferred as possible. The metal bowl was then placed on a conductive heater at 90°C and the slurry was stirred using metal stirrer until the slurry was dried into a powder (Kenwood KM080). This powder was moved to a pyrex beaker and left to dry further in a drying oven at 150°C for 12 hours.

The powder was then sieved through a 300µm mesh (Plastok) using a pestle, to remove any large clumps of powder that may have formed during the drying step. The milled, dried and sieved mixture of reagents was then transferred to an alumina crucible for calcination.

4.1.5 Calcination

The calcination step is a heat treatment of the reagents that allows them to react, forming the ceramic powder desired. It removes any of the extra carbon and oxygen atoms and ideally combines the reagents to produce the ABO_3 perovskite powder.

The calcination regime used for all of the KN-based samples can be seen in Figure 4.3. The powder was heated at 100°C/h to 850°C, kept at this temperature for 4 hours, and the cooled at a rate of 150°C/h to room temperature. Upon cooling, a small sample of calcined powder was removed for XRD characterisation.

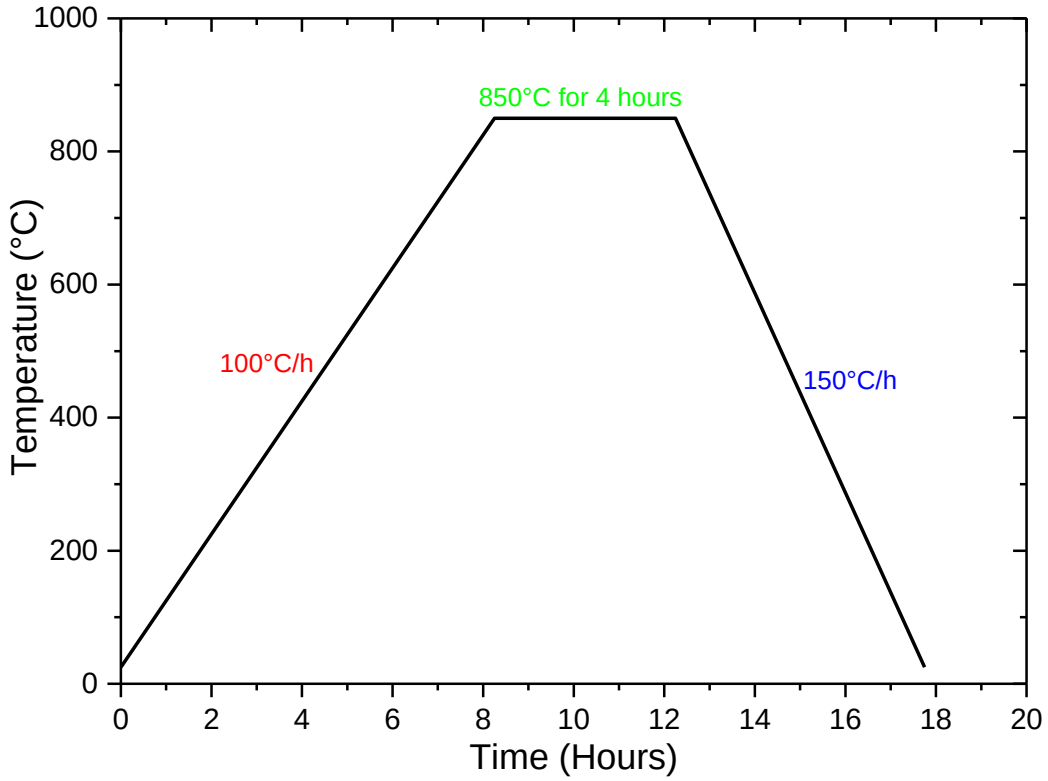

Figure 4.3: The temperature profile of the calcination for all $KNbO_3$-based samples.

The BCTZ powder was calcined using a different heating regime. It was heated to 500°C at a rate of 100°C/h and then further heated to 1250°C at a rate of 300°C/h. It was held at 1250°C for 3 hours before being cooled at a rate of 300°C/h to room temperature. The calcination temperature profile of BCTZ can be seen in Figure 4.4.

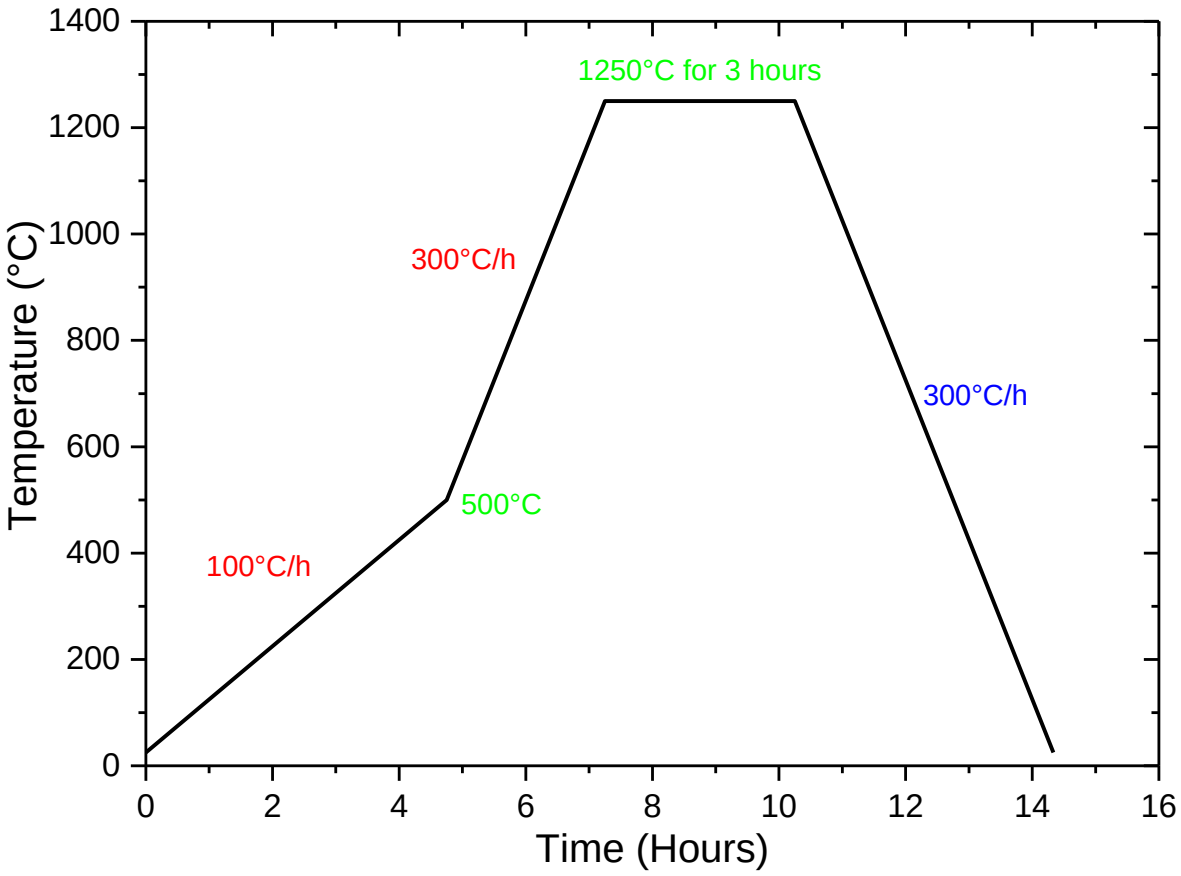

Figure 4.4: The temperature profile of calcination of the BCTZ powder.

4.1.6 Binder incorporation and pressing

2% by weight of Glascol binder was added to the calcined powder to aid in the subsequent pressing step. The powder and binder was mixed with IPA, ball milled, dried and sieved repeating the previous steps.

The powder was then weighed into 0.4g samples and pressed using 5.0kN of pressure using a 10mm steel die. This was to produce a round pellet of ≈1.2mm thickness and 10mm in diameter. The geometry and mass of the pellet was then measured to calculate a 'green' geometric density.

4.1.7 Sintering

Sintering is the step that turns a ceramic powder into a dense sample that can be used for characterisation or in a device. It allows for densification of the sample by growing the polycrystalline grains. The process is done at a higher temperature than calcination which can lead to volatile elements being lost from the system. To reduce this loss pelleted samples were placed inside a bed of its corresponding powder with more atmospheric powder added over it. Potassium is a very volatile element and begins to

evaporate at relatively low temperatures, as a result a more complex set up was used to sinter the potassium niobate samples in this work, a schematic of which can be seen in Figure 4.5.

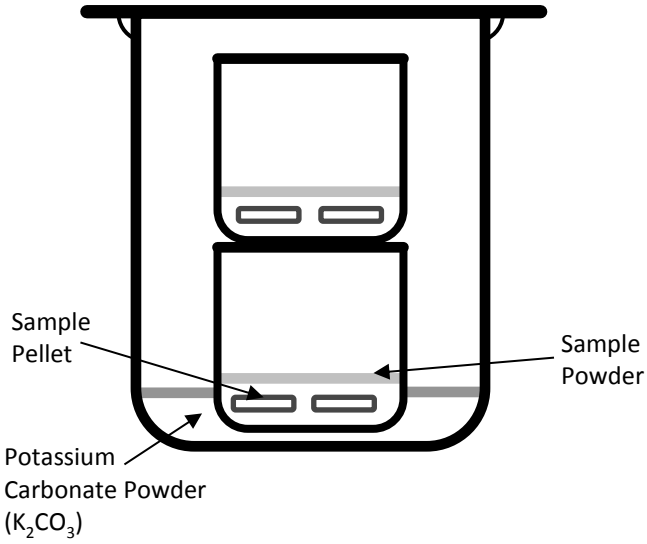

Figure 4.5: Sintering set up for the potassium niobate based samples.

An extra, larger crucible is used to hold the crucible containing the green samples and the atmospheric powder. The aim of using this set up was to introduce excess potassium in the atmosphere in order to reduce potassium loss in the samples. Using this set up an extra crucible could be included so that 2 different compositions could be sintered at the same time. The lid of the larger crucible was cemented in place using alumina cement.

The sintering regime used for the KN-based materials is seen in Figure 4.6. There was an initial slow heating rate of 50°C/h to 550°C, this was to burn off the binder and slowly remove any moisture that may have been in the sample. From 550°C to the desired sintering temperature (T_{sint}) the heating rate was 100°C/h. The sintering temperature was held for 2 hours and then the temperature was decreased rapidly at 300°C/h to room temperature.

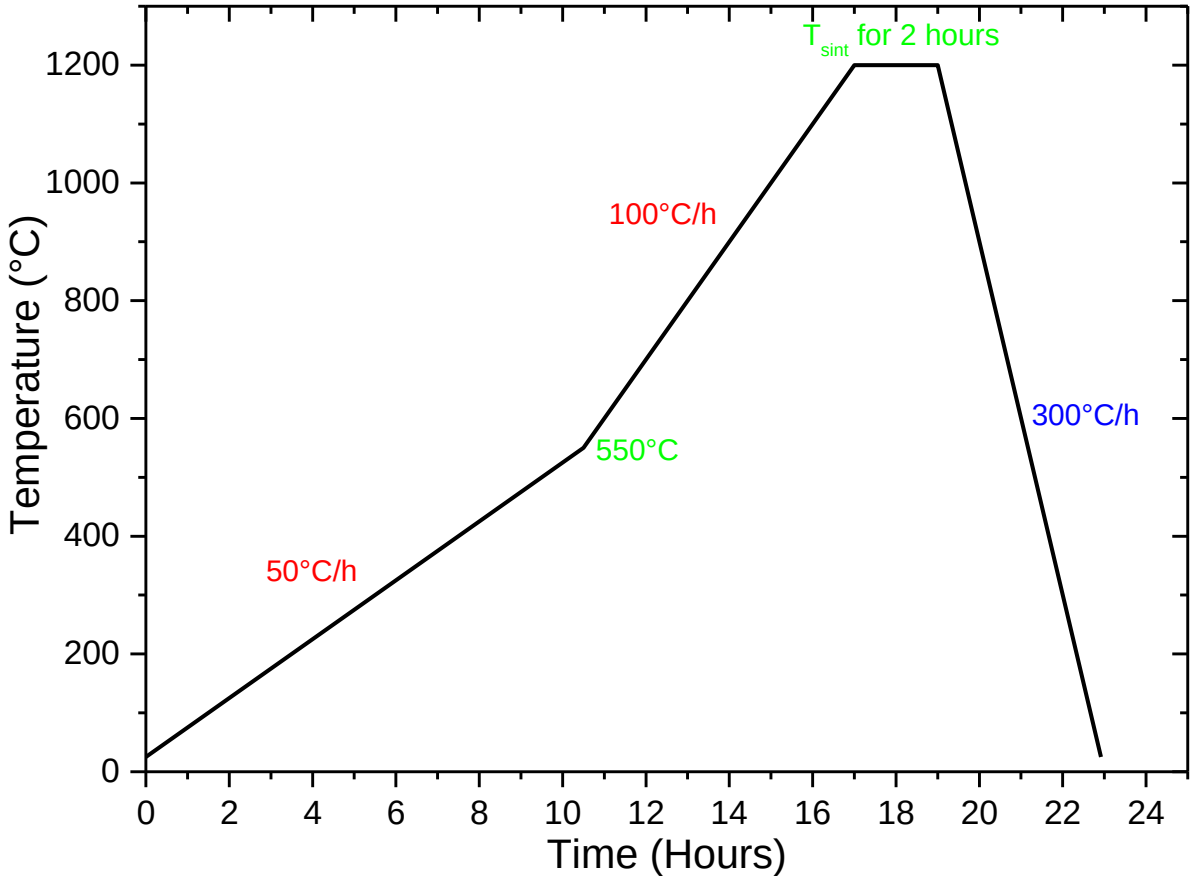

Figure 4.6: Sintering regime for the KN-based samples.

The sintering temperature varies between compositions and materials. The optimum sintering temperature allows for the densest sample without melting or deformation.

The BCTZ samples were sintered using a different regime (Figure 4.7). As the samples were larger (25mm diameter, ~5mm thick), they required a longer binder burn out step. Samples were heated to 220°C at 60°C/h then the heating rate was lowered to 10°C/h until reaching 300°C. At 300°C, the heating rate was increased to 90°C/h until reaching 620°C where the temperature was held for 6 hours. After the dwell, the sample was heated to 1440°C at a rate of 300°C/h and held there for 2 hours. Finally it was cooled to room temperature from 1440°C at a rate of 300°C/h.

As part of the sintering process the samples shrunk. Post sintering a geometric density was measured and compared to the green geometric density measured before sintering.

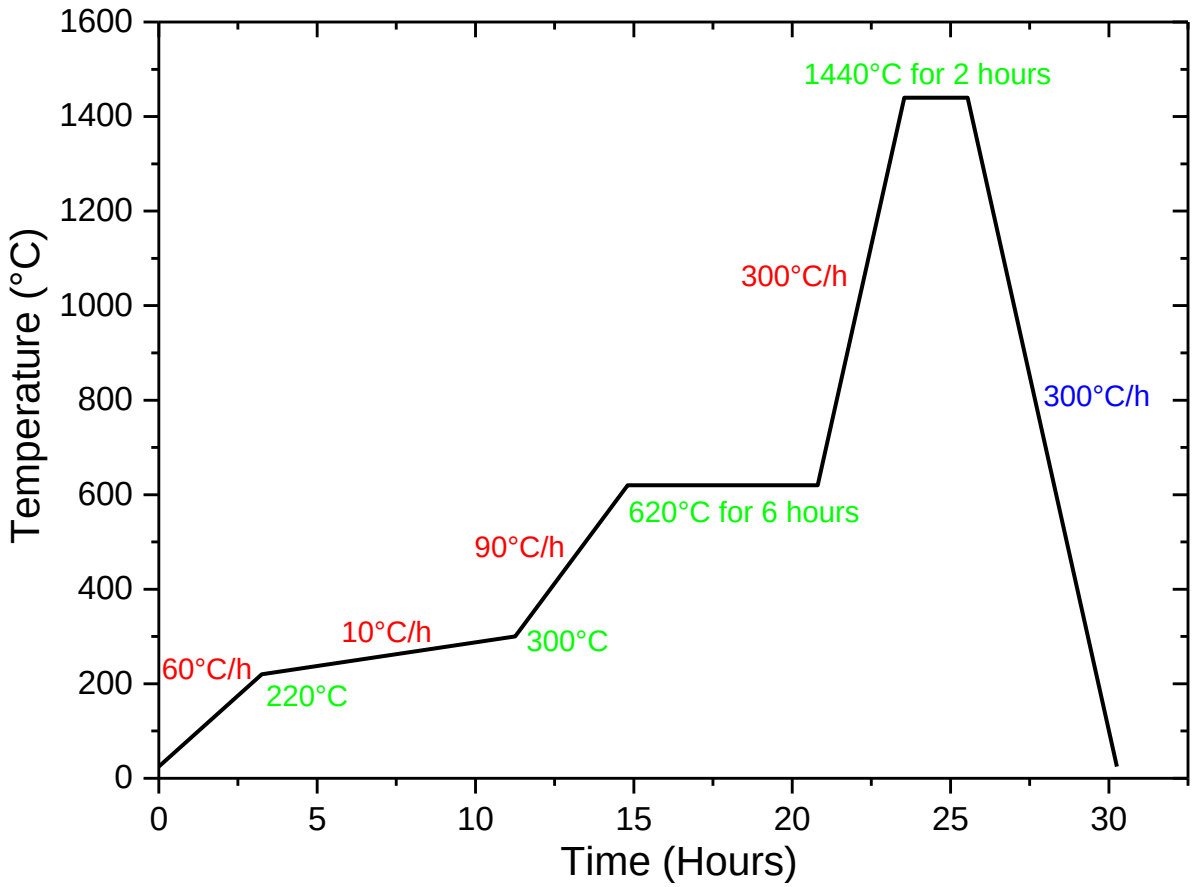

Figure 4.7: Sintering regime of the BCTZ samples.

4.1.8 Grinding

Sintered samples were ground to around ~1mm in thickness using Buehler P400 Carbimet SiC abrasive paper. This was to remove any atmospheric powder stuck to the sample and also to aid in the electrical characterisation process. Ensuring uniform thickness and parallel sides.

4.1.9 Electroding

Silver electrodes were painted on the samples that were to be characterised electrically. One side was painted and left in an oven to dry at 120°C, then the other side was painted. The samples were then heated to 550°C for 30 minutes to complete the electrode firing process. Care was taken to ensure that any silver paint bonded to the side of the samples was removed using abrasive paper to reduce the chance of samples electrically shorting or arching under an electric field.

4.2 Sample Characterisation

4.2.1 Crystallographic Characterisation

4.2.1.1 X-Ray Diffraction (XRD)

The crystallographic characterisation technique used throughout the project was X-ray Diffraction (XRD). XRD is a technique used to determine the phase and purity of the samples synthesised. To help describe the process, discussed below is the x-ray source, the experimental configuration and how the x-rays interact with the sample.

The x-rays are produced in the diffractometer x-ray tube where a tungsten filament is heated by an electrical current emitting electrons. These electrons are drawn to a metal, in the case of this work copper, however aluminium, molybdenum, magnesium and silver can also be used. This induces an electron to be ejected from the metal atom, see Figure 4.8.

The electron from the filament causes an inner-shell electron to be excited to a higher energy level. An electron is then demoted to fill the inner-shell and an x-ray is produced. The most intense emitted x-ray (Kα) will have an energy/wavelength that is unique to the metal used, in the case of copper the wavelength is 1.541Å. Other X-rays (Kβ or Lα) are emitted, however their low intensity means they are readily absorbed and can be filtered using a monochromator.

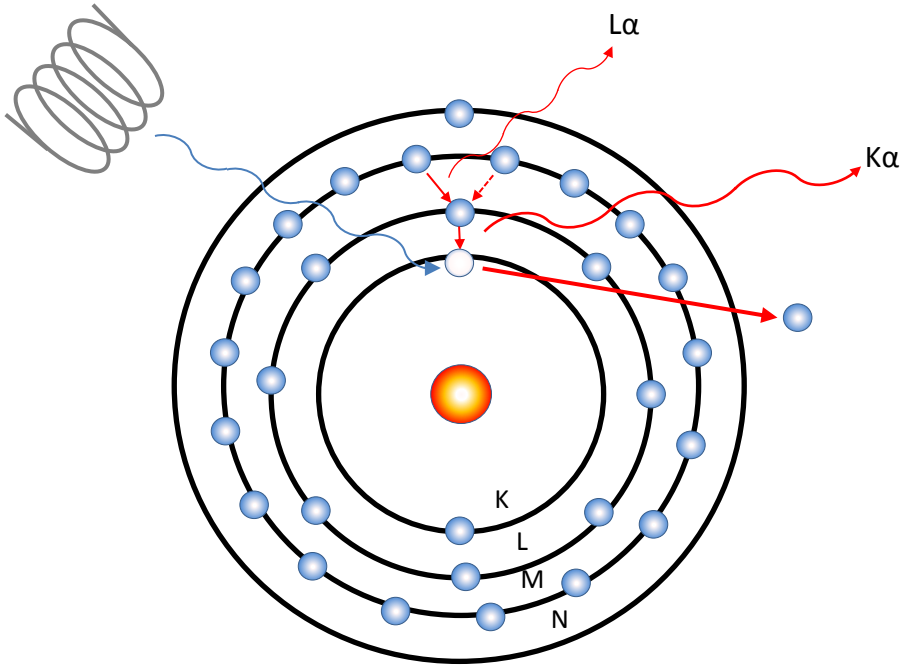

Figure 4.8: A diagram of the source of x-rays in a diffractometer.

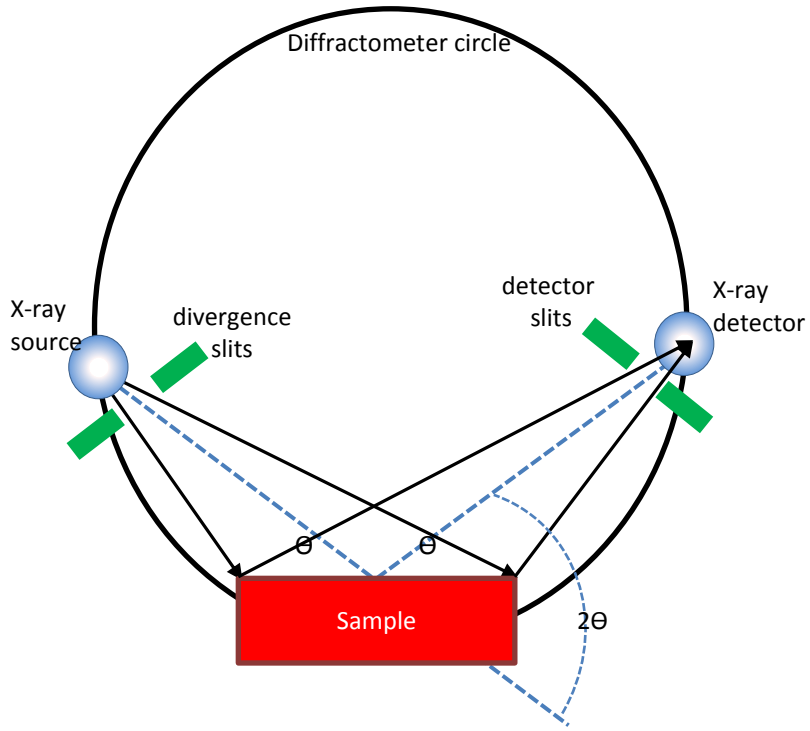

Figure 4.9: A schematic of an x-ray diffraction experiment.

The x-ray source is aimed at the sample passing through divergence slits which narrow the source beam (Figure 4.9). The source, or the sample, is then moved so that the incident angle of the x-ray beam on the sample changes. The x-rays are then able to interact with the sample and if Bragg's law is satisfied then diffracted x-rays are detected by the x-ray detector.

Bragg's law describes the relationship between the x-ray wavelength, the space between planes of atoms and the incident angle of the x-ray beams.

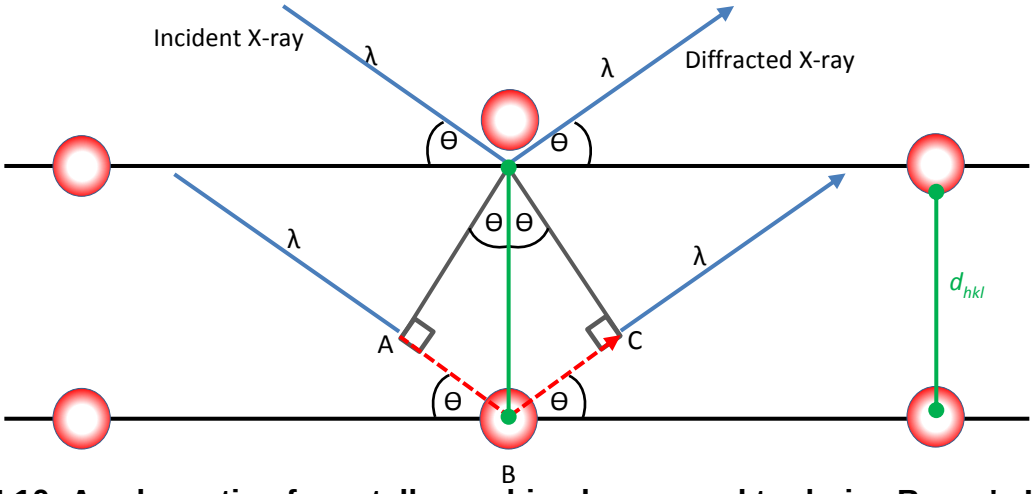

Figure 4.10: A schematic of crystallographic planes used to derive Bragg's Law.

Consider Figure 4.10, the parallel x-rays of wavelength, λ, are separated by a distance, *d*. In order for there to be a constructive interference between at point B, the extra distance *(AB+BC)* the lower beam must travel must be an integer, n, number of wavelengths. Using trigonometry the distance between A and B, is equal to dsinΘ and since AB and BC are equal;

$$\boldsymbol{AB + BC = dsin(\theta) + dsin(\theta)} \qquad \textbf{Equation 4.1}$$

$$\boldsymbol{n\lambda = 2dsin(\theta)} \qquad \textbf{Equation 4.2}$$

Where λ is the x-ray wavelength, *d* is the distance between planes, and Θ is the angle of incident.

If Bragg's law is satisfied then the diffracted x-rays will be detected as a large intensity. As the angle changes, peaks in intensity are seen along the detected x-ray plot. The angle can also represent the space between atomic planes known as the d-spacing.

$$\boldsymbol{d = \frac{n\lambda}{2\sin(\theta)}} \qquad \textbf{Equation 4.3}$$

For a cubic system;

$$\boldsymbol{\frac{1}{d^2} = \frac{h^2+k^2+l^2}{a^2}} \qquad \textbf{Equation 4.4}$$

Where *d* is the distance between the planes *(h,k,l)* (see 2.1.3), and *a* is the unit cell length.

If there is more than one unit cell length, e.g. in a tetragonal system, or different angles in the unit cell, e.g. a rhombohedral system, then more peaks will be seen on the plot as there are extra inter-plane distances. This is known as peak splitting. Each crystal system theoretically splits a group of planes differently, the number of peaks for each group of planes can be seen in Table 4.2.

Table 4.2: Number of peaks arriving from peak splitting of planes in different crystal systems.

h	k	l	Cubic	Tetragonal	Orthorhombic	Rhombohedral	Monoclinic
0	0	1	1	2	2	1	3
1	1	0	1	2	3	2	4
1	1	1	1	1	2	2	2
0	0	2	1	2	2	1	3
0	1	2	1	3	4	2	8
1	1	2	1	2	4	3	6
2	2	0	1	2	3	2	4
0	0	3	1	2	2	1	3
2	2	1	1	2	4	3	6
1	0	3	1	3	4	2	8
2	2	2	1	1	2	2	2
1	2	3	1	3	6	4	8
3	3	0	1	2	3	2	4

Using the peak splitting and the different intensities of the split peaks, the phase of the material can be determined.

Extra peaks present can be an indicator of secondary phases. This may be due to a second phase of the same composition being present or an impurity within the sample. It can be very difficult to determine a coexistence of two phases within a sample as the peaks are close together, usually appearing as a broad peak rather than two or more separate peaks. This is due to the unit cell parameters of different phase of a material only differing by a small amount (Figure 4.11).

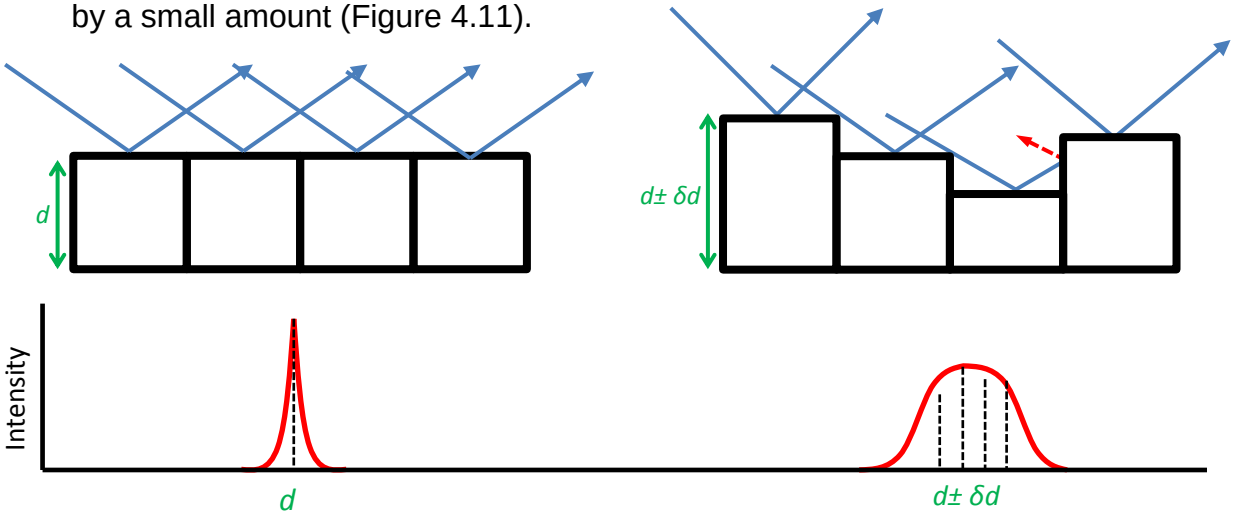

Figure 4.11: Peak broadening in x-ray diffraction.

The x-ray diffractometer mainly used in this project was a Bruker D8. The scans were taken between 20-80° with a scan step of 0.033425°, for a total scan time of 20mins.

4.2.1.2 Rietveld Refinement

Rietveld refinement creates a model diffraction pattern that is compared to the observed data. The differences between the model and the observed data is then minimized by varying different parameters in the model. When the modelled, and experimental diffraction patterns match, the model can be used as a representation of the original sample and so more information about the sample is determined.

This modelling technique was used during the project to determine the different phases present. Rietveld refinement gives a best fit score, allowing for the likelihood of each combination of phases to be rated. Using peak intensity values it can give the percentage of each phase present.

The software used during this project was High Score made by Panalytical. Each refinement was conducted with the same parameters in the same order unless otherwise stated. The initial phases were that of pure $KNbO_3$ and can be found in Table 4.3.

Table 4.3: Initial phases used during Rietveld Refinement.

Crystal System	Space Group	ICDD code
Orthorhombic	Amm2	04-015-8615
Tetragonal	P4mm	04-008-4706
Cubic	Pm $\overline{3}$ m	04-014-0625
Rhombohedral	R3m	01-083-3858

The dopant atoms were added to the unit cell and the occupancy adjusted accordingly. After the background was determined the scale factors were refined. The zero shift was then refined, followed by the unit cell parameters of each phase. The W, U and V parameters (used in the Cagliotti function) were then refined separately, which refined the peak width. W and U were constrained to be positive and V to be negative. Finally the peak shape was refined, whilst constrained between 0 and 1. This refined the ratio of Gaussian and Lorentzian profile shapes. Different space groups were not refined as the space groups initially used were the best fit, accounting for all the peak present.

4.2.2 Electrical Characterisation

4.2.2.3 Permittivity versus temperature

The permittivity of the samples was measured as a function of temperature and frequency. The permittivity of the sample changes as the phase of the sample changes and so it can be used as an indicator of phase transitions. The Curie point of a material can also be determined by the temperature of maximum permittivity.

Measuring the permittivity as a function of frequency at each temperature can also reveal any divergence. This, along with a broad peak for a phase transition can indicate if a material is a relaxor (see section 2.2.10).

The permittivity was measured using a Hewlett-Packard 4192A. The sample was housed in a tube furnace with a K-type thermocouple to measure the temperature using a National Instruments USB-TC01. It was heated at 3°C/h to 550°C and cooled at the same rate.

4.2.2.4 Impedance Measurements and PRAP

Impedance measurements were measured using an Agilent 4192A. The resonance spectra were analysed using a Piezoelectric Resonance Analysis Program (PRAP). This fits a model to the experimental data which is used to calculate the piezoelectric coefficients. In order for a full matrix of coefficients to be determined, several different cuts of material need to be made (see 5.3).

4.2.2.5 Polarization- Electric Field

Measuring the polarization as a function of electric field is a fundamental technique when attempting to synthesise a ferroelectric. One defining property of a ferroelectric is the ability to switch between two states with the application of an electric field.

The polarization of each composition was measured using a precision materials analyser (Precision LC Radiant technologies Inc.) at increasing electric fields using a Trek model 5/80 high voltage amplifier. The measurements began at 1kV/mm and were taken in 0.5kV/mm increments until the 5kV/mm, or until sample breakdown. Double bipolar measurements were made with full loop taking 1000 μs.

The polarization was compensated for leakage current. This was done by deducting the current from the resistor component of the ceramic at peak electric field.

4.2.2.6 Strain- Electric Field

The strain of each composition was measured concurrently to the polarization using an MTI-200 fotonic™ sensor. This measures the displacement of the material as an electric field is applied using fibre optic probes and an unclamped copper body which is attached to the sample, a schematic diagram of the setup can be seen in Figure 4.12.

As the copper body is moved by the ceramic under an electric field, there is a change in the intensity of the light that is received by the receiving filament. After calibration, this received output corresponds to an accurate distance between the target and the probe.

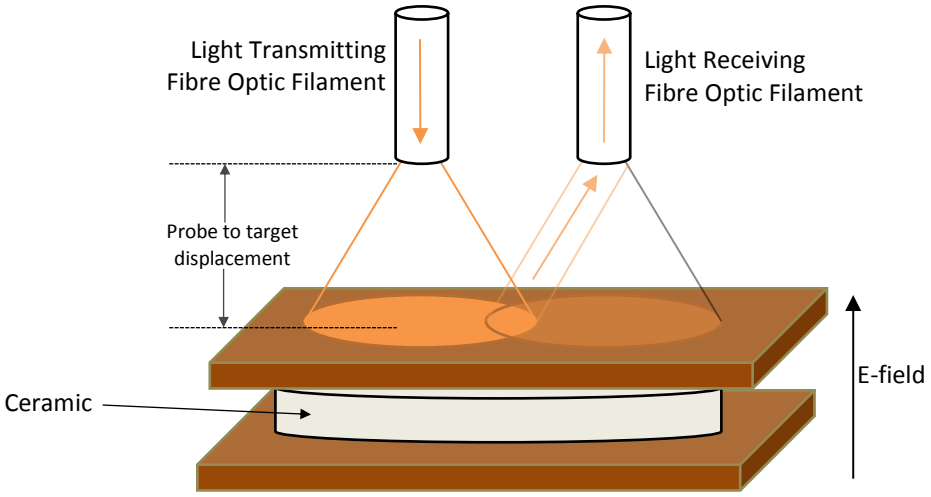

Figure 4.12: Schematic diagram of the strain-field measurement setup.

The change in distance between the probe and the target is then converted into strain by dividing by the sample thickness. High-field d_{33} (d_{33}*) is obtained from the slope of the strain-electric field. A 'low'-field d_{33} was also obtained by calculating the gradient of the strain-electric field at relatively low fields.

5 BCTZ Piezoelectric Devices

5.1 Introduction

This chapter will cover the synthesis of Barium Calcium Titanate Zirconate (BCTZ). The sample preparation and full matrix characterisation of BCTZ. It will show the results of a poling study, as well as the process used to produce the ring and disk samples that were subsequently used in two types of devices. Finally it will describe the manufacturing steps of the devices and the characterisation of said devices.

5.2 BCTZ Synthesis, sample characterisation and poling

The BCTZ composition, $(Ba_{0.85}Ca_{0.15})(Ti_{0.90}Zr_{0.10})O_3$ was synthesised using the mixed oxide method outlined in section 4.1. The calcination and sintering temperatures were taken from the paper by Wu *et al* (172).

10mm samples were made with 0.8g of calcined powder and 4.9kN of pressure. Larger pellets of BCTZ were made with 7g of calcined powder being uniaxially pressed using a 25mm die and 14.7kN of pressure. This produced green pellets with an average geometric density of 2.93g/cm^3. Due to a binder burn out issue (seen in Figure 5.1), a binder burnout method developed using thermogravimetric analysis on a ceramic with a binder of a similar composition was used during sintering (173).

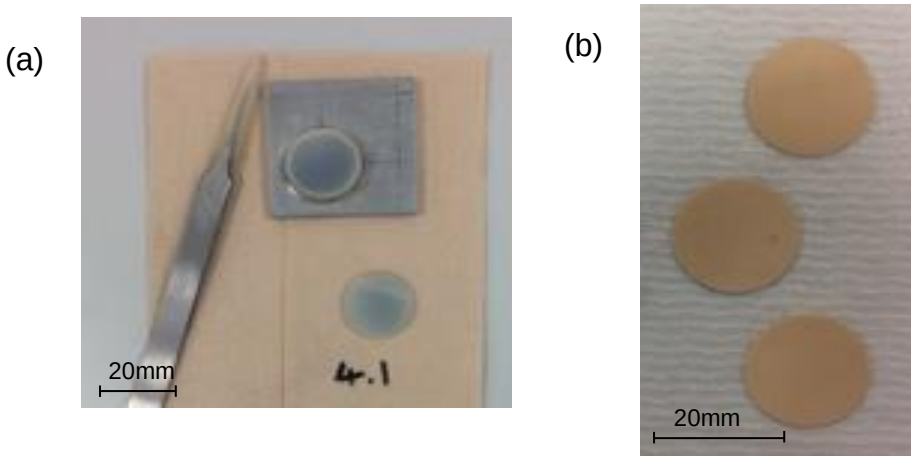

Figure 5.1: Effect of binder burnout rate on sample during sintering

(a) short binder burnout, (b) long binder burnout

5.2.1 X-ray Diffraction Results and Discussion

XRD results of the calcined and sintered samples can be seen in Figure 5.2. There is a slight shift in peak position between the calcined powder and sintered pellet. This could be due to the sintered sample being less flat in the device holder than the sample in powder form. There is an increase in peak intensity after the sample is sintered. This is due to grain growth under the sintering process. Both samples show a pure perovskite material.

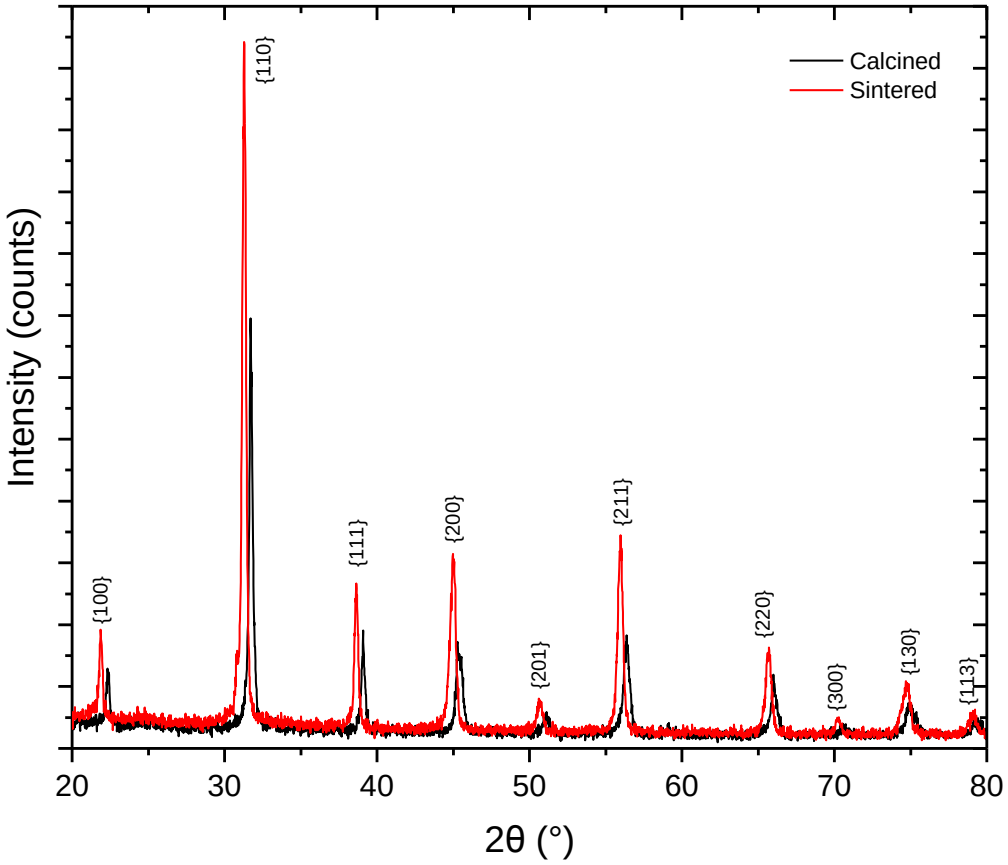

Figure 5.2: XRD results of calcined and sintered BCTZ from 20-80°.

Literature values for the density of this composition of BCTZ are between 5.4-5.5g/cm^3 (174). After sintering the geometric density of the pellets was measured, with an average of 5.39g/cm^3 (98-99% of the literature values).

5.2.2 Permittivity Results and Discussion

The relative permittivity and tan(δ) of the BCTZ material was measured between room temperature and 180°C and at different frequencies. The results can be seen in Figure 5.3. The peak in relative permittivity, which corresponds to the T_C, is found at 90°C. There is minimal permittivity difference between frequencies.

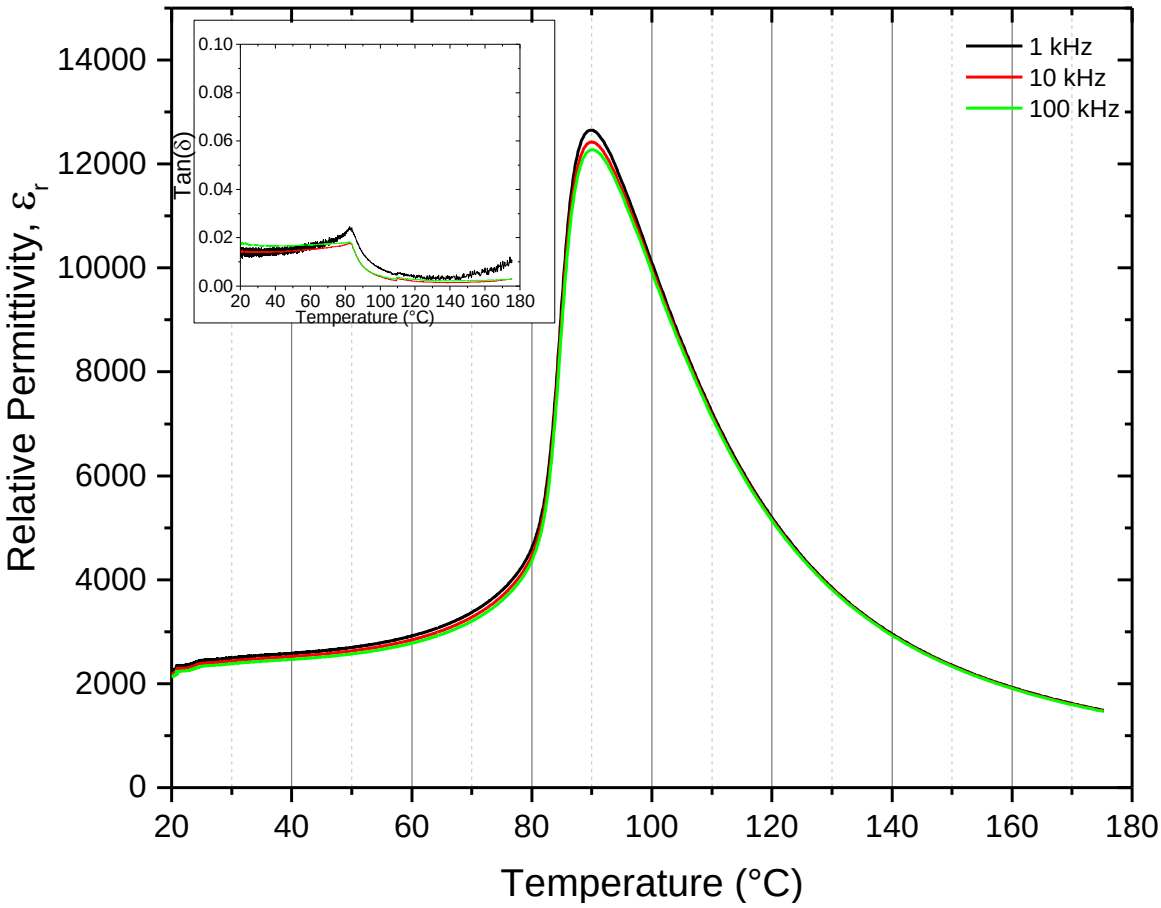

Figure 5.3: Permittivity data of the BCTZ material.

5.2.3 Polarization-Electric Field and Strain-Electric Field Results and Discussion.

The polarization and strain of the material was measured from 0.5 to 3.0kV/mm at 0.5kV/mm increments using the method described in sections 4.2.2.5 and 4.2.2.6. Shown in Figure 5.4 are the results, with the polarization in black and the strain in red.

The P_s, P_r, and P_{max} of BCTZ were 15.55, 9.04 and 18.15μC/cm^2 respectively. The coercive field, E_C, was measured to be 0.2kV/mm. Calculating the average gradient between -0.2 to 1.0kV/mm, and -1.0kV/mm to -0.2kV/mm gives a figure for the 'low'-field d_{33}* of 745pC/N. The high-field d_{33}*, or the average gradient between 2.0kV/mm to 3.0kV/mm, and -2.0kV/mm to -3.0kV/mm was calculated to be 287pC/N.

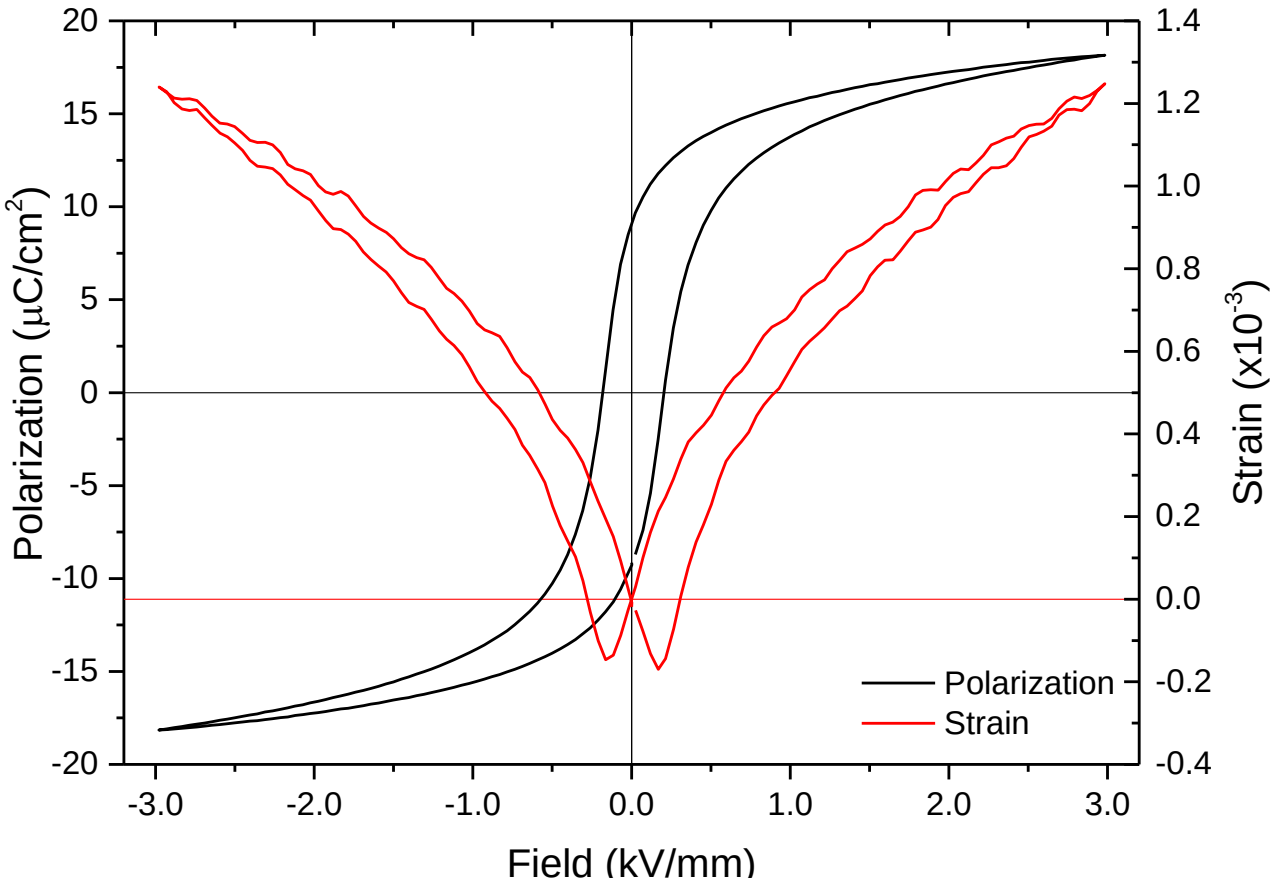

Figure 5.4: Polarization-electric field and Strain-electric field results at a peak field of 3.0kV/mm.

5.2.4 BCTZ Poling Study

In order to determine a poling regime, 12 10mm pellets were made. After grinding to below a millimetre in thickness and electroding, the samples were poled. They were poled at voltages ranging from 0.5kV/mm to 5kV/mm for 15 minutes. Different samples were poled in silicon oil at 2 different temperatures, room temperature and 50°C. The higher temperature of 50°C was used as it improved the mobility of the charge carriers whilst remaining below the T_C.

The resulting d_{33}, capacitance and tanδ measurements (Table 5.1) were taken 24 hours after poling, and are an average of 3 measurements in order to reduce error, measured using the Berlincourt method (Piezotest PM300).

Table 5.1: The results of the poling study, samples 1-6 poled at room temperature and 7-12 at 50°C.

Pellet	Thickness (mm)	Diameter (mm)	Field (kV/mm)	d_{33} (pC/N)	Capacitance (pF)	Tan(δ)
1	0.866	8.274	0.5	116	546	0.0213
2	0.808	8.287	1.0	219	643	0.0194
3	0.908	8.266	2.0	188	475	0.0193
4	0.937	8.216	3.0	239	314	0.0177
5	0.904	8.201	4.0	209	427	0.0580
6[1]	0.98	8.175	5.0	160	271	0.117
7	0.981	8.226	0.5	213	456	0.0604
8	0.970	8.274	1.0	250	1461	0.0521
9	0.842	8.226	2.0	172	49.5	0.0459
10	0.882	8.085	3.0	206	1284	0.0313
11	1.004	8.095	4.0	263	1456	0.0373
12	0.883	8.195	5.0	185	1479	0.0300

[1] This sample short circuited after 1 minute of poling

Pellet numbers 1-6 were poled at room temperature and 7-12 were poled at 50°C. It can be seen that there was a large increase in d_{33} from 116 to 219pC/N between poling voltages 0.5kV/mm and 1.0kV/mm at room temperature. A poling field increase from 1.0kV/mm to 2.0kV/mm made the d_{33} decrease to 188pC/N. Before increasing to 239pC/N at 3.0kV/mm and remaining high at 209pC/N at 4.0kV/mm. There is a decrease in d_{33} at 5.0kV/mm this may be due to the voltage only being applied for 1 minute,due to short circuiting. However it can also be seen in the corresponding samples poled at 50°C.

The samples poled at 50°C followed the same trend, 213, 250, 172 and 206pC/N at 0.5, 1.0, 2.0 and 3.0kV/mm respectively. There was an increase in d_{33} after 3.0kV/mm, from 206 to 263pC/N at 4.0kV/mm which is not seen in the room temperature samples. The d_{33} then decreased when poled at 5.0kV/mm.

The capacitance varied wildly with poling field and was consistently larger in the samples poled at 50°C over the room temperature samples, with the exception of pellet number 9, which may have been an anomaly. The losses (tan δ) were consistent and larger for samples poled at the higher temperature, with the exception of pellet 6 which was compromised in the poling process.

The poling conditions that were used during the project were 1.0kV/mm at 50°C. While the increase in d_{33} from 0.5kV/mm to 1.0kV/mm was significant, further increasing the poling field had little, if any, desirable change in d_{33}. Consequently the poling temperature of 50°C was chosen as the d_{33} was much larger than for the comparable voltage at room temperature.

5.3 Full matrix characterisation of BCTZ

5.3.1 Sample Preparation

The large samples were mounted on to an aluminium substrate using an adhesive (Loctite 162075) and left to dry for 12 hours. These samples were then cut into 3 different geometries using a precision cutter (Struers Accutom-5). The speed of the blade was 3000rpm and the feed was 0.025mm/s. Figure 5.5 illustrates the order of the cutting process.

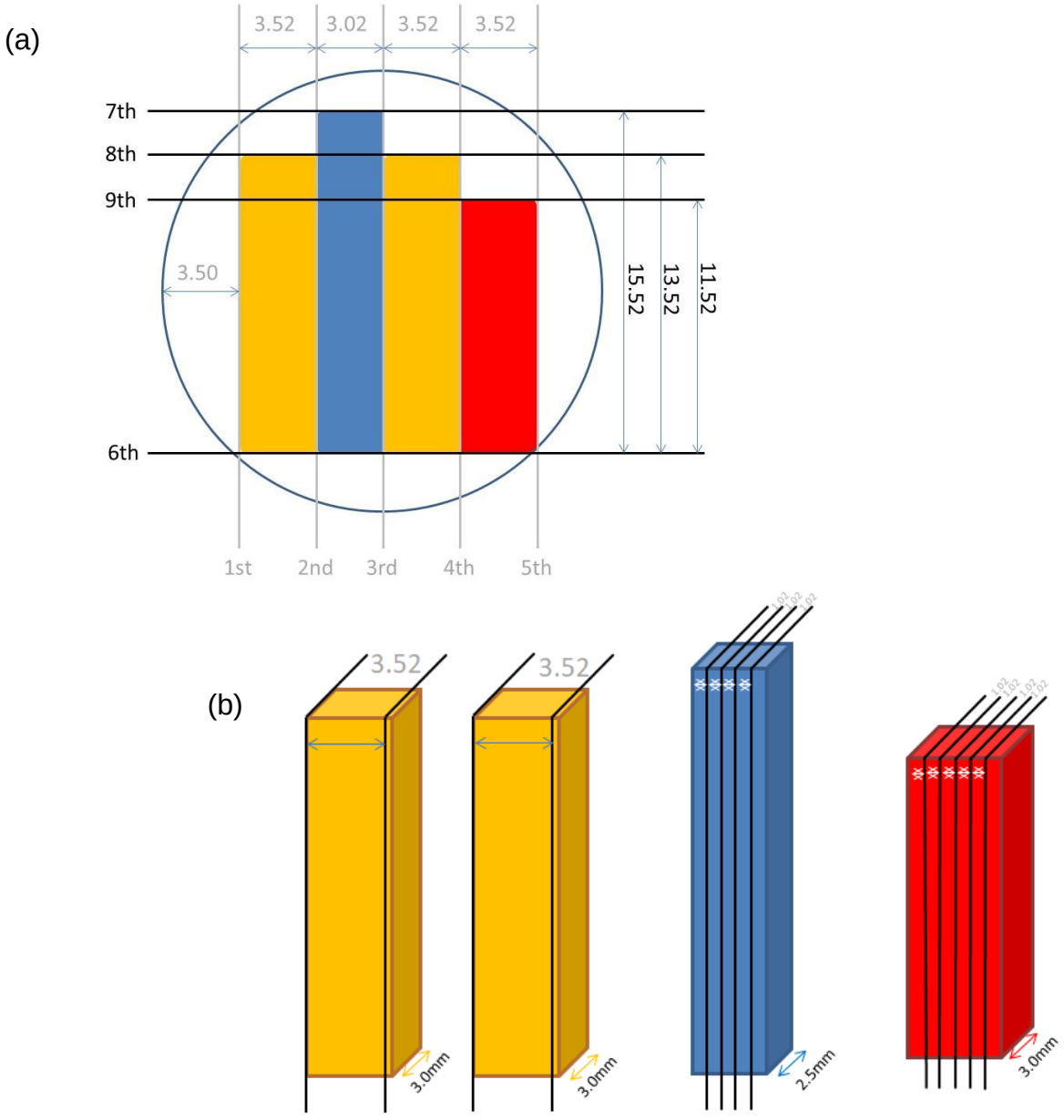

Figure 5.5: Cutting regime of the BCTZ pellets to manufacture the geometries need for full matrix characterisation. (a) length and width cuts, (b) thickness cuts.

The larger samples were removed before the 8th and 9th cuts as well as the 9th and 10th cuts. The samples were then mounted again 90° to their previous mounting in order to cut the correct thickness. One pellet was cut across the face to produce the radial and thickness extension mode samples of diameter 20mm and thickness 0.5mm. The geometries cut from each pellet can be seen in Table 5.2. Figure 5.6 has a picture of the initial range of the samples.

Table 5.2: The samples cut and the modes they were measured in.

Mode	Length (mm)	Width (mm)	Thickness (mm)
Length Extensional (LE)	13.0	3.0	3.0
Shear (S)	11.0	3.0	0.5
Longitudinal Thickness Extension (LTE)	15.0	2.5	0.5
Thickness Shear (TS)[2]	10.0	10.0	1.0
Thickness Extension (TE2)[2]	10.0	10.0	1.0
Mode	**Diameter (mm)**	**Thickness (mm)**	**-**
Thickness Extension (TE)	20.0	0.5	-
Radial (RAD)	20.0	0.5	-

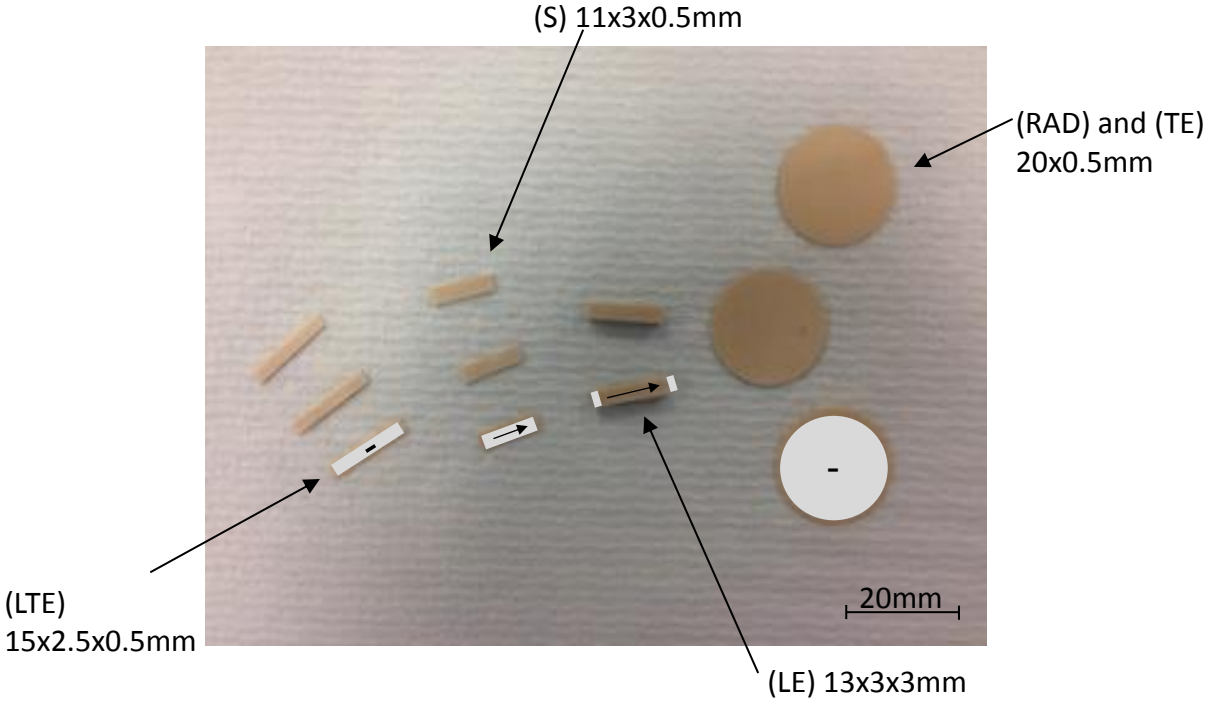

Figure 5.6: Image of all the cuts initially produced from 2 samples, with electrodes in grey and the poling direction as arrows and as – if polled perpendicular to the page.

[2] These samples were cut following later results but have been included in this table for completeness.

These samples were then electroded using a dual target sequential sputter coater (Quorum Q300TD). First a 20nm layer of titanium was placed and then a 200nm layer of silver. Hi-Bond (HB830) amber electrical tape was used as a mask. Each of the cut samples was then poled; the samples that needed a poling voltage above 10kV were poled at Ionix Advanced Technologies[3]. The shear samples were poled and then electrodes were removed and more added to 90° of the poling direction.

5.3.2 Matrix Measurements

The cut, electroded, and poled samples were measured at the University of Glasgow so that the piezoelectric matrix could to be obtained[4]. The impedance (Z) of the samples was measured as a function of frequency, concurrently with the phase (Θ_z). This data was then converted to resistance (R) and reactance (X) for use in a piezoelectric resonance analysis program (PRAP) (Equation 5.1and Equation 5.2). The frequency range used to measure each cut can be seen in Table 5.3.

$$\boldsymbol{R = Z \times \cos(\Theta z)} \qquad \textbf{Equation 5.1}$$

$$\boldsymbol{X = Z \times \sin(\Theta z)} \qquad \textbf{Equation 5.2}$$

Table 5.3: The measured frequency range of impedance per cut.

Mode	Sample Dimensions (mm)	Impedance Spectra (MHz)
Length Extensional (LE)	13x3x3	0.14-0.17
Shear (S)	11x3x0.5	2.00-3.50
Longitudinal Thickness Extension (LTE)	15x2.5x0.5	0.09-0.16
Thickness Shear (TS)[5]	10x10x1	0.95-1.50
Thickness Extension (TE2)[5]	10x10x1	1.00-3.00
Thickness Extension (TE)	20x0.5	4.50-6.50
Radial (RAD)	20x0.5	0.10-0.38

[3] The author wishes to thank Dr Tim Comyn for their assistance.

[4] The author wishes to acknowledge Nicola Fenu for their invaluable assistance.

[5] These samples were measured at a later date but have been included for completeness

An average of 16 impedance sweeps was measured per sample, with 801 points taken per sweep. The sweep time was 3.14 seconds and the source was set at 15V, using an Agilent 4294a. The impedance analyser was calibrated upon switch on using the open and closed circuit process after the fixture was fitted, and also calibrated using a 50Ω resistor.

After the conversion of the data from impedance and phase to resistance and reactance, the data was analysed using PRAP (version 3.1). The impedance curve was modelled using the software and the statistics of the modelled curve produced corresponds to the materials properties. Each cut was analysed with different properties modelled. Table 5.4 presents the properties that were obtained from each cut. The PRAP software then used the results from each of the cuts to produce a composition file which contained the matrix of the material.

Table 5.4: Properties obtained from each cut with PRAP.

Length Extensional (LE)	Thickness Shear (TS)	Longitudinal Thickness Extension (LTE)	Thickness Extension (TE)	Radial (RAD)
k_{33} s^{D}_{33} s^{E}_{33} d_{33} g_{33} $\varepsilon^{S3=0}_{33}$ ε^{T}_{33}	k_{15} c^{E}_{55} c^{D}_{55} s^{D}_{55} s^{E}_{55} e_{15} h_{15} d_{15} g_{15} ε^{T}_{11} ε^{S}_{11}	k_{31} s^{E}_{11} ε^{T}_{33} d_{31} g_{31}	k_{t} c^{D}_{33} c^{E}_{33} e_{33} h_{33} ε^{S}_{33}	s^{E}_{11} s^{E}_{12} d_{31} ε^{T}_{33} k_{P} k_{p} ε^{p}_{33} c^{p}_{11} e^{p}_{31} s^{E}_{66} c^{E}_{66}

5.3.3 Impedance and Phase Results

Each impedance measurement in this section are of each type of geometry or cut. Each graph of data shows the impedance frequency sweep as a solid line above the phase measurements, seen as a dashed line (Figure 5.7 to Figure 5.13).

The data obtained from shear mode samples seen in Figure 5.8 and the thickness extension samples seen in Figure 5.10 were of poor quality. This may be due to the relatively thin samples not being cut as parallel as necessary given their small size and as a result, several resonant frequencies or modes were measured during the shear mode. The electrodes for these samples were fragile and had a tendency to peel which also had an adverse effect on the sample. The circular thickness extension samples only gave a very small signal.

Due to the poor quality of the spectra obtained, samples of 10x10x1mm were cut, electroded and poled at a later date. The thickness shear mode can be seen in Figure 5.12 and the thickness extension mode can be seen in Figure 5.13.

It can be seen that the quality of the data from the shear mode sample (Figure 5.8) is much clearer in Figure 5.12 where the shear sample was changed from 11x3x0.5 to 10x10x1mm. The TE2 sample using the 10x10x1mm geometry gave a larger much signal than the TE sample using the circular 20x0.5mm. This may be due to less clamping of the mode in the new cut.

It should be noted that 801 points were taken for each measurement, regardless of the spectrum range. Therefore, the length extensional mode measurements of 140-170 kHz will have a higher density of points and so are more of an accurate measurement than the thickness extension mode measurement of 1.00-3.00 MHz.

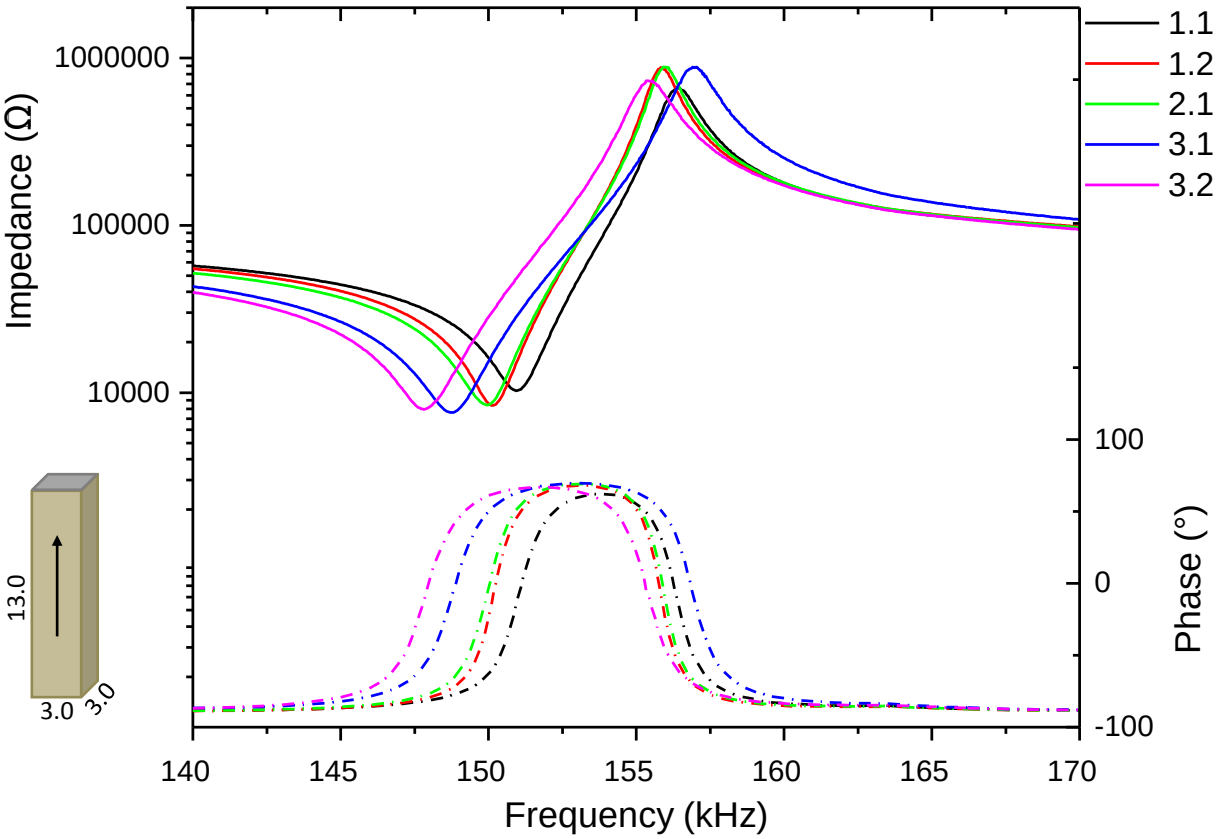

Figure 5.7: Length extensional mode measurements of BCTZ with schematic of sample cut (in mm), electrodes in grey and poling direction indicated by arrow.

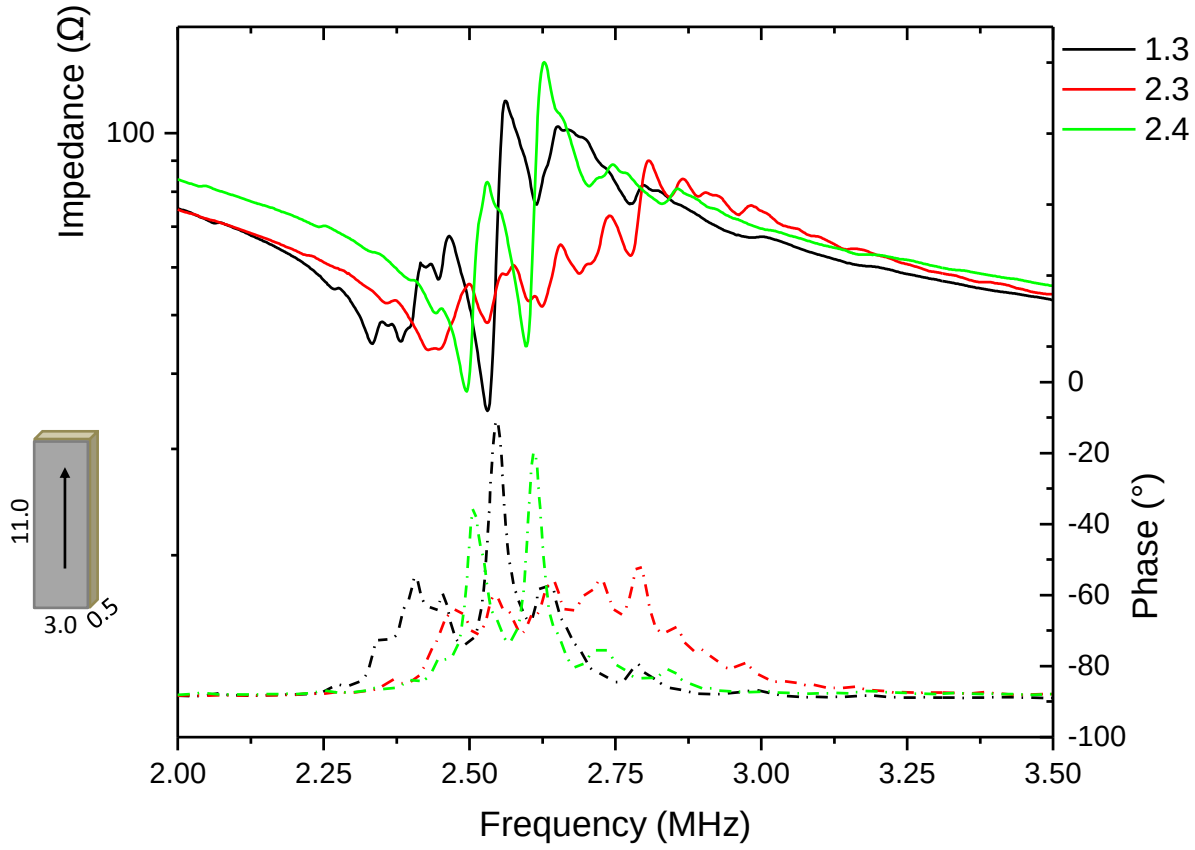

Figure 5.8: Shear mode measurements of BCTZ with schematic of sample cut (in mm), electrodes in grey and poling direction indicated by arrow.

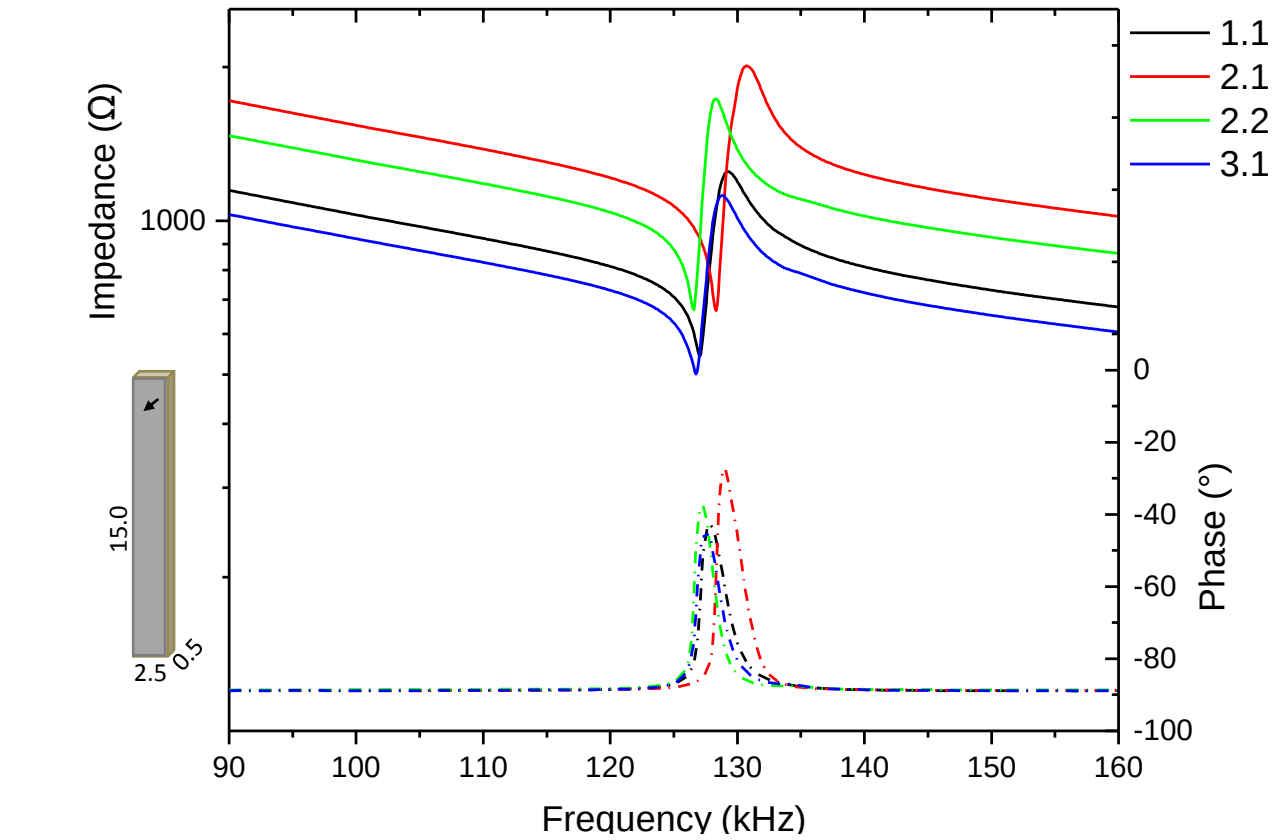

Figure 5.9: Longitudinal Thickness Extension mode measurements of BCTZ with schematic of sample cut (in mm), electrodes in grey and poling direction indicated by arrow.

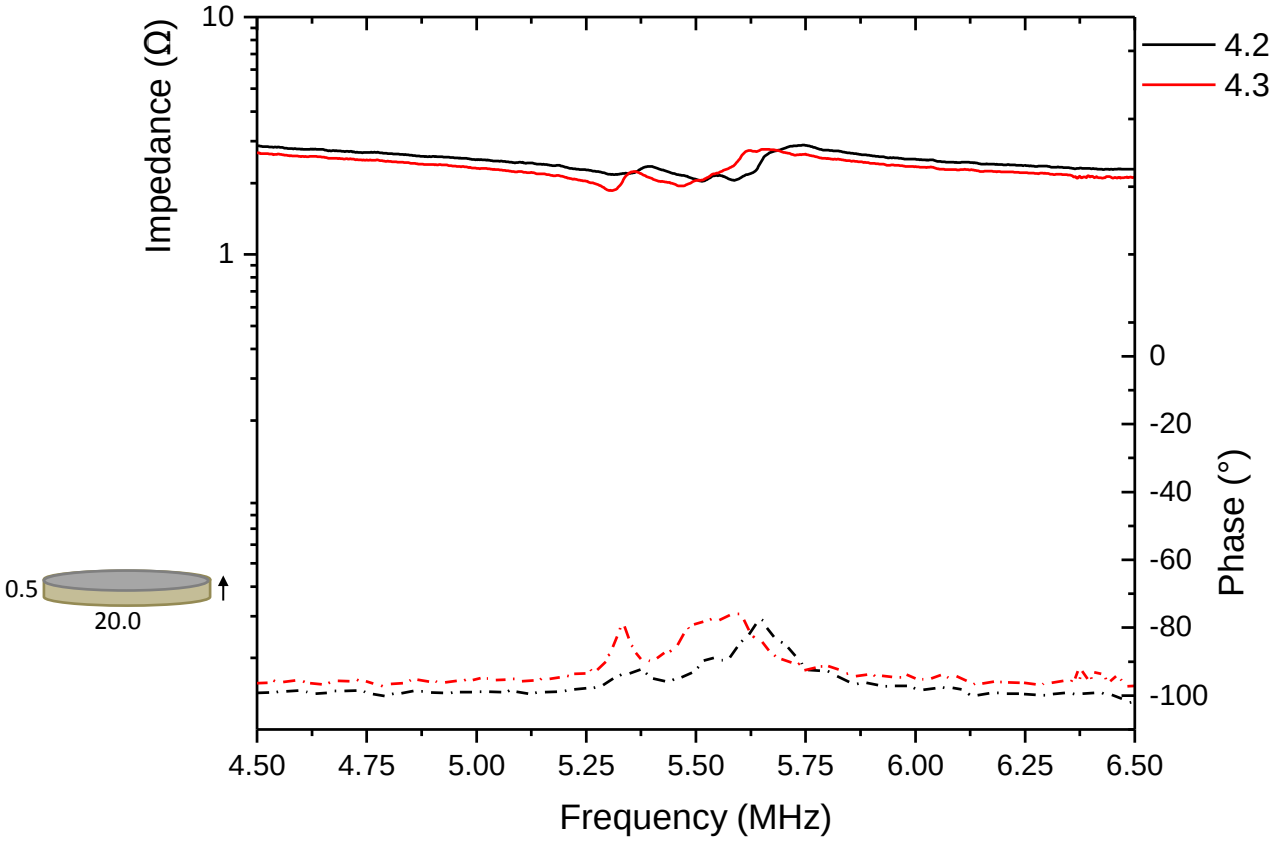

Figure 5.10: Thickness Extension mode measurements of BCTZ with schematic of sample cut (in mm), electrodes in grey and poling direction indicated by arrow.

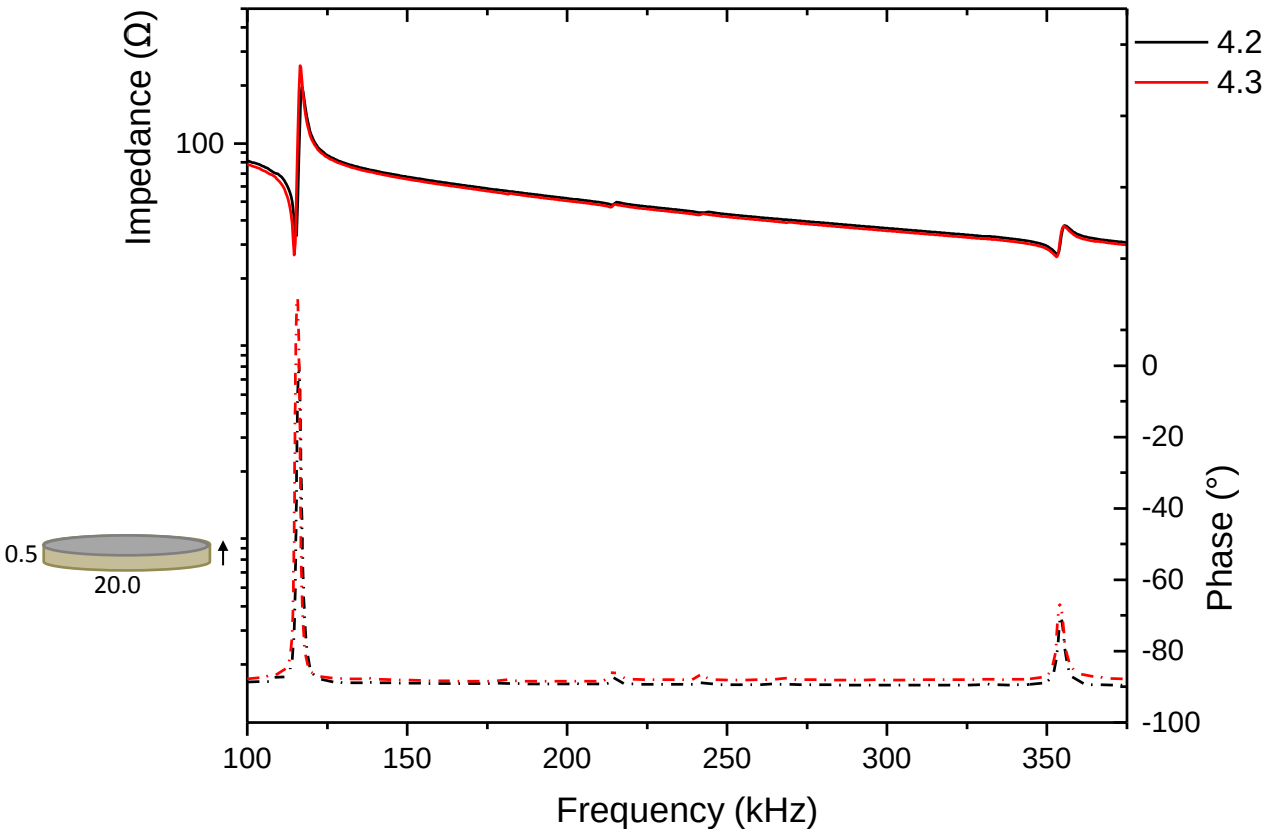

Figure 5.11: Radial mode measurements of BCTZ with schematic of sample cut (in mm), electrodes in grey and poling direction indicated by arrow.

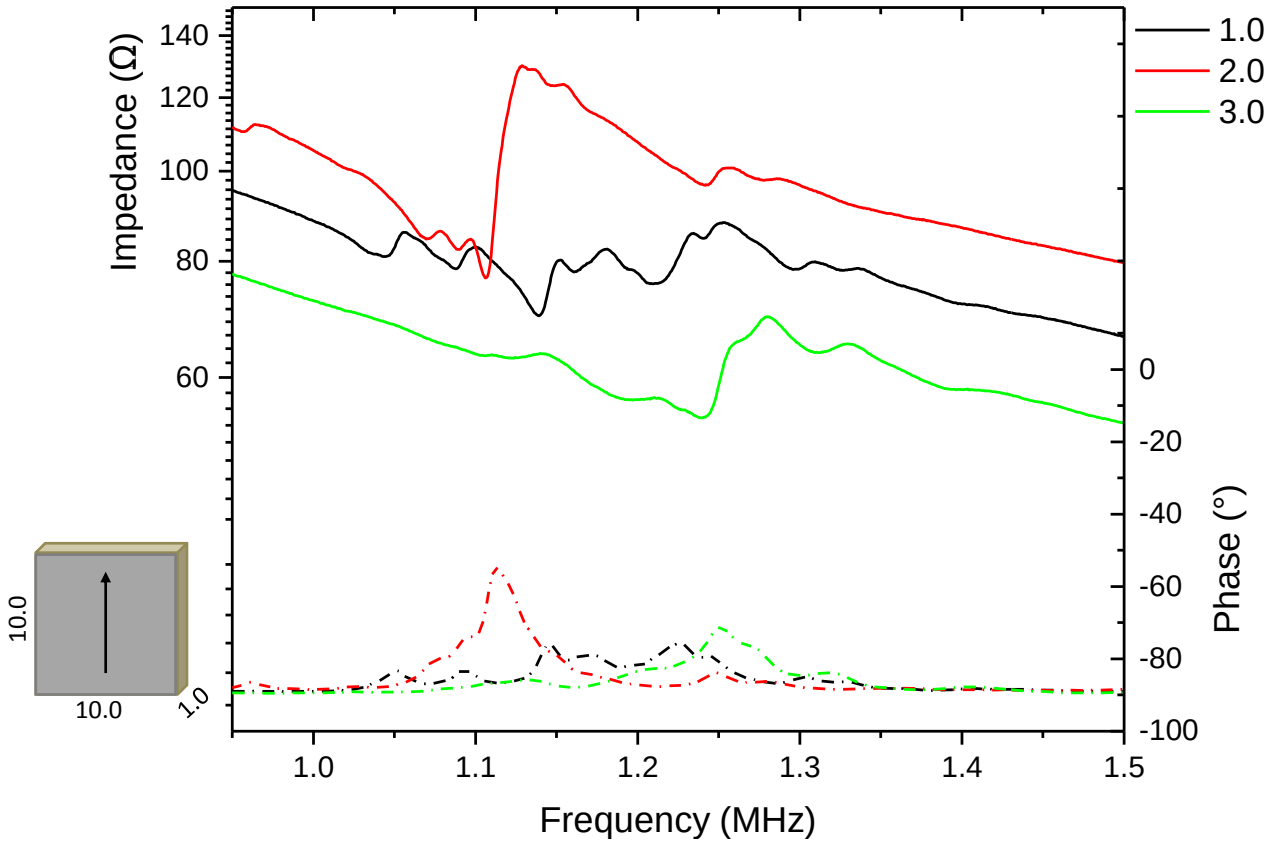

Figure 5.12: Thickness shear mode measurements of BCTZ with schematic of sample cut (in mm), electrodes in grey and poling direction indicated by arrow.

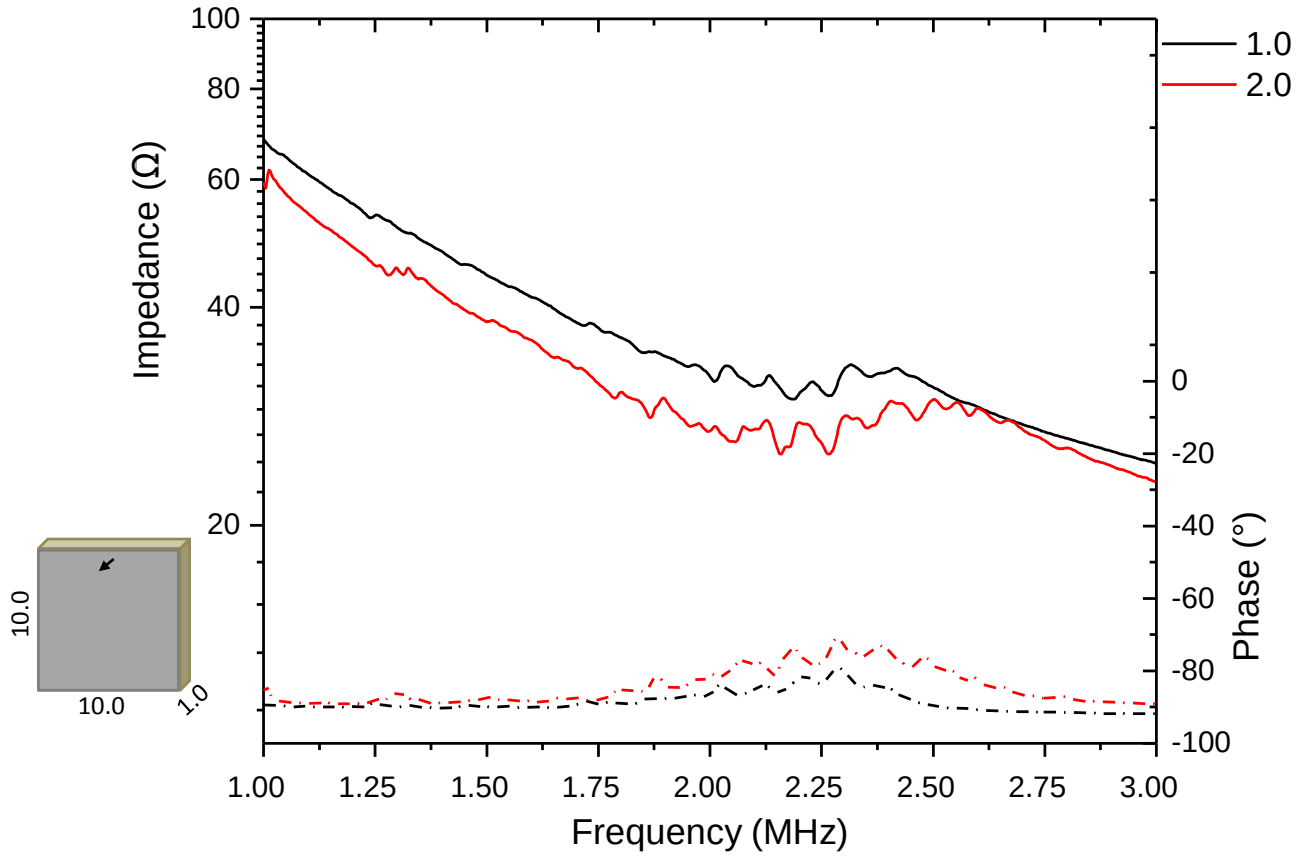

Figure 5.13: Thickness extension mode measurements of BCTZ with schematic of sample cut (in mm), electrodes in grey and poling direction indicated by arrow.

5.3.4 PRAP Results and Discussion

The final PRAP analysis was done on all of the samples of each cut to give a more accurate representation of the material. The alternative thickness shear and thickness extension cuts were used as they gave higher quality data. The piezoelectric matrix and geometric cut that gave the coefficient can be seen in Table 5.5.

The PRAP results are inconsistent with the finite element modelling (FEM) results obtained by Tung *et al* (175). PRAP was developed to measure the IEEE standard samples and assumptions were used in the calculations that heavily relied on PZT. It may be that PRAP is ill equipped to deal with lead-free systems. This may be due to different ferroelectric domains being present which may exhibit nonlinearity and aging effects that are not 'within the scope of the IEEE standard' (176).

It should also be noted that the d_{33} measurements obtained by the Berlincourt method were consistently lower than quoted in numerous scientific papers. This is likely due to the BCTZ synthesis not being optimised, as the project was to determine the feasibility of low Curie point lead-free material being used in a device.

Table 5.5: PRAP results of the; (a) elastic stiffness, c, charge, d, and mechanical, e, coefficients and the resonant frequencies of BCTZ and (b) the voltage, g, stiffness, h, elastic compliance, s, coefficients, the electromechnical coupling, k, and the permittivity of BCTZ, with the geometric cuts they came from.

(a)

Cut	Coefficient	Value
		$1x10^{8}$ (N/m^2)
TE	c^{D}_{33}	16.83
TS	c^{D}_{55}	3.73
TE	c^{E}_{33}	16.41
TS	c^{E}_{55}	3.49
RAD	c^{E}_{66}	5.31
RAD	c^{p}_{11}	9.33
		$1x10^{-12}$ (C/N)
TS	d_{15}	178.12
LTE RAD	d_{31}	257.39
LE	d_{33}	161.26
		$1x10^{1}$ (C/m^2)
TS	e_{15}	6.23
TE	e_{33}	8.93
RAD	e^{p}_{31}	4.69
		$1x10^{5}$ (Hz)
	f_p	1466.11
	f_{p1}	116.61
	f_s	1440.13
	f_{s1}	114.95
	f_{s2}	353.86

(b)

Cut	Coefficient	Value
		$1x10^{-3}$ (Vm/N)
TS	g_{15}	10.25
LTE	g_{31}	20.34
LE	g_{33}	7.50
		$1x10^{8}$ (V/m)
TS	h_{15}	3.83
TE	h_{33}	4.65
TS	k_{15}	0.25
LTE	k_{31}	0.12
LE	k_{33}	0.31
RAD	k^{P}	0.10
RAD	k_p	0.15
TE	k_t	0.16
		$1x10^{-12}$ (m^2/N)
LE	s^{D}_{33}	11.51
TS	s^{D}_{55}	26.84
LTE RAD	s^{E}_{11}	313.28
RAD	s^{E}_{12}	1.50
LE	s^{E}_{33}	12.73
TS	s^{E}_{55}	28.68
RAD	s^{E}_{66}	18.83
		$1x10^{8}$(F/m)
RAD	ε^{p}_{33}	2.42
TS	ε^{S}_{11}	1.62
LE	$\varepsilon^{S3=0}_{-33}$	1.94
TE	ε^{S}_{33}	1.90
TS	ε^{T}_{11}	1.73
LE+LTE RAD	ε^{T}_{33}	2.08

5.4 BCTZ machining and characterisation

Two devices were fabricated using BCTZ as the active ceramic material. A stacked transducer known as a Tonpilz device and a simple hydrophone device was made with a disk shaped ceramic.

5.4.1 Ceramic Machining

Two different ceramic geometries were required for the two different devices fabricated. The first was a ring shape used in the Tonpilz devices and the second a disk which was used in the hydrophone devices.

The rings were cut using a water guided laser cutter (Synova MCS300)[6]. The disks were not machined, as the sintered pellet was within the boundaries of the necessary sample size. Both shapes were electroded using the process found in section 5.3.1.

5.4.2 Ceramic Ring Characterisation

The 15 ceramic rings were made in two batches. The first batch to determine the feasibility of using the laser to machine the samples, and the second batch once the laser was confirmed to be effective. There was a large difference between the batches. It can be seen in Figure 5.14 that the quality of the first set of samples was better than the second. This was reflected in the piezoelectric coefficients of the rings (Table 5.6). One side of the samples from batch 2 was more dense than the other. This was due to the uniaxial press used for the second batch of samples not having parallel plates.

(a) **(b)**

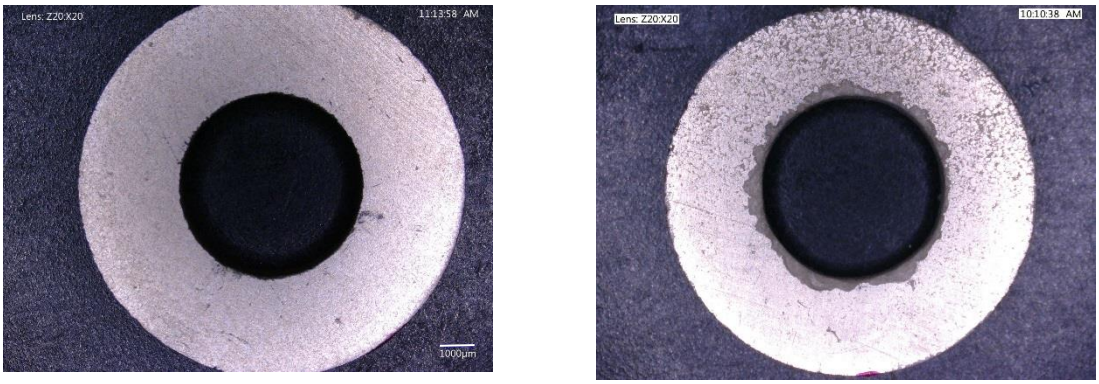

Figure 5.14: Optical microscopy image of a ring from (a) batch 1 (b) batch 2

[6] The author would like to thank Graham Brown at University of Leeds for their assistance.

The samples were then poled using the poling regime discussed previously (section 5.2.4). Due to the variation between batches, there was some disparity between the ring properties. The rings were measured using a Berlincourt device which directly measured the d_{33}, capacitance and tan(δ). The impedance of the rings was also measured and PRAP was used to determine the d_{33}, g_{33} and k_{33} from the modelled PRAP fitting. The results of both measurements can be seen in Table 5.6. It can be seen that the PRAP modelled d_{33} is consistently smaller than the Berlincourt measured d_{33}.

Table 5.6: Berlincourt and PRAP properties of the ceramic rings.

	Berlincourt Measurements			**PRAP Modelled Properties**		
Ring	**d_{33} (pC/N)**	**Capacitance (μF)**	**tan(δ)**	**d_{33} (pC/N)**	**g_{33} (mVm/N)**	**k_{33}**
1	72.33	1299.67	0.025	20.80	1.00	0.041
2	47.00	1171.67	0.028	10.80	0.30	0.016
3	24.67	1360.00	0.027	22.20	0.98	0.041
4	34.67	1380.00	0.027	25.40	1.03	0.045
5	13.67	1381.67	0.025	12.50	0.52	0.022
6	14.50	1387.67	0.024	15.50	0.84	0.032
7	47.00	1279.67	0.025	17.00	0.60	0.027
8	44.50	1070.33	0.026	25.30	1.12	0.047
9	25.50	1431.00	0.025	13.70	0.57	0.025
10	101.50	1167.67	0.027	86.60	3.38	0.134
11	138.67	1148.67	0.020	105.40	5.40	0.212
12	187.33	1184.33	0.020	139.40	6.58	0.264
13	187.00	1211.67	0.030	136.40	6.92	0.276
14	177.67	1216.00	0.024	141.60	6.48	0.259
15	146.33	1160.00	0.021	122.80	5.65	0.229

Three Tonpilz devices were made, with 4 rings per device. The rings were split into different qualities with a Bronze, Silver and Gold standard. The 4 rings with the best d_{33} measurements using the Berlincourt device were used in the gold standard, the next best were used in the Silver standard, and the third best were used in the bronze standard device. The capacitance of the rings was also measured using a multimeter at 1kHz. The grouped rings and the device they were used in can be seen in Table 5.7.

Table 5.7: The ceramic rings used in each Tonpilz device.

Tonpilz Device	Ring number	Berlincourt d_{33} (pC/N)	Capacitance at 1kHz (μF)
Discarded	3	24.67	1342.80
	5	13.67	1379.00
	6	14.50	1396.60
Bronze	8	44.50	1075.80
	2	47.00	1172.50
	4	34.67	1378.10
	9	25.50	1431.40
Silver	10	101.50	1096.20
	11	138.67	1112.70
	7	47.00	1293.80
	1	72.33	1300.60
Gold	15	146.33	1126.00
	14	177.67	1127.60
	12	187.33	1158.20
	13	187.00	1182.10

5.4.3 Ceramic Disk Characterisation

The d_{33} and d_{31}* of the disks were measured using the Berlincourt method. As the samples were large and the poling apparatus used a narrow rod, the samples were measured 4 times turning 90° after each measurement was taken, and the average calculated. The d_{31} was calculated using Equation 5.3, where *t* is the sample thickness and *d* is the diameter (177). The results can be seen Table 5.8.

$$d_{31} = \frac{d_{31}^{*}/t}{d} \qquad \textbf{Equation 5.3}$$

Table 5.8: d_{33} and d_{31} of the ceramic disks.

Disc Number	Thickness (mm)	Diameter (mm)	d_{33} (pC/N)	d_{31}* (pC/N)	d_{31} (pC/N)
1	4.80	21.29	115.5	-204.25	-46.05
2	4.78	21.25	76.25	-225.25	-50.68
3	4.40	21.18	30.75	-199.25	-41.41
4	4.46	21.17	66.75	-236.5	-49.80

The impedance, *Z*, phase, Θ_Z, resistance, *R*, reactance, *X*, admittance, *Y*, conductance, *G* and susceptance, *B,* of the disk samples were measured between 100kHz to 1500kHz. Each of these measurements can be calculated from the impedance and phase measurements (Equation 5.1 and Equation 5.2 above, and Equation 5.4-Equation 5.7 below) and so only these are presented (Figure 5.15). The capacitance (at 1kHz) and the tan(δ) of the samples was measured using an Agilent 4990a, with 1601 points being averaged 3 times and can be seen in Table 5.9.

$$Z = \sqrt{R^2 + X^2} \qquad \textbf{Equation 5.4}$$

$$Y = \sqrt{G^2 + B^2} = \frac{1}{Z} = \frac{1}{\sqrt{R^2+X^2}} \qquad \textbf{Equation 5.5}$$

$$G = \frac{1}{R} \qquad \textbf{Equation 5.6}$$

$$B = \frac{1}{X} \qquad \textbf{Equation 5.7}$$

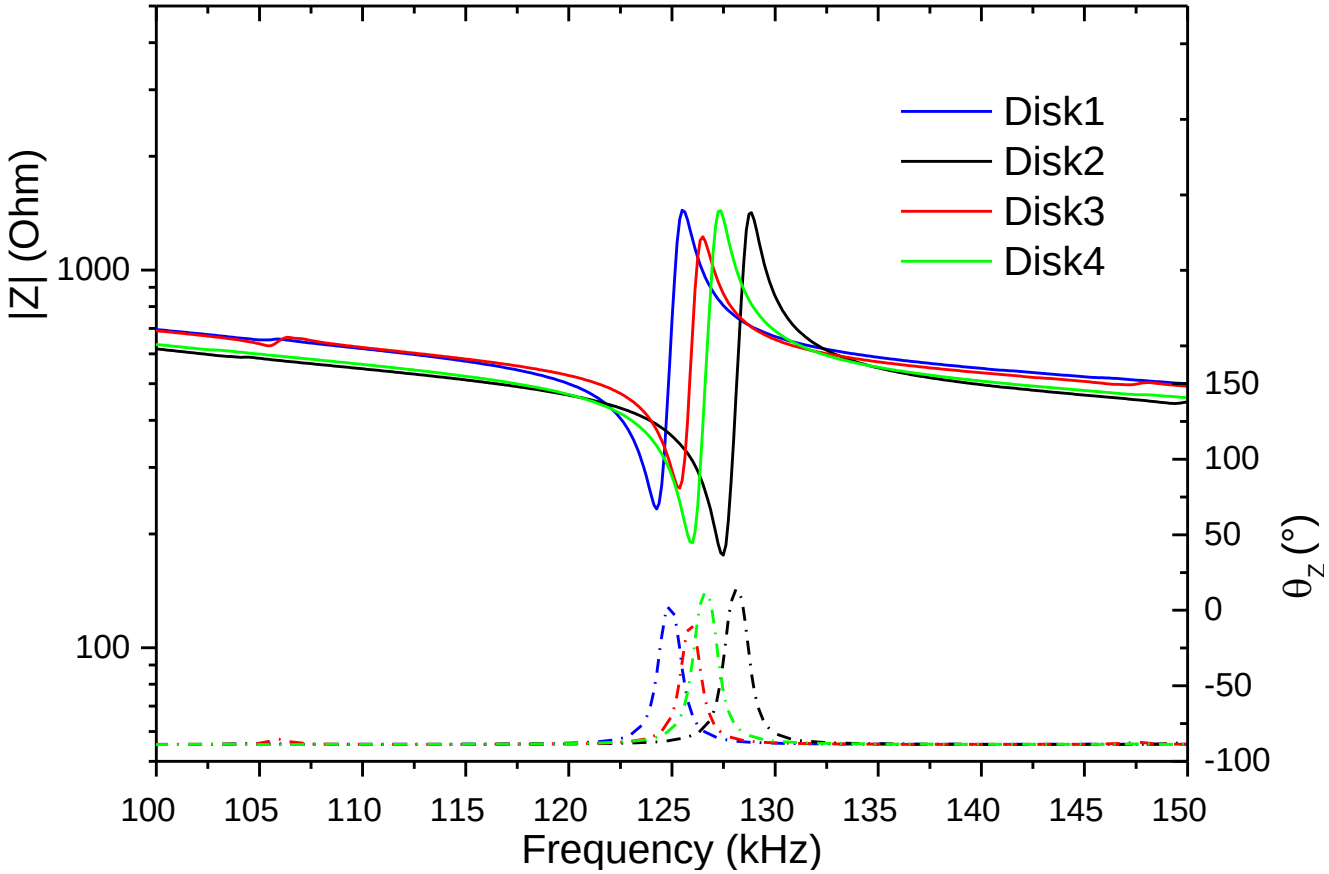

Figure 5.15: Impedance and Phase measurements of Disks 1-4 from 100-150kHz.

Table 5.9: Table of Capacitance and tan(δ) of BCTZ disk samples

Disk Number	Thickness (mm)	Diameter (mm)	Capacitance (μF)	Tan (δ)
1	4.80	21.29	0.00234	0.0168
2	4.78	21.25	0.00266	0.0171
3	4.40	21.18	0.00237	0.0177
4	4.46	21.17	0.00257	0.0163

Impedance measurements between 100-150kHz show a resonant frequency around 125kHz.

The conductance versus susceptibility of the disks can be seen in Figure 5.16, known as a G-B loop. This helps predict the responsivity of the devices. The larger the diameter of the loop, the more responsive.

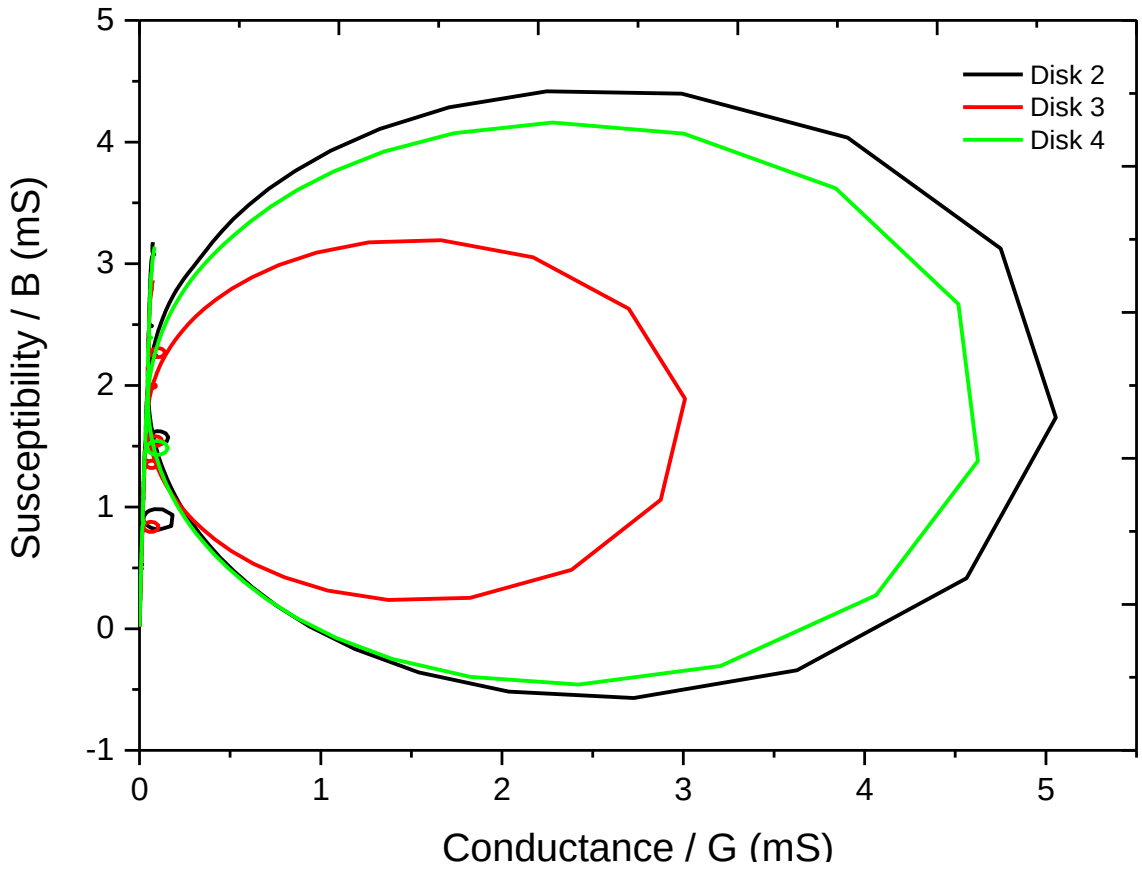

Figure 5.16: G-B loop of the disk samples.

Both types of samples were thoroughly characterised in order to help estimate the best samples to be included in the devices, or in order for a comparison of free samples (not in devices) and clamped samples (in the devices) to be made. They were also used an indicators for which samples would produce the most sensitive devices.

Upon completion of the measurements the samples were incorporated into devices. The next section describes the types of devices made, describes the measurements done on said devices, and the results of the device characterisation.

5.5 Lead-free Devices

5.5.1 Device Schematics

5.5.1.1 A Tonpilz device

A Tonpilz design device uses a piezoelectric stack between a piston head mass which radiates into the water and a tail mass at the rear which provides inertial backing (178). The ceramic rings were used to make this device, a schematic of a Tonpilz device can be seen in Figure 5.17, which was adapted from (179).

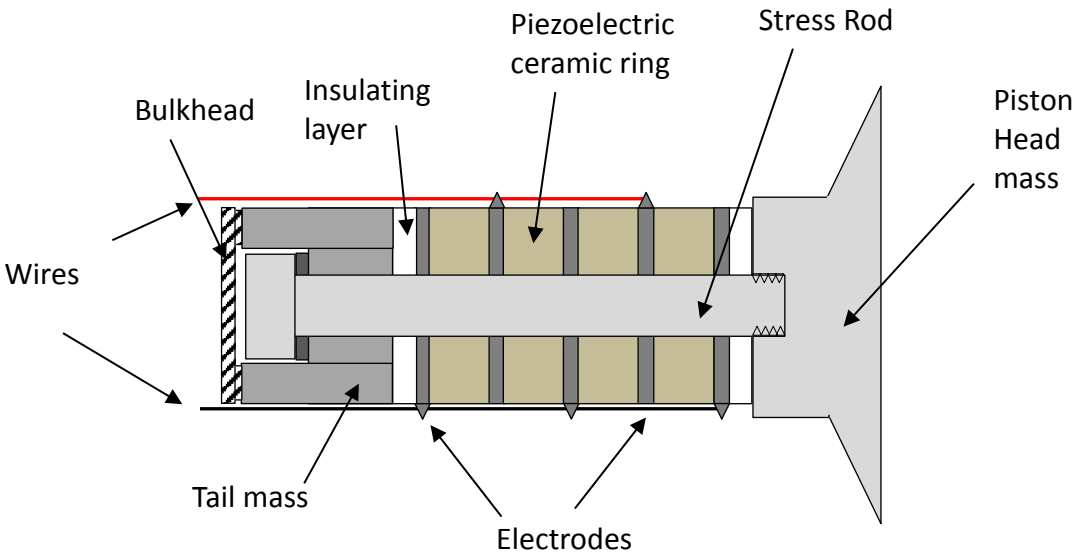

Figure 5.17: Cross section of a Tonpilz device.

5.5.1.2 The hydrophone device

The hydrophone devices were made using the disk shaped ceramic samples. The simple design was a piezoelectric ceramic connected to two wires via silver paste on silver tape. This design was used so as to remove any heat treatment that conventional soldering techniques would introduce to the ceramic.

The whole arrangement was then covered in a ρ-c polyurethane. A ρ-c material allows sound to propagate at the same speed as in water, acting as an acoustic window, whilst environmentally protecting the device from water. In order to make sure the ceramic was at the centre of the mould when curing, small rods of cured ρ-c material of the same composition was used (as seen in the schematic found in Figure 5.18).

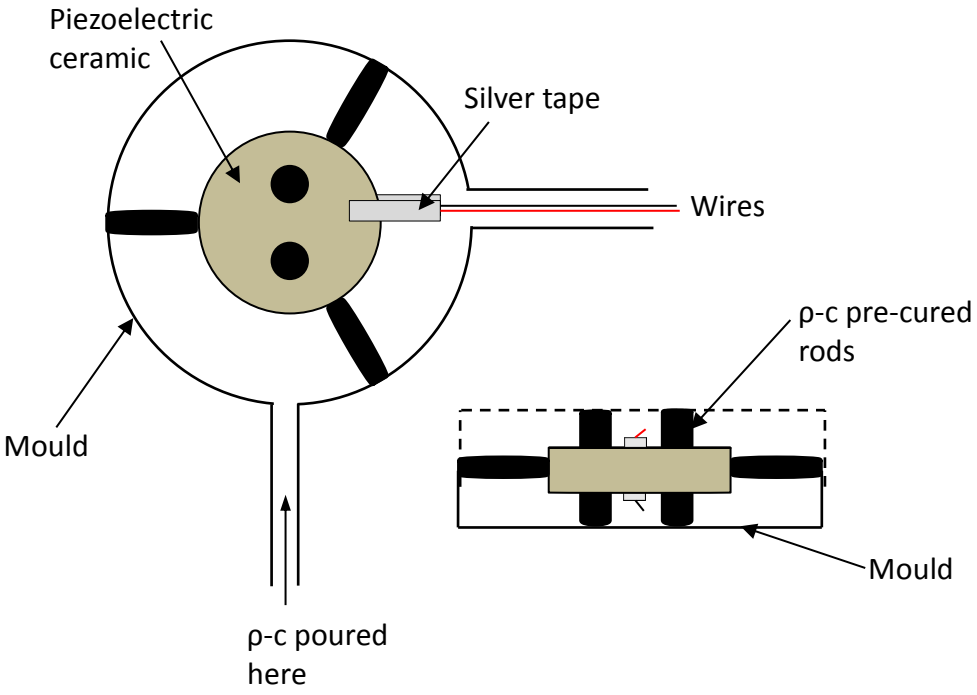

Figure 5.18: Schematic of the simple hydrophone device in the mould (before pouring the ρ-c material).

As the ρ-c material was poured and the devices were cured[7], the temperature of the devices was measured in order to guarantee it did not exceed the Curie point of 90°C. The temperature of the curing material reached a maximum of 30°C within the first two hours and then remained far below this temperature afterwards (Figure 5.19). The curing process was done at ambient temperature over 12 days.

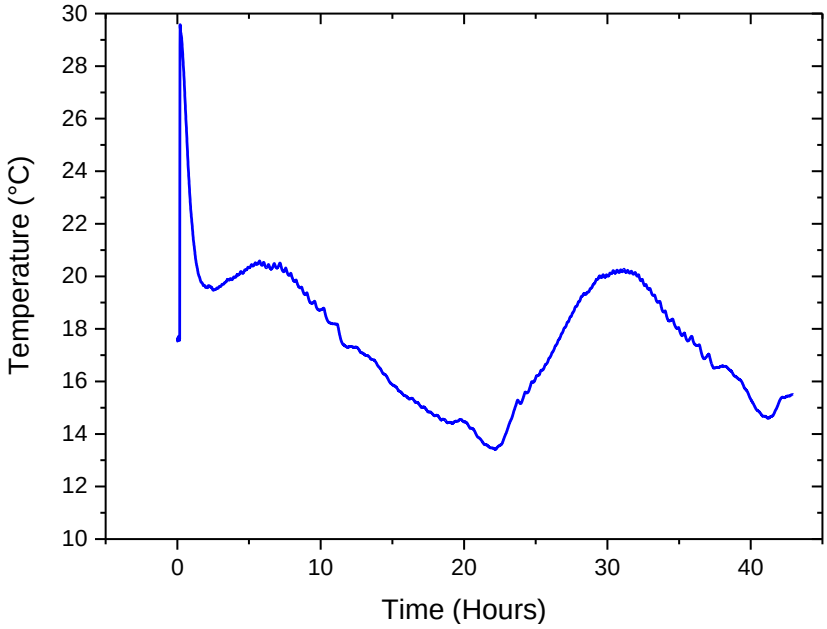

Figure 5.19: Temperature of the devices as the ρ-c material was cured.

[7] The author would like to acknowledge and thank Bo Tyson for potting and wiring the samples.

5.5.2 Device characterisation signal processing

In order to describe how the device characterisation was accomplished, a signal processing outline can be seen in Figure 5.20.

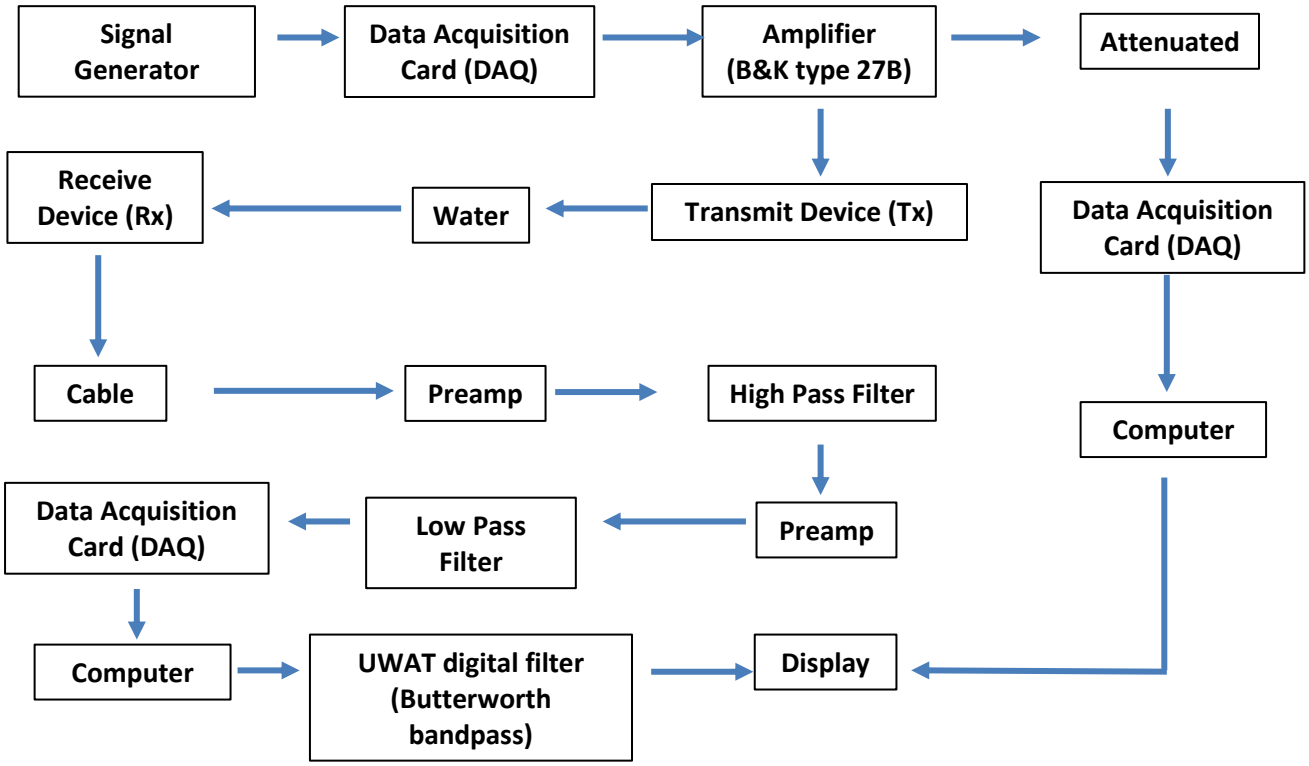

Figure 5.20: Acoustic signal processing used during receive sensitivity characterisation.

The signal was generated with specified characteristics (frequency or amplitude) by the Thales proprietary software. This was then converted from a digital signal to an analogue signal using the data acquisition card (DAQ), which is then amplified by 40dB (~ x100) by an amplifier. The signal was sent two ways. One was sent back to the computer display, after being attenuated by -40dB, and converted back to digital.

The second was sent to a hydrophone which vibrated making an acoustic pressure wave in the water. This acoustic wave was then sent through the water to the device. The distance between the hydrophone and the device varied but was around 1.66m, the signal took 1.097µS to get from the source to the device, and the speed of sound in the water was therefore 1513.2 m/s.

The device then sensed the pressure being sent from the hydrophone and the piezoelectric material converts the mechanical signal back into an electrical charge signal which is sent through a long cable. In the long cable

some charge is lost and so the signal appears smaller than it should. This was corrected for later. The signal was then sent to a preamp which amplified the signal by 20dB for the hydrophone device, the signal was not amplified for the Tonpilz devices due to clipping. The signal passes through a high pass filter which allows through anything above the high frequency threshold. This high frequency threshold is usually set to twice the highest frequency generated. After the high pass filter 20dB amplification is applied before the signal passes through a low pass filter. The low pass is usually set to half the lowest frequency generated. The signal is then converted to a digital signal from an analogue signal using another DAQ, and sent to the computer. A Butterworth bandpass is applied which removes any signal missed by both the high and low pass filters from being displayed by the Thales proprietary software.

5.5.2.1 Transmit Voltage Response measurements

The transmit voltage response (TVR) is defined as the output sound intensity level generated at 1m range by a transducer per 1V of input voltage as a function of frequency (180). The device is driven at a constant driving voltage over a range of frequencies and the output is measured by a receiving device.

5.5.2.2 Beam Pattern Measurement

A directionality pattern, or beam pattern, is the sound intensity level as a function of angle on the same horizontal plane at a given frequency (180). The device is spun 360° and either transmits or receives a pressure. The measured response is displayed as a polar plot with 0° representing broadside. Within this chapter each segment of the polar plot is 30° and each ring is the equivalent of 10dB re µPa at 1 m if measuring the receive sensitivity or 10 dB re V/µPa if measuring the transmit sensitivity.

5.5.3 Tonpilz device characterisation and results

5.5.3.1 In Air testing

The Tonpilz devices were housed in a steel housing to keep the direction of the devices consistent and to protect the devices from the water. Impedance measurements were taken in air in August 2018 and October 2018 to see if there was any aging to the devices under preloading.

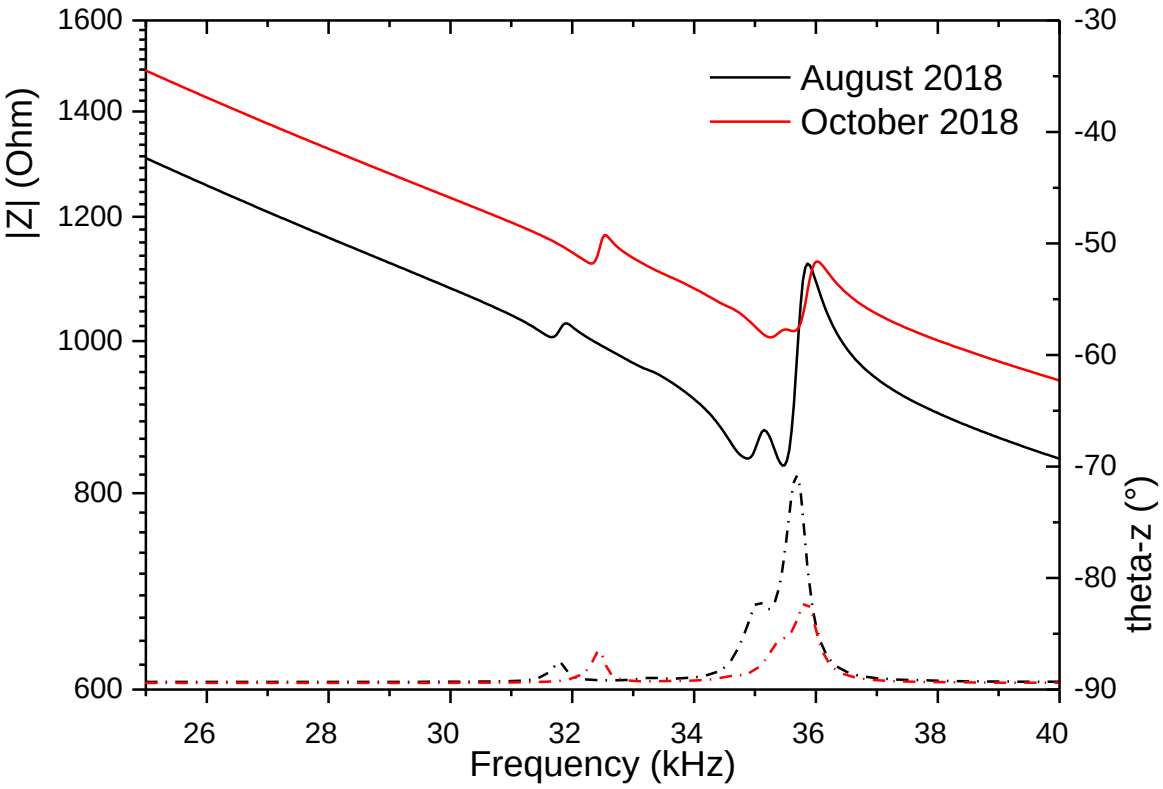

Figure 5.21: Impedance and phase of the Gold Tonpilz device in August and October 2018.

The Gold device had the largest impedance peak of the three devices. This is due to the ceramic being of the highest quality and the highest piezoelectric d_{33}. It can be seen that there is a large decrease in performance with time (Figure 5.21). The Gold device resonant peak is at a higher frequency than the Bronze and Silver devices at just below 36kHz, whereas the Bronze and Silver devices were at 32.7kHz and 35kHz respectively.

Two smaller peaks can be seen, the first at 31.2kHz increases with time, this may be an due to the ceramic stack being forced to deform overtime increasing the prominence of this feature. The second smaller peak just before the resonant peak decreases and its presence, may be due to some non-uniformity in the ceramic rings.

It should be noted that each of the devices had a reduction in overall impedance with time. This is also reflected in the capacitance and loss of the devices. The capacitance dropping is an indication that there was a loss in overall piezoelectric performance.

Table 5.10: Capacitance and tan (δ) of the devices measured in August and October 2018.

Tonpilz Device	Capacitance (μF)		tan (δ)	
	August	October	August	October
Bronze	0.00485	0.00457	0.0281	0.0176
Silver	0.00481	0.00443	0.0188	0.0148
Gold	0.00493	0.00435	0.0181	0.0131

Long cables were soldered to the devices in the housing so that the transmittance and sensitivity measurements could be taken in water. The capacitance of the devices, C_T, and the capacitance of the cable, C_C are used in Equation 5.8:

$$\boldsymbol{dB\ Correction = 20 \times log_{10}(1 + \frac{C_C}{C_T})} \qquad \textbf{Equation 5.8}$$

When measuring the receive sensitivity, dB correction is required as charge is lost in the cable leading to a lower voltage reading. The dB correction for the Bronze, Silver and Gold devices in the housing was calculated to be 1.50, 1.51 and 1.57dB respectively. Transmit voltage response measurements do not require this correction.

5.5.3.2 Receive Sensitivity

When measuring the receive sensitivity as a function of frequency of a device, the fast Fourier transform (FFT) of the data is also displayed. The points where the FFT follows the same trend as the signal received is the point at which the signal received can be seen above the noise. The receive sensitivity of the Tonpilz devices is shown in Figure 5.22.

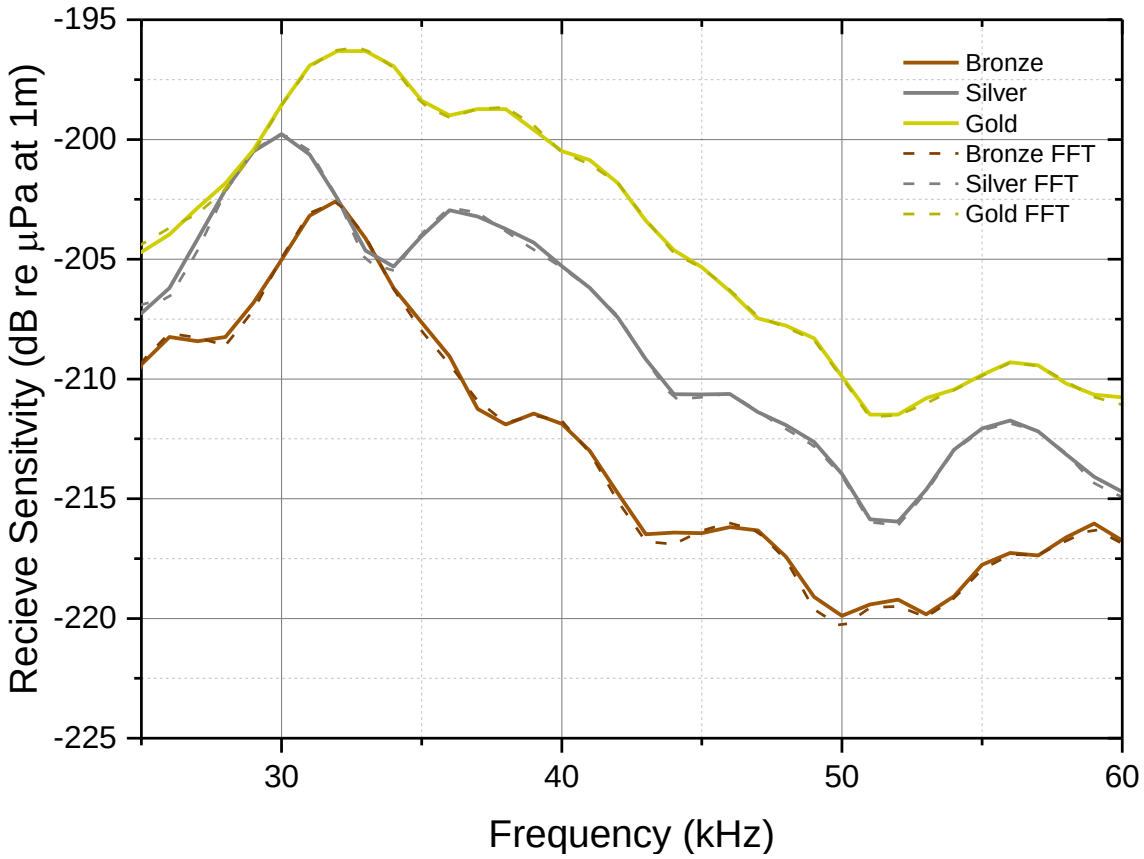

Figure 5.22: Receive Sensitivity of the Tonpilz Bronze, Silver and Gold Devices from 25kHz to 60kHz.

There is a broad peak in sensitivity between 30-34kHz depending on the device. The most sensitive device is the Gold, followed by the Silver and finally the Bronze. The largest recorded received sensitivity was -197dB re µPa at 1 m at 32-33kHz.

The receive sensitivity as a function of angle of each device can be seen in Figure 5.23. The constant frequency used was 40kHz, as it was off-resonance but remained a high sensitivity frequency.

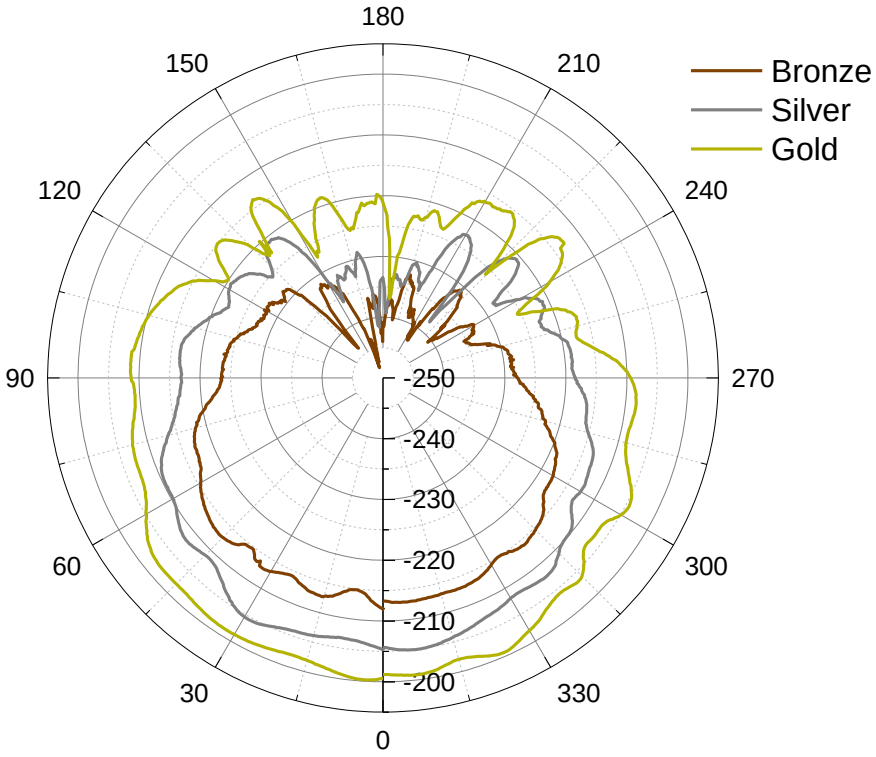

Figure 5.23: Receive Sensitivity beam pattern of each Tonpilz device for comparison.

The devices receive the largest pressure signal at broadside, with gold having the largest sensitivity of -200dB re µPa at 1 m. Followed by the silver device at -205dB re µPa at 1 m and the bronze at -214dB re µPa at 1m. All of the beam patterns appear fairly symmetrical either side of broadside.

5.5.3.3 Transmit Sensitivity

A comparison of each of the devices driven at 111V (RMS) can be seen in Figure 5.24.

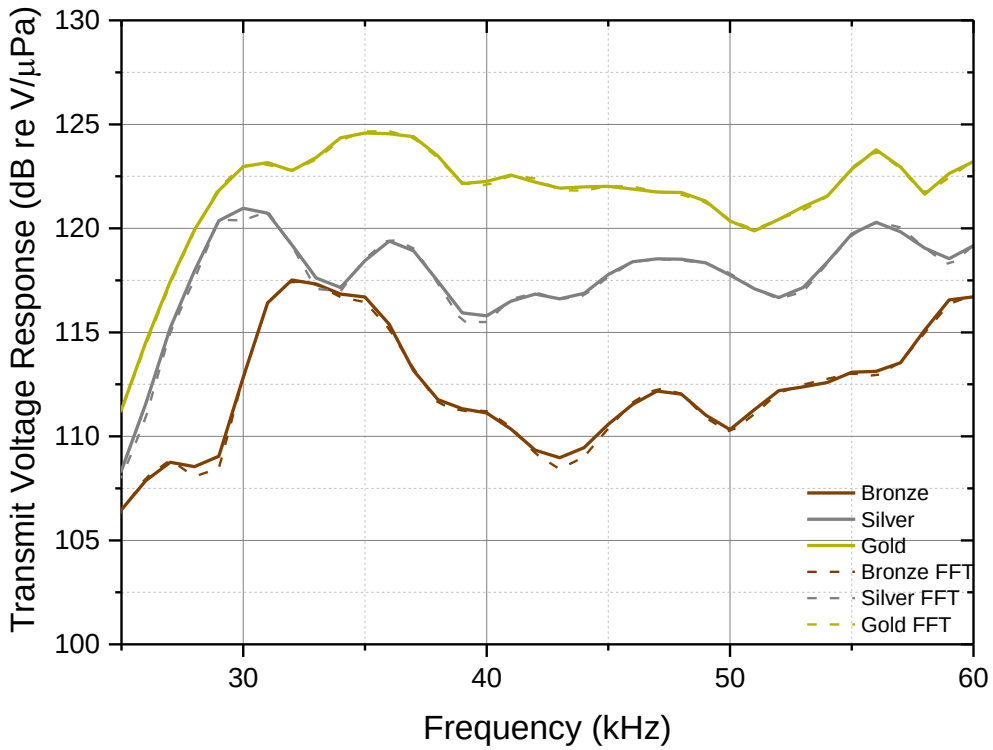

Figure 5.24: Transmit voltage response (TVR) of each device driven at 111V.

The bronze device response increases from 107dB re V/µPa at 25kHz to 117.5dB re V/µPa at 32.5kHz. After this the signal decreases slightly to 110dB re V/µPa and remains fairly constant to 60kHZ. The silver device follows the same trend, peaking at 120.5dB re V/µPa at 31kHz, and remaining between 115 and 118dB re V/µPa until 60kHz. The gold device also follows this trend, with a peak response of 124dB re V/µPa at 35kHz and remaining between 121 and 125dB re V/µPa to 60kHz.

The transmit signal received by the hydrophone as a function of angle at a frequency of 40kHz can be seen below (Figure 5.25). At a driving voltage of 111V (RMS) the beam pattern is fairly symmetrical.

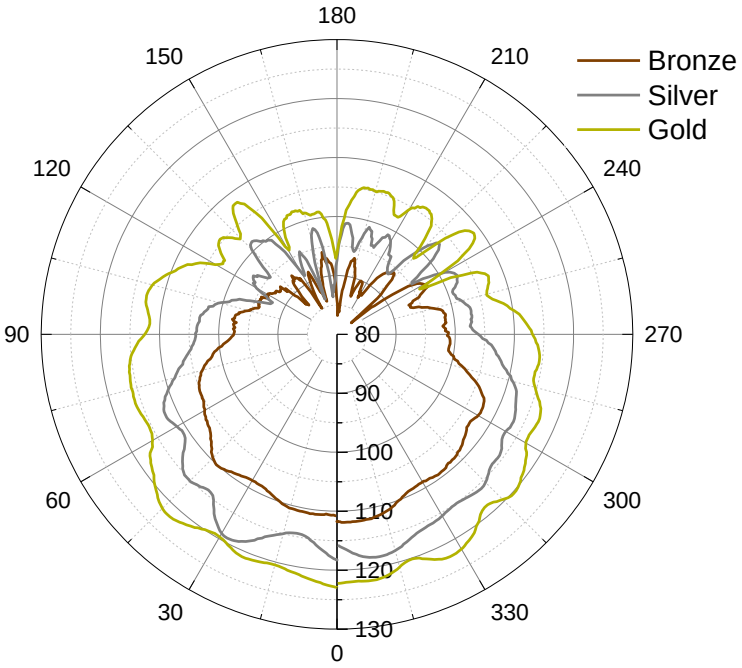

Figure 5.25: A comparison of the transmit sensitivity at 1m versus angle results of each Tonpilz device at 111V (RMS) and 40kHz.

5.5.4 Hydrophone device characterisation and results

5.5.4.1 In Air testing

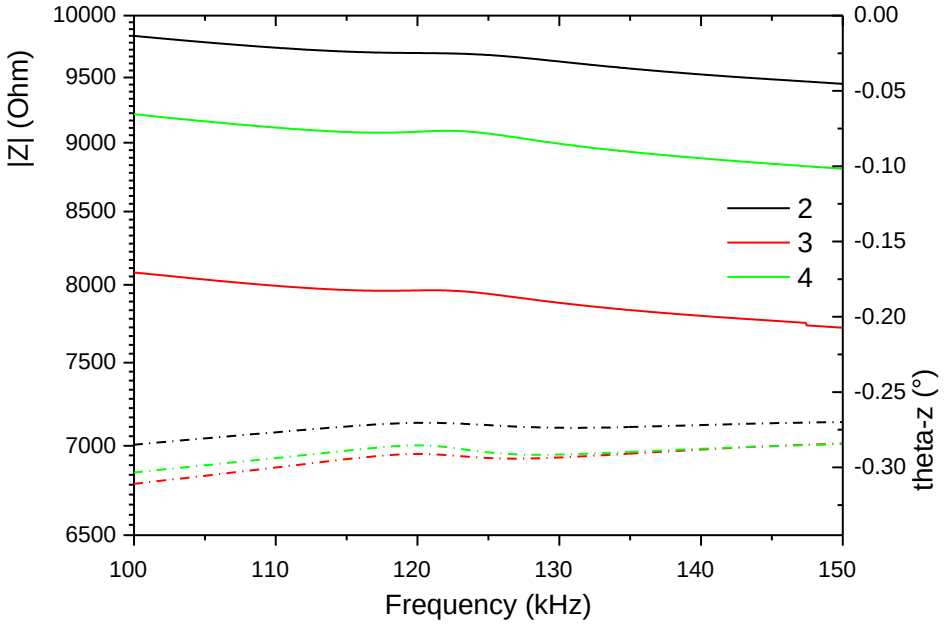

Figure 5.26: Impedance (solid line) and phase (dashed line) measurements of devices 2-4 from 100-150kHz.

There is a large difference in impedance between the hydrophone devices as disk samples (Figure 5.15) and devices (Figure 5.26). The peak at 125kHz has been heavily damped, this is also reflected in the phase data where there is almost no phase change. To see this more clearly, Figure 5.27 is the difference between the impedance of disk 2 and the impedance of the device 2. The sample becomes heavily damped when encapsulated in polyurethane.

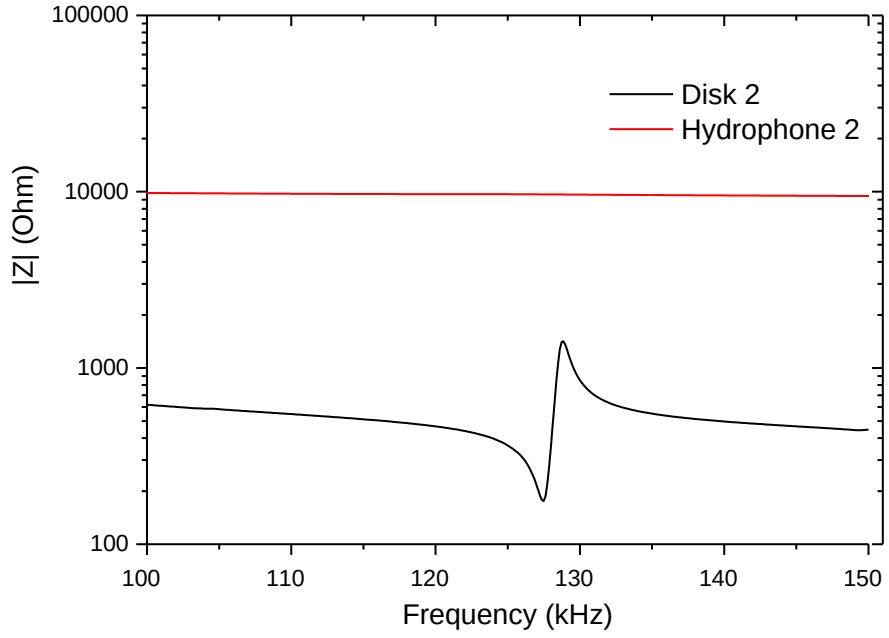

Figure 5.27: Comparison of the impedance of disk 2 and hydrophone 2.

5.5.4.2 Receive Sensitivity

The receive sensitivity of the hydrophone devices between 25kHz and 140kHz can be seen in Figure 5.28. The dB correction for devices 2, 3 and 4 was calculated to be 4.39dB, 4.53dB and 4.49dB respectively.

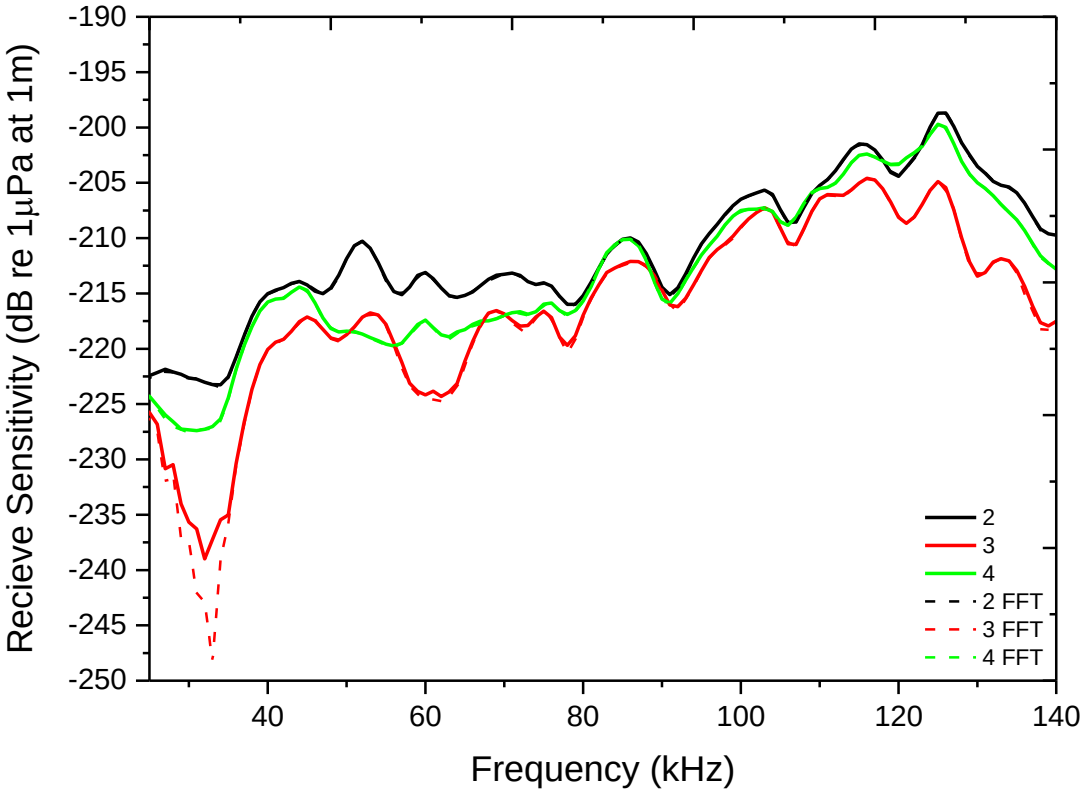

Figure 5.28: Hydrophone receive sensitivity between 25-140kHz.

The receive sensitivity is constantly above -225dB re µPa at 1m from 40kHz to 140kHz and reaches a maximum at the resonance (~120kHz) of -200 dB re µPa at 1m. Generally device 2 is the most sensitive followed by device 4 and finally device 3, which aligns with the diameters of the G-B loops measured in the disk samples (Figure 5.16).

5.5.4.3 Transmit Sensitivity

The hydrophone device 4 was driven at 30V and 80V between 25 and 150kHz. The transmittance was above 105 dB re V/µPa between 40kHz and 150kHz, and peaked at 140 dB re V/µPa at 120kHz. Hydrophone devices are not usually used to project a pressure. It is compelling that it survived at all.

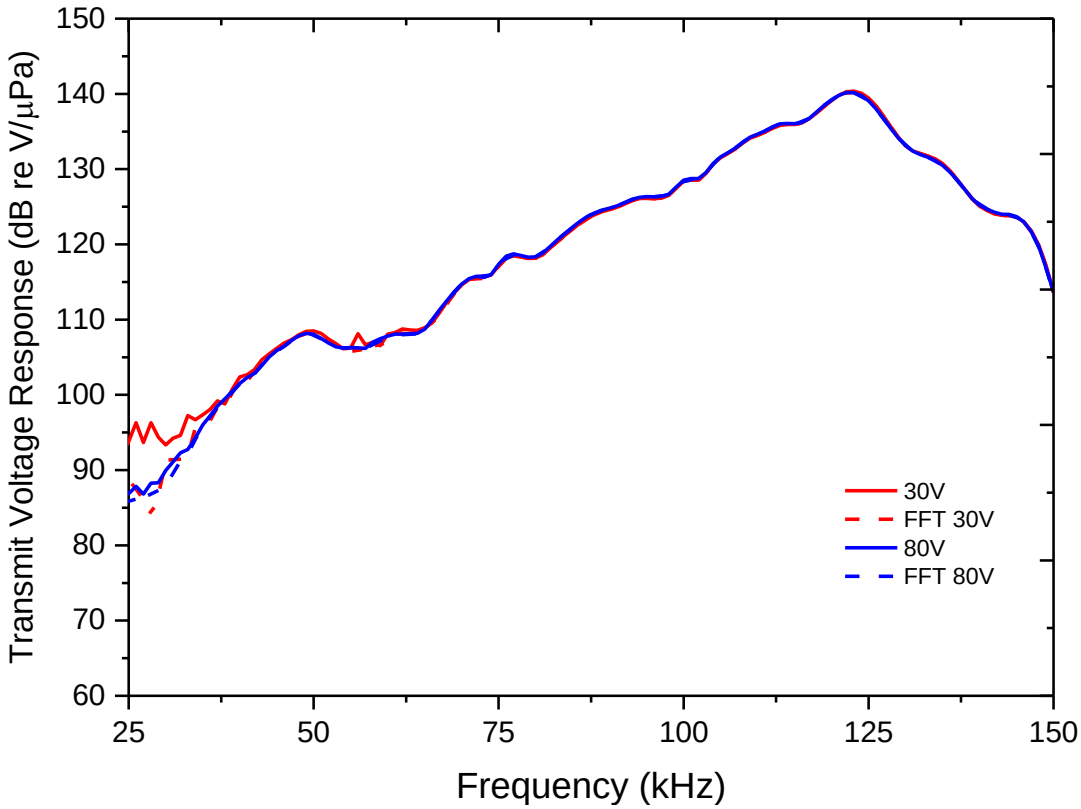

Figure 5.29: Transmit Voltage Response at 1m of Hydrophone 4 driven at 30V and 80V from 25kHz to 150kHz

5.6 Conclusion

The project proved that fabricating a lead-free transducer for SONAR applications is achievable and that with some adjustment to the procedure, the low Curie point of the material can be circumvented. However, there is still the issue of storage, where the device could feasibly reach temperatures as high as 70°C.

The ability to produce large, dense ceramic samples of BCTZ was fundamental to this outcome. It allowed the samples to be machined to shape, as well as heavily preloaded in the device. This is why it is paramount that other lead-free candidates must be made to be as just as solid and tough. Optimisation of the synthesis of BCTZ would improve the overall piezoelectric performance. This could be done by isopressing samples before sintering, optimising the sintering temperature, and improving poling regime such as poling whilst cooling through the Curie point.

The project also brought into question PRAP's ability to correctly model the piezoelectric properties of lead-free materials. This may be due to assumptions in the development of the software.

6. $KNbO_3$ based materials

KNN-based materials have been widely researched, with the main aim of tailoring the phase transitions to occur at room temperature, or the operating window of a device. This is done by doping or substitution of different ions into the base material, producing a solid solution. This chapter covers why the base material of this thesis is $KNbO_3$, the effect substitution of $CaZrO_3$, and $LiNbO_3$ has on the phase of $KNbO_3$ and the processing complications that arose. The aim of the work was to produce a $KNbO_3$ based material with a rhombohedral phase at room temperature and another $KNbO_3$ based material with a tetragonal phase at room temperature and then combine them to replicate the mixed phase found in PZT or BCTZ.

6.1 Pure Potassium Niobate

6.1.1 $KNbO_3$ as a base material

The phase transitions of pure $(K_{0.5}Na_{0.5})NbO_3$ occur at -120°C, 200°C and 420°C for the T_{R-O}, T_{O-T} and T_{T-C} respectively (113). This means that in order to bring the T_{R-O} transition up to room temperature it must be tailored to move 145°C and to bring the T_{O-T} transition down to room temperature it must be moved by 175°C. As the inclusion of most ions reduces the Curie point of a material, it is favourable to add the minimum number of ions required for the desired outcome.

Pure $KNbO_3$ on the other hand has phase transitions that occur at -10°C, 225°C and 435°C for the T_{R-O}, T_{O-T} and T_{T-C} respectively. This means that to tailor the T_{R-O} phase transition to room temperature it must be moved up 35°C, significantly less than KNN. The T_{O-T} transition must be moved 200°C to room temperature, more than KNN by 25°C. The Curie point (or T_{T-C} or T_C) of $KNbO_3$ is slightly higher than KNN by 15°C.

It was therefore determined that, although there is much less research associated with it, the phase transitions temperatures of $KNbO_3$ may make it a superior base material to KNN. $KNbO_3$ and KNN are isomorphous (albeit at different temperatures) and almost identical in unit cell parameters. It was therefore assumed that doping $KNbO_3$ with similar ions to the research on KNN would produce a similar outcome (181, 182).

6.1.2 Pure $KNbO_3$ Synthesis

$KNbO_3$ was synthesised using the mixed oxide method outlined in section 4.1. The sintering temperature (T_{sint}) was 1025°C. Initially, the sintering setup was as standard in electroceramic synthesis, pressed pellets surrounded by $KNbO_3$ powder placed on an alumina tile, with an upside down alumina crucible acting as a lid. However the XRD results obtained from a crushed sample did not match the ICDD data on $KNbO_3$. Rietveld refinement was performed and from this the occupancy of the potassium atoms was determined to be 0.621. This meant that the potassium lost during conventional sintering set up was 37.9%.

The revised sintering setup seen in section 4.1.7 was proposed, the idea being that the atmosphere would have an increased amount of potassium, increasing the partial pressure and therefore decreasing the potassium lost from the pellets. Pellets made using this sintering setup were crushed and XRD was performed on them. Both refinements were undertaken using the same steps to make them comparable and the occupancy of the potassium atoms remained at 1. This suggests that the overall potassium loss during the sintering process was drastically reduced, with the modelled refinement indicating there was no loss at all.

6.1.3 Characterisation, Results and Discussion

6.1.3.1 XRD data

The crushed pellets were measured between 20-80°, with a scan step of 0.033425°, the total scan time being 20 minutes using a Bruker D8 diffractometer. The XRD data was analysed using Rietveld refinement following the process outlined in 4.2.1.2 with the addition of the occupancy of the potassium atom being refined as the $KNbO_3$ sintered conventionally was inconsistent with the ICDD data.

The XRD data of the conventionally sintered sample can be seen in Figure 6.1. The (001) and (100) peak intensities are relatively higher than observed in the ICDD data (108). The ICDD data has the (001) intensity at 43.3% the height of the largest (011) peak. The conventionally sintered (001) peak was 84.8% the intensity of the (011) peak. This was the indication that there was substantial potassium loss. The (001) peak of the K-rich atmosphere sintered $KNbO_3$ with much less potassium loss had the peak intensity at 44.9% that of the (011) peak (Figure 6.2). Indexed as pseudo-monoclinic.

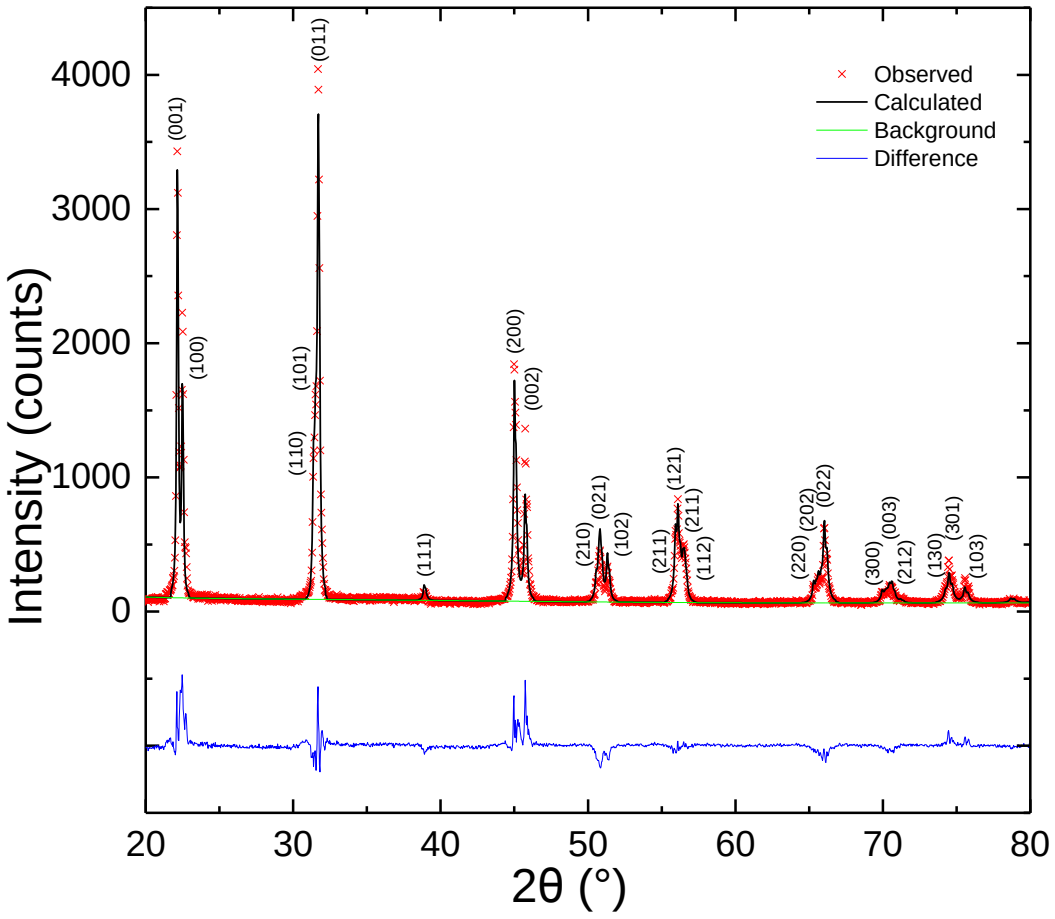

Figure 6.1: XRD of $KNbO_3$ synthesised using the conventional sintering set up.

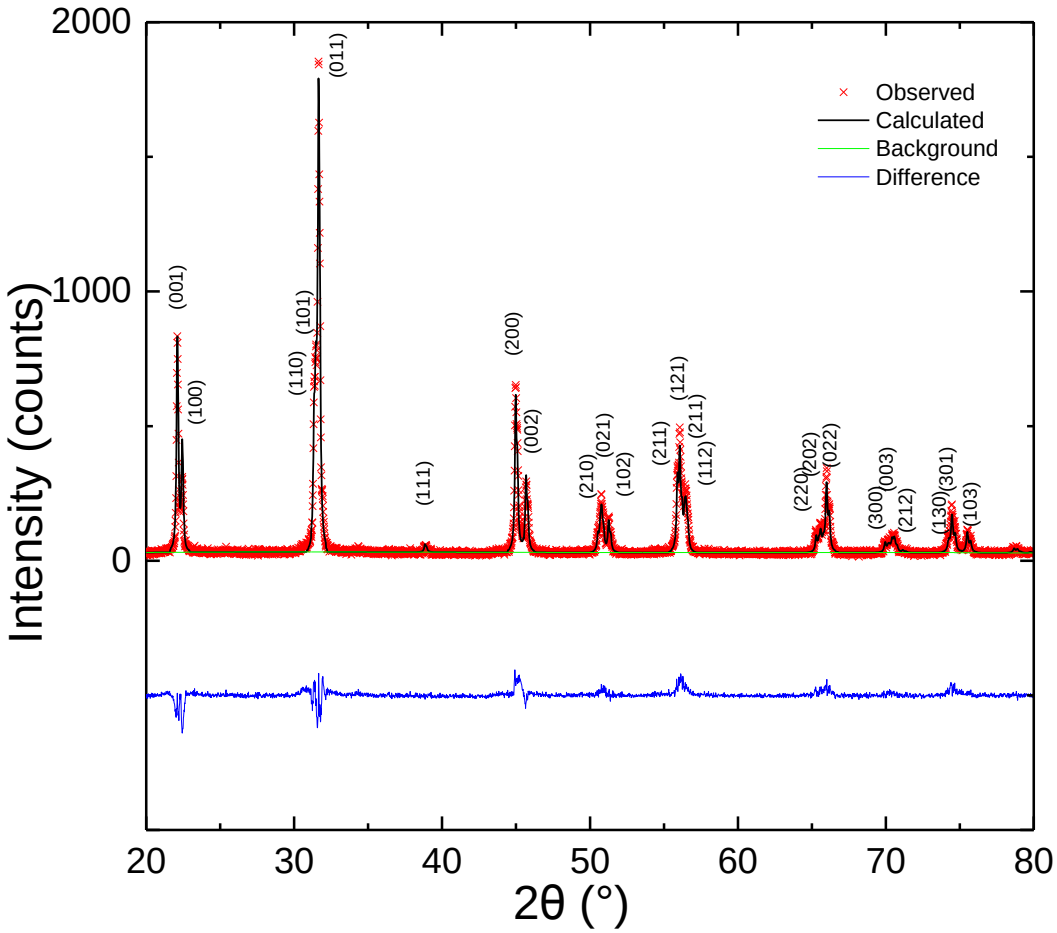

Figure 6.2: XRD of $KNbO_3$ synthesised with K-rich atmosphere sintering set up.

The Rietveld refinement results can be seen in Table 6.1. The weighted R profile (WRP) is the overall fitting score of a refinement, this ideally should be below 10. R expected value or R_{exp} is the ideal score of a refinement and is an indicator of the quality of the raw data.

The WRP of the refinements are high. This is due to the quality of the XRD data, as the R_{exp} was also high. The number of x-rays detected was low, this may be due to the diffractometer requiring a new filament tube at the time of scanning. The orthorhombic parameters were calculated by the software and converted manually to the pseudo-monoclinic parameters which were used to index the peaks of the XRD data.

Table 6.1: Table of Rietveld refinement results of KNbO3 sintered conventionally and with a K-rich atmosphere.

Factor	**Sintering set up**	
	Conventional	**K-rich atmosphere**
	Rietveld Refinement Score	
WRP	16.884	16.632
R_{exp}	8.031	12.999
	Orthorhombic Parameters (Å)	
a	3.977	3.976
b	5.697	5.695
c	5.723	5.718
	Pseudo-monoclinic Parameters (Å)	
a	4.037	4.035
b	4.037	4.035
c	3.977	3.976
β	89.74	89.77
	Potassium loss (%)	
	38.70	0.00
	Density (g/cm^3)	
	3.825	4.271
	Theoretical Percentage (%)	
	90.39	92.62

The theoretical density of the samples was calculated using the unit cell parameters modelled in the Rietveld refinement (Table 6.1). The molar mass of the unit cell assumed to be 108.0026g. The percentage of the theoretical density of the K_2CO_3 sintered pellets was 93% whereas for the conventionally sintered pellets it was 90%. The density was calculated using the geometric measurements as the conventionally sintered pellets would

dissolve in the water, which was not the case for the K-rich atmosphere sintered pellets.

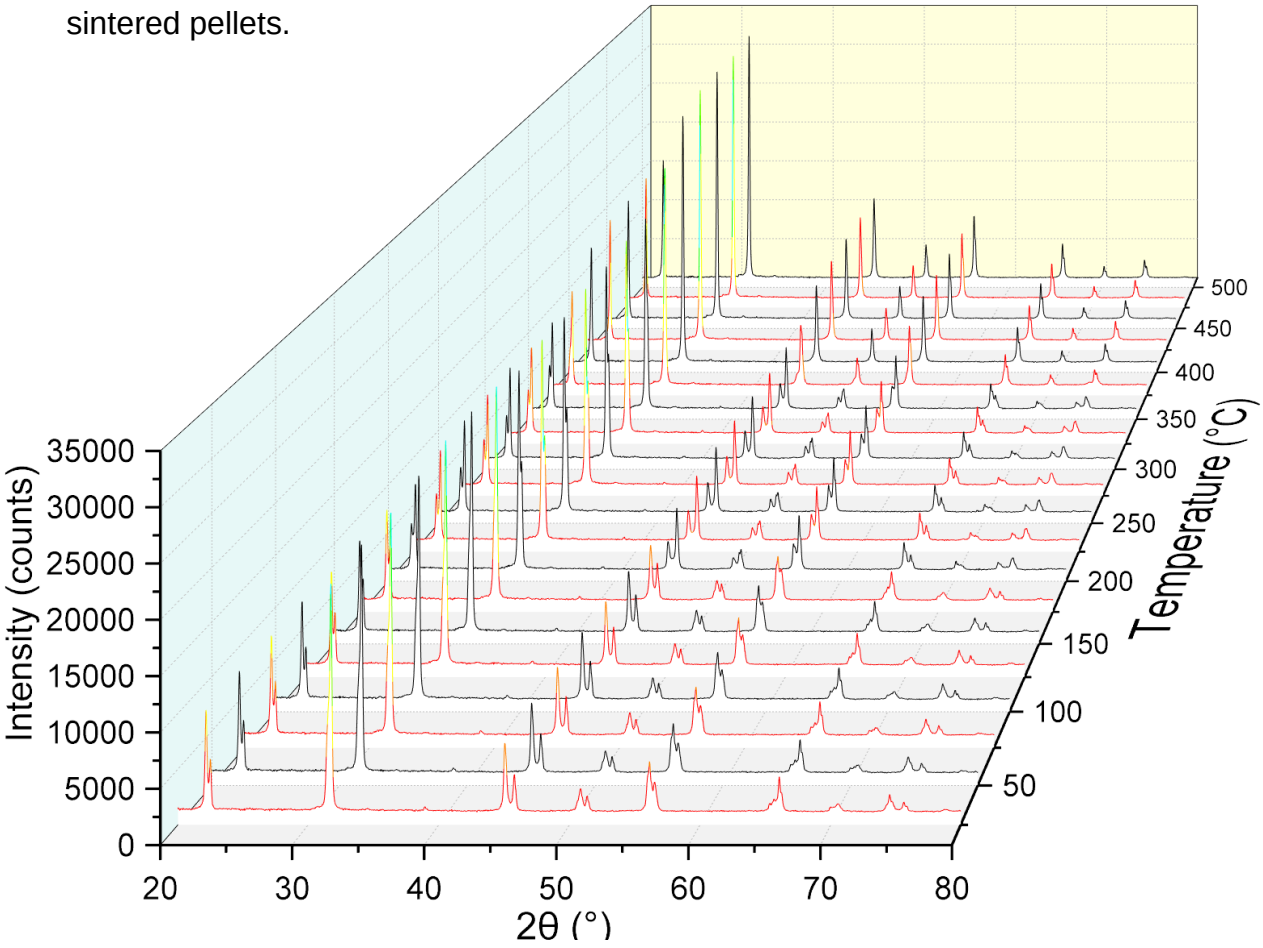

Figure 6.3: XRD against scan temperature for $KNbO_3$ sintered in K-rich atmosphere.

Table 6.2: Rietveld refinement results of $KNbO_3$ with temperature.

Temperature (°C)	Phases	High Score Fraction	WRP
25	O		3.979
175	O		4.274
175	O T	99.9 0.1	4.254
200	T		5.276
350	T		4.149
350	T C	80.1 19.9	3.523
375	T	100.0	7.362
375	T C	50.5 49.5	3.660
375	C		7.551
400	T C	0.0 100.0	4.526
500	C		4.223

XRD was undertaken from 25°C to 500°C at 25°C intervals, using the hot stage attachment of a X'pert Diffractometer. The sample remains orthorhombic (Amm2) until 200°C, where it switches to tetragonal (P4mm).

The 175°C scan was refined as pure orthorhombic and as a mixture of orthorhombic and tetragonal with the best score being a mixture of 99.9% orthorhombic and 0.1% tetragonal. The large bias towards orthorhombic and a c/a ratio of the refined tetragonal phase changing from 1.015 to 0.918 brings into question whether the refinement of the mixed phase is accurate. Given the small difference in score, the more sensible analysis of the sample at 175°C is that of a pure orthorhombic sample.

It remains purely tetragonal form 200°C until 350°C. At 350°C the best refinement has a mixture of 80.1% tetragonal and 19.9% cubic. At 375°C the most accurate refinement is a mixture of tetragonal and cubic (Pm-3m) phases, 50.5% and 49.5% respectively. At 400°C a mixture of tetragonal and cubic was refined, with the model eliminating the likelihood of a tetragonal phase being present, the sample therefore becoming pure cubic in phase, which remains to 500°C. These results suggest that the tetragonal-cubic phase transition is continuous, or 2nd order, rather than the 1st order that is seen between orthorhombic and tetragonal at 200°C. The XRD results and the Rietveld refinement results are found in Figure 6.3 and Table 6.2 respectively. The {200} peaks surrounding the 45° are an excellent indication of the phase of the sample. The key temperature scans can be seen in Figure 6.4.

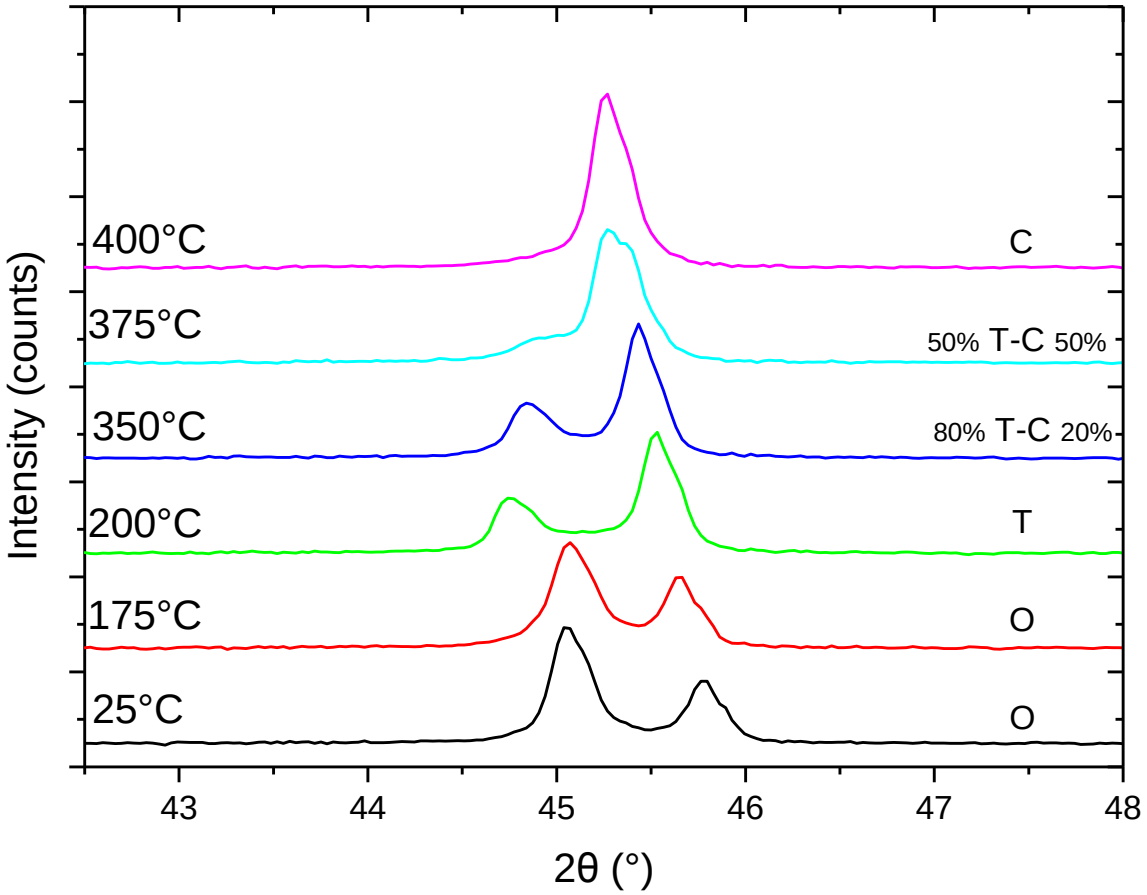

Figure 6.4: The {200} peaks of pure $KNbO_3$ with temperature of scan.

6.1.3.2 Permittivity data

The permittivity of the K-rich atmosphere sintered $KNbO_3$ was measured against temperature and frequency and the results can be seen in Figure 6.5. The tan(δ) data is shown in the inset. The phase transitions can be seen as peaks in the permittivity, the T_{O-T} transition occurring at 200°C and the T_{T-C} (or T_C) can be seen at 392°C. These phase transformation temperatures are in agreement with the XRD versus temperature data. There is some dispersion with frequency, this may be due to porosity or other inhomogeneity within the sample.

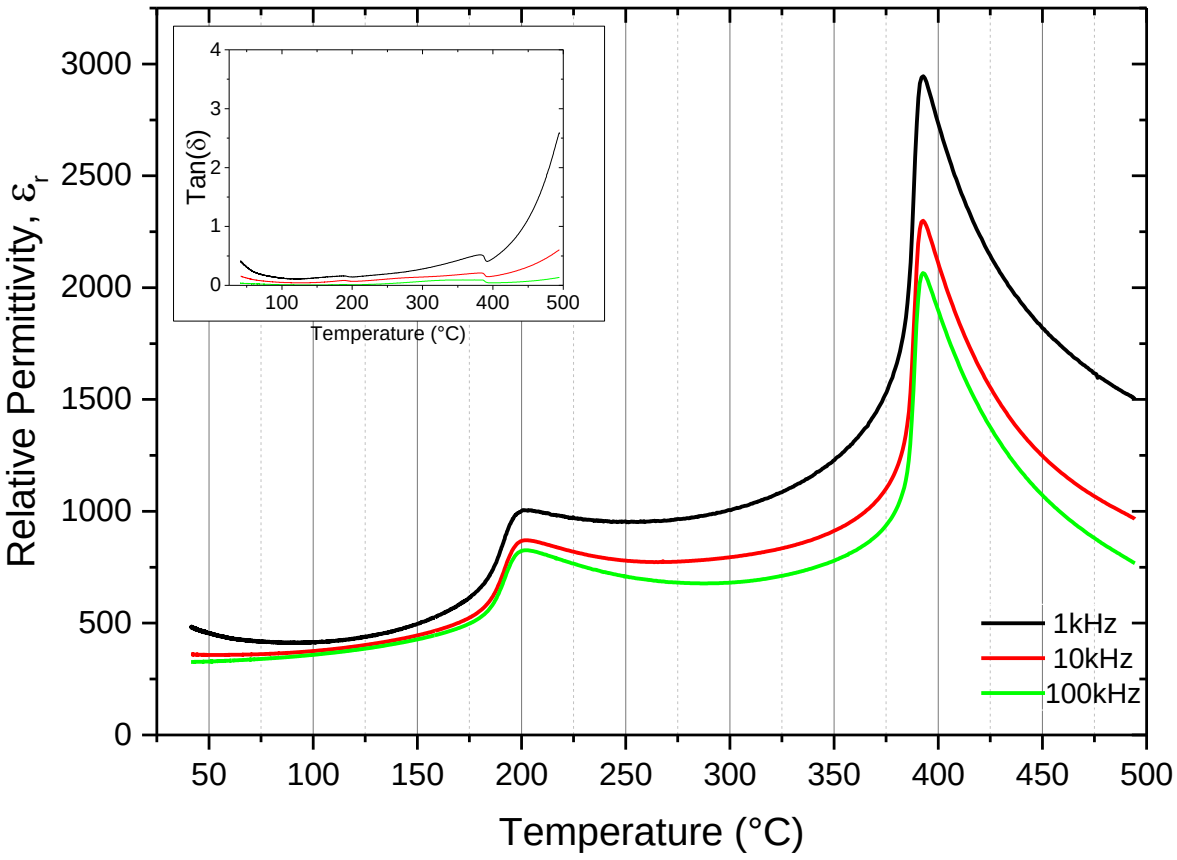

Figure 6.5: Permittivity and tan(δ) of $KNbO_3$ as a function of temperature and frequency.

6.1.4 Conclusion

The sintering regime was optimised to produce pure potassium niobate with minimum potassium loss. This sintering set up was used throughout the work. The phase transition temperatures measured in the pure potassium niobate were in agreement with the temperatures found in the literature, and will be used to compare the phase transitions of the doped samples in the work proceeding this section.

6.2 $KNbO_3$ – $CaZrO_3$

Substituting KNN with $CaZrO_3$ increases the T_{R-O} phase transition to room temperature (150). It was proposed that this may also be the effect for $KNbO_3$.

6.2.1 (1-x)$KNbO_3$-x$CaZrO_3$ (KNCZ) synthesis

Five different compositions were synthesised, where x=0.01, 0.02, 0.03, 0.06, and 0.09 by the mixed oxide process outlined in section 4.1. The sintering temperature ($T_{sint)}$ increased as the amount of $CaZrO_3$ increased, x=0.01 and 0.02 had a T_{sint} of 1100°C and x= 0.03-0.09 had a T_{sint} of 1150°C. The sintering process produced samples with poor density, unfit for high electric field characterisation. Samples were ground and electrodes were applied for permittivity measurements, however the samples were prone to breaking.

6.2.2 Characterisation, Results and Discussion

6.2.2.1 XRD data at 25°C

The crushed pellets were measured between 20-80°, with a scan step of 0.033425°, the total scan time being 20 minutes using an X'Pert diffractometer with a hot stage attachment. A comparison of the XRD results at 25°C for each composition can be seen in Figure 6.6, and the Rietveld refinement results can be seen in Table 6.3. The {200} peaks near 45° for each composition can be seen in Figure 6.7.

Pure $KNbO_3$ (x=0.00) is orthorhombic, with the refinement score being vastly improved as the quality of data was improved. The 0.01 composition remains purely orthorhombic. An attempt to refine a coexistence of orthorhombic and rhombohedral phases resulted in the WRP increasing from 5.473 to 10.498.

The best refinement for the 0.02 composition was a mixed phase of orthorhombic and rhombohedral. However, the model calculated the unit cell parameters of the rhombohedral phase as impossible, the α angle being above 90°. This would suggest that the rhombohedral phase was forced into the model and may not be present in the sample, or present but with less phase fraction. For this reason, the 0.02 will be classed as orthorhombic. However, the high score phase fraction of the orthorhombic-rhombohedral refinement is compatible with the compositions succeeding it.

The compositions 0.03 and 0.06 are best modelled as orthorhombic-rhombohedral phase mixture. The percentage of rhombohedral phase present increases with $CaZrO_3$ substitution, from 37.9% in 0.03 to 61.1% in 0.06.

The 0.09 composition is best modelled as a mixture of orthorhombic and cubic phases. This is due to the cubic phase becoming more stable at lower temperatures as the amount of $CaZrO_3$ is increased. This will be shown in section 6.2.2.2. When refined as a mixture of orthorhombic and rhombohedral, the rhombohedral unit parameters are impossible as α is above 90°.

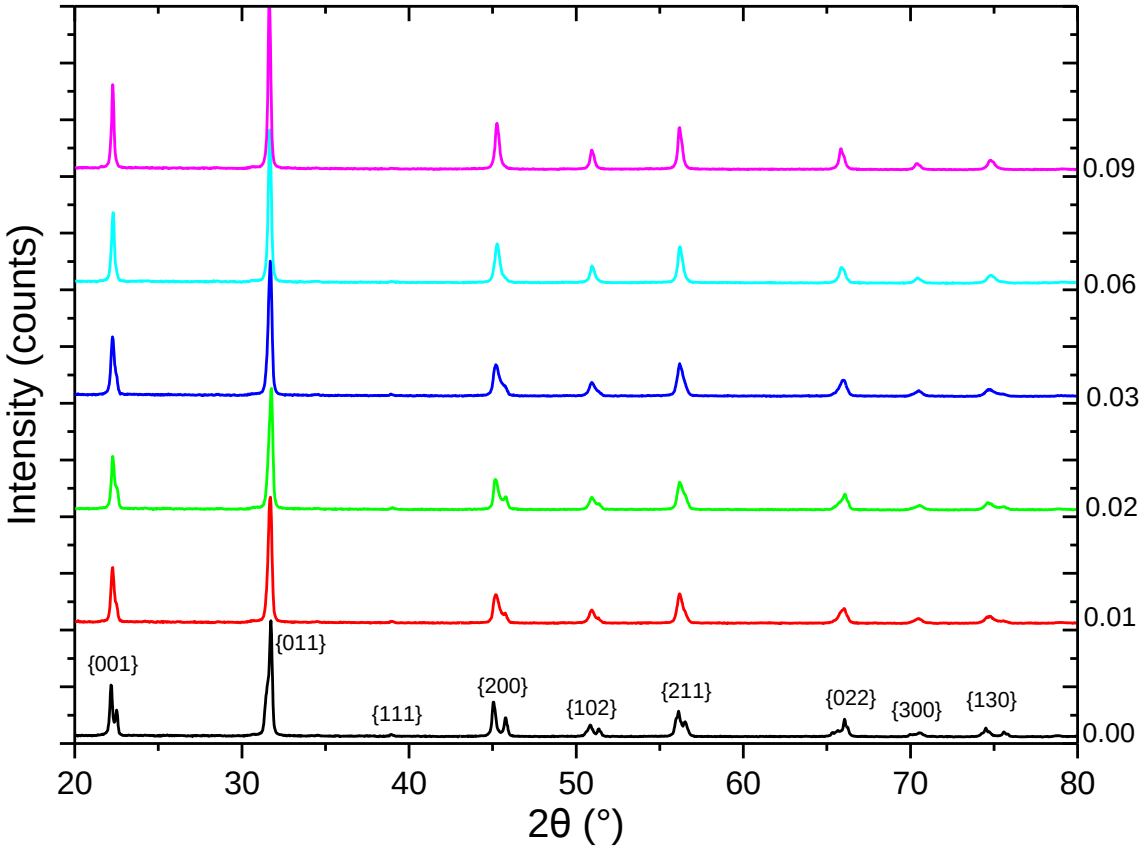

Figure 6.6: XRD results of every $KNbO_3$-$CaZrO_3$ composition at 25°C.

Table 6.3: Table of Rietveld refinement results of (1-x)$KNbO_3$-x$CaZrO_3$ compositions at room temperature.

Composition (x)	Phases	High Score Fraction (%)	WRP	Pseudo-monoclinic				Rhombohedral / Cubic	
				a (Å)	b (Å)	c (Å)	β (°)	a (Å)	α (Å)
0.00	O		3.979	4.011	4.011	3.977	89.538		
0.01	O		5.473	4.028	4.028	3.994	89.874		
0.02	O R	71.8 28.2	3.578	4.034	4.034	3.982	89.815	4.016	**90.008**
0.02	O		5.018	4.030	4.030	3.989	89.845		
0.03	O R	62.1 37.9	3.606	4.033	4.033	3.985	89.799	4.016	89.979
0.06	O R	38.9 61.1	3.453	4.032	4.032	3.992	89.844	4.017	89.996
0.09	O R	35.5 64.5	3.438	4.031	4.031	3.999	89.839	4.018	**90.007**
0.09	O C	52.3 47.7	3.331	4.028	4.028	4.002	89.891	4.018	

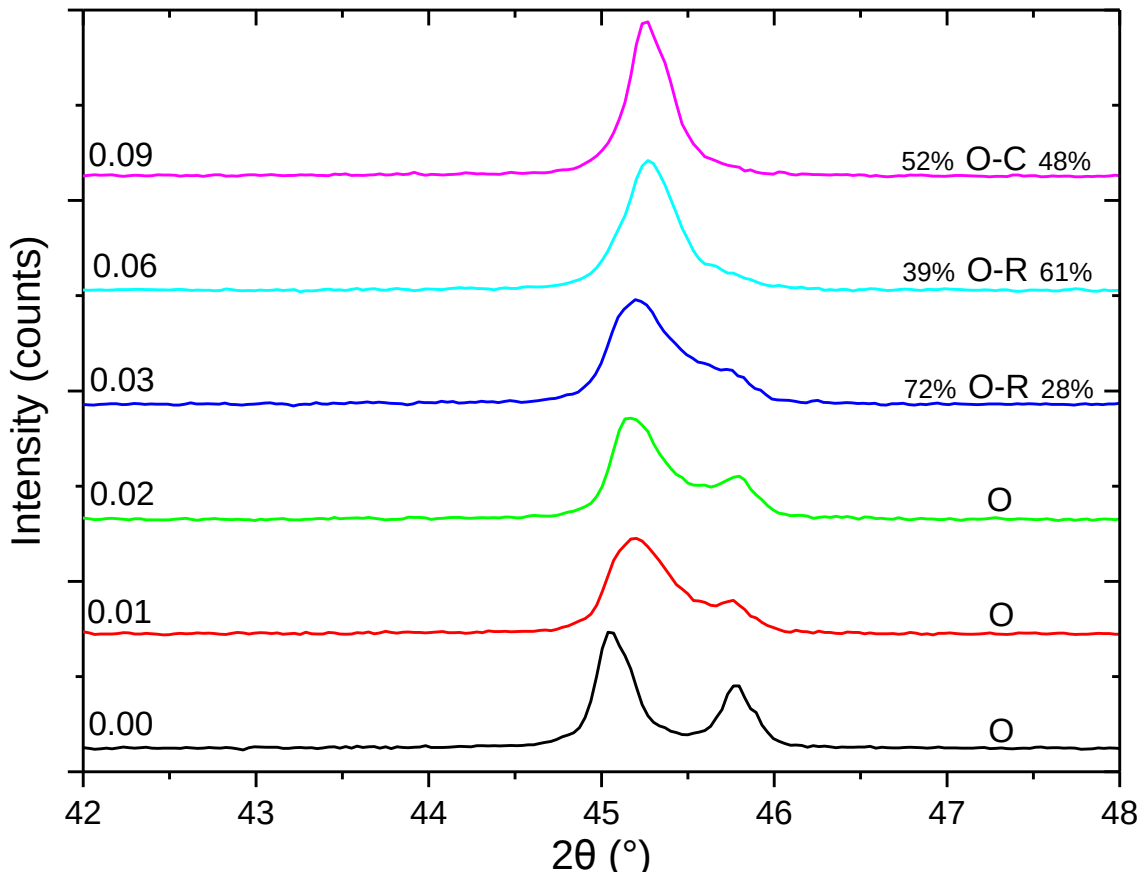

Figure 6.7: The {200} peaks of each $KNbO_3$-$CaZrO_3$ composition at 25°C.

6.2.2.2 XRD with temperature

An XRD phase study was performed on each composition over a range of temperatures using a PANalytical X'Pert diffractometer and a temperature controller. From 25°C to 500°C at 25°C intervals. This was to identify the phase(s) present at room temperature and in order to see the effect the substitution had on the T_{O-T} and the T_{T-C} phase transitions. The scans at a range of temperatures would also contribute to an explanation for the shape of the permittivity data seen in section 6.2.2.3.

6.2.2.2.1 $0.99KNbO_3$-$0.01CaZrO_3$

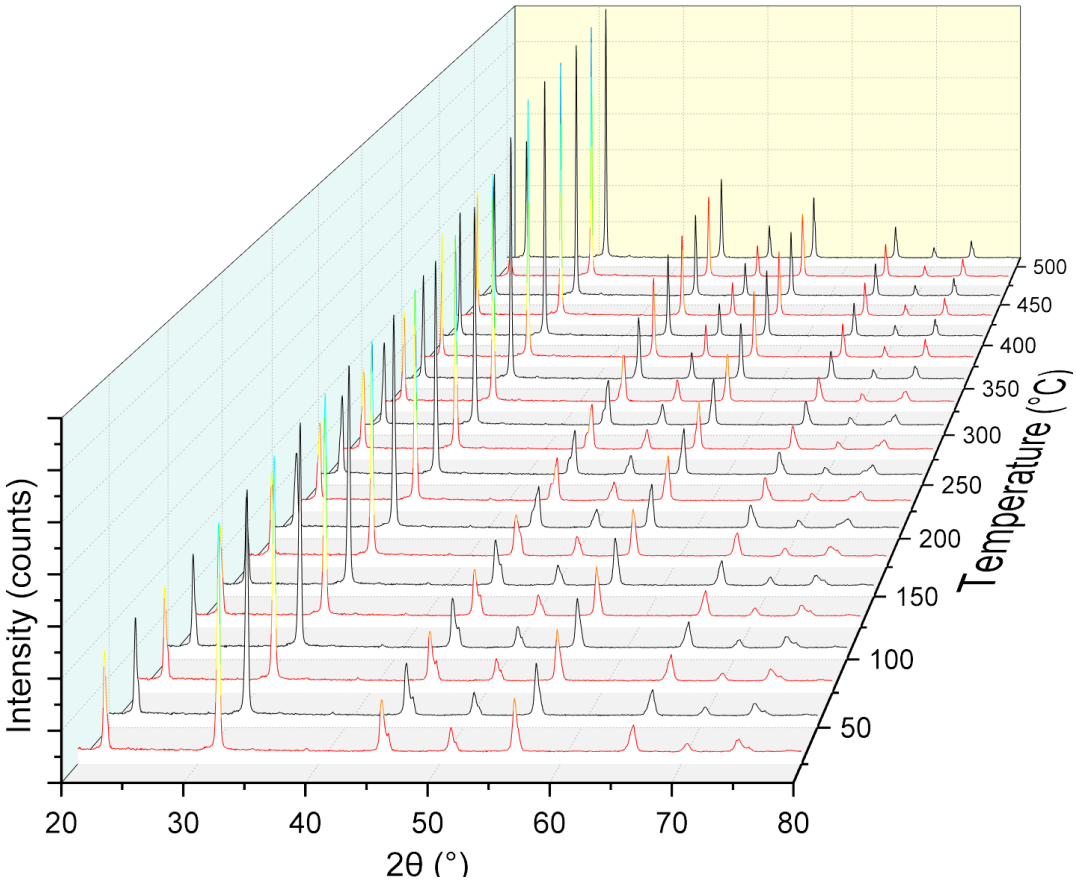

Figure 6.8: XRD with scan temperature of $0.99KNbO_3$-$0.01CaZrO_3$.

Figure 6.8 shows the XRD measurements as a function of temperature for 1% $CaZrO_3$ substitution. When x=0.01, the material remains orthorhombic until 175°C. At 200°C the material had a phase mixture of orthorhombic and tetragonal, 44.7% and 55.3% respectively. There was no pure tetragonal material as the best fitting model was a tetragonal-cubic phase coexistence at 225°C, with the phase fraction being 62.1% to 37.9% respectively. This phase mixture remained in the same range until 275°C. The cubic phase fraction then increased to 46.7% at 325°C, 56.8% at 350°C and then 64.5% at 375°C. Finally at 400°C the best fit was purely cubic. The

Rietveld refinement results can be seen in Table 6.4 and the {200} peaks at notable temperatures are seen in Figure 6.9.

Table 6.4: Rietveld refinement results of $0.99KNbO_3$-$0.01CaZrO_3$ with temperature.

Temperature (°C)	Phases	High Score Fraction (%)	WRP	Monoclinic/Cubic (Å)				Tetragonal (Å)		
				a	b	c	β (°)	a	c	c/a
25	O		5.4733	4.028	4.028	3.994	89.874			
175	O		4.4669	4.030	4.030	4.001	89.953			
175	OT	100, 0	3.3968	4.030	4.030	4.001	89.967			
200	OT	44.7, 55.3	3.7022	4.028	4.028	4.011	89.979	4.002	4.055	1.013
225	TC	62.1, 37.9	3.8821	4.023	4.023	4.023		4.003	4.053	1.012
325	TC	53.3, 46.7	3.6536	4.025	4.025	4.025		4.011	4.051	1.010
350	TC	43.2, 56.8	3.5146	4.025	4.025	4.025		4.011	4.051	1.010
350	C		5.4697	4.024	4.024	4.024				
375	TC	35.5, 64.5	3.4445	4.025	4.025	4.025		4.022	4.040	1.004
375	C		4.2361	4.025	4.025	4.025				
400	C		4.4435	4.026	4.026	4.026				

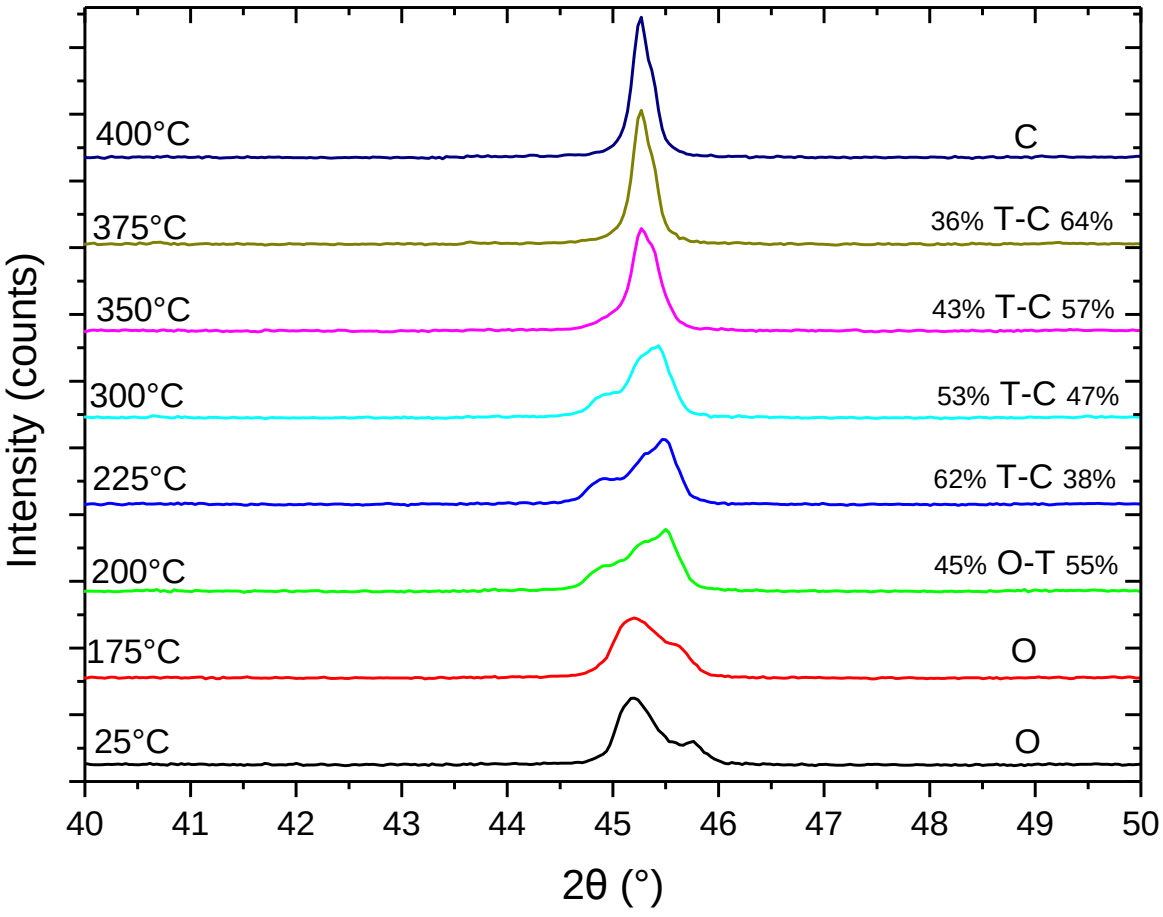

Figure 6.9: The {200} peaks of $0.99KNbO_3$-$0.01CaZrO_3$ with scan temperature.

The T_{O-T} phase transition (200°C) does not appear to have been reduced by the substitution of 1% $CaZrO_3$.The result once again suggests that the tetragonal-cubic phase is a continuous, 2nd order transition. It also implies that the cubic phase of the material is present at a much lower temperature of 225°C rather than in pure $KNbO_3$ where it appeared at 350°C. However it becomes purely cubic at the same temperature as pure $KNbO_3$, at 400°C.

6.2.2.2.2 $0.98KNbO_3$-$0.02CaZrO_3$

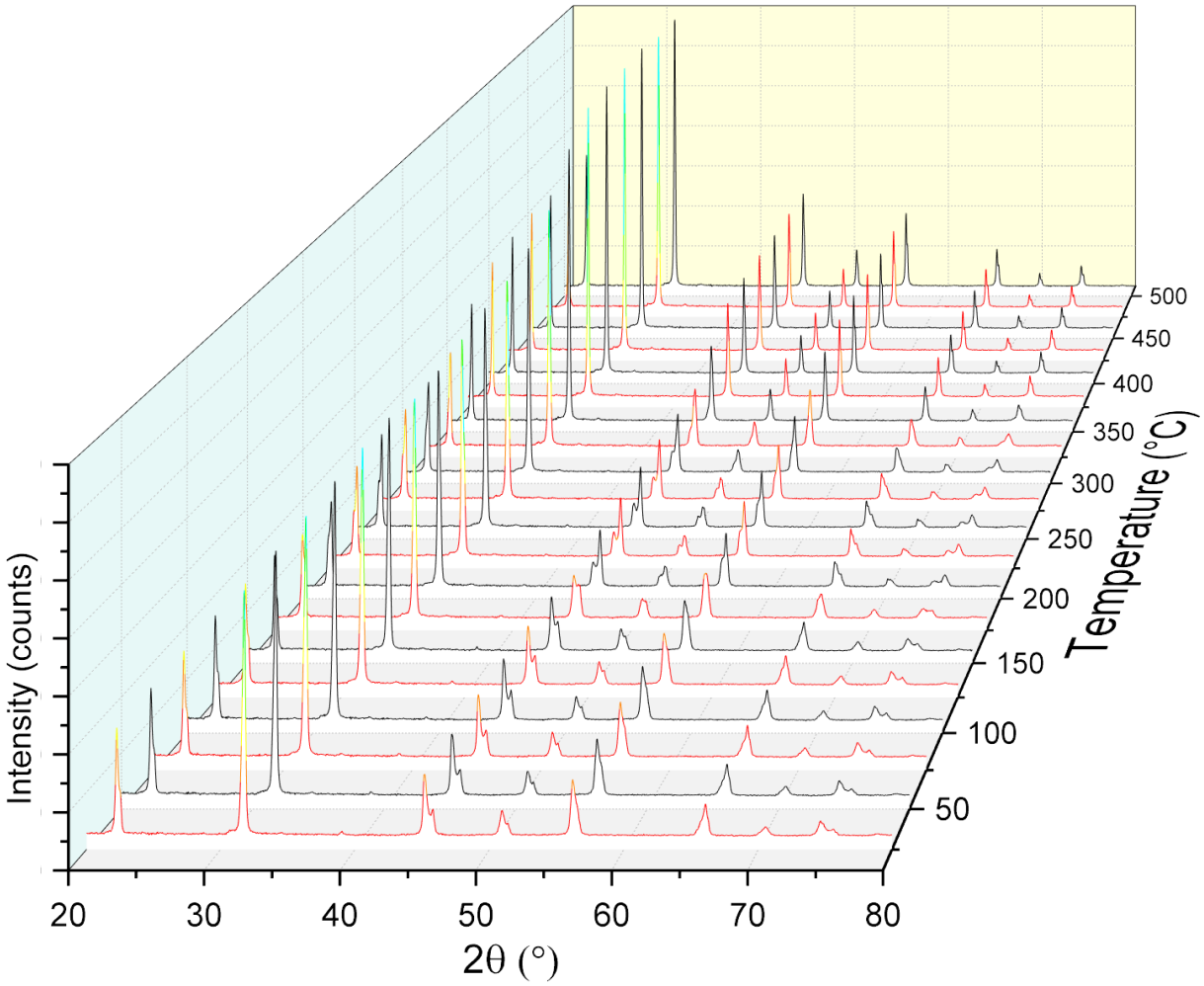

Figure 6.10: XRD with scan temperature of $0.98KNbO_3$-$0.02CaZrO_3$.

Similar to x=0.01, when x=0.02 (XRD versus temperature results seen in Figure 6.10) the phase remains orthorhombic until 175°C where the tetragonal phase is introduced. The phase mixture starts at 50.9% orthorhombic, 49.1% tetragonal at 175°C. The tetragonal phase grows significantly to 73.4% at 200°C, which is the last temperature the orthorhombic phase is present. From 225°C to 375°C a tetragonal-cubic

phase coexistence is found. The cubic phase is constantly increasing in fraction, becoming the dominant phase at 350°C. The refinement at 400°C is best represented as this same mixture, with the tetragonal phase representing 2.4% of the sample. The tetragonal phase in the model has an unrealistic c/a ratio of 1.128 suggesting the refinement is forcing a fit. In this case, the slightly higher scoring pure cubic phase may be more accurate; visually, there are no shoulders either side of the cubic peak (see Figure 6.11 of the {200} peaks). A summary of the Rietveld refinement results can be seen in Table 6.5.

Table 6.5: Rietveld refinement results of 0.98KNbO$_3$-0.02CaZrO3 with temperature.

Temperature (°C)	Phases	High Score Fraction (%)	WRP	Monoclinic / Cubic (Å)				Tetragonal / Rhombohedral (Å)		
				a	b	c	β	a	c or α (°)	c/a
25	O		5.0179	4.030	4.030	3.989	89.814			
25	OR	71.8, 28.2	3.5777	4.034	4.034	3.982	89.815	4.016	**90.008**	
175	OT	50.9, 49.1	3.6794	4.033	4.033	3.993	89.813	4.008	4.048	1.010
200	OT	26.6, 73.4	3.7919	4.031	4.031	4.006	89.835	4.003	4.057	1.014
225	TC	78.6, 21.4	4.0075	4.024	4.024	4.024		4.005	4.056	1.013
275	TC	74.7, 25.3	3.9286	4.025	4.025	4.025		4.007	4.055	1.012
325	TC	59.4, 40.6	3.9709	4.025	4.025	4.025		4.011	4.051	1.010
350	TC	42.5, 57.5	3.8157	4.024	4.024	4.024		4.016	4.046	1.008
375	TC	27.7, 72.3	3.6684	4.025	4.025	4.025		4.022	4.044	1.005
375	C		4.5622	4.025	4.025	4.025				
400	TC	2.4, 97.6	4.1306	4.026	4.026	4.026		3.656	4.124	**1.128**
400	C		4.3741	4.026	4.026	4.026				
425	TC	0.0, 100.0	4.4627	4.027	4.027	4.027				

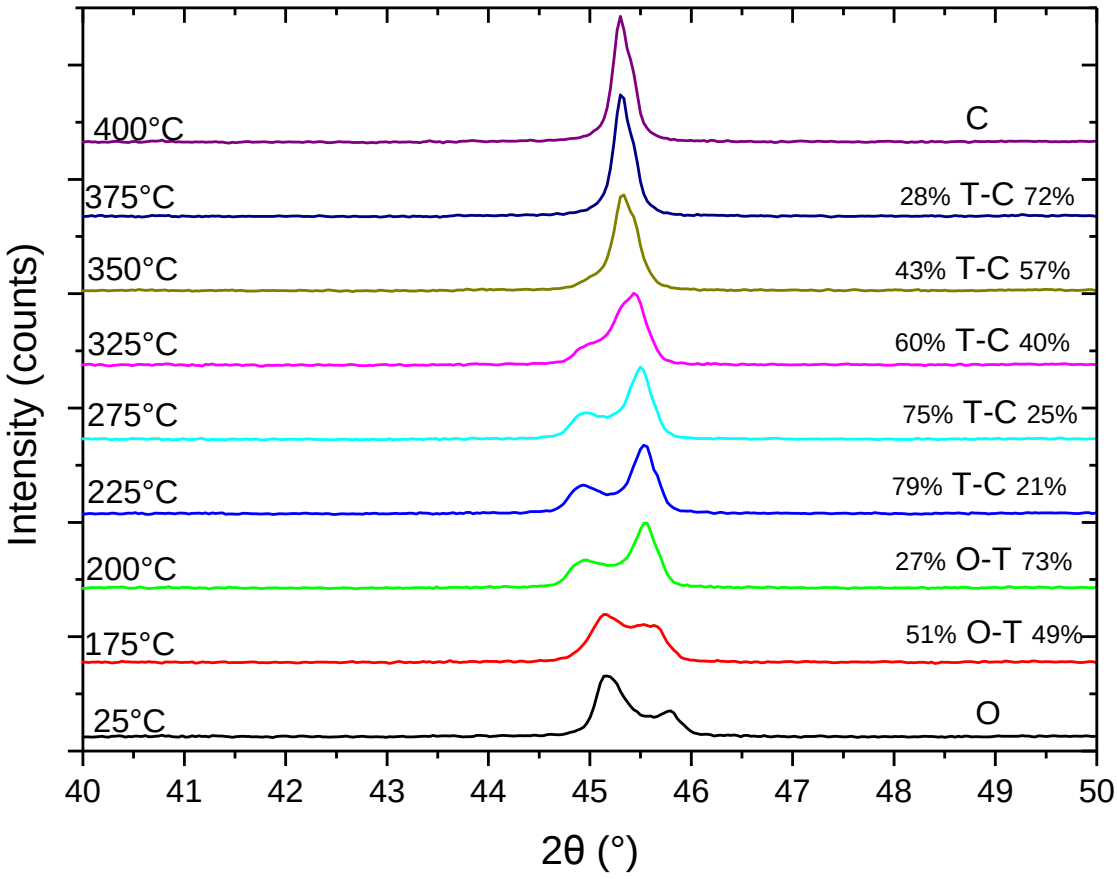

Figure 6.11: The {200} peaks of $0.98KNbO_3$-$0.02CaZrO_3$ with temperature.

6.2.2.2.3 $0.97KNbO_3$-$0.03CaZrO_3$

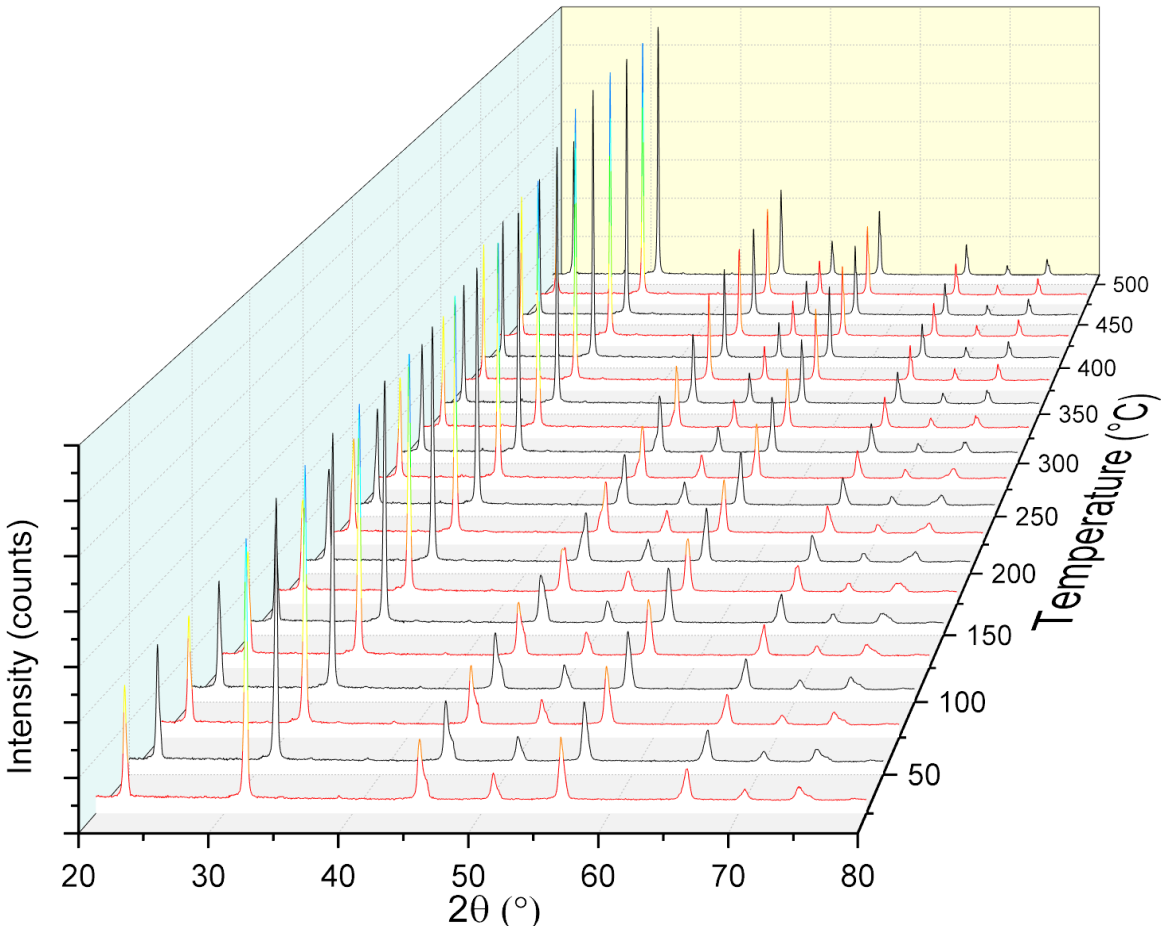

Figure 6.12: XRD with temperature of $0.97KNbO_3$-$0.03CaZrO_3$.

Table 6.6: Rietveld refinement results of $0.97KNbO_3$-$0.03CaZrO_3$ with temperature.

Temperature (°C)	Phases	High Score Fraction (%)	WRP	Pseudo-Monoclinic / Cubic (Å)				Tetragonal / Rhombohedral (Å)		
				a	b	c	β	a	c or α(°)	c/a
25	OR	62.1, 37.9	3.6058	4.033	4.033	3.990	89.799	4.016	89.979	
100	OR	73.1, 26.9	3.6717	4.034	4.034	3.990	89.851	4.017	89.984	
125	OC	70.1, 29.9	3.4412	4.034 4.017	4.034	3.992	89.884			
150	OC	67.6, 32.4	3.8371	4.036 4.017	4.036	3.994	89.920			
175	OTC	38.3, 43.1, 18.6	3.4875	4.035 4.021	4.035	3.992	89.803	4.008	4.047	1.010
200	TC	76.0, 24.0	4.1531	4.023				4.006	4.048	1.010
225	TC	70.4, 29.6	3.9615	4.023				4.006	4.051	1.011
250	TC	63.4, 36.6	3.9559	4.023				4.007	4.052	1.011
275	TC	55.8, 44.2	3.8847	4.024				4.008	4.053	1.011
325	TC	49.7, 50.3	3.7928	4.025				4.012	4.052	1.010
350	TC	47.1, 52.9	3.7333	4.025				4.014	4.049	1.009
375	TC	35.6, 64.4	3.7808	4.025				4.020	4.046	**1.006**
375	C		4.7961	4.025						

The phase remains purely orthorhombic for x=0.01 and 0.02. However, for x=0.03 the rhombohedral phase appears with the orthorhombic phase at room temperature, with a phase fraction of 37.9%. The XRD scan results for x=0.03 from 25 to 500°C can be seen in Figure 6.12 and the Rietveld refinement results can be seen in Table 6.6. This coexistence remains until 100°C, with the rhombohedral phase being reduced to 26.9%. The increased $CaZrO_3$ substitution brings the cubic phase down to appear at 125°C, however it is not the only phase as the orthorhombic phase remains. At 175°C the tetragonal phase appears with the orthorhombic and cubic phase, with the orthorhombic phase disappearing at 200°C. This leaves the tetragonal and cubic phases to coexist, with the phase fraction of the cubic phase increasing with temperature, from 24% at 200°C to 52.9% at 350°C.

The tetragonal-cubic phase coexistence is the best refinement at 375°C, however the c/a ratio of the tetragonal unit cell modelled is much smaller than that modelled at lower temperatures. This, along with the fact that the tetragonal {200} peaks cannot be seen in the 375°C XRD scan (Figure 6.13) would suggests that at 375°C the sample is pure cubic.

The refinement results further confirm that the tetragonal-cubic phase transformation is a 2nd order continuous transition. They also suggest that the cubic phase is heavily affected by the $CaZrO_3$, its presence being found ~300°C lower than it is in pure $KNbO_3$. The rhombohedral phase found at

lower temperatures may be a false refinement and could also be the cubic phase. To counter this point, the refinement scores themselves are better for the rhombohedral phase, and the unit cells modelled are realistic. Also, the phase fraction decreases with an increasing temperature until the cubic phase appears, which would be expected for a phase that is usually present below room temperature.

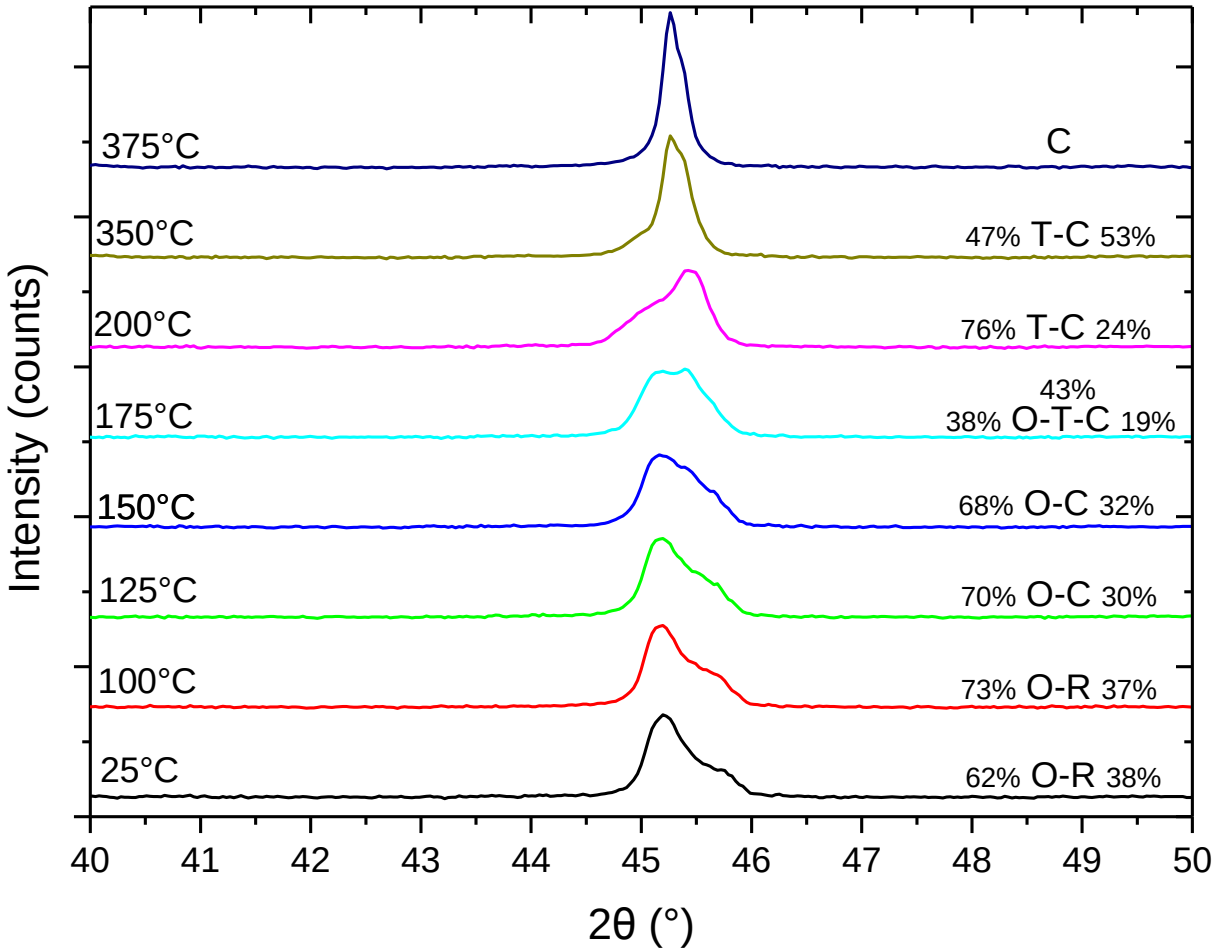

Figure 6.13: The {200} peaks of $0.97KNbO_3$-$0.03CaZrO_3$ with temperature.

6.2.2.2.4 $0.94KNbO_3$-$0.06CaZrO_3$

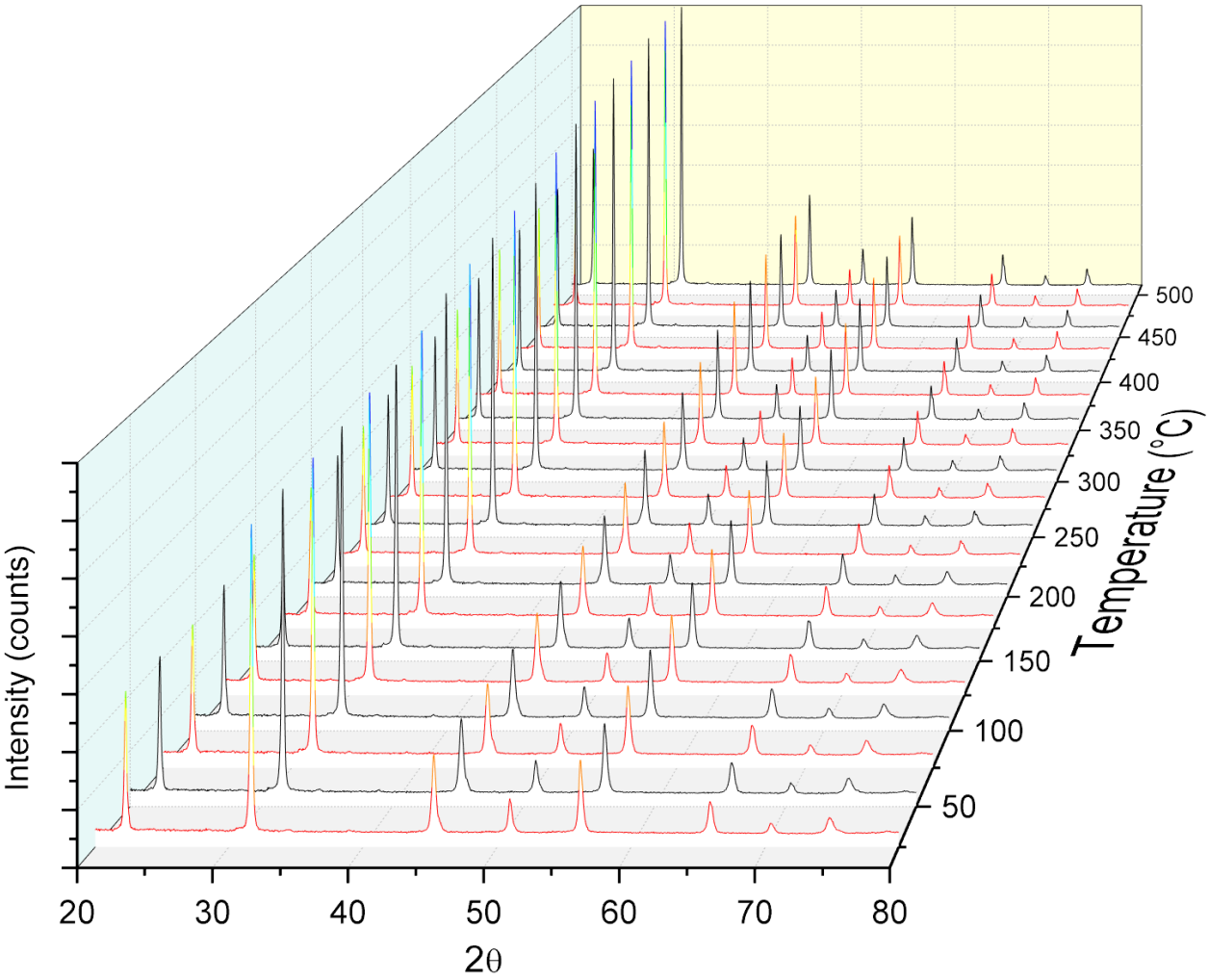

Figure 6.14: XRD with temperature of $0.94KNbO_3$-$0.06CaZrO_3$.

The full XRD scans of x=0.06 can be seen Figure 6.14, with the {200} peaks being highlighted in Figure 6.15. The Rietveld refinements results from the full scans can be seen in Table 6.7.

The rhombohedral-orthorhombic phase coexistence found in x=0.03 is also seen in x=0.06 with the rhombohedral phase making up an increased 61.1% of the sample. This coexistence remains until a higher 125°C, with the rhombohedral phase being reduced to 47.1%. The coexistence of orthorhombic, tetragonal and cubic also appears at 175°C. However the cubic phase makes up much more of the sample at this temperature compared to the x=0.03 composition. From 200°C until 350°C both tetragonal and cubic phases are present. The cubic phase becomes the dominant phase at the lower temperature of 225°C, peaking at roughly the same percentage of 64.5% at 350°C.

At 375°C, the cubic phase stops growing and shifting and the tetragonal {200} shoulders are not present. The sample becomes pure cubic.

Table 6.7: Rietveld refinement results of $0.94KNbO_3$-$0.06CaZrO_3$ with temperature.

Temperature (°C)	Phases	High Score Fraction (%)	WRP	Pseudo-Monoclinic / Cubic (Å)				Tetragonal / Rhombohedral (Å)		
				a	b	c	β	a	c or α(°)	c/a
25	OR	38.9, 61.1	3.4531	4.032	4.032	3.992	89.844	4.017	89.996	
25	OC	37.7, 62.3	3.4755	4.033	4.033	3.991	89.839			
				4.017						
100	OC	55.9, 44.1	3.5369	4.033	4.033	3.995	89.916			
				4.019						
150	OR	52.9, 47.1	3.8011	4.037	4.037	3.995	89.890	4.020	89.997	
150	OC	49.1, 50.9	3.6271	4.035	4.035	3.997	89.964			
				4.020						
175	OTC	29.1,29.6, 41.3	3.5099	4.034	4.034	3.996	89.832	4.013	4.041	1.007
				4.021						
200	TC	54.7, 45.3	3.7219	4.022				4.011	4.043	1.008
225	TC	47.3, 52.7	3.4753	4.022				4.009	4.047	1.009
250	TC	45.8, 54.2	3.5900	4.024				4.011	4.048	1.009
300	TC	41.7, 58.3	3.5760	4.025				4.014	4.048	1.009
325	TC	44.4, 55.6	3.4480	4.026				4.017	4.045	1.007
350	TC	35.5, 64.5	3.5905	4.026				4.020	4.045	**1.006**
350	C		4.4416	4.026						
375	C		4.016	4.027						

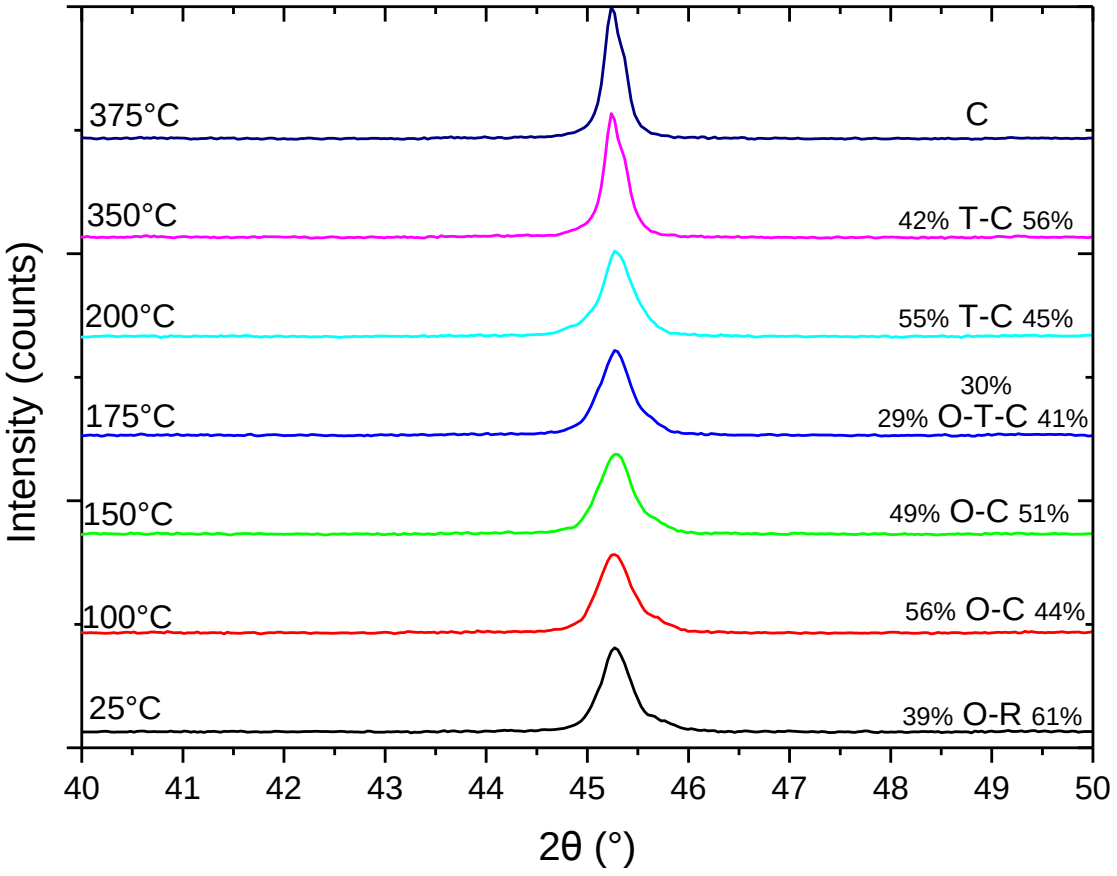

Figure 6.15: The {200} peaks of $0.94KNbO_3$-$0.06CaZrO_3$ with scan temperature.

6.2.2.2.5 $0.91KNbO_3$-$0.09CaZrO_3$

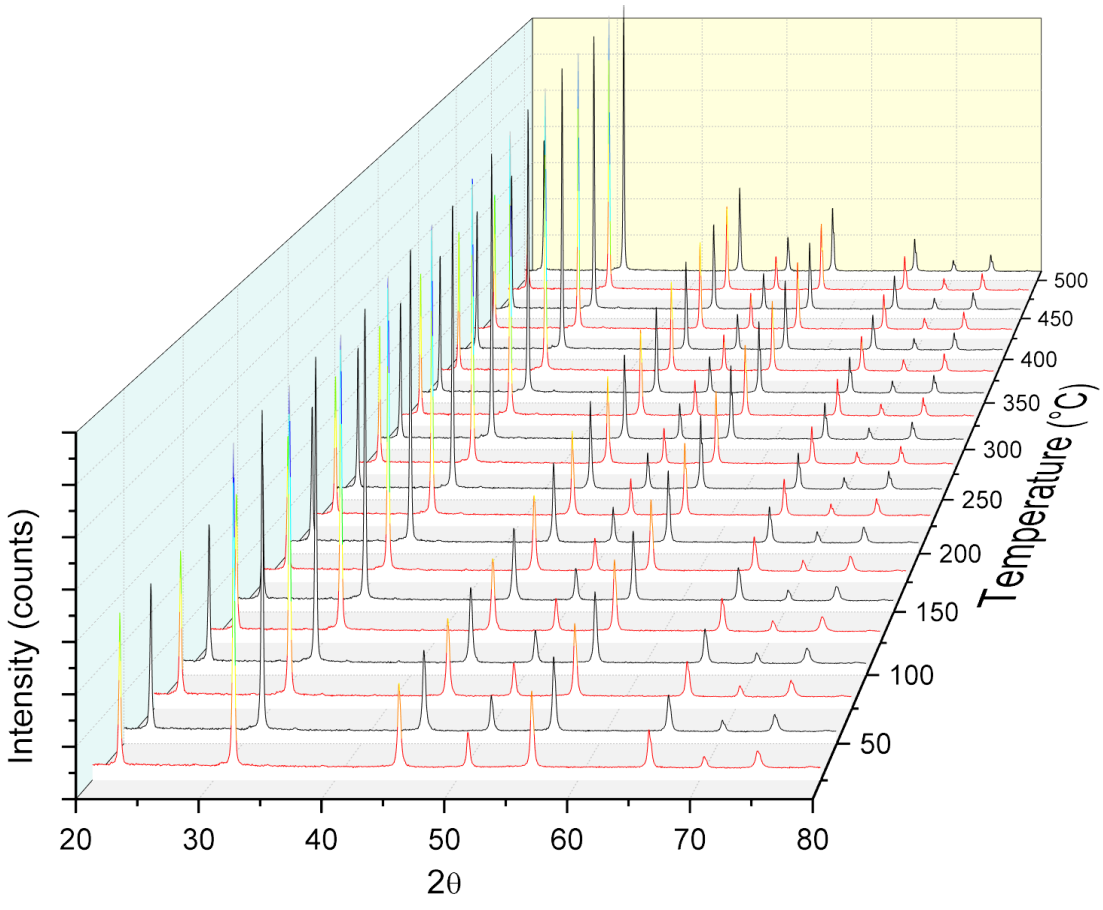

Figure 6.16: XRD with scan temperature of $0.91KNbO_3$-$0.09CaZrO_3$.

Table 6.8: Rietveld refinement results of $0.91KNbO_3$-$0.09CaZrO_3$ with temperature.

Temperature (°C)	Phases	High Score Fraction (%)	WRP	Pseudo-Monoclinic / Cubic (Å)				Tetragonal / Rhombohedral (Å)		
				a	b	c	β	a	c or α(°)	c/a
25	OR	35.5, 64.5	3.4382	4.031	4.031	3.999	89.835	4.018	**90.01**	
25	OC	52.3, 47.7	**3.3312**	4.028	4.028	4.002	89.891			
				4.018						
150	OR	35.4, 64.6	3.9200	4.035	4.035	4.002	89.906	4.021	**90.01**	
150	OC	39.4, 60.6	**3.6858**	4.034	4.034	4.003	89.895			
				4.021						
175	TC	72.4, 27.6	3.5987	4.022				4.017	4.033	1.004
200	TC	45.3, 54.7	3.6169	4.022				4.016	4.039	1.006
225	TC	40.0, 60.0	3.4817	4.023				4.016	4.042	1.007
250	TC	36.1, 63.9	3.5032	4.024				4.017	4.043	1.007
300	TC	38.4, 61.6	3.5145	4.025				4.020	4.042	1.006
325	TC	37.3, 62.7	3.6127	4.026				4.022	4.042	1.005
350	TC	32.8, 67.2	3.5073	4.027				4.023	4.042	1.005
375	C		4.2600	4.028						

The full XRD scans of the x=0.09 composition can be seen in Figure 6.16, the Rietveld refinement results of key temperatures can be seen in Table 6.8. The {200} peaks of the scans at further key temperatures can be seen in Figure 6.17.

At x=0.09 the cubic phase is present at room temperature. The rhombohedral phase may be present however if it is, it is masked by the cubic phase. The orthorhombic-cubic phase coexistence is the best refined model until 175°C. From 175°C to 350°C a tetragonal-cubic phase is the best model. The percentage of tetragonal to cubic should be contested, as the tetragonal phase has a much lower c/a ratio than in other models. There is also a large difference between the amount of cubic phase modelled with the orthorhombic phase at 150°C and with the tetragonal phase at 175°C. If the c/a ratio was more realistic, the phase fraction would be lower and more in line with the trend found from x=0.01 to 0.06. The sample does not become purely cubic until 375°C, similar to other compositions.

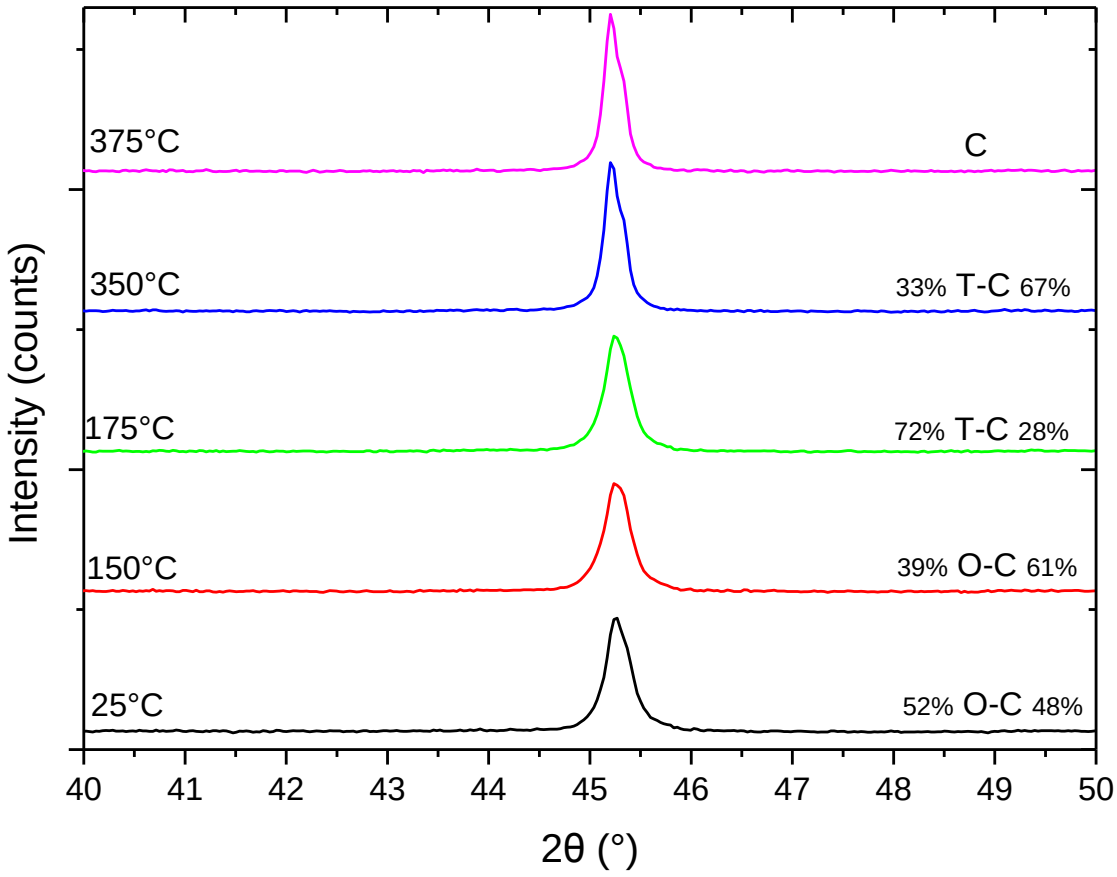

Figure 6.17: The {200} peaks of 0.91$KNbO_3$-0.09$CaZrO_3$ with scan temperature.

6.2.2.2.6 KNCZ Phase Diagram

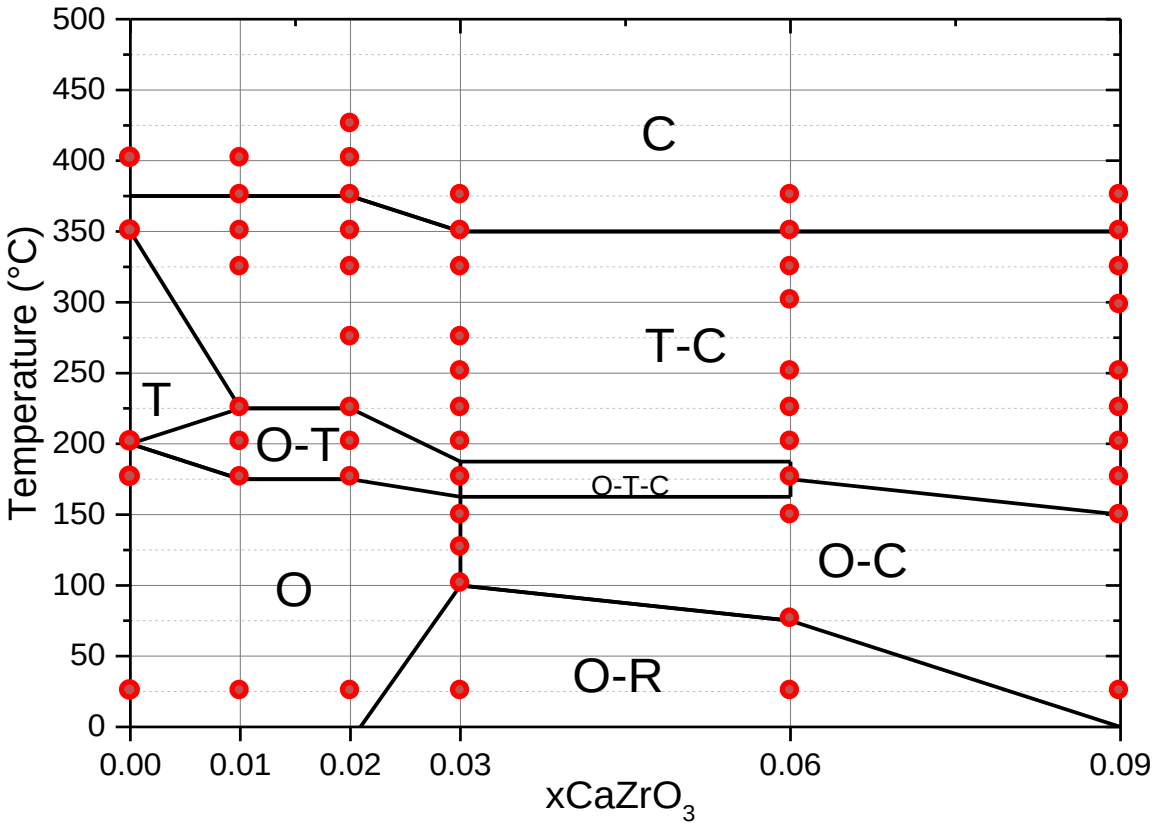

Figure 6.18: Phase Diagram of (1-x)$KNbO_3$-x$CaZrO_3$, each grid line intersection indicating a scan point and each red dot indicating a Rietveld refinement point.

This phase diagram of (1-x)$KNbO_3$-$CaZrO_3$ with temperature (Figure 6.18) was made using the results from the XRD with temperature and is a summary of the analysis provided in the previous sections. It can be seen that the temperature region where the tetragonal and cubic phases coexist increases with x. The minimum temperature for the tetragonal phase to appear is reduced, however the cubic phase is affected the most by the $CaZrO_3$ substitution. The rhombohedral phase is present at room temperature from x=0.03, where it coexists with orthorhombic. When the cubic phase is reduced to room temperature it may mask any presence of the rhombohedral phase at x=0.09.

6.2.2.3 Permittivity data

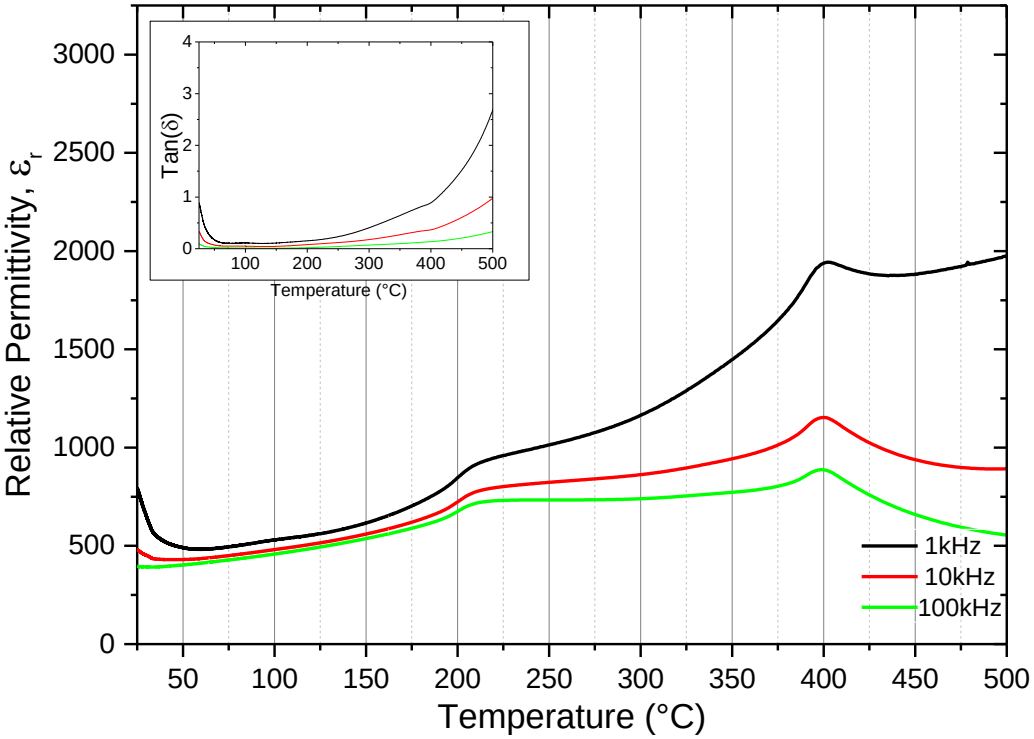

Figure 6.19: Relative permittivity and tan (δ) of $0.99KNbO_3$-$0.01CaZrO_3$ with temperature and frequency.

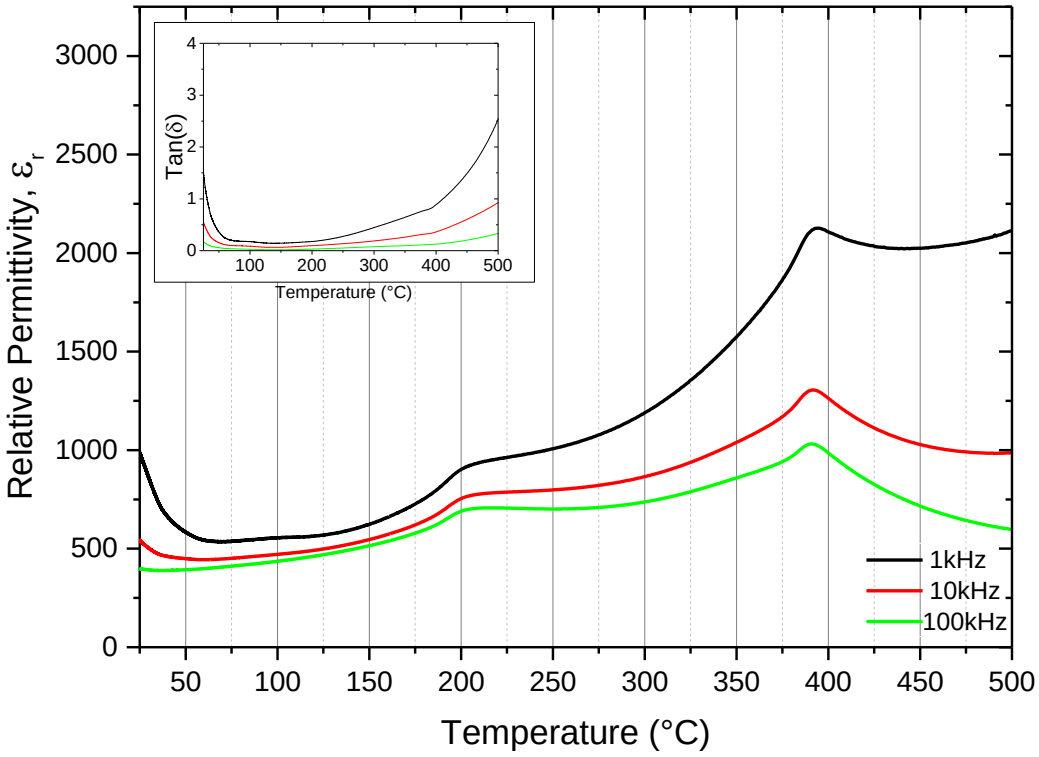

Figure 6.20: Relative permittivity and tan (δ) of $0.98KNbO_3$-$0.02CaZrO_3$ with temperature and frequency.

The permittivity data for x=0.01 (Figure 6.19) and x=0.02 (Figure 6.20) are very similar to pure potassium niobate (Figure 6.5) however, the phase transition peaks are broader. They are found at the same temperatures as the phase transitions in the XRD data, just below 200°C and 400°C. The Curie point near 400°C in the x=0.02 composition is shifted to a slightly lower temperature to the x=0.01. The gradient leading up to the Curie point is much smaller than in pure potassium niobate, this may be due to the continuous transition in the material from tetragonal to cubic. There is a decrease in permittivity from room temperature to ~60°C, which is seen in each sample, albeit with much narrower temperature range in the pure potassium niobate. This may be due to charge carriers or pores in the sample being affected by the alternating current before being fixed in place. There is an increase in frequency dispersion with temperature, although the peaks in permittivity all appear at the same temperature at each frequency.

All of the compositions suffer from conductivity at higher temperatures. This is seen as an increase in permittivity after the initial decrease after the Curie point.

When x=0.03, Figure 6.21, there is a large change in the shape of the permittivity with temperature graph when compared to x=0.00, 0.01 and 0.02. There is some noise and outlying data at the lower temperatures and around 175°C which may indicate a poor sample-wire contact.

After the initial decrease in permittivity to ~50°C there is some stability until around 125°C when it then starts to increase. There is a very broad bump in permittivity just below ~200°C, where the OTC phase mixture appears, this is more noticeable in the tan(δ) data. The permittivity then increases linearly to the peak permittivity at just below 400°C. There is noticeable difference in the shape of the tan(δ) with frequency in this composition, with the OTC bump appearing at different temperatures. There is also a large difference in the permittivity with frequency at the Curie point. This, along with the very broad OTC peak, may be an indication of relaxor-like behaviour.

The permittivity results of x=0.06 (Figure 6.22) and x=0.09 (Figure 6.23) have a peak at a much lower temperature than the Curie point, which is also an indication of a relaxor. There is also a small bump in both samples which may occur where the tetragonal phase finally disappears and the pure cubic phase remains at 375°C.

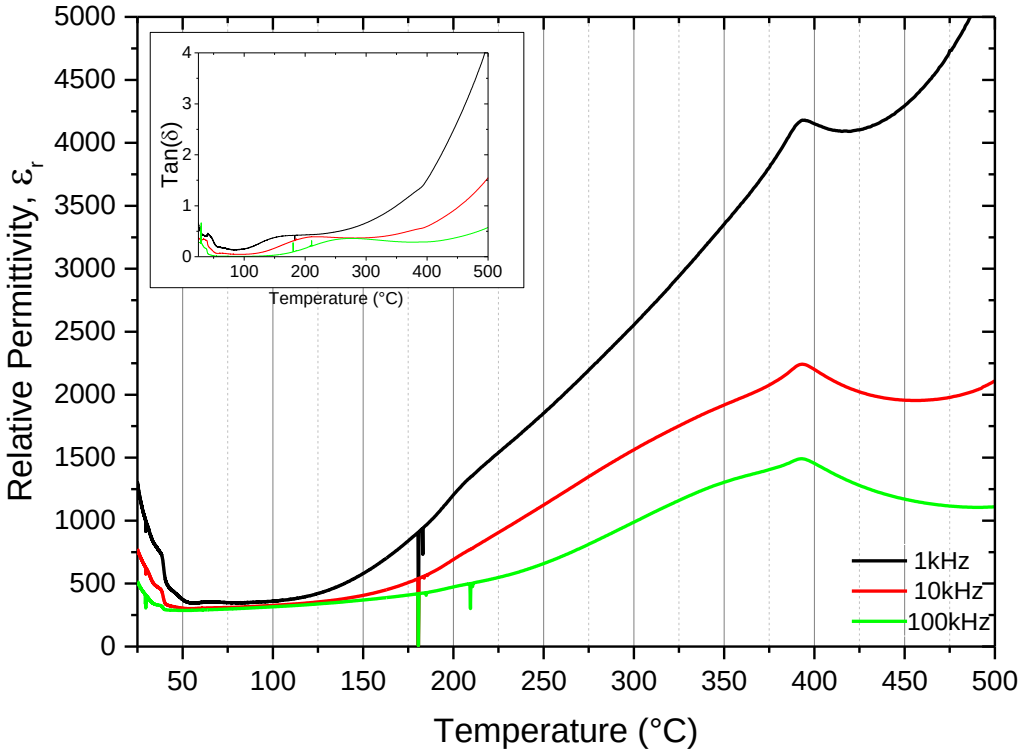

Figure 6.21: Relative permittivity and tan (δ) of $0.97KNbO_3$-$0.03CaZrO_3$ with temperature and frequency.

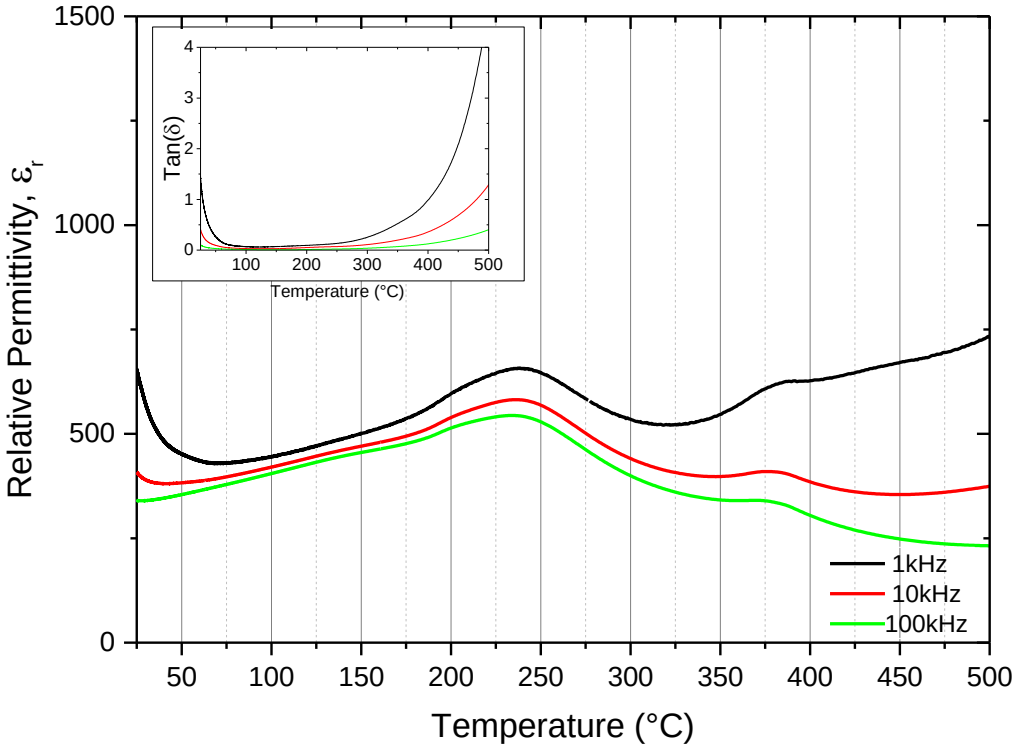

Figure 6.22: Relative permittivity and tan (δ) of $0.94KNbO_3$-$0.06CaZrO_3$ with temperature and frequency.

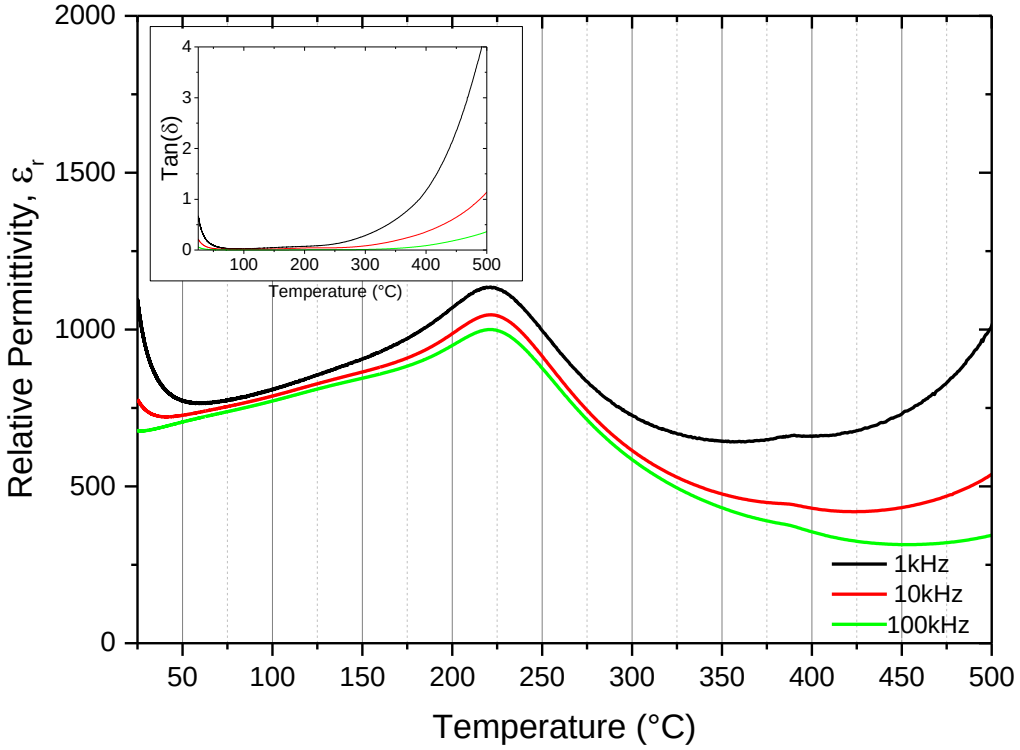

Figure 6.23: Relative permittivity and tan (δ) of $0.91KNbO_3$-$0.09CaZrO_3$ with temperature and frequency.

For ease of comparison the relative permittivity with temperature for each composition can be seen below (Figure 6.24).

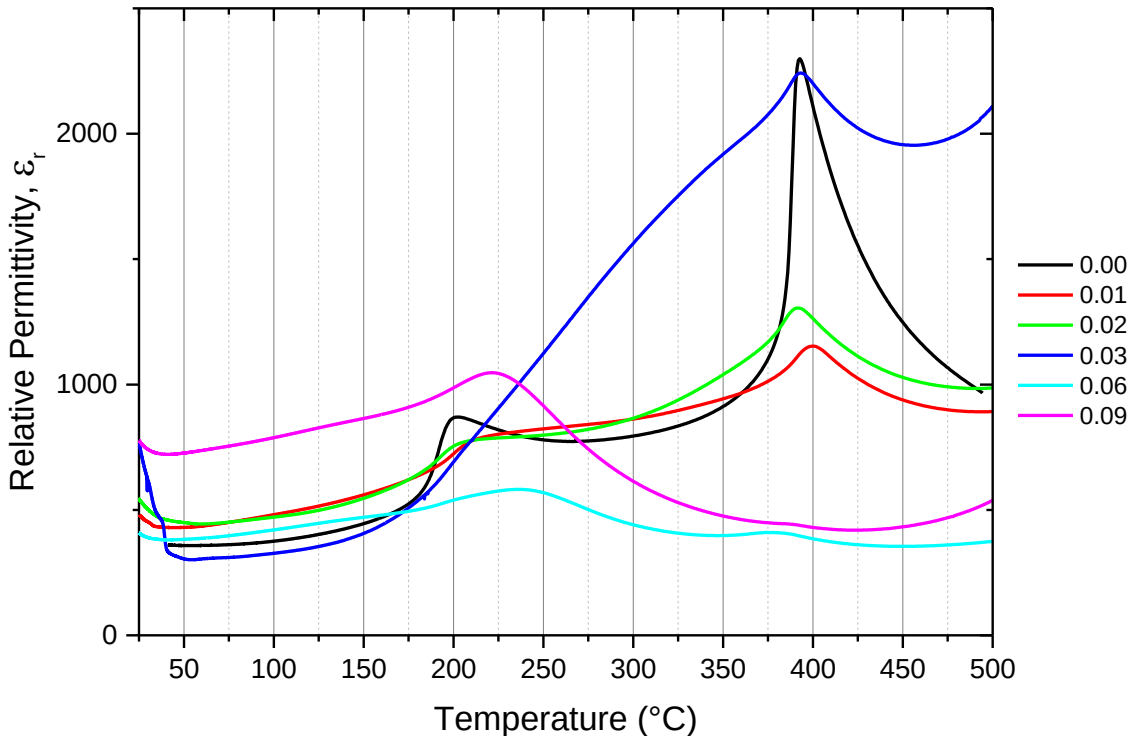

Figure 6.24: Relative permittivity of all $KNbO_3$-$CaZrO_3$ compositions with temperature at 10kHz.

6.2.3 Conclusion

Substitution of $KNbO_3$ with $CaZrO_3$ increases the temperature of the rhombohedral phase up to room temperature at x=0.03. Although it is never the most energetically favourable phase, always coexisting with the orthorhombic phase. $CaZrO_3$ reduces T_{O-T} slightly, but decreases the temperature at which the cubic phase can be present by much more. The substitution also broadens the T_{O-T} and T_{T-C} phase transitions. At $x \geq 0.03$ some relaxor-like behaviour occurs in the material.

6.3 $KNbO_3$ – $LiNbO_3$

Substituting $LiNbO_3$ into $(K,Na)NbO_3$ reduces the T_{O-T} phase transition down to room temperature (134). It was proposed that this also may be the case for $KNbO_3$.

6.3.1 $(1-x)KNbO_3$-$xLiNbO_3$ (KNLN) synthesis

Six compositions were synthesised, where x=0.03, 0.04, 0.07, 0.08, 0.09, and 0.10 by the mixed oxide method outlined in section 4.1. The sintering temperature decreased as the amount of $LiNbO_3$ increased, x=0.03 and 0.04 had a T_{sint} of 1050°C, 0.07 had a T_{sint} of 1030°C and compositions x=0.08-0.10 had a T_{sint} of 950°C. The samples were ground and silver electrodes were applied for electrical characterisation.

6.3.2 Characterisation, Results and Discussion

6.3.2.1 X-ray Diffraction data

Sintered and crushed pellets were measured between 20-80° using a Bruker D8 X-ray diffractometer, with a scan step of 0.033425° for a total scan time of 20 minutes, the results can be seen in Figure 6.25. Rietveld refinement was carried out on the samples to determine the phase of the material and index the peaks.

The substitution of potassium for lithium had no effect on the phase of the material, every composition was pure orthorhombic. A secondary phase identified as $K_3Li_2Nb_5O_{15}$ was found and increased in phase fraction with an increase in lithium substitution (Table 6.9). This suggests that there is finite amount of lithium that can be introduced into the perovskite $KNbO_3$ structure. When x=0.03 there is 1.8% of the secondary phase, this increased to 13.2% at x=0.10. The WRP of the refinements are high but are below the 10 threshold. This should be expected as introducing a secondary phase increase the number of refinement parameters that could be refined.

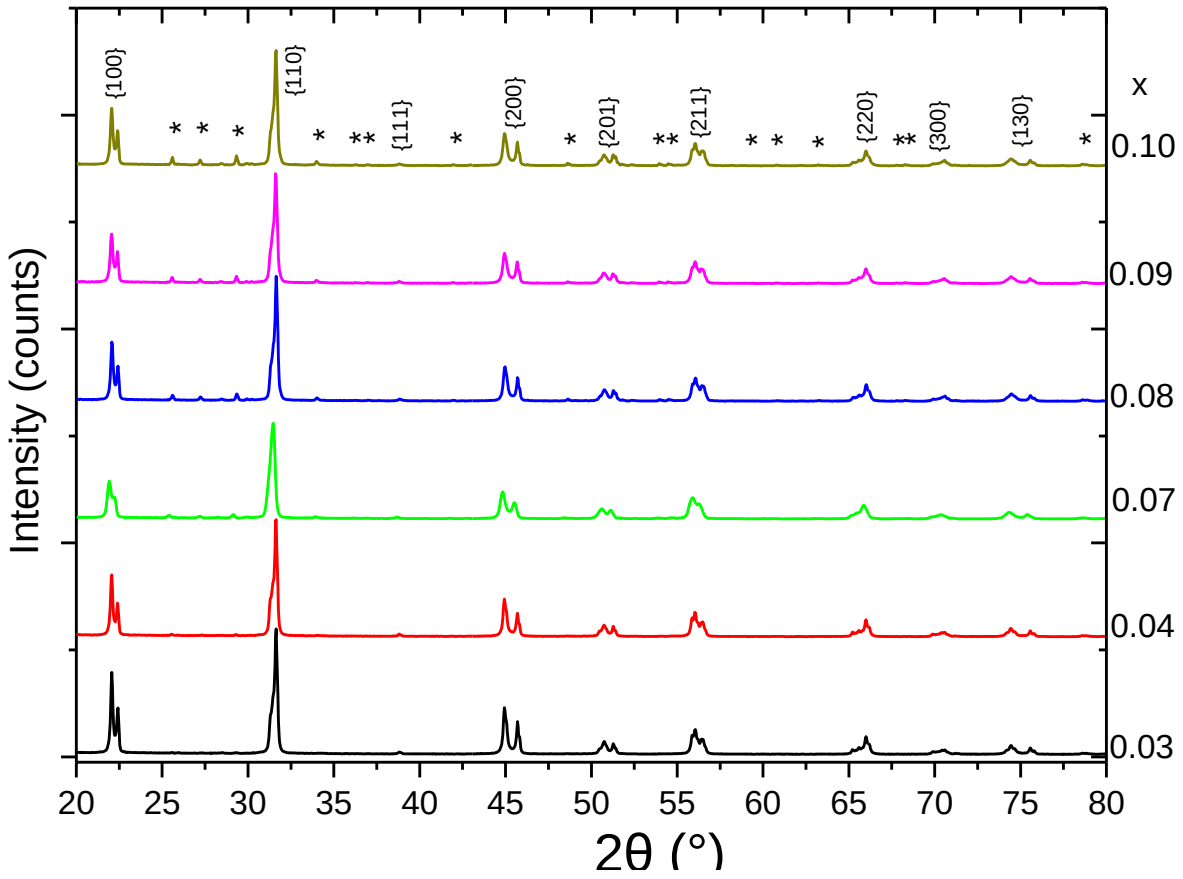

Figure 6.25: X-ray diffraction results of (1-x)$KNbO_3$-x$LiNbO_3$, indexed using as psuedo-monclinic and asteriks indicating secondary phase peaks.

Table 6.9: Rietveld Refinement results of (1-x)$KNbO_3$-$LiNbO_3$ compositions.

Composition	High Score Phase Fraction (%)		WRp	Pseudo-monoclinic unit cell parameters			
	Orthorhombic $KNbO_3$-$LiNbO_3$	$K_3Li_2Nb_5O_{15}$		a (Å)	b (Å)	c (Å)	β (°)
0.03	98.2	1.8	8.3332	4.0340	4.0340	3.9719	89.73
0.04	97.9	2.1	6.5292	4.0336	4.0336	3.9712	89.73
0.07	91.2	8.8	8.6239	4.0292	4.0292	3.9741	89.77
0.08	90.8	9.2	7.2154	4.0326	4.0326	3.9726	89.74
0.09	90.2	9.8	7.6313	4.0320	4.0320	3.9732	89.74
0.10	86.8	13.2	7.1232	4.0324	4.0324	3.9725	89.74

6.3.2.2 Permittivity data

Although the introduction of lithium had no effect on the crystallographic phase at room temperature, the permittivity results suggest there is a change in phase transition temperatures (Figure 6.26). The phase transitions of pure $KNbO_3$ are seen at 200°C and 390°C for the T_{O-T} and T_C, respectively. These transitions occur around 20°C lower than those found in the literature which may be an indication that the thermocouple used to measure the temperature was experiencing a lower temperature than the sample. The thermocouple was positioned as close as possible to the sample for the remaining compositions.

Unlike when $CaZrO_3$ was added to $KNbO_3$, $LiNbO_3$ substitution does not cause the phase transitions to broaden, also there is no change in frequency dispersion[8]. This suggests there is no relaxor behaviour within the samples.

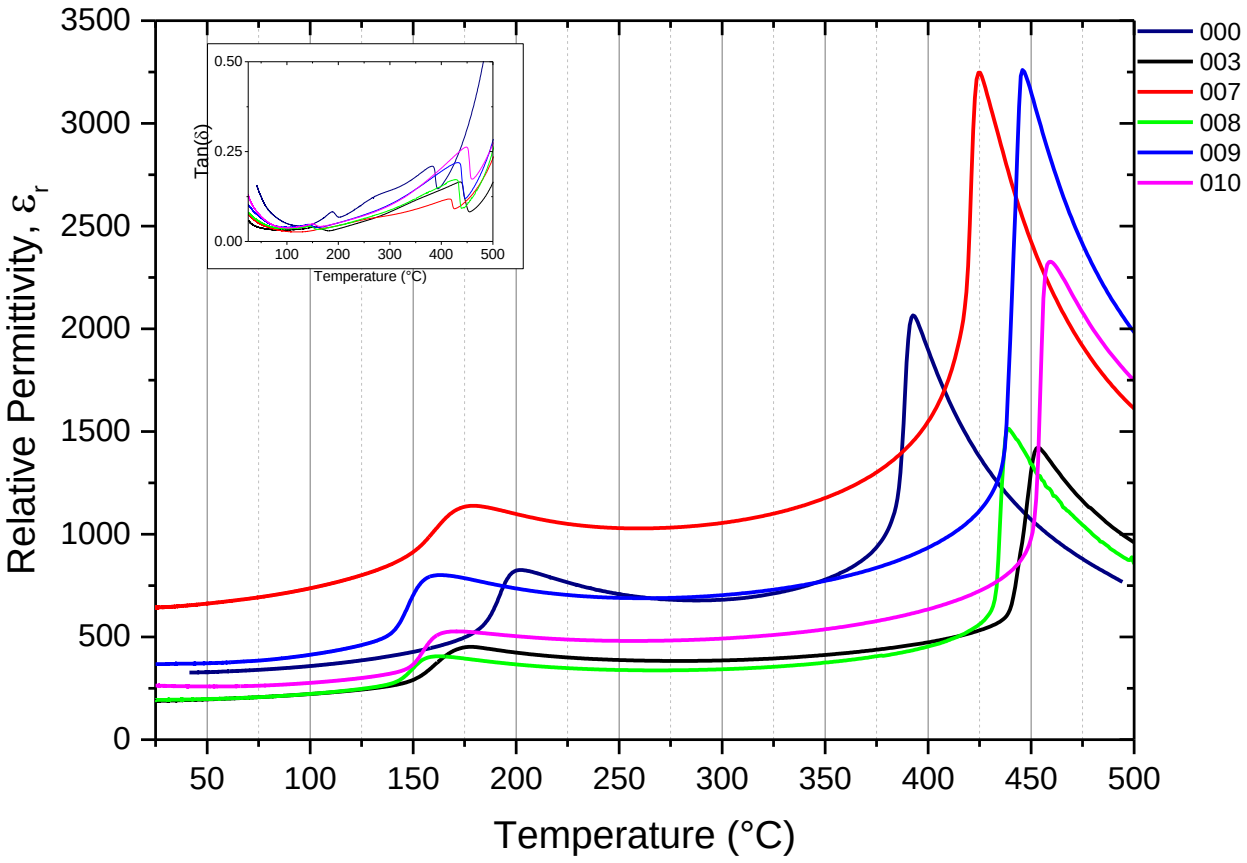

Figure 6.26: Relative permittivity of all $KNbO_3$-$LiNbO_3$ compositions with temperature at 10kHz.

[8] Permittivity measurements at 1kHz, 10kHz, and 100kHz between 25-500°C for each composition can be seen in the Chapter 6 Appendix.

The addition of $LiNbO_3$ causes the T_{O-T} to decrease with increasing $LiNbO_3$, moving from 200°C in pure $KNbO_3$ to 160°C at x=0.10. After the initial decrease in T_{O-T}, the transition temperature stabilises at around 160°C from x=0.07. Adding lithium causes the T_C to increase, from 390°C (or 420°C in the literature (113)) , to 460°C when x=0.10. The phase transition temperatures of each composition can be seen in Figure 6.27.

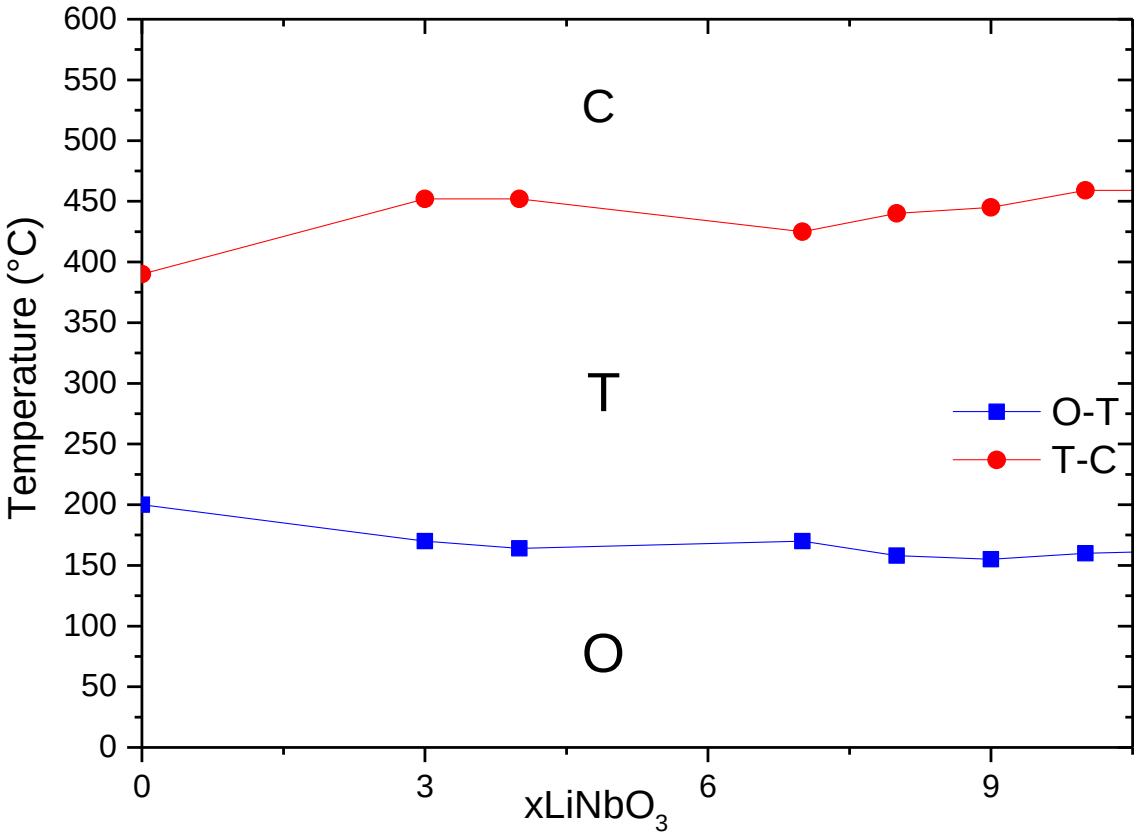

Figure 6.27: Phase transitions from the permittivity data of all $KNbO_3$-$LiNbO_3$ compositions.

6.3.2.3 Polarization- Field and Strain- Field data

The polarization was measured as a function of electric field applied in 0.5kV/mm steps from 1kV/mm to 5kV/mm. All compositions survived the maximum available field that could be applied by the voltage amplifier. This is an indication that the samples were well sintered, even with a large amount of secondary phase found in compositions with increased x. The full results can be seen in the appendix however, Figure 6.28 shows the polarization loops for each composition at 4.5kV/mm.

Each sample is fully saturated at 4.5kV/mm as seen by the pinching of the loops at the extreme fields. 4.5kV/mm is far above the switching field of every sample. The coercive field, E_C, of each composition as well as other polarization properties can be seen in Table 6.10. With the exception of x=0.08, there is a tendency for the saturated polarization, P_s, and the remnant polarization, P_r, to decrease with an increased amount of $LiNbO_3$. The composition where x=0.08 is an outlier in most cases, this may be due to poor synthesis of the sample or poor electrode application. The coercive field, E_C, at first decreases with an increase in x to 0.07, and then increases from x=0.07 to 0.10. This was also seen by Du *et al* when $LiNbO_3$ was substituted into KNN (183)

Table 6.10: Polarization-electric field properties of the $KNbO_3$-$LiNbO_3$ system.

$xLiNbO_3$	P_s ($\mu C/cm^2$)	P_r ($\mu C/cm^2$)	E_C (kV/mm)
0.03	13.23	10.12	1.83
0.07	13.54	9.17	1.08
0.08	8.09	5.89	1.24
0.09	12.08	9.01	1.12
0.10	9.41	6.84	1.58

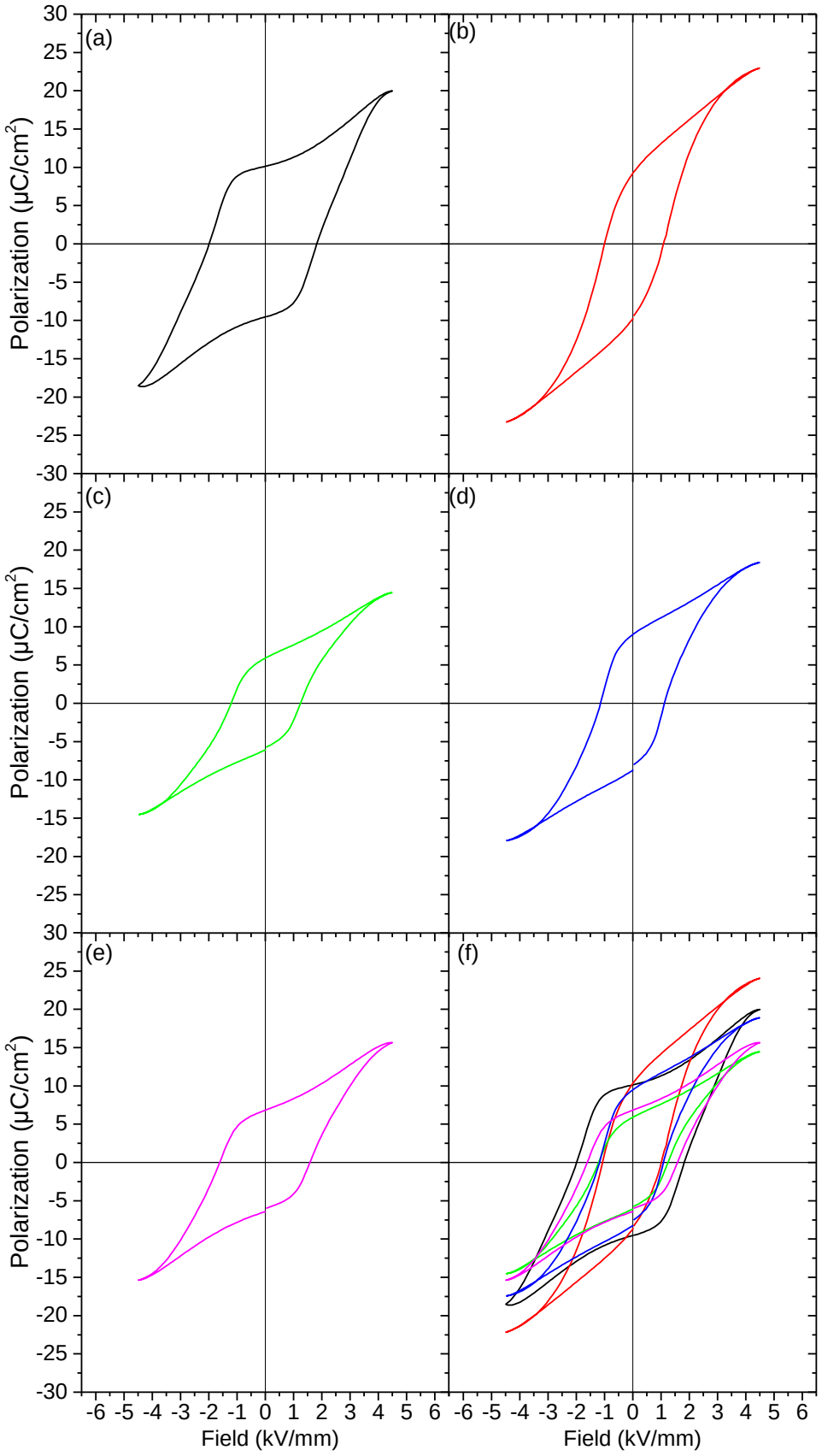

Figure 6.28: Compensated polarization-electric field results at 4.5kV/mm for $KNbO_3$-$LiNbO_3$ compositions, for x= (a) 0.03, (b) 0.07, (c) 0.08, (d) 0.09, (e) 0.10, and (f) every composition.

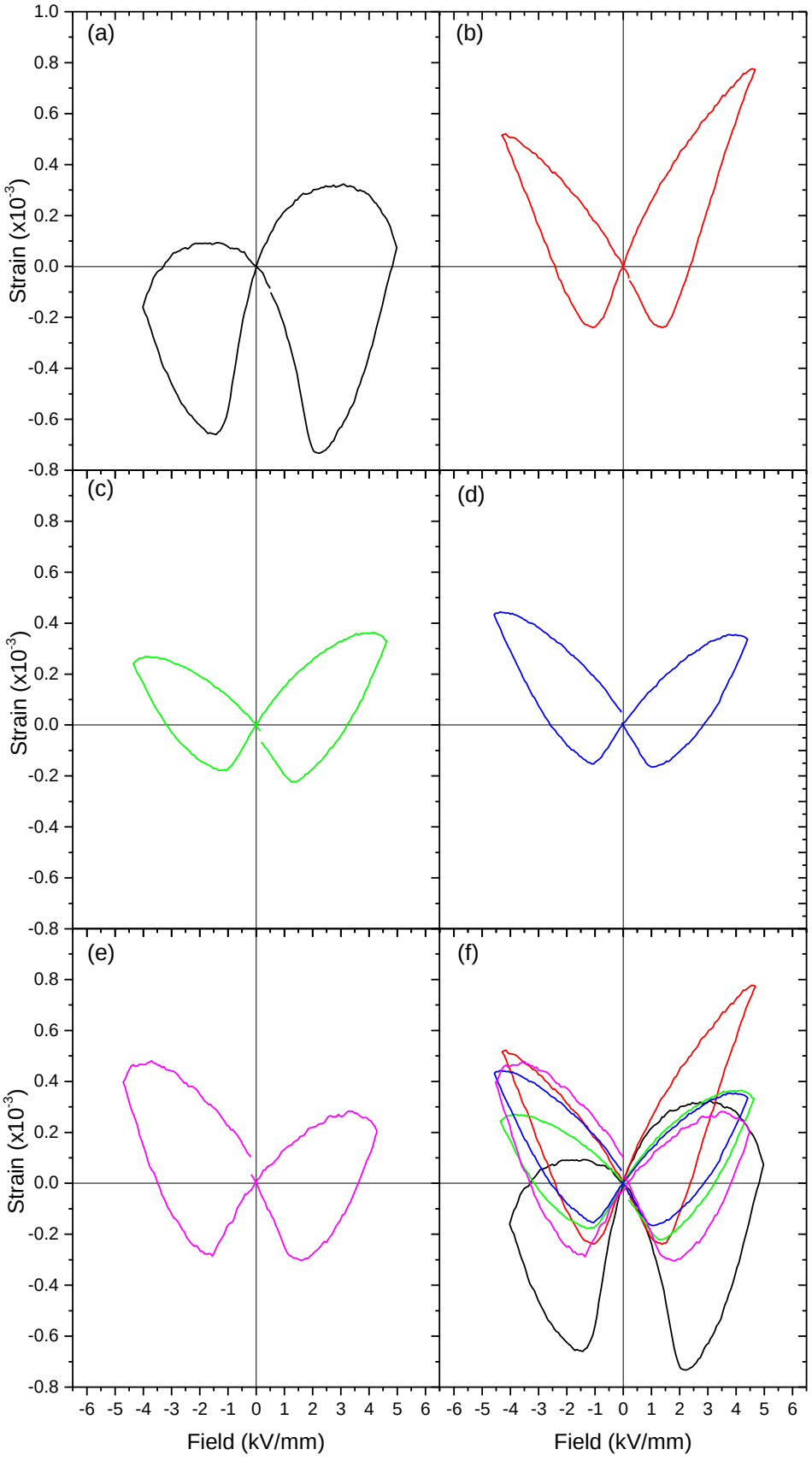

Figure 6.29: Strain-electric field results at 4.5kV/mm for $KNbO_3$-$LiNbO_3$ compositions, for x= (a) 003, (b) 007, (c) 008, (d) 009, (e) 010, and (f) every composition.

The strain-electric field results of every composition with a peak field of 4.5kV/mm can be seen in Figure 6.29. Some of the notable properties can also be seen in Table 6.11. The 'low'-field d_{33}* was determined by the gradient of the strain-electric field loop from -1kV/mm to 1kV/mm, the high-filed d_{33}* was determined by the average of the gradients found between 30 to 40kV/mm and -30 to -40kV/mm. This type of analysis appears to exaggerate the piezoelectric response of x=0.03 and x=0.10 as they have curved extremities likely due to conductivity.

S_{max} and E_{max} are the maximum strain and the electric field at which the maximum strain is found. As the strain measurement is the change in strain against electric field, the spontaneous strain (or the material strain at 0kV/mm) is equal to the minimum strain in Figure 6.29 for each composition.

Table 6.11: Strain-electric field results of the KNLN system.

x$LiNbO_3$	**'Low'-field d_{33}* (pV/m)**	**High-field d_{33}* (pV/m)**	**S_{max} ($x10^{-3}$)**	**E_{max} (kV/mm)**	**S_{max}/E_{max} (pV/m)**	**Spontaneous Strain ($x10^{-3}$)**
0.03	245.71	309.25	-	-	-	0.73
0.07	191.26	311.15	0.77	4.60	167.39	0.24
0.08	156.77	198.53	0.35	4.43	79.01	0.22
0.09	180.84	210.83	0.44	4.51	97.56	0.17
0.10	179.15	301.10	0.46	4.38	105.02	0.30

6.3.3 Conclusion

The incorporation of $LiNbO_3$ into $KNbO_3$ had no effect on the crystallographic phase at room temperature, although a secondary phase increases in fraction with an increase in $LiNbO_3$. $LiNbO_3$ did reduce T_{O-T} by 40°C, which theoretically would make the tetragonal phase more energetically favourable to spontaneously appear at room temperature when compared to pure $KNbO_3$. The lithium acted as a sintering aid, allowing the KN-based samples to be characterised under large electric-fields.

The polarization and strain data implies that every sample is ferroelectric, and that composition x=0.07 would have the best piezoelectric response.

6.4 Ternary System

6.4.1 (1-x-y)$KNbO_3$-x$CaZrO_3$-y$LiNbO_3$ synthesis

After the crystallographic characterisation of the KNCZ and KNLN systems, both were incorporated into a ternary system (KNCZLN). The idea being that the sintering aid of $LiNbO_3$ would allow for the KNCZ samples to be measured under electric field. Six compositions were synthesised by the mixed oxide method outlined in section 4.1. Figure 6.30 shows the varied amounts of $CaZrO_3$ and $LiNbO_3$ substituted into $KNbO_3$ for each composition. This is also shown in Table 6.12, along with the sintering temperatures.

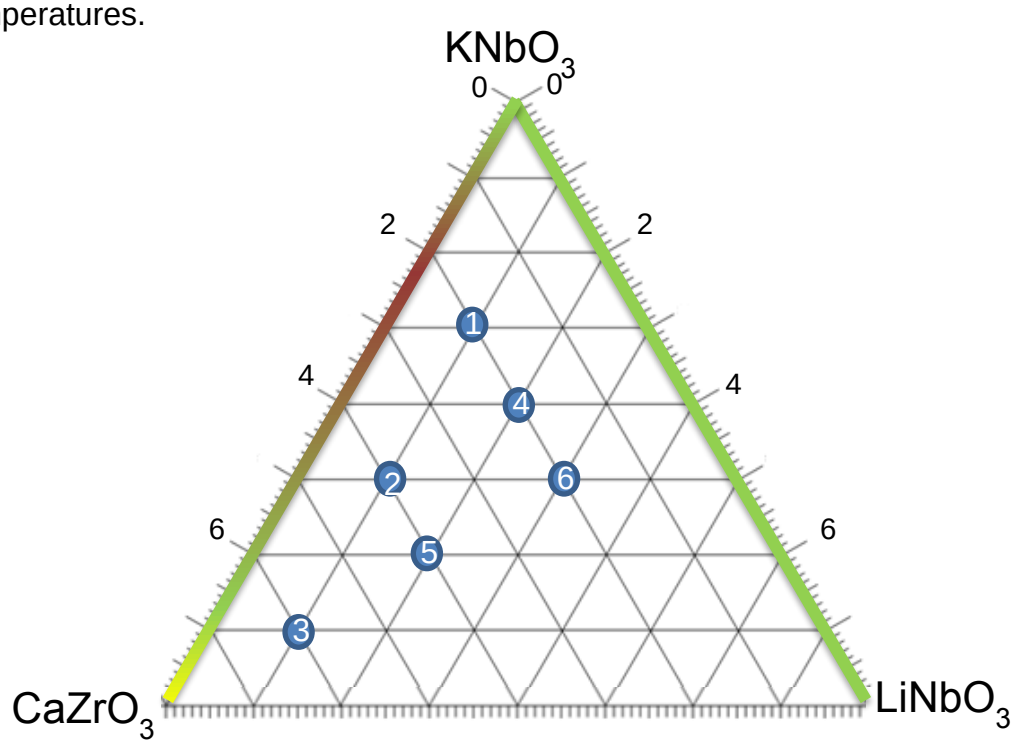

Figure 6.30: KNCZLN compositions synthesised.

Table 6.12: (1-x-y)$KNbO_3$-x$CaZrO_3$-y$LiNbO_3$ compositions and sintering temperatures.

Composition	(1-x-y) $KNbO_3$	$CaZrO_3$ (x)	$LiNbO_3$ (y)	Sintering Temperature (°C)
0	1.00	0.00	0.00	1020
1	0.97	0.02	0.01	1100
2	0.95	0.04	0.01	1125
3	0.93	0.06	0.01	1125
4	0.96	0.02	0.02	1100
5	0.94	0.04	0.02	1125
6	0.95	0.02	0.03	1125

For ease of comparison, the characterisation analysis will be split into compositions with equal $CaZrO_3$ percentages (compositions 1, 4 and 6 or 2 and 5) and equal $LiNbO_3$ percentages (compositions 1, 2 and 3, or 4 and 5) wherever possible. Samples 2 and 5 were very conductive and as a result, high-field characterisation was not possible.

6.4.2 Characterisation, Results and Discussion

6.4.2.1 X-Ray Diffraction Data

Sintered and crushed pellets were measured between 20-80° using a Bruker D8 X-ray diffractometer, with a scan step of 0.033425° for a total scan time of 20minutes. Rietveld refinement was carried out on the samples to determine the phase of the material. The results of which can be seen in Table 6.13. The full scan results can be seen in Figure 6.31, and a comparison of the {200} peaks can be seen in Figure 6.32, where composition 0 is pure $KNbO_3$ for comparison.

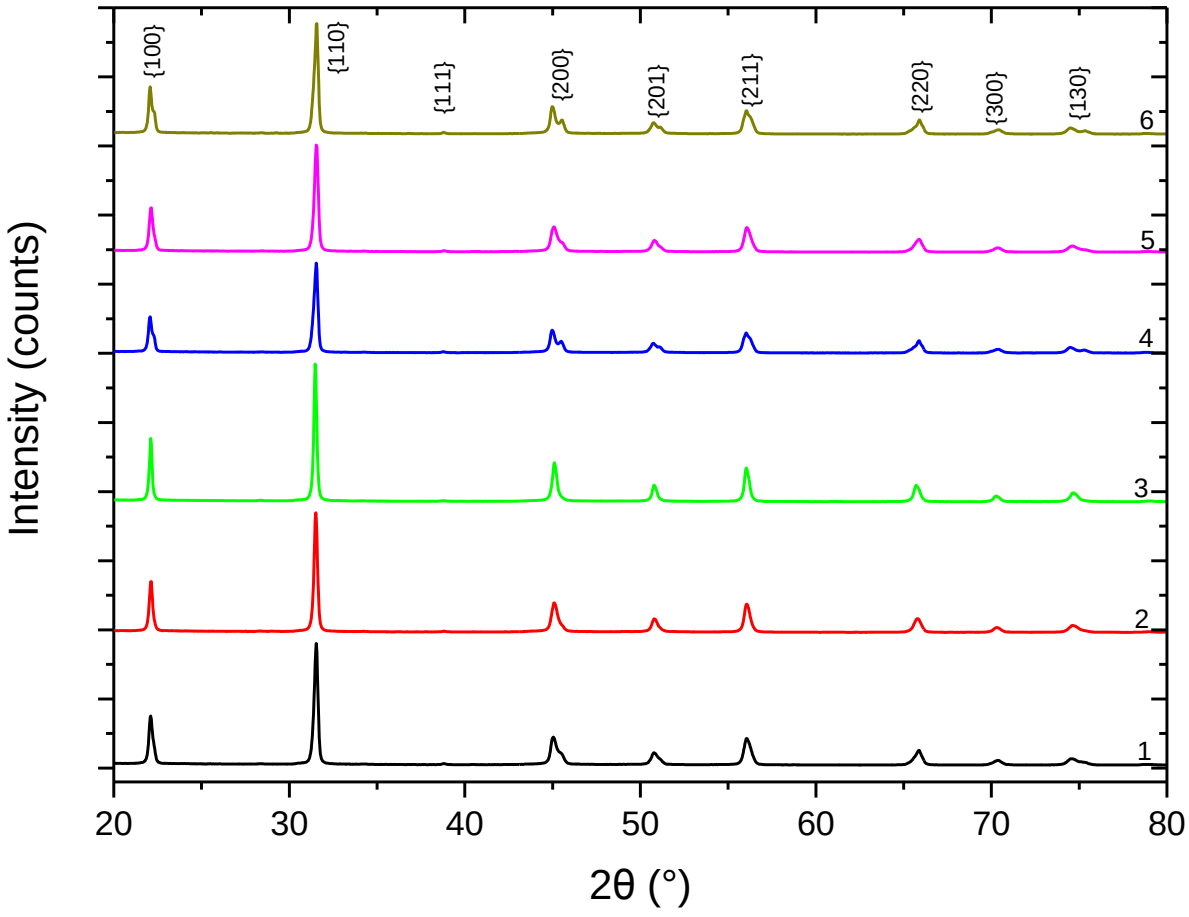

Figure 6.31: X-ray Diffraction data of each KNCZLN composition.

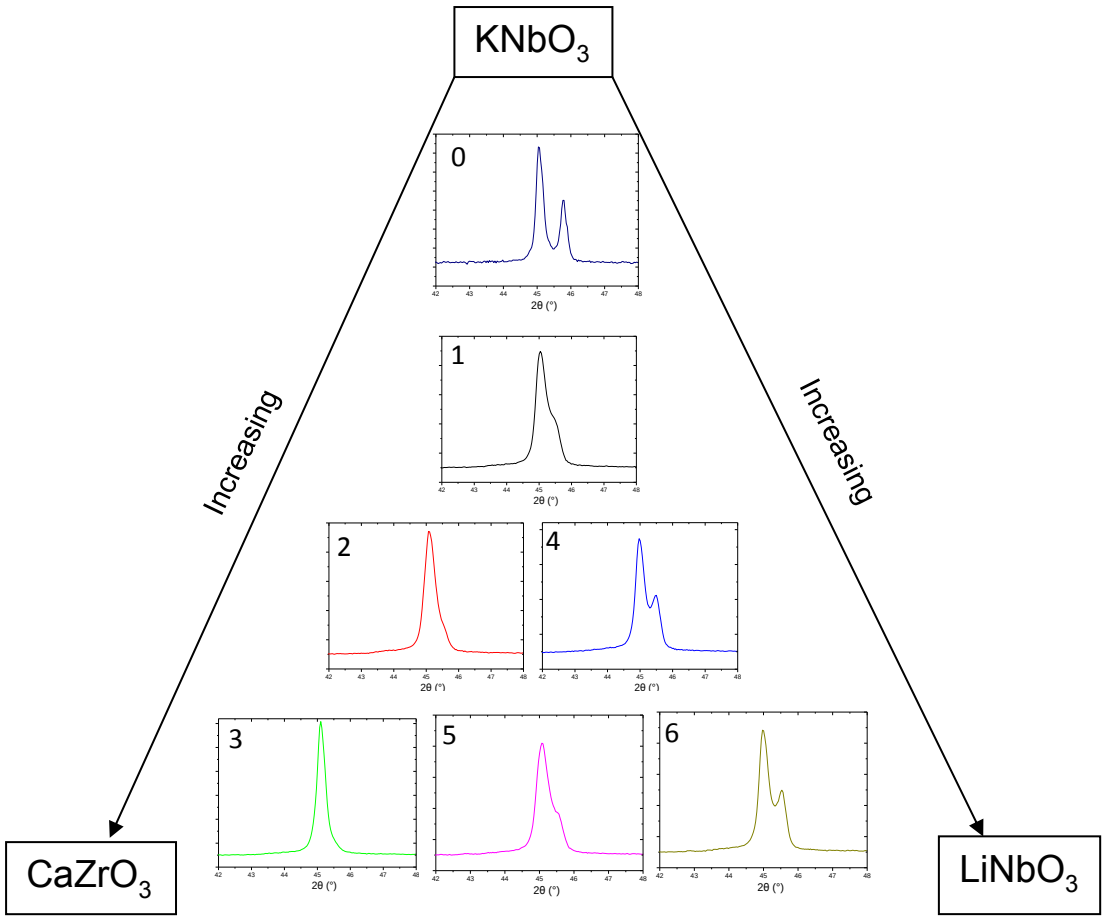

Figure 6.32: {200} peaks of pure $KNbO_3$ and each KNCZLN composition.

Table 6.13: Rietveld refinement results of each KNCZLN composition.

Composition	High Score Fraction (%)		WRp	Pseudo-monoclinic unit cell parameters				Rhombohedral unit cell parameters	
	O	R		a (Å)	b (Å)	c (Å)	β (°)	a (Å)	α (°)
1	68.8	31.2	5.3245	4.030	4.030	3.985	89.84	4.013	89.99
2	47.9	52.1	5.8047	4.030	4.030	3.988	89.88	4.015	89.97
3	44.9	55.1	5.3381	4.029	4.029	3.993	89.87	4.015	89.97
4	83.5	16.5	5.8302	4.030	4.030	3.984	89.83	4.011	89.98
5	67.8	32.2	5.2574	4.031	4.031	3.984	89.83	4.013	89.99
6	83.1	16.9	5.6477	4.030	4.030	3.982	89.81	4.011	89.98

Rietveld refinement results of the KNCZLN system can be seen in Table 6.13. Compositions 1, 2 and 3 follow a similar trend to the KNCZ system. As the amount of $CaZrO_3$ was increased so did the rhombohedral phase fraction from 31.2% to 55.1%. This is also seen when comparing compositions 4 and 5, where the rhombohedral percentage increased from 16.5% to 32.2%.

When the $CaZrO_3$ percentage remains constant and $LiNbO_3$ is increased, the rhombohedral phase fraction is decreased, this is seen in samples 1 and 4. The refinement of composition 6 calculated the rhombohedral phase fraction to be slightly increased compared to that of

composition 4. This may be due to the increase in lithium inducing the secondary phase found in the KNLN system, and therefore reducing the amount of lithium incorporated into the perovskite structure. This in turn would reduce the amount the orthorhombic phase is stabilised. However, the secondary phase cannot be seen in the XRD scan.

6.4.2.2 Permittivity Data

A comparison of the permittivity data at 10kHz over a temperature range of 25-500°C for each composition can be seen in Figure 6.33. Each composition was measured at a range of frequencies, the results of which can be found in the Chapter 6 Appendix.

Increasing $CaZrO_3$ caused the peaks to broaden and made T_C decrease. Comparing samples 1, 2 and 3, it is clear that the more $CaZrO_3$ led to broader transition peaks. When comparing samples 1 and 4, it can be seen that increasing $LiNbO_3$ reverses the peak broadening, which is further reduced in sample 6. The $LiNbO_3$ also increases the T_C, reversing the effect 2% $CaZrO_3$ addition had on $KNbO_3$. Increasing the amount of $LiNbO_3$ also reduced T_{O-T} in the ternary system.

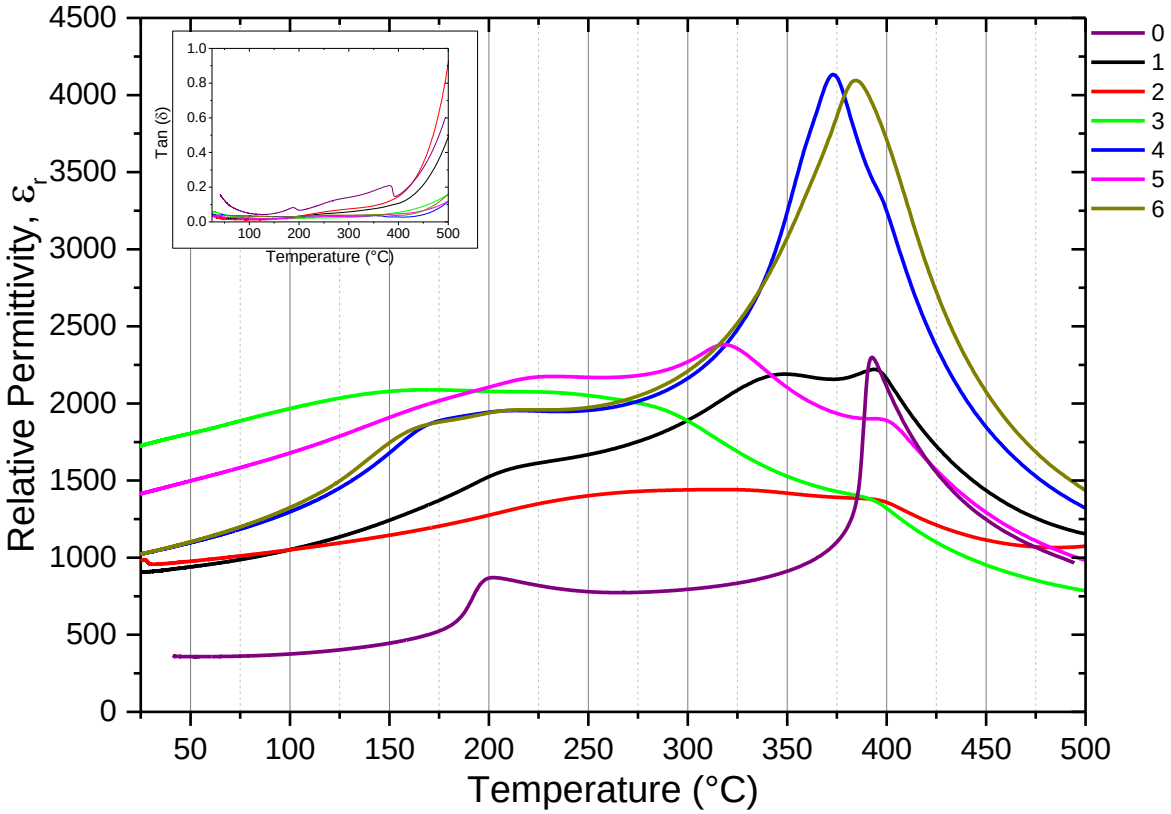

Figure 6.33: Relative permittivity of all KNCZLN compositions with temperature at 10kHz.

6.4.2.3 Polarization-Field and Strain-Field Data

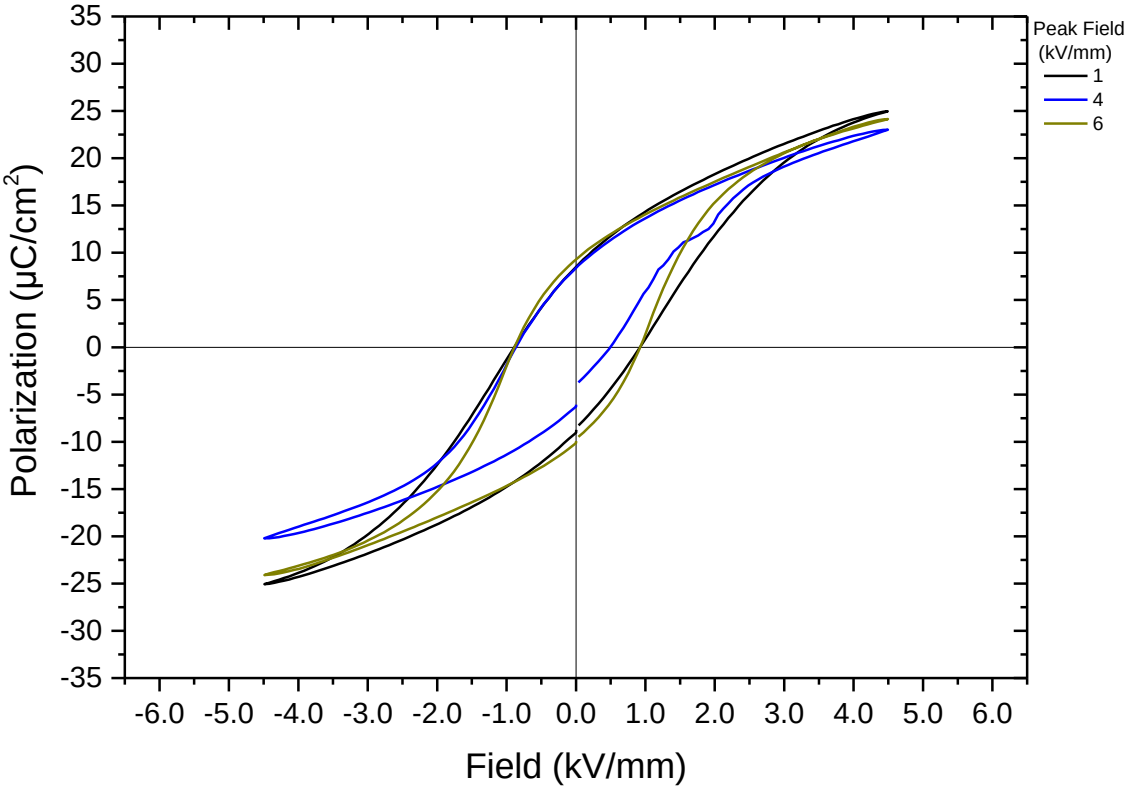

Figure 6.34: Compensated polarization-Electric Field data for KNCZLN compositions 1, 4 and 6 (increasing $LiNbO_3$) at a peak field of 4.5kV/mm.

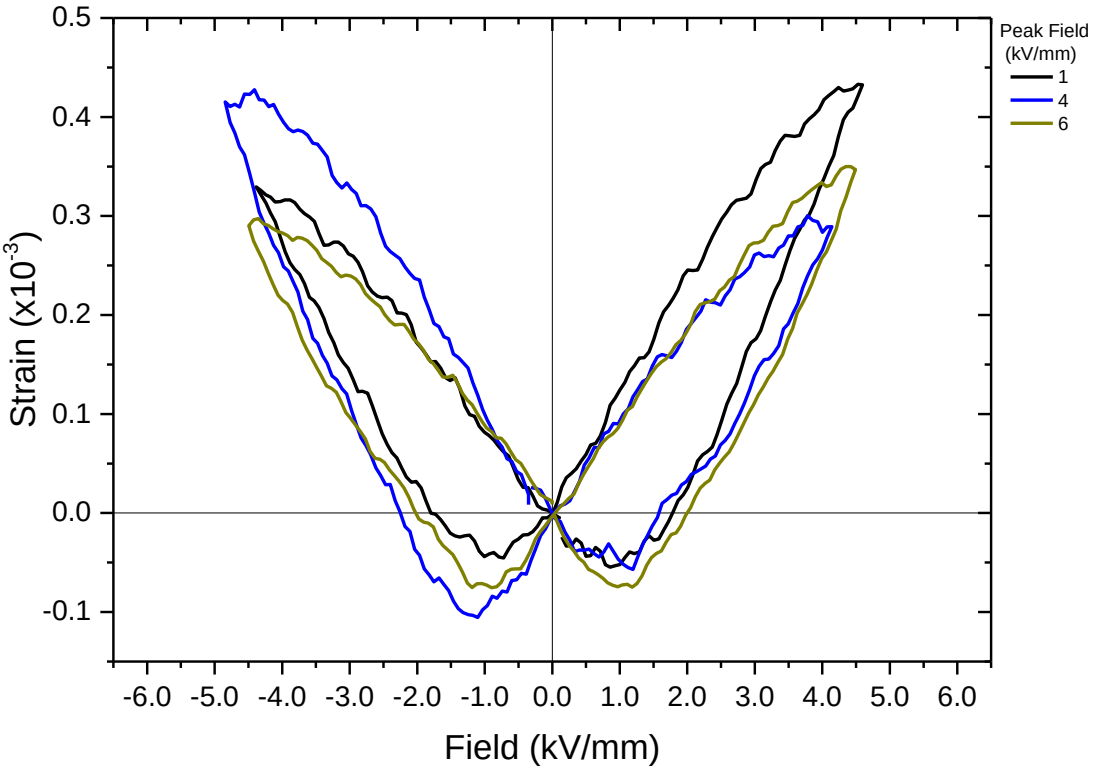

Figure 6.35: Strain-Electric Field data for KNCZLN compositions 1, 4 and 6 (increasing $LiNbO_3$) at a peak field of 4.5kV/mm.

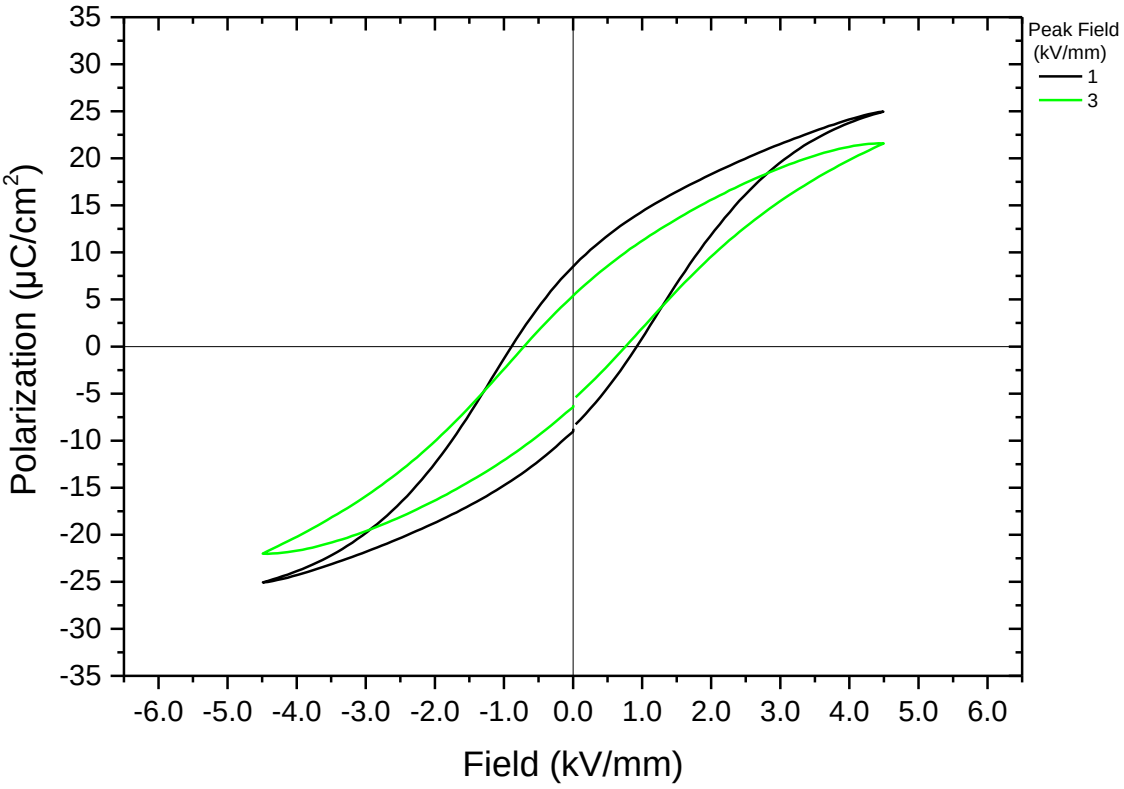

Figure 6.36: Compensated polarization-Electric Field data for KNCZLN compositions 1 and 3 (increasing $CaZrO_3$) at a peak field of 4.5kV/mm.

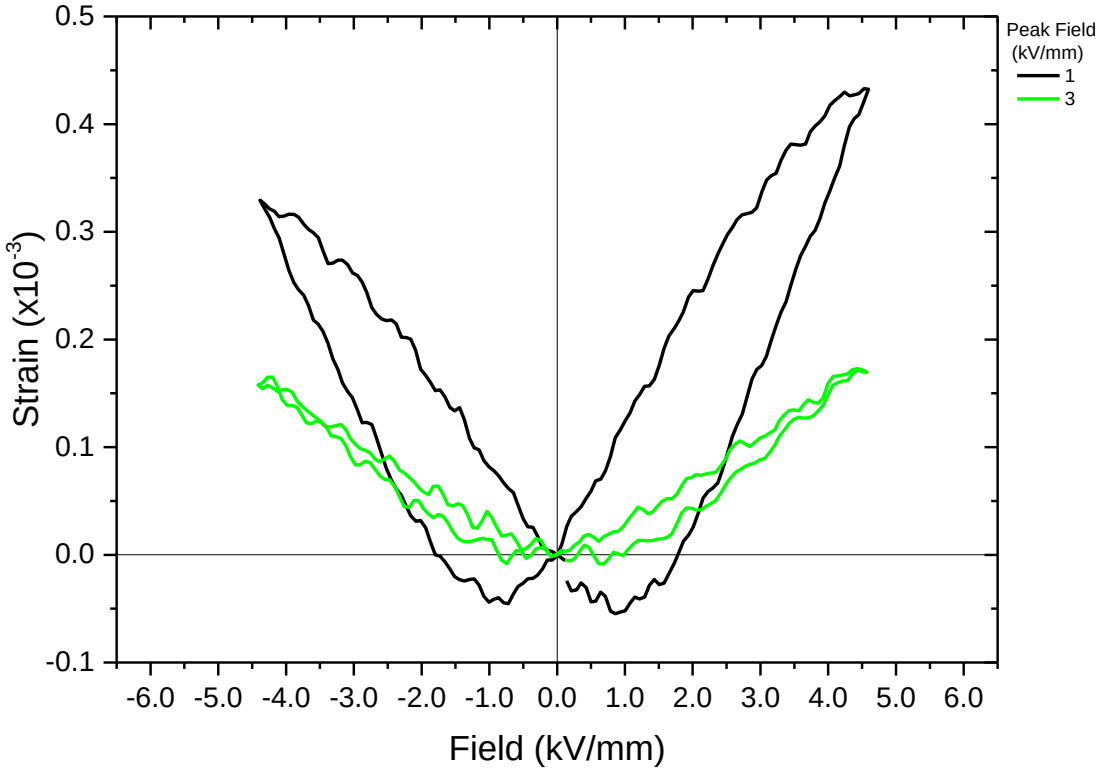

Figure 6.37: Strain-Electric Field data for KNCZLN compositions 1 and 3 (increasing $CaZrO_3$) at a peak field of 4.5kV/mm.

The polarization and strain of compositions 1, 4 and 6 can be seen in Figure 6.34 and Figure 6.35 respectively. This is to compare the effect an increasing amount of $LiNbO_3$ has on the KNCZLN system. Figure 6.36 and Figure 6.37 are the polarization and strain results for compositions 1 and 3, these figure help compare the effect and increasing $CaZrO_3$ content has on the KNCZLN system.

Table 6.14: Polarization-electric field properties of each KNCZLN composition.

KNCZLN	P_s ($\mu C/cm^2$)	P_r ($\mu C/cm^2$)	E_C (kV/mm)
1	16.71	8.51	0.90
2	-	-	-
3	15.41	5.58	0.73
4	14.86	8.41	0.87
5	-	-	-
6	14.1	9.16	0.89

Table 6.15: Strain-electric field results of each KNCZLN composition.

KNCZLN	'Low'-field d_{33}* (pC/N)	High-field d_{33}* (pC/N)	S_{max} ($x10^{-3}$)	E_{max} (kV/mm)	S_{max}/E_{max} (pC/N)	Remnant Strain ($x10^{-3}$)
1	61.10	143.07	0.43	4.58	93.89	0.056
2	-	-	-	-	-	-
3	9.07	52.89	0.17	4.49	37.86	0.007
4	87.46	124.50	0.42	4.58	91.70	0.105
5	-	-	-	-	-	-
6	82.61	135.15	0.35	4.44	78.83	0.074

When the amount of $LiNbO_3$ is increased, there is an initial increase in the remnant strain and calculated 'low'-field d_{33}* from 1 to 2%, but this then a decreased when 3% $LiNbO_3$ is added. However, the high-field d_{33}* decreases when the $LiNbO_3$ goes from 1 to 2% before increasing from 2 to 3%. The d_{33} calculated at the maximum strain when the maximum field is applied tends to decrease when $LiNbO_3$ is increased, decreasing a small amount from 1 to 2% $LiNbO_3$ before decreasing by a larger amount from 2 to 3% $LiNbO_3$.

Every calculated piezoelectric coefficient is decreased with an increase in $CaZrO_3$. From the strain-field data in Figure 6.37 it can be seen that the electrostriction effect is dominant in composition 3 as there is minimum negative relative strain.

6.4.3 Conclusion

Generally, the ternary phase diagram follows the trends of the two individual constituent systems.

An increase in $CaZrO_3$ causes an increase in the presence of the rhombohedral phase at room temperature. It also broadens or widens the boundary of the phase transition. Polarization and strain versus electric field shows a decrease in piezoelectric performance with an increase in $CaZrO_3$. This could not be shown in the KNCZ samples as high-field characterisation was not possible due to poor sample sintering. There is also a tendency for the material to become very conductive with an increase in $CaZrO_3$ as shown by the lack of high-field characterisation of compositions 2 and 5.

Adding $LiNbO_3$ to KNCZ improved the overall sinterability of the material. With an increased addition of $LiNbO_3$ there is an increase in the orthorhombic phase at room temperature. $LiNbO_3$ also reduces the effect of phase transition broadening found when adding $CaZrO_3$. The piezoelectric performance of the samples at first is increased and then decreases with more $LiNbO_3$ addition.

6.5 Chapter 6 Appendix

6.5.1 KNLN supplementary data

6.5.1.1 Permittivity data of each composition

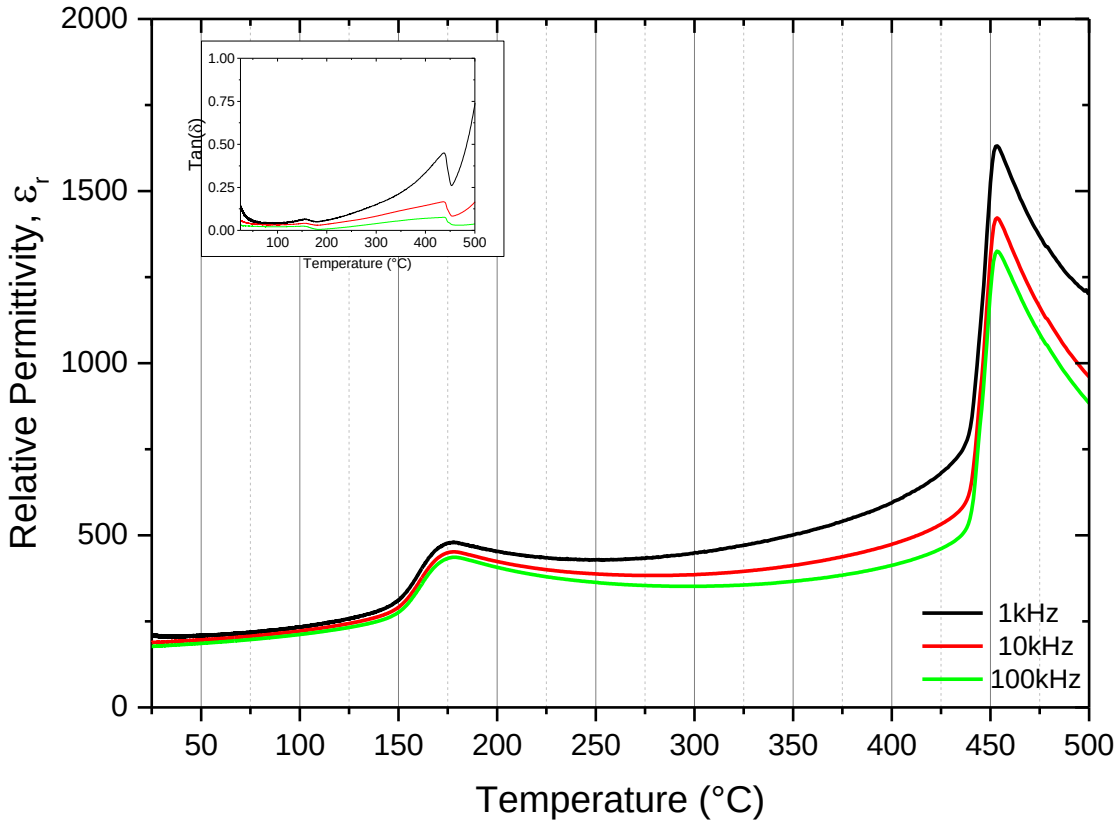

Figure 6.38: Relative permittivity and tan (δ) of $0.97KNbO_3$-$0.03LiNbO_3$ with temperature and frequency.

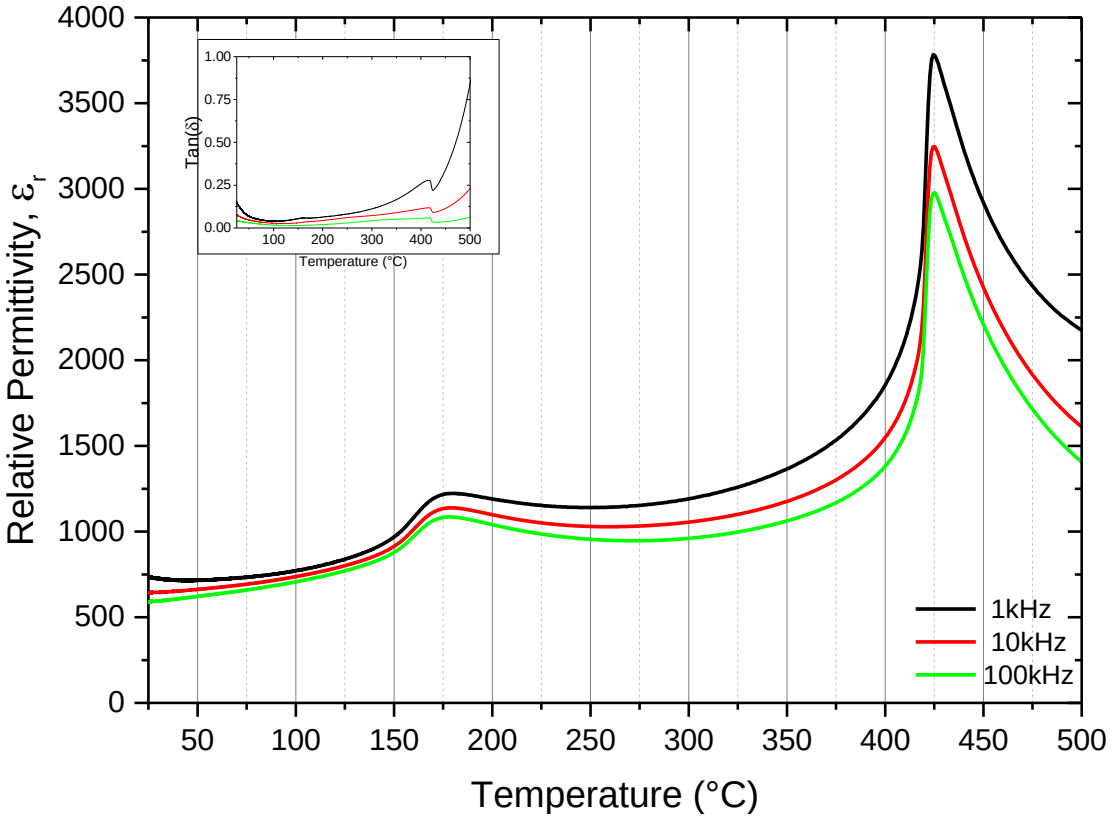

Figure 6.39: Relative permittivity and tan (δ) of $0.93KNbO_3$-$0.07LiNbO_3$ with temperature and frequency.

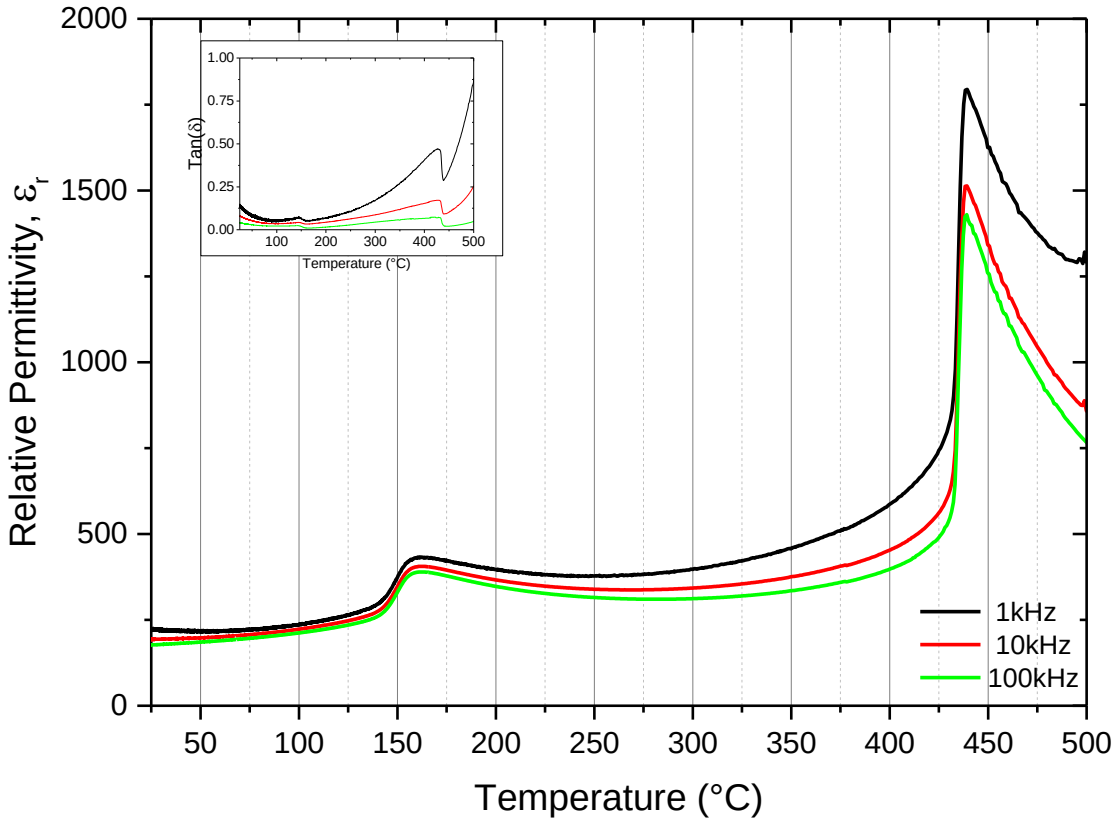

Figure 6.40: Relative permittivity and tan (δ) of $0.92KNbO_3$-$0.08LiNbO_3$ with temperature and frequency.

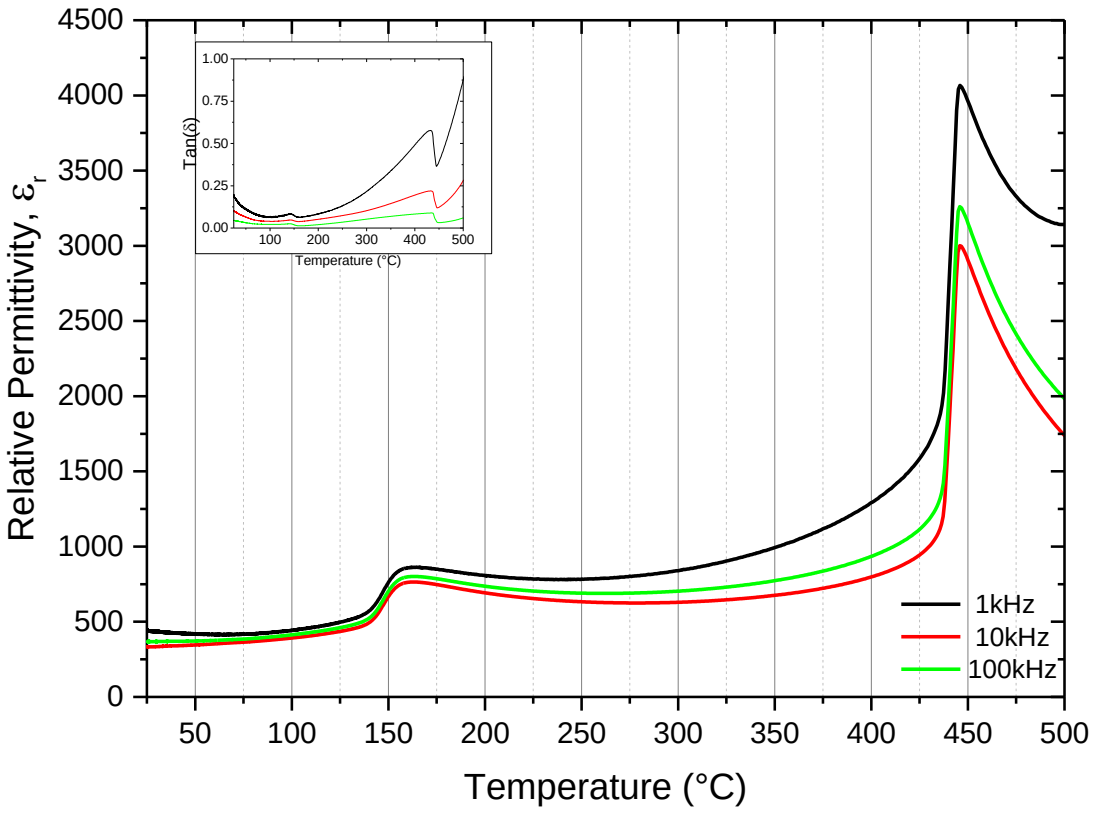

Figure 6.41: Relative permittivity and tan (δ) of $0.91KNbO_3$-$0.09LiNbO_3$ with temperature and frequency.

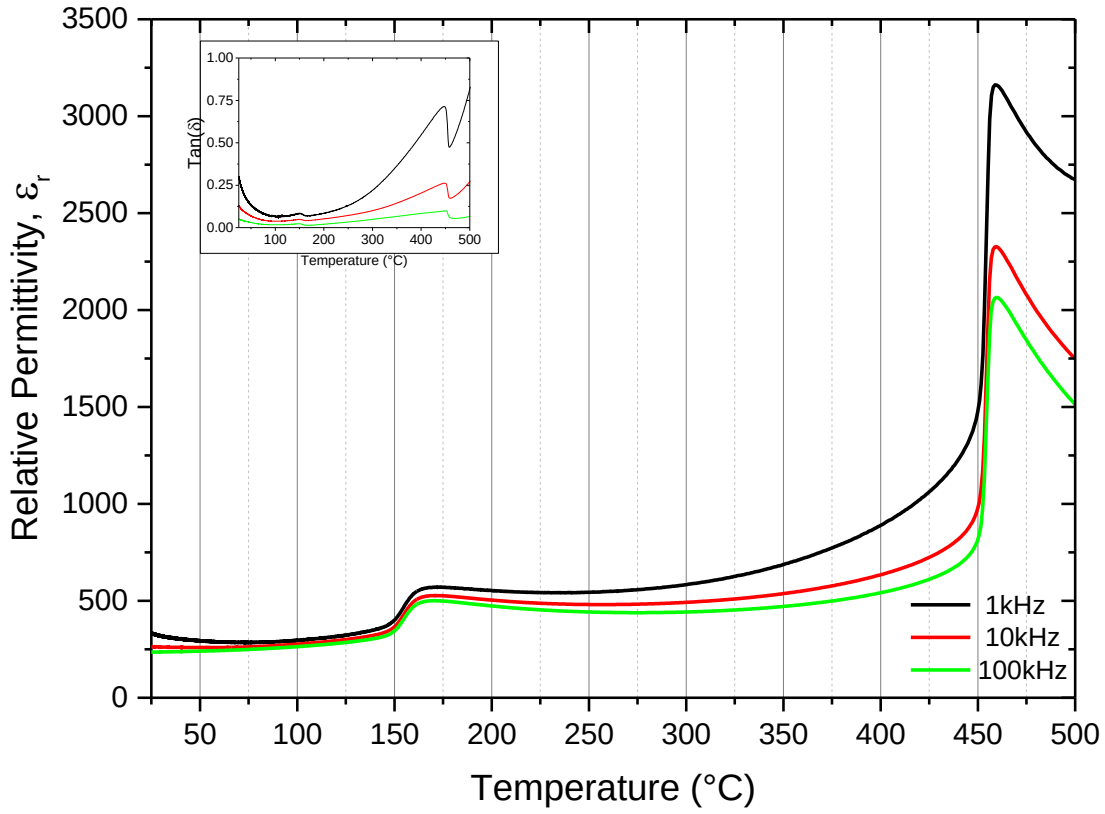

Figure 6.42: Relative permittivity and tan (δ) of $0.90KNbO_3$-$0.10LiNbO_3$ with temperature and frequency.

6.5.1.2 Polarization-electric field data at each peak field.

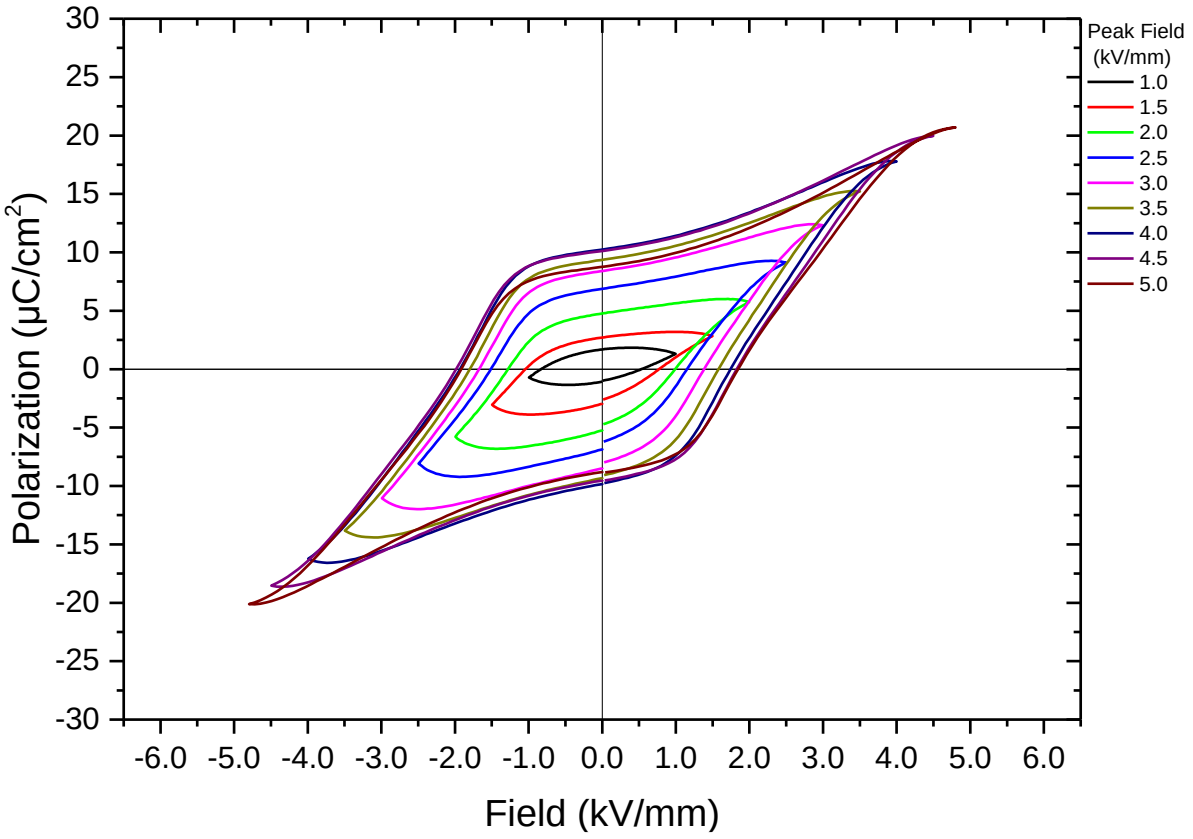

Figure 6.43: Compensated Polarization-Electric Field data for $0.97KNbO_3$-$0.03LiNbO_3$ with increasing fields.

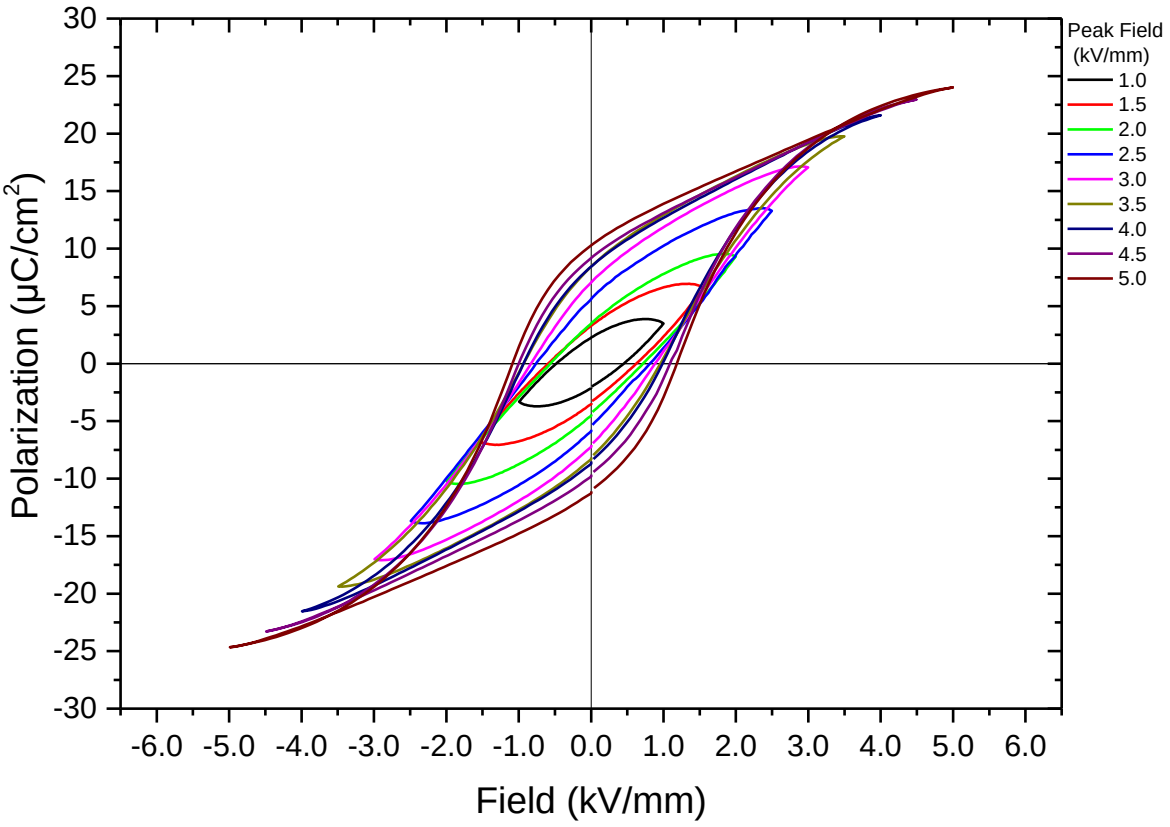

Figure 6.44: Compensated Polarization-Electric Field data for $0.93KNbO_3$-$0.07LiNbO_3$ with increasing fields.

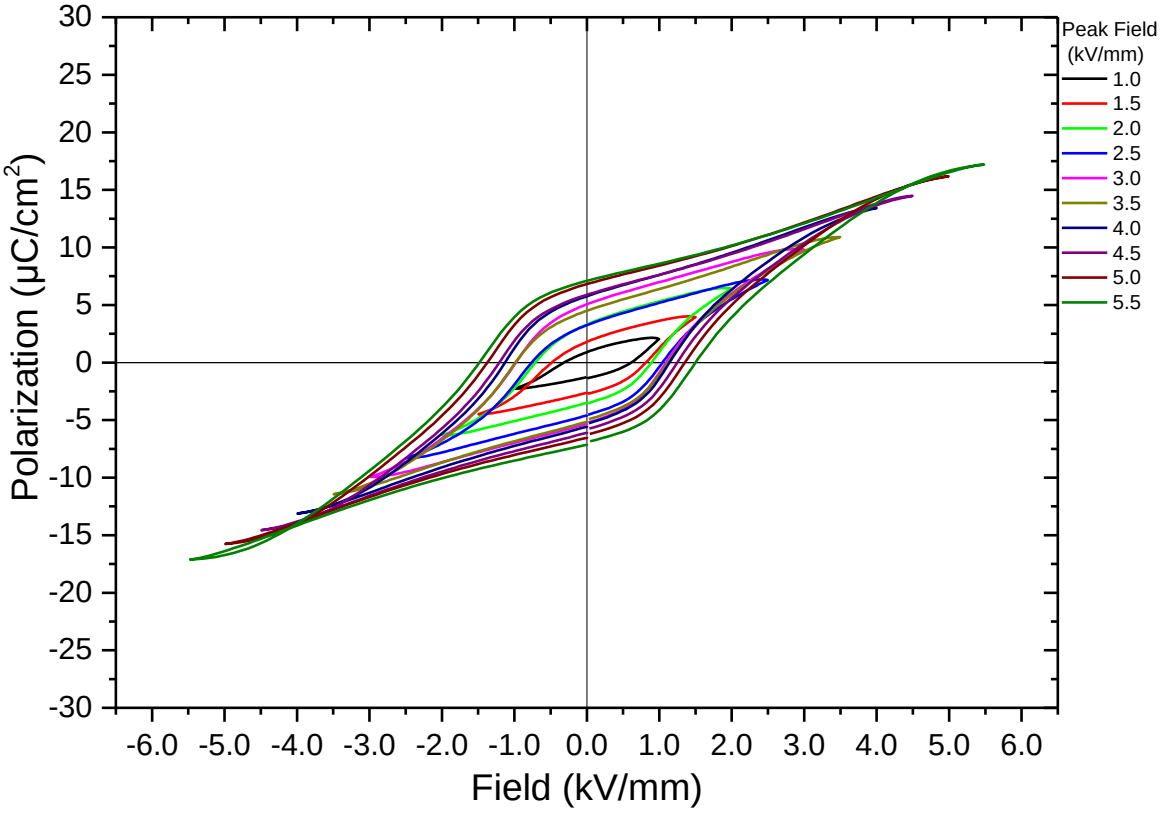

Figure 6.45: Compensated Polarization-Electric Field data for $0.92KNbO_3$-$0.08LiNbO_3$ with increasing fields.

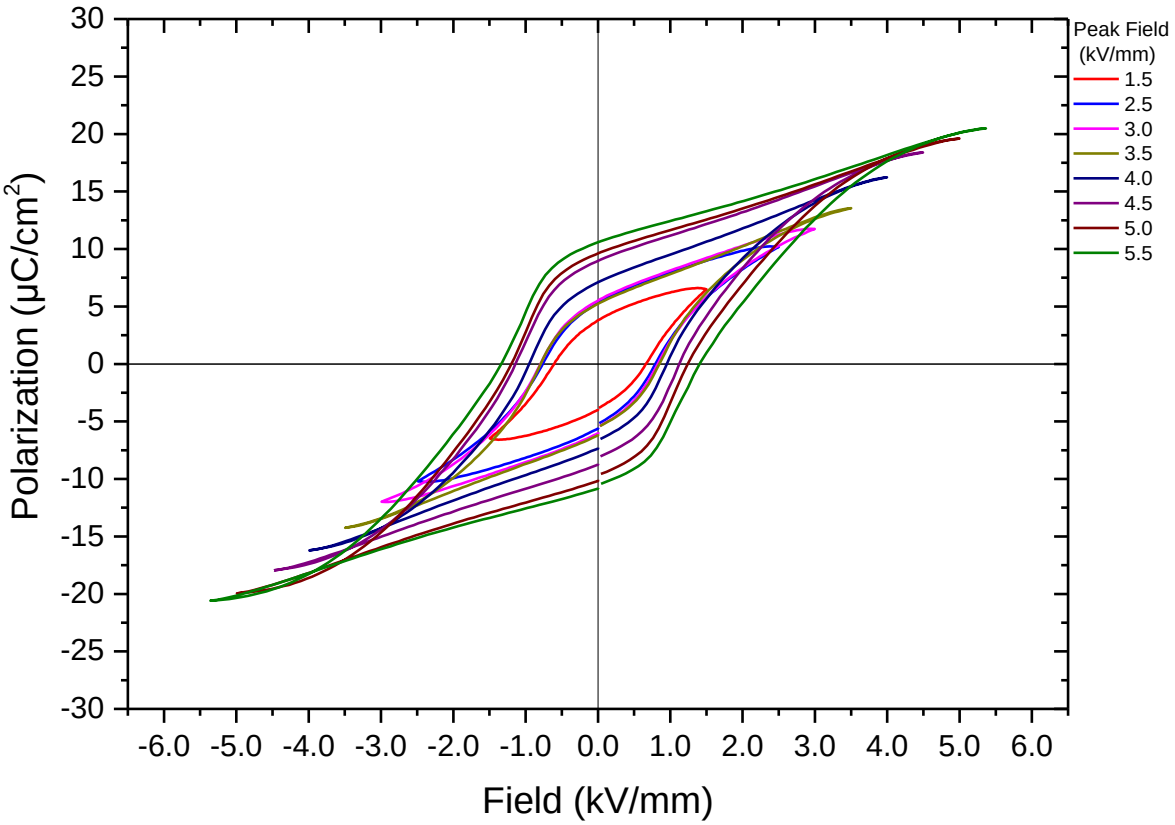

Figure 6.46: Compensated Polarization-Electric Field data for $0.91KNbO_3$-$0.09LiNbO_3$ with increasing fields.

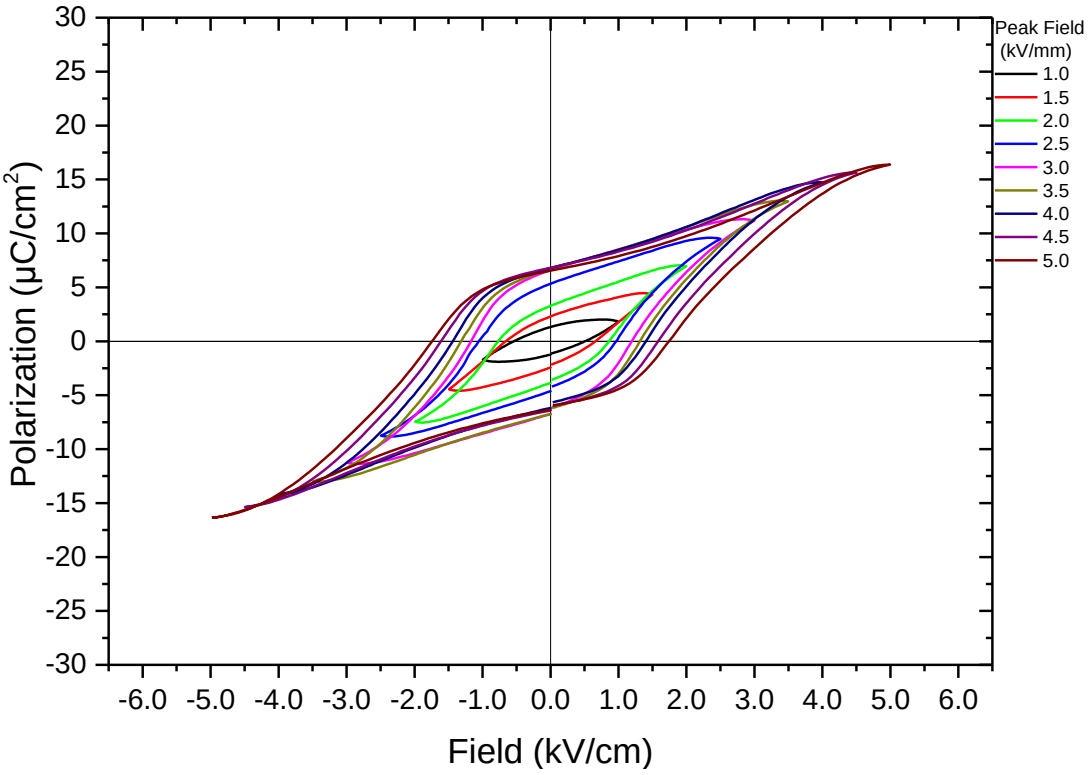

Figure 6.47: Compensated Polarization-Electric Field data for $0.90KNbO_3$-$0.10LiNbO_3$ with increasing fields.

6.5.1.3 Strain-electric field data at each peak field.

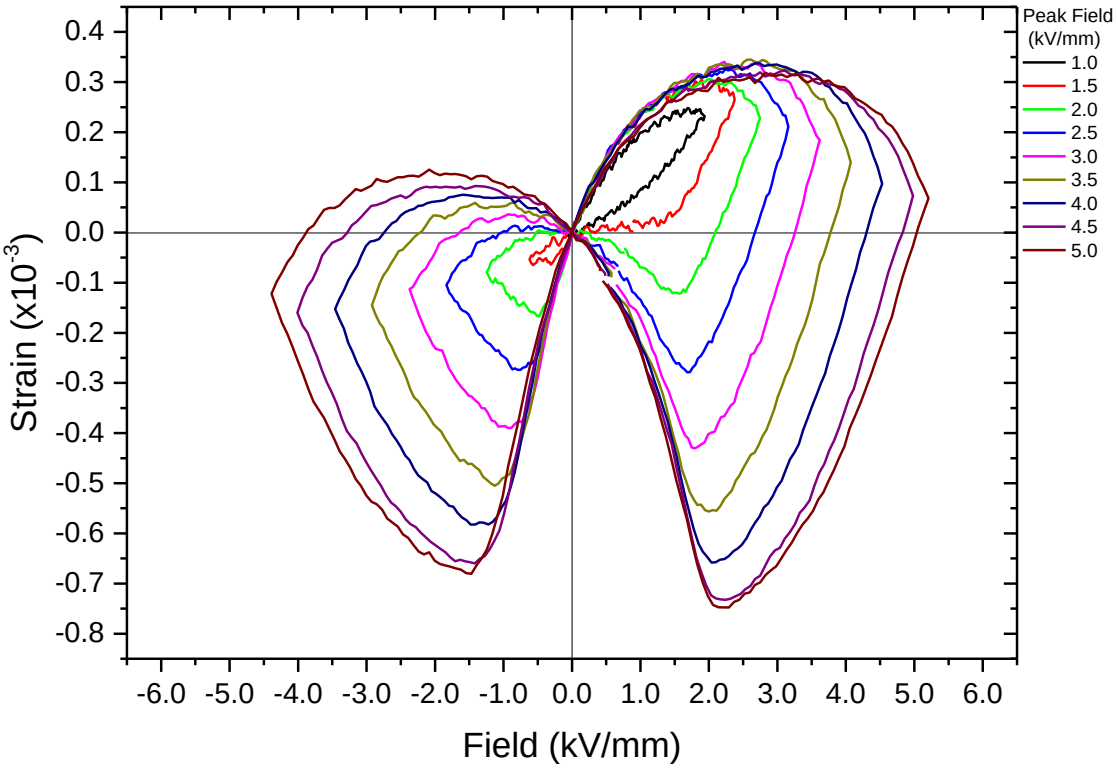

Figure 6.48: Strain-Electric Field data for $0.97KNbO_3$-$0.03LiNbO_3$ with increasing fields.

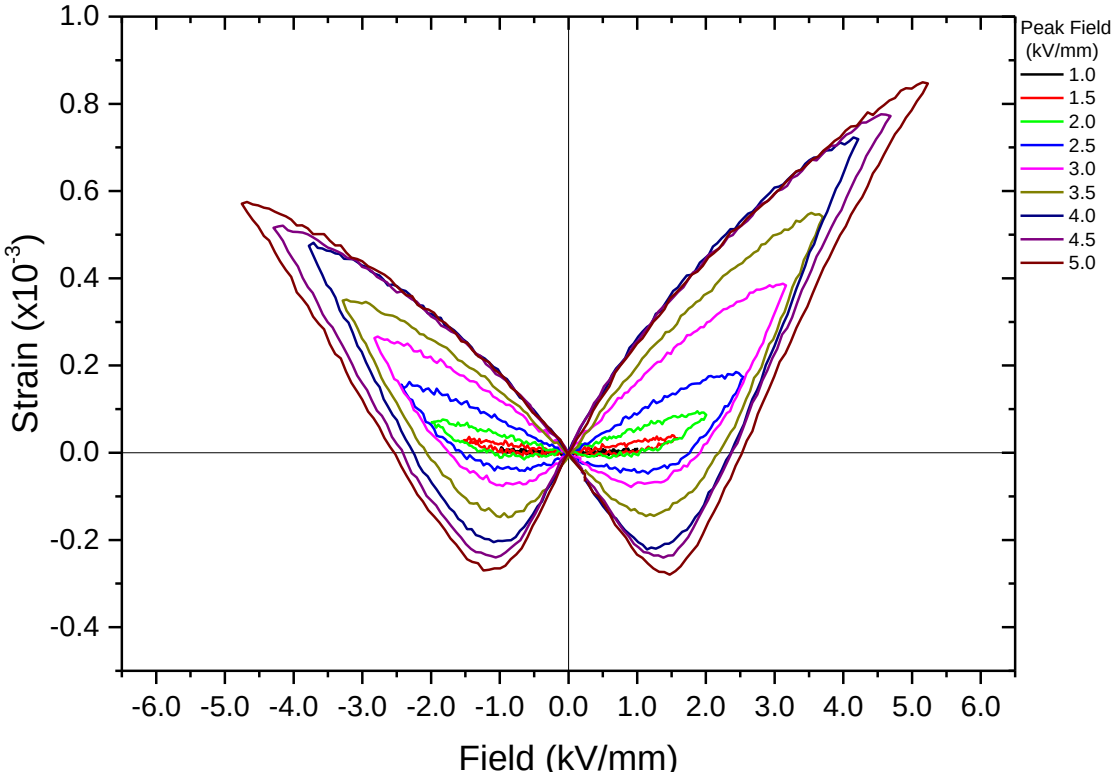

Figure 6.49: Strain-Electric Field data for $0.93KNbO_3$-$0.07LiNbO_3$ with increasing fields.

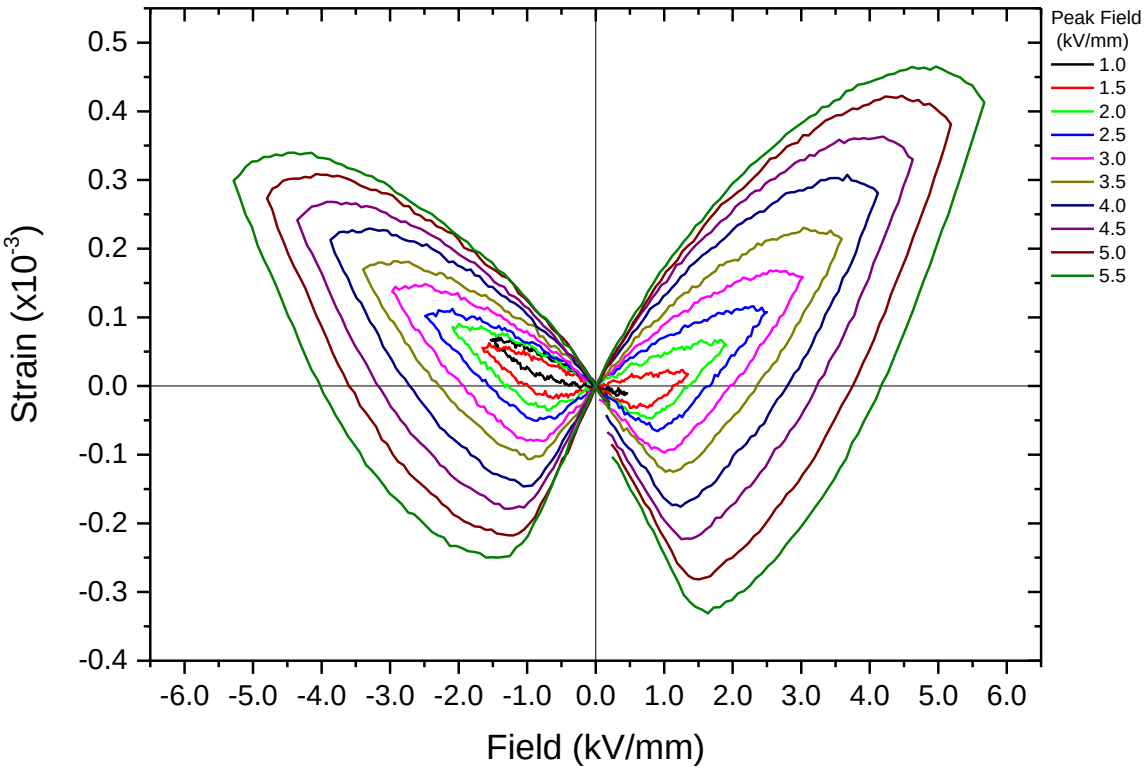

Figure 6.50: Strain-Electric Field data for $0.92KNbO_3$-$0.08LiNbO_3$ with increasing fields.

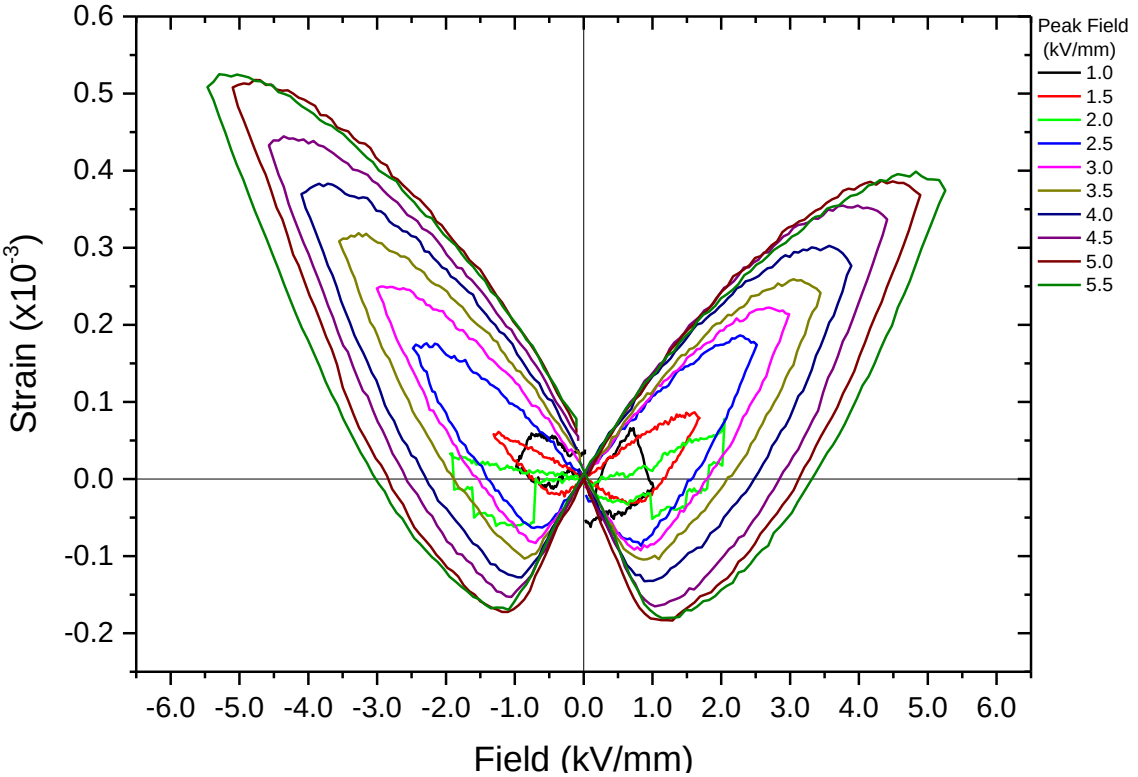

Figure 6.51: Strain-Electric Field data for $0.91KNbO_3$-$0.09LiNbO_3$ with increasing fields.

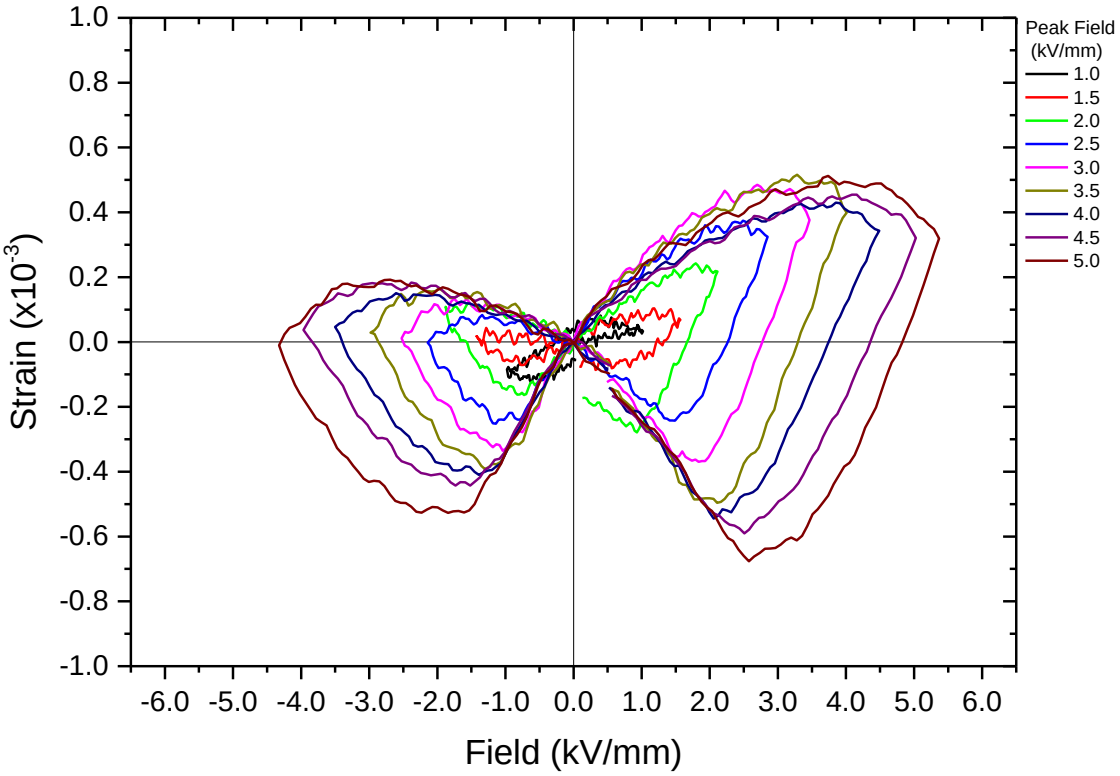

Figure 6.52: Strain-Electric Field data for $0.90KNbO_3$-$0.10LiNbO_3$ with increasing fields.

6.5.2 KNCZLN supplementary data

6.5.2.1 Permittivity data of each composition.

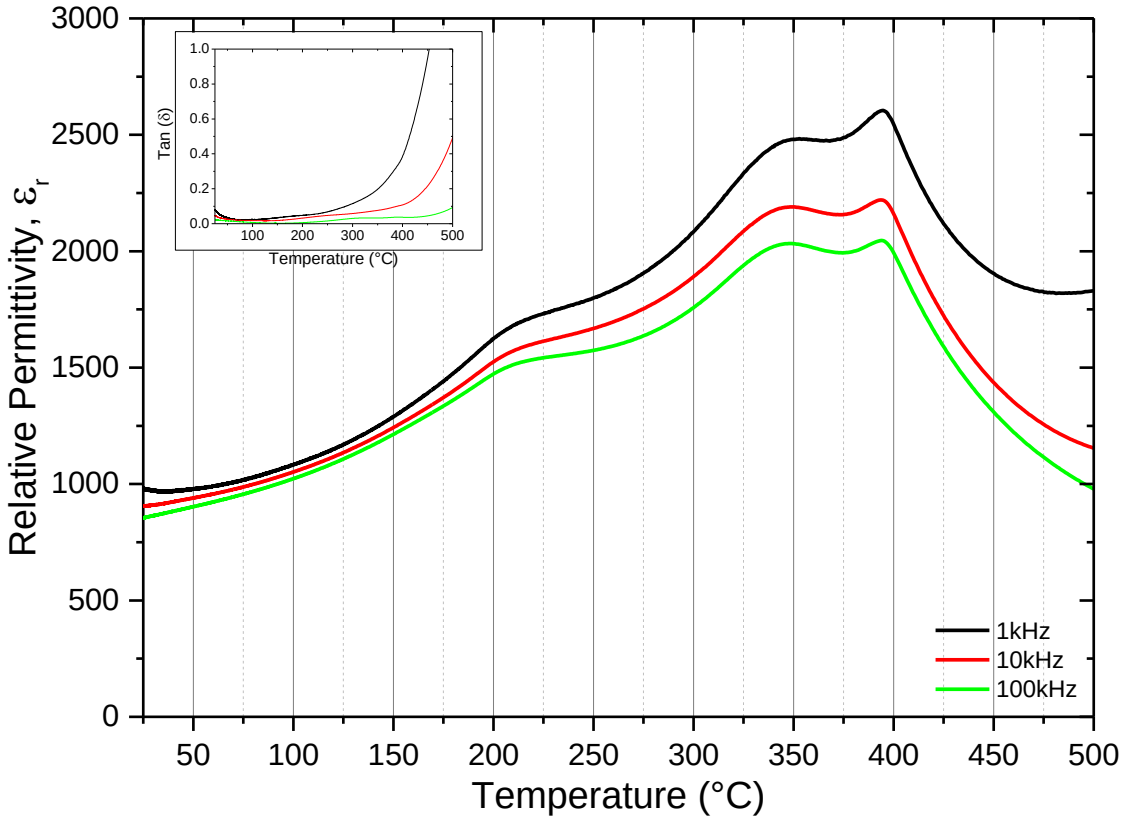

Figure 6.53: Relative permittivity and tan (δ) of KNCZLN composition 1 with temperature and frequency.

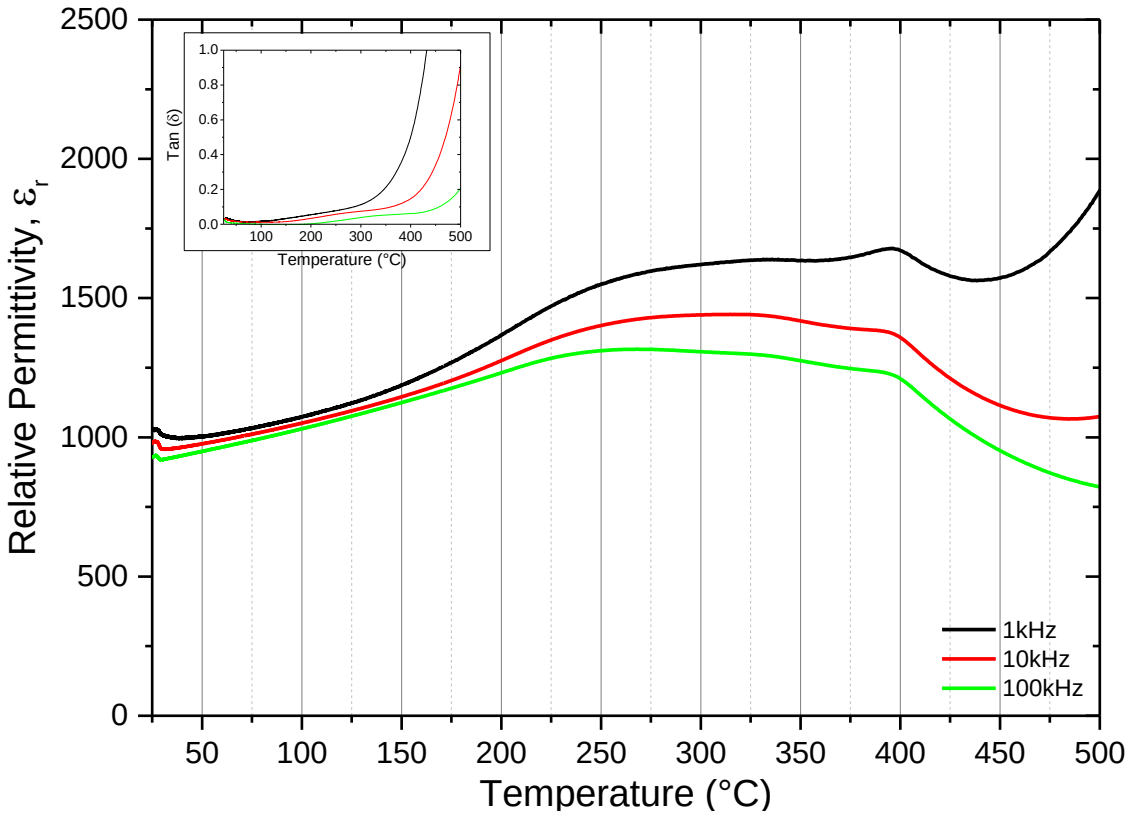

Figure 6.54: Relative permittivity and tan (δ) of KNCZLN composition 2 with temperature and frequency.

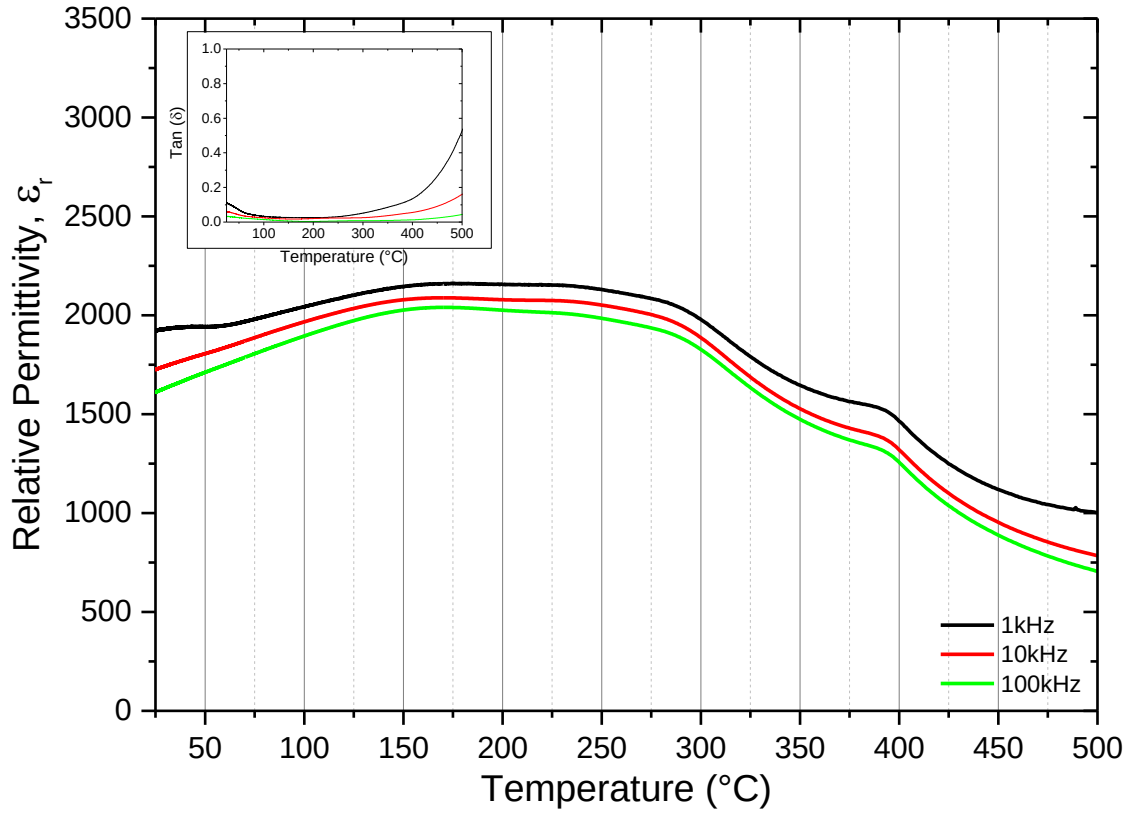

Figure 6.55: Relative permittivity and tan (δ) of KNCZLN composition 3 with temperature and frequency.

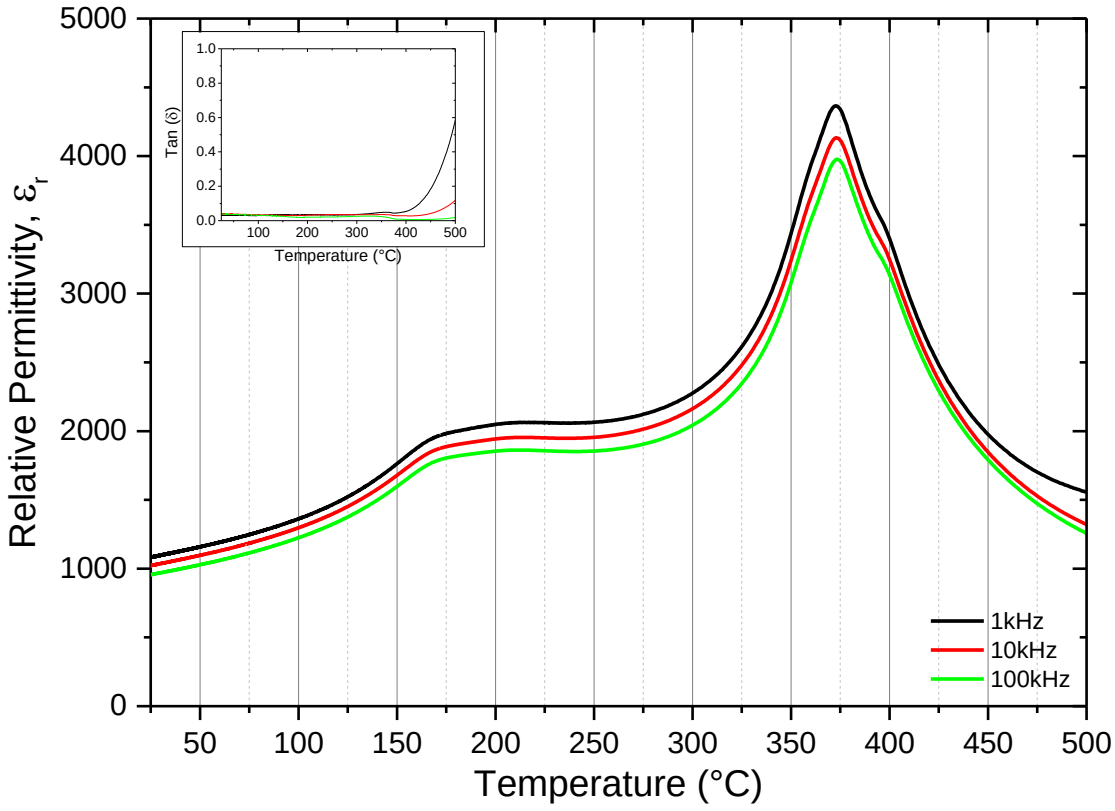

Figure 6.56: Relative permittivity and tan (δ) of KNCZLN composition 4 with temperature and frequency.

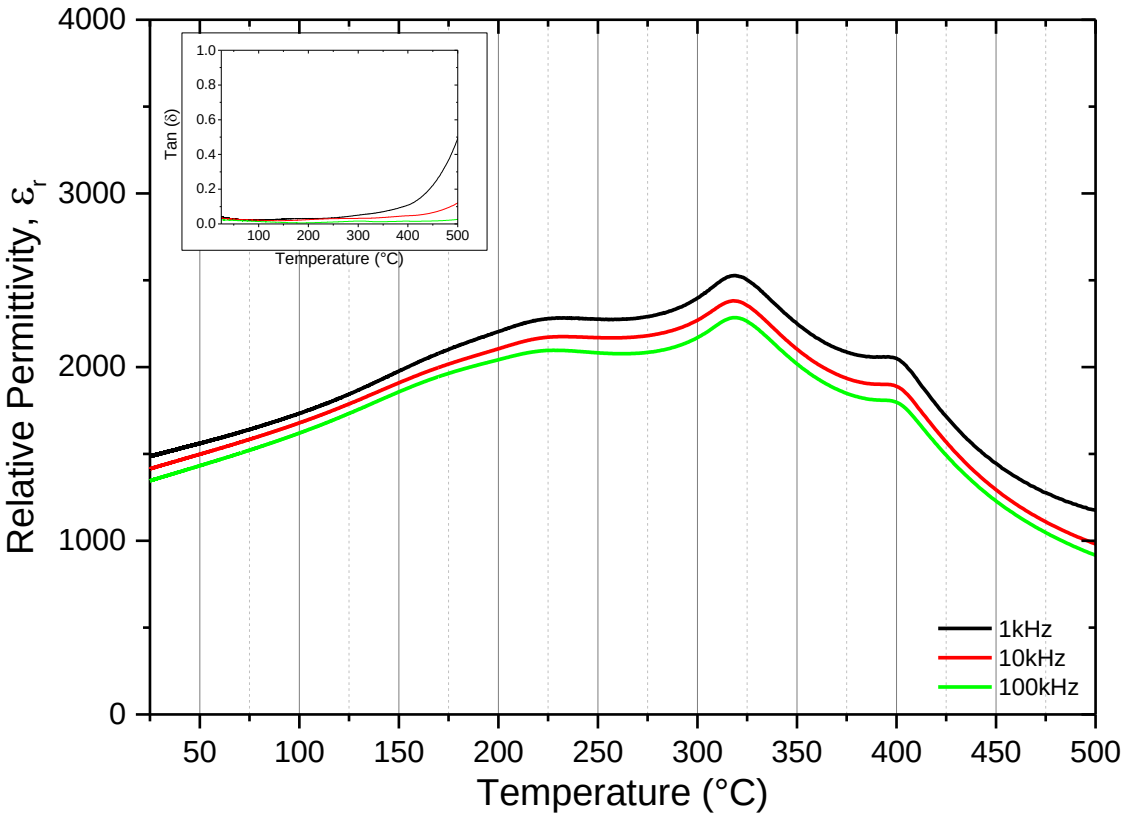

Figure 6.57: Relative permittivity and tan (δ) of KNCZLN composition 5 with temperature and frequency.

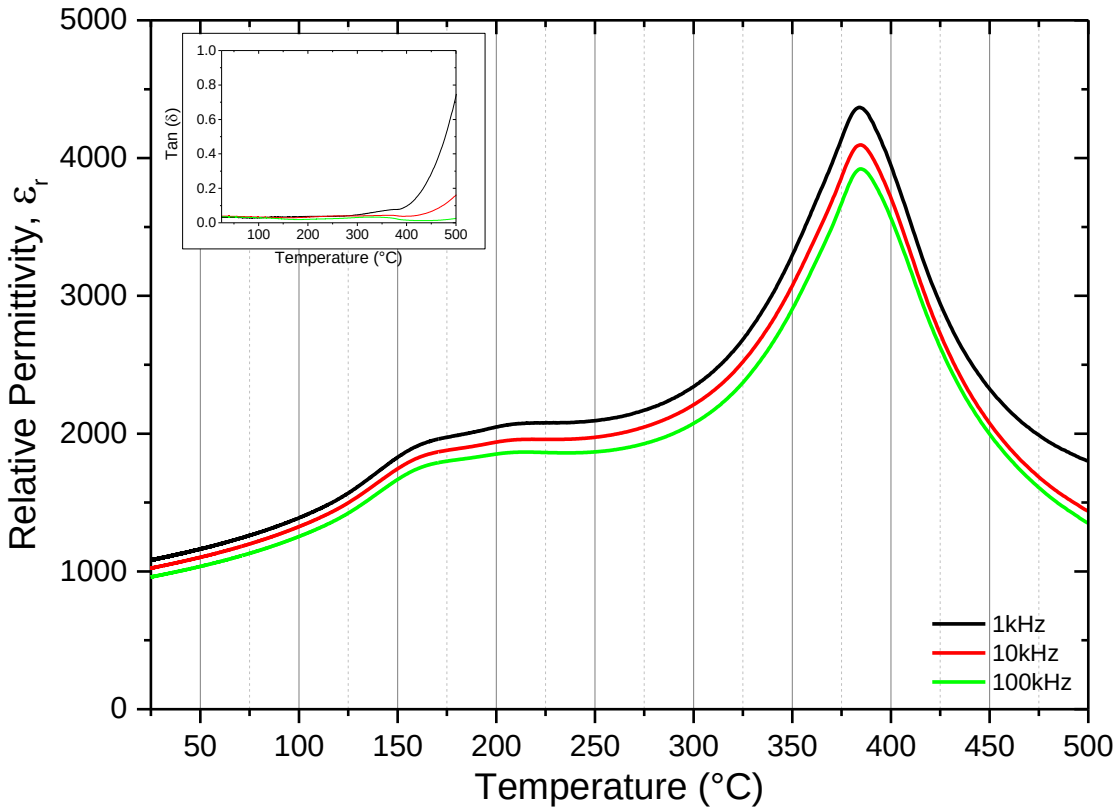

Figure 6.58: Relative permittivity and tan (δ) of KNCZLN composition 6 with temperature and frequency.

6.5.2.2 Polarization- electric field data at each peak field.

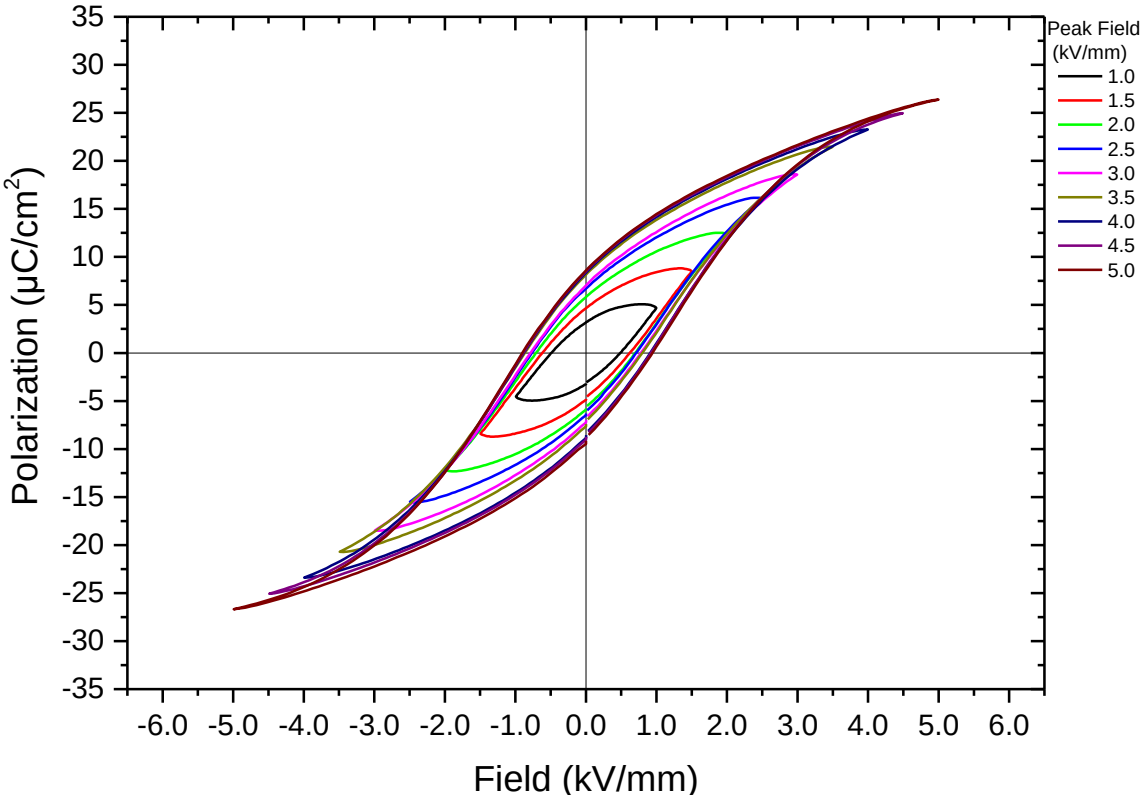

Figure 6.59: Compensated Polarization-Electric Field data for KNCZLN composition 1 with increasing fields.

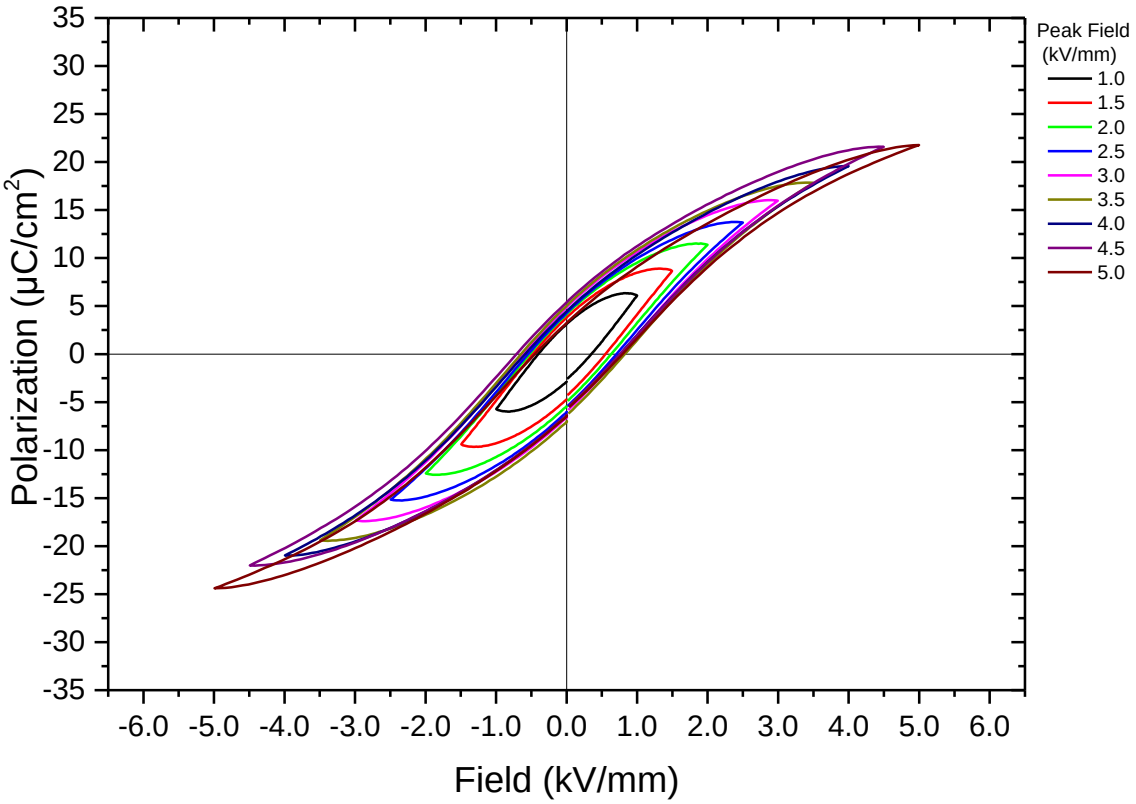

Figure 6.60: Compensated Polarization-Electric Field data for KNCZLN composition 3 with increasing fields.

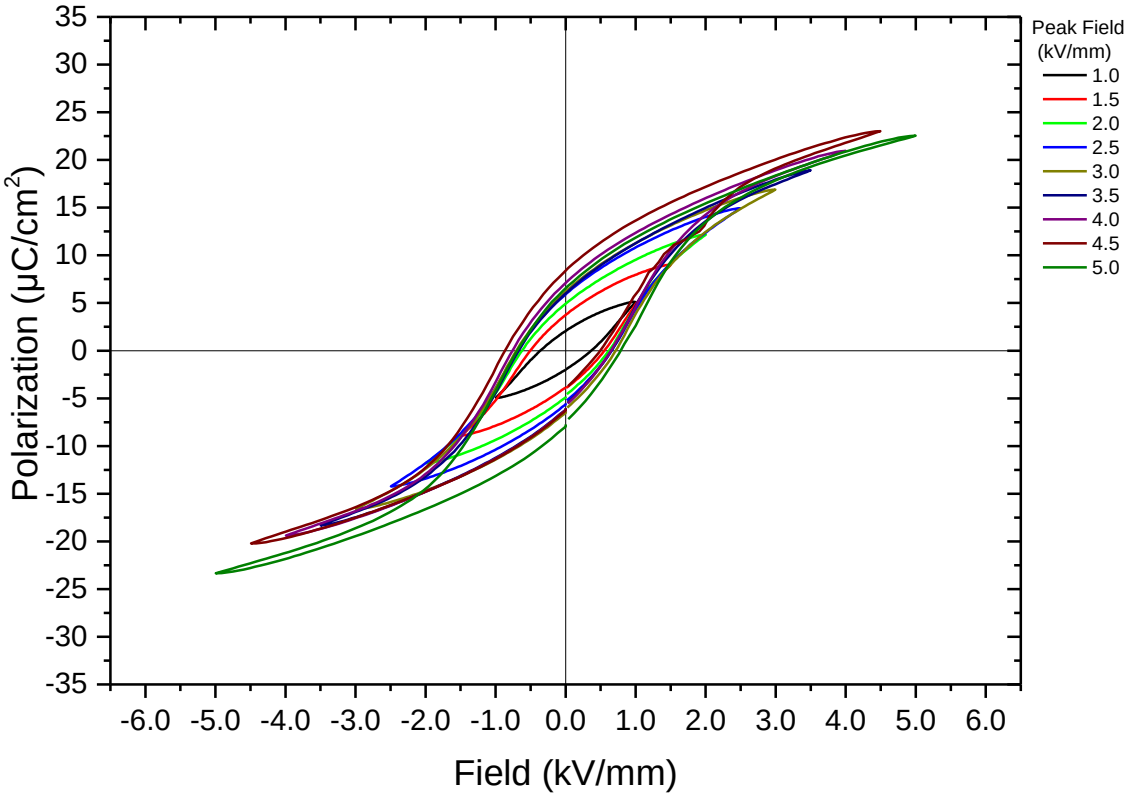

Figure 6.61: Compensated Polarization-Electric Field data for KNCZLN composition 4 with increasing fields.

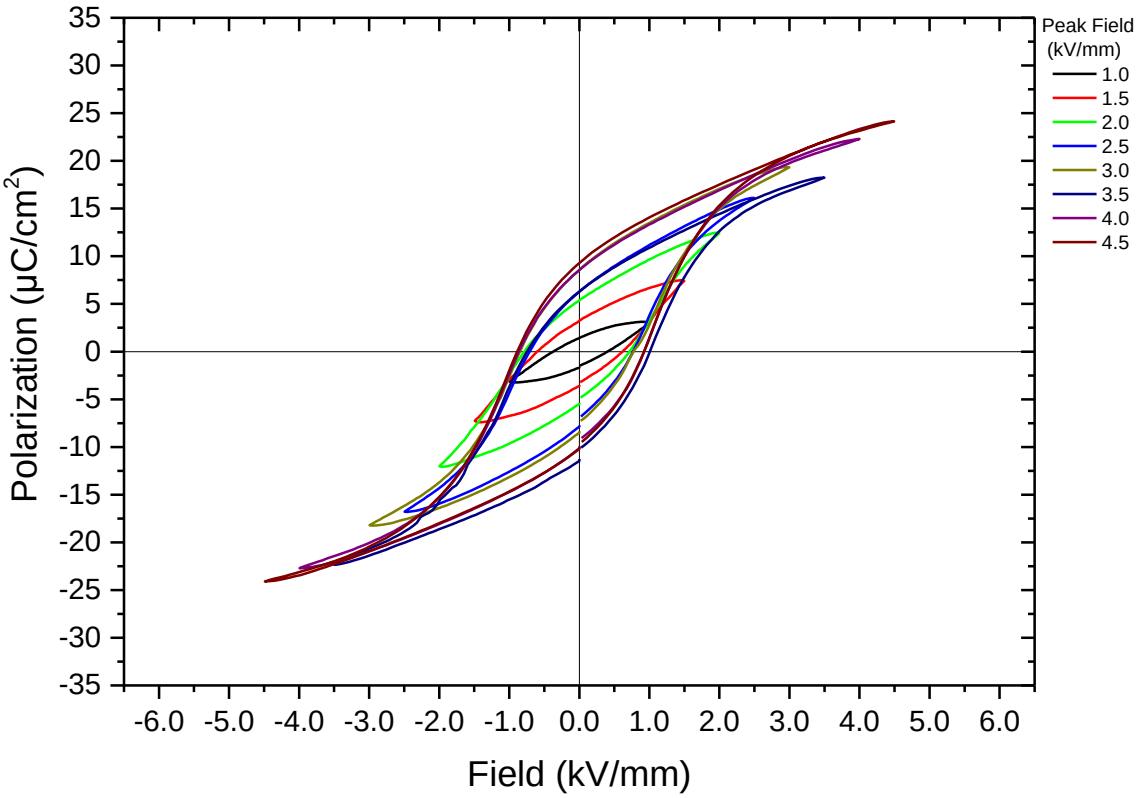

Figure 6.62: Compensated Polarization-Electric Field data for KNCZLN composition 6 with increasing fields.

6.5.2.3 Strain-electric field data at each peak field.

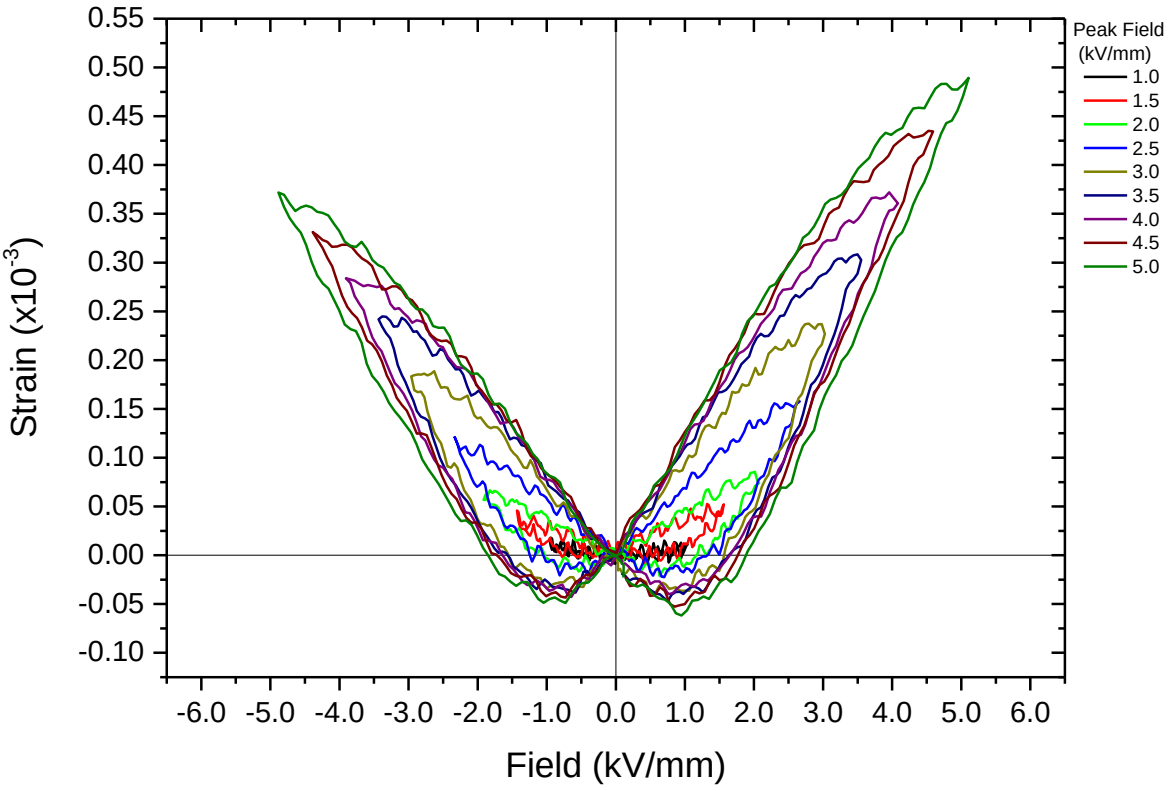

Figure 6.63: Strain-Electric Field data for KNCZLN composition 1 with increasing fields.

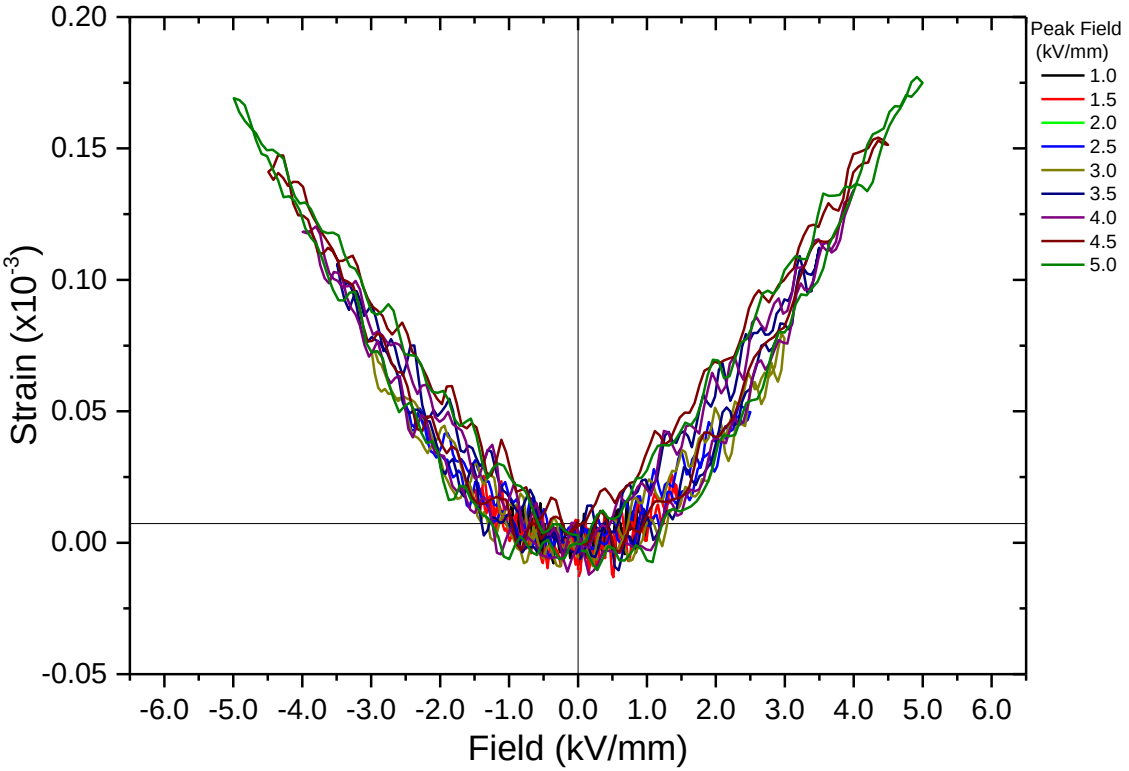

Figure 6.64: Strain-Electric Field data for KNCZLN composition 3 with increasing fields.

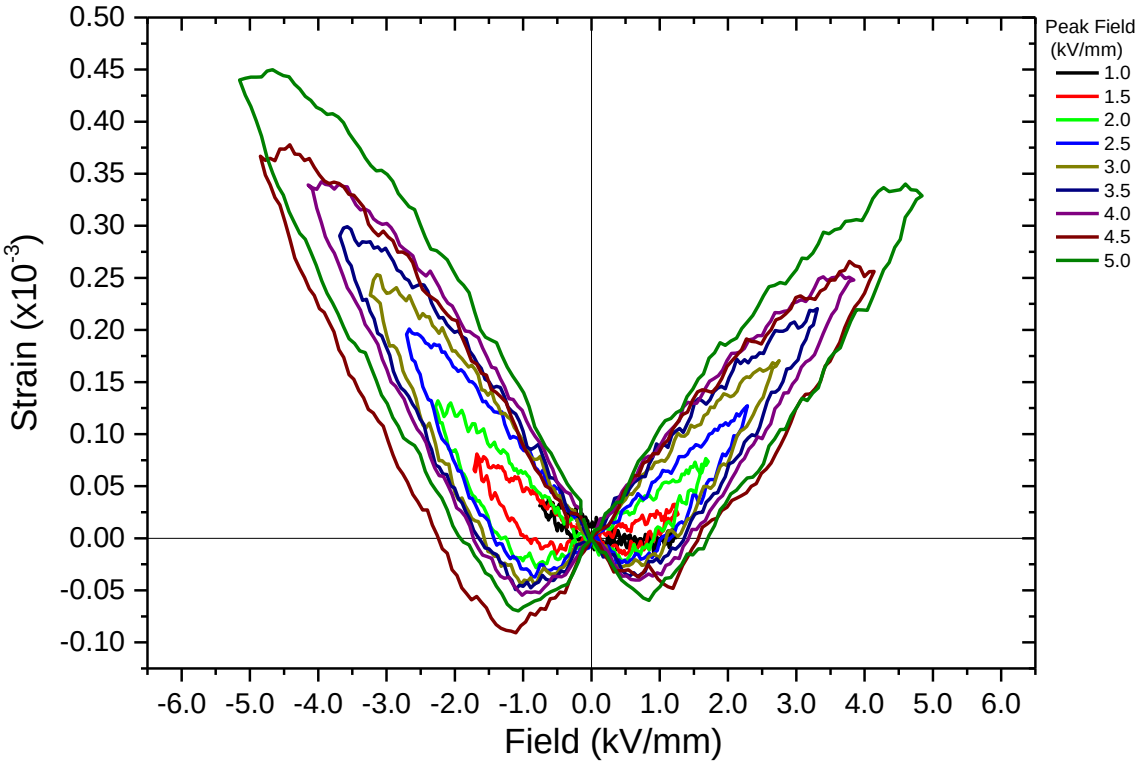

Figure 6.65: Strain-Electric Field data for KNCZLN composition 4 with increasing fields.

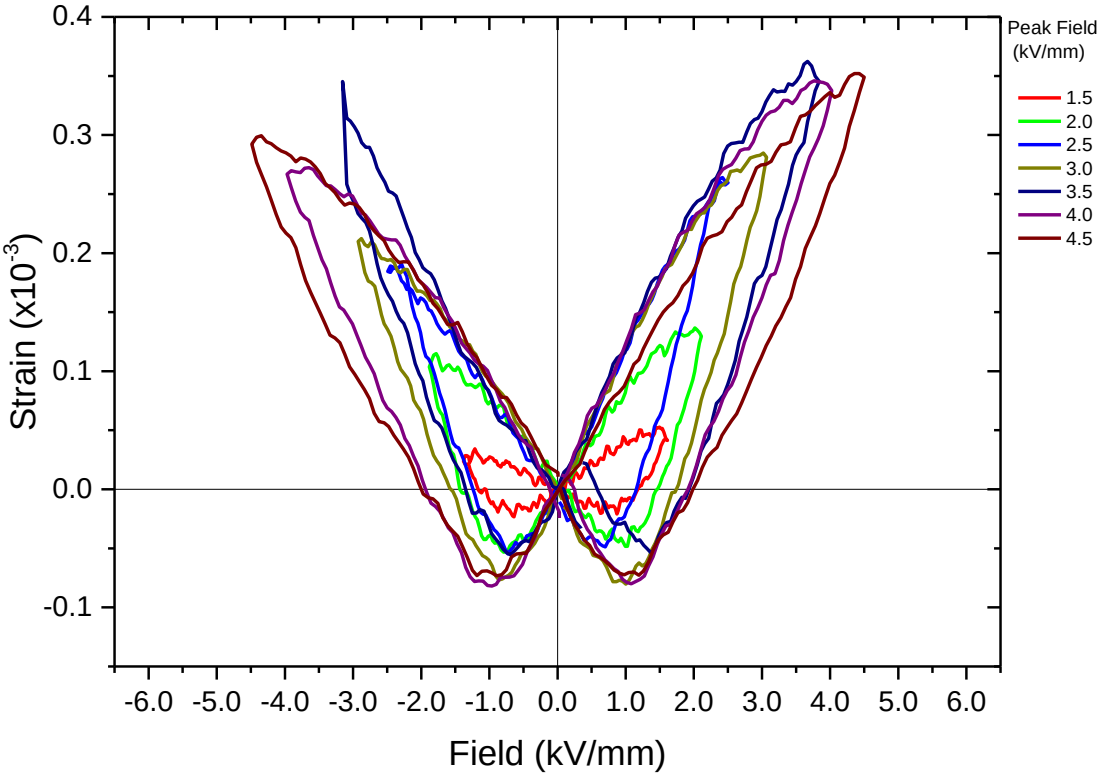

Figure 6.66: Strain-Electric Field data for KNCZLN composition 6 with increasing fields.

7 Summary and Conclusion

Due to EU legislation, there is a need to find an alternative to lead for use in piezoelectric transducers.

In this work the full piezoelectric matrix of pure $(Ba_{0.85}Ca_{0.15})(Ti_{0.90}Zr_{0.10})O_3$ was characterised. This BCTZ material was then used in two types of devices and the devices themselves were characterised.

A poling study was done to determine the correct poling conditions and large BCTZ, dense, ceramic samples were synthesised and machined into specific geometries. Impedance measurements were made and the results used in PRAP to produce a compositional file with the full piezoelectric matrix of the material. The properties calculated were not self-consistent, producing some unrealistic values. This brought into question the ability of PRAP to calculate the properties of the lead-free system.

The project proved the feasibility of a low Curie point material being used in a device with minimum adjustments to the procedure. There was a reasonable level of transmittance and sensitivity from the devices, especially when considering the devices were not designed specifically for BCTZ.

A novel lead-free ferroelectric material was made with the aim of reproducing the phase coexistence found in both PZT and BCTZ. Potassium niobate was used as the base material and $CaZrO_3$ and $LiNbO_3$ were used as dopants, the phase and electrical properties of the materials produced were then characterised. The dopants did bring the T_{O-R} and T_{O-T} phase transitions closer to room temperature. However no pure rhombohedral or tetragonal phase was detected at room temperature.

The sinterability of the $KNbO_3$-$CaZrO_3$ samples was poor. This was overcome by the introduction of $LiNbO_3$ which acted as a sintering aid. This allowed for high field characterisation techniques to be used. Strain-field analysis allowed for a d_{33}* figure to be calculated. $LiNbO_3$ improved the piezoelectric coefficient of pure $KNbO_3$, however the incorporation of $CaZrO_3$ did not.

KNCZLN composition 4, and the BCTZ material made during this project are compared with a leading KNN material and PZT (Navy Type I) in **Table 7.1**. It can be seen that although KNCZLN composition 4 has a higher T_C than BCTZ, the overall piezoelectric performance is worse, the

temperature stability figure of merit proposed in section 3.2.3 is also calculated to be less.

Table 7.1: Comparison of properties BCTZ and KNCZLN composition 4 made in this project with a leading KNN material and PZT.

Material	T_C (°C)	d_{33} or d_{33}^* (pC/N)	F.O.M ($pCN^{-1}K$)
BCTZ (from this study)	80	745.0	59,575
KNCZLN comp. 4 (from this study)	375	87.5	30,625
Best KNN (159)	300	319.0	87,725
PZT (Navy type 1)	325	307.0	92,100

Whilst the research done here has been worthwhile and explores a compositional space not previously looked at, the material properties investigated here suggest that KNCZLN is unlikely to become a suitable replacement for PZT and so the search continues.

Further Work

There are a number of further work opportunities which spring from the work undertaken in this thesis. First would be to increase the understanding of the synthesised materials produced. This could include a microstructure study of the materials using optical or scanning electron microscopy. This would help determine the conductivity issues in the KNCZ compositions as well as the effect $LiNbO_3$ has on grain growth during sintering. Other sintering aids could be used to improve the sample density such as CuO. Any increase in density and decrease in conductivity would allow for the samples to be more readily characterised using high electric field techniques.

The optimisation of the synthesis of BCTZ would help improve the overall piezoelectric response from the material and therefore improve the sensitivity or transmittance of the device. This would include a complete study of the sintering temperatures and dwell times, the optimum milling lengths, including different milling techniques such as attrition milling. Different grades or size of starting reagents could be used. Optimising the uniaxial pressure required for the best green density as well as isopressing. Different machining techniques could be applied such as cutting out the ring before sintering, or pressing rings directly. Using the full matrix of the optimally synthesised material, a device could be designed specifically for the material. This would involve increasing or decreasing the end tail mass or changing the length of the stress rod.

The project highlighted the potential for using KN rather than KNN as a base material for doping. This offers plenty of research opportunities to synthesis and characterise more binary and ternary solid solutions. As well as fundamental studies into the loss of volatile elements and sintering in general.

References

1. *Official Journal of the European Union*, 2003, **46**, p.4.
2. YI LI, KYOUNG-SIK MOON and C.P. WONG. Electronics without lead. *Science*, 2005, **308**(5727), p.2.
3. LI, J.-F., K. WANG, F.-Y. ZHU, L.-Q. CHENG, F.-Z. YAO and D.J. GREEN. (K,Na)NbO3-Based Lead-Free Piezoceramics: Fundamental Aspects, Processing Technologies, and Remaining Challenges. *Journal of the American Ceramic Society*, 2013, **96**(12), pp.3677-3696.
4. ZHANG, S., R. XIA and T.R. SHROUT. Lead-free piezoelectric ceramics vs. PZT? *Journal of Electroceramics*, 2007, **19**(4), pp.251-257.
5. MAEDER, M.D., D. DAMJANOVIC and N. SETTER. Lead Free Piezoelectric Materials. *Journal of Electroceramics*, 2004, **13**, pp.8,.
6. MAUGUIN, C. Sur le symbolisme des groupes de répetition ou de symétrie des assemblages cristallins. *Zeitschrift für Kristallographie – Crystalline Materials*, 1931, **76**, p.16.
7. HAHN, T. International Tables for Crystallography Space-group symmetry. 2002, **A**.
8. HAMMOND, C. *The Basics of Crystallography and Diffraction* 3ed. Oxford Univeristy Press, 2009.
9. MOULSON, A.J. and J.M. HERBERT. *Electroceramics.* 2 ed. Wiley, 2003.
10. MITCHELL, R.H. *Perovskites: Modern and Ancient.* Almaz Press, 2002.
11. COHEN, R.E. Origin of ferroelectricity in perovskite oxides. *Nature*, 1992, **358**, p.3.
12. SHANNON, R.D. Revised Effective Ionic Radii and Systematic Studies of Interatomie Distances in Halides and Chaleogenides. *Acta Cryst.*, 1976, **A32**, p.17.
13. GLAZER, A.M. The Classification of Tilted Octahedra in Perovskite. *Acta Cryst.*, 1972, **B28**, p.12.
14. GOLDSCHMIDT, V.M. Die Gesetze der Krystallochemie. *Naturwissenschaften*, 1926, **14**(21), p.9.
15. EITEL, R.E., C. RANDALL, T.R. SHROUT, R.P. W., W. HACKENBERGER and S.-E. PARK. New High Temperature Morphotropic Phase Boundary Piezoelectrics Based on Bi(Me)O3–PbTiO3 Ceramics. *The Japanese Society of Applied Physics*, 2001, **1**(10), p.4.
16. ROTH, R.S. Classificaiton of Perovskite and Other ABO3-type compounds. *Journal of Research of the National Bureau of Standards*, 1957, **58**(2), p.14.
17. GALASSO, F.S. *Structure, Properties and Preparation of Perovskite-Type Compounds.* Oxford: Pergamon Press, 1969.
18. JAFFE, B., W.R. COOK and H. JAFFE. *Piezoelectric Ceramics.* London: Academic Press 1971.

19. TOUMANARI, A., E.-S. EL-FRIKHE and D. KHATIB. Spontaneous polarization in the tetragonal, orthorhombic and rhombohedral phases of KNbO3. *physica status solidi (c)*, 2006, **3**(9), pp.3351-3354.
20. MARTON, P., I. RYCHETSKY and J. HLINKA. Domain walls of ferroelectricBaTiO3within the Ginzburg-Landau-Devonshire phenomenological model. *Physical Review B*, 2010, **81**(14).
21. AHART, M., M. SOMAYAZULU, R.E. COHEN, P. GANESH, P. DERA, H.K. MAO, R.J. HEMLEY, Y. REN, P. LIERMANN and Z. WU. Origin of morphotropic phase boundaries in ferroelectrics. *Nature*, 2008, **451**(7178), pp.545-8.
22. MABUD, S.A. The Morphotropic Phase Boundary in PZT Solid Solutions. *J. Appl. Cryst.*, 1980, **13**, p.6.
23. EHMKE, M.C., F.H. SCHADER, K.G. WEBBER, J. RÖDEL, J.E. BLENDELL and K.J. BOWMAN. Stress, temperature and electric field effects in the lead-free (Ba,Ca)(Ti,Zr)O 3 piezoelectric system. *Acta Materialia*, 2014, **78**, pp.37-45.
24. PANDA, P.K. Review: environmental friendly lead-free piezoelectric materials. *Journal of Materials Science*, 2009, **44**(19), pp.5049-5062.
25. ALBINO, M., P. HEIJBOER, F. PORCHER, R. DECOURT, P. VEBER, M. MAGLIONE and M. JOSSE. Metastable ferroelectric phase and crossover in the Ba2NdFeNb4−xTaxO15 TTB solid solution. *Journal of Materials Chemistry C*, 2018, **6**(6), pp.1521-1534.
26. CHOUKRI, E., Y. GAGOU, M. D., M. ELMARSSI, Z. ABKHAR, M. ELAATAMNI, I. LUK'YANCHUK and P. SAINT-GREGOIRE. Phase diagram of TTB ferroelectric compounds Pb1−xK2xNb2O6. *M. J. Condensed Matter*, 2010, **12**(2), p.5.
27. OLSEN, G.H., U. ASCHAUER, N. SPALDIN, S.M. SELBACH and T. GRANDE. Origin of ferroelectric polarization in tetragonal tungsten-bronze-type oxides. *Physical Review B*, 2016, **93**, p.5.
28. LIU, S.T. and J.D. ZOOK. Evaluation of curie constants of ferroelectric crystals from pyroelectric response. *Ferroelectrics*, 1974, **7**(1), pp.171-173.
29. HALL, D.A. Review Nonlinearity in piezoeelctric ceramics. *Journal of Materials Science*, 2001, **36**, p.27.
30. YAO, F.-Z., K. WANG, W. JO, J.-S. LEE and J.-F. LI. Effect of poling temperature on piezoelectricity of CaZrO3-modified (K, Na)NbO3-based lead-free ceramics. *Journal of Applied Physics*, 2014, **116**(11), p.114102.
31. ROZANA A. M. OSMAN, M.S.I., ZUL AZHAR ZAHID JAMAL, SANNA TAKING, SYARIFAH NORFAEZAH SABKI, PRABAKARAN A/L POOPALAN, MOHD NATASHAH NORIZAN, ILI SALWANI MOHAMAD. Ferroelectric and Relaxor Ferroelectric to Paralectric Transition Based on Lead Magnesium Niobate (PMN) Materials *Advanced Materials Research*, 2013, **795**, p.7.
32. SMOLENSKY, G. Ferroelectrics with diffuse phase transition. *Ferroelectrics*, 1984, **53**, p.7.
33. CROSS, L.E. Relaxor Ferroelectrics. *Ferroelectrics*, 1987, **76**, p.27.
34. INTELLIGENCE, A.M. Global Piezoelectric Device Market. *Market Report*, 2017, p.532.
35. CURIE, P. and J. CURIE. *Comptes rendus de l'Acedemie des sciences*, 1880, **91**.

36. MASON, W.P. Piezoelectricity, its history and applications. *Journal of the Acoustical Society of America*, 1981, **70**(6).
37. KASSAIN, J.-M. Tartaic Acid. *Ullman's Encyclopedia of Inustrial Chemistry*, 2008.
38. VIJATOVIC, M.M., J.D. BOBIC and B.D. STOJANOVIC. History and challenges of barium titanate: Part I. *Science of Sintering*, 2008, **40**(2), pp.155-165.
39. WAINER, E. High Titania Dielectrics. *Transactions of The Electrochemical Society*, 1943, **83**(1), p.189.
40. T., O. On barium titanate ceramics (In Japanese). *Busseiron Kenkyu*, 1947, **6**, p.26.
41. UCHINO, K. Glory of piezoelectric perovskites. *Sci Technol Adv Mater*, 2015, **16**(4), pp.046001-046001.
42. M., V.B. High and ultrahigh dielectric constant materials (in Russian). *Electrichestvo.*, 1946, **3**, p.12.
43. THURNAUER, H. *The Rochester Engineer*, 1942, **21**, p.2.
44. KOLEŻYŃSKI, A. and K. TKACZ-ŚMIECH. From the Molecular Picture to the Band Structure of Cubic and Tetragonal Barium Titanate. *Ferroelectrics*, 2005, **314**(1), pp.123-134.
45. GOODMAN, G. Ferroelectric Properties of Lead Metaniobate. *Journal of the American Ceramic Society*, 1953, **36**(11), p.4.
46. GUPTA, R., S. VERMA, V. SINGH and K.K. BAMZAI. Preparation, Structural, Electrical, and Ferroelectric Properties of Lead Niobate–Lead Zirconate–Lead Titanate Ternary System. *Journal of Ceramics*, 2015, **2015**, pp.1-12.
47. SHIRANE, G. and A. TAKEDA. Phase Transitions in Solid Solutions of PbZrO3 and PbTiO3 (I) Small Concentrations of PbTiO3. *Journal of the Physical Society of Japan*, 1952, **7**(1), pp.5-11.
48. JAFFE, B., R.S. ROTH and S. MARZULLO. Piezoelectric Properties of Lead Zirconate-Lead Titanate Solid-Solution Ceramics. *Journal of Applied Physics*, 1954, **25**(6), pp.809-810.
49. PANDA, P.K. and B. SAHOO. PZT to Lead Free Piezo Ceramics: A Review. *Ferroelectrics*, 2015, **474**(1), pp.128-143.
50. SAWAGUCHI, E. Ferroelectricity versus Antiferroelectricity in the Solid Solutions of PbZrO3 and PbTiO3. *Journal of the Physical Society of Japan*, 1953, **8**(5), pp.615-629.
51. NOHEDA, B., D.E. COX, G. SHIRANE, J.A. GONZALO, L.E. CROSS and S.E. PARK. A monoclinic ferroelectric phase in the Pb(Zr1−xTix)O3 solid solution. *Applied Physics Letters*, 1999, **74**(14), pp.2059-2061.
52. GLAZER, A.M., P.A. THOMAS, K.Z. BABA-KISHI, G.K.H. PANG and C.W. TAI. Influence of short-range and long-range order on the evolution of the morphotropic phase boundary inPb(Zr1−xTix)O3. *Physical Review B*, 2004, **70**(18).
53. EITEL, R. and C.A. RANDALL. Octahedral tilt-suppression of ferroelectric domain wall dynamics and the associated piezoelectric activity inPb(Zr,Ti)O3. *Physical Review B*, 2007, **75**(9).
54. NOMURA, S., T. TAKAHASHI and Y. YOKOMIZO. Ferroelectric Properties in the System Pb(Zn1/3Nb2/3)O3-PbTiO3. *Journal of the Physical Society of Japan*, 1969, **27**(1), pp.262-262.

55. SHROUT, T.R., Z.P. CHANG, N. KIM and S. MARKGRAF. Dielectric behavior of single crystals near the (1−X) Pb(Mg1/3Nb2/3)O3-(x) PbTiO3morphotropic phase boundary. *Ferroelectrics Letters Section*, 1990, **12**(3), pp.63-69.
56. YIN, Z.-W., H.-S. LUO, P.-C. WANG and G.-S. XU. Growth, characterization and properties of relaxor ferroelectric PMN-PT single crystals. *Ferroelectrics*, 1999, **229**(1), pp.207-216.
57. SUN, P., Q. ZHOU, B. ZHU, D. WU, C. HU, J.M. CANNATA, J. TIAN, P. HAN, G. WANG and K.K. SHUNG. Design and Fabrication of PIN-PMN-PT Single-Crystal High-Frequency Ultrasound Transducers. *IEEE Transactions on Ultrasonics, Ferroelectrics and Frequency Control*, 2009, **56**(12), p.4.
58. GUO, Y., H. LUO, T. HE and Z. YIN. Peculiar properties of a high Curie temperature Pb(In1/2Nb1/2)O3–PbTiO3 single crystal grown by the modified Bridgman technique. *Solid State Communications*, 2002, **123**, p.4.
59. ZHANG, S., S.M. LEE, D.H. KIM, H.Y. LEE and T.R. SHROUT. Characterization of Mn-modified Pb(Mg(13)Nb(23))O(3)-PbZrO(3)-PbTiO(3) single crystals for high power broad bandwidth transducers. *Appl Phys Lett*, 2008, **93**(12), p.122908.
60. HATANAKA, T. and H. HASEGAWA. Dielectric Properties of Pb(ZrxTi1-x)O3 single crystals including monoclinic zirconia. *Japanese Journal of Applied Physics*, 1995, **34**, p.3.
61. UNION, E. DIRECTIVE 2002/95/EC OF THE EUROPEAN PARLIAMENT AND OF THE COUNCIL of 27 January 2003 on the restriction of the use of certain hazardous substances in lectrical and electronic equipment. *Official Journal of the European Union*, 2003, p.5.
62. ---. Exemption of lead oxides used in manufacture of piezo ceramic materials under Article 58(2) REACH. *Ref. Ares*, 2015, **5114646**, p.13.
63. BELLAICHE, L., A. GARCÍA and D. VANDERBILT. Finite-Temperature Properties of PbZr12xTixO3 Alloys from First Principles. *Phys Rev Lett*, 2000, **84**(23), p.4.
64. EICHEL, R.A., E. ERUNAL, M.D. DRAHUS, D.M. SMYTH, J. VAN TOL, J. ACKER, H. KUNGL and M.J. HOFFMANN. Local variations in defect polarization and covalent bonding in ferroelectric Cu(2+)-doped PZT and KNN functional ceramics at the morphotropic phase boundary. *Phys Chem Chem Phys*, 2009, **11**(39), pp.8698-705.
65. JO, W., R. DITTMER, M. ACOSTA, J. ZANG, C. GROH, E. SAPPER, K. WANG and J. RÖDEL. Giant electric-field-induced strains in lead-free ceramics for actuator applications – status and perspective. *Journal of Electroceramics*, 2012, **29**(1), pp.71-93.
66. BECHMANN, R. Elastic, Piezoelectric, and Dielectric Constants of Polarized Barium Titanante Ceramic and Some Applications of the Piezoelectric Eqautions. *Journal of the Acoustical Society of America*, 1596, **28**(3), p.4.
67. ZHANG, L., E. ERDEM, X. REN and R.-A. EICHEL. Reorientation of „MnTi−VO••…Ã defect dipoles in acceptor-modified BaTiO3 single crystals: An electron paramagnetic resonance study. *Applied Physics Letters*, 2008, **93**, p.3.

68. ROGAN, R.C., N. TAMURA, G.A. SWIFT and E. ÜSTÜNDAG. Direct measurement of triaxial strain fields around ferroelectric domains using X-ray microdiffraction. *Nature Materials*, 2003, **2**, p.379.
69. BERLINCOURT, D. and H. JAFFE. Elastic and Piezoelectric Coefficients of Single-Crystal Barium Titanate. *Physical Review*, 1958, **111**(1), pp.143-148.
70. ROBERTS, S. Dielectric and Piezoelectric Properties of Barium Titanate. *Physical Review*, 1947, **71**(12), pp.890-895.
71. GRAY, R.B. and E. PA. *Transducer and method of making the same*. Patent number:
72. TAKAHASHI, H., Y. NUMAMOTO, J. TANI and S. TSUREKAWA. Considerations for BaTiO3Ceramics with High Piezoelectric Properties Fabricated by Microwave Sintering Method. *Japanese Journal of Applied Physics*, 2008, **47**(11), pp.8468-8471.
73. GUILLEMET-FRITSCH, S., Z. VALDEZ-NAVA, C. TENAILLEAU, T. LEBEY, B. DURAND and J.Y. CHANE-CHING. Colossal Permittivity in Ultrafine Grain Size BaTiO3–x and Ba0.95La0.05TiO3–x Materials. *Advanced Materials*, 2008, **20**(3), pp.551-555.
74. KARAKI, T., K. YAN, T. MIYAMOTO and M. ADACHI. Lead-Free Piezoelectric Ceramics with Large Dielectric and Piezoelectric Constants Manufactured from BaTiO3Nano-Powder. *Japanese Journal of Applied Physics*, 2007, **46**(No. 4), pp.L97-L98.
75. KARAKI, T., K. YAN and M. ADACHI. Barium Titanate Piezoelectric Ceramics Manufactured by Two-Step Sintering. *Japanese Journal of Applied Physics*, 2007, **46**(10B), pp.7035-7038.
76. WADA, S., S. SUZUKI, T. NOMA, T. SUZUKI, M. OSADA, M. KAKIHANA, S.E. PARK, L. ERIC CROSS and T.R. SHROUT. Enhanced piezoelectric property of barium titanate single crystals with engineered domain configurations. *Japanese Journal of Applied Physics, Part 1: Regular Papers and Short Notes and Review Papers*, 1999, **38**(9 B), pp.5505-5511.
77. SMOLENSKI, G.A., V.A. ISUPOV and A.I. AGANOVSKAYA. *J. Sov. Phys. Solid State*, 1961, **2**, p.2651.
78. JONES, G.O. and P.A. THOMAS. Investigation of the structure and phase transitions in the novel A-site substituted distorted perovskite compound Na0.5Bi0.5TiO3. *Acta Crystallographica Section B*, 2002, **58**(2), pp.168-178.
79. TAKENAKA, T., K.-I. MARUYAMA and K. SAKATA. (Bi1/2Na1/2)TiO3-BaTiO3 System for Lead-Free Piezoelectric Ceramics. *Japanese Journal of Applied Physics*, 1991, **30**(9B), p.4.
80. HIRUMA, Y., H. NAGATA and T. TAKENAKA. Thermal depoling process and piezoelectric properties of bismuth sodium titanate ceramics. *Journal of Applied Physics*, 2009, **105**.
81. SAKATA, K. and Y. MASUDA. Ferroelectric and antiferroelectric properties of (Na 0.5Bi 0.5)TiO3-SrTiO3 solid solution ceramics. *Ferroelectrics*, 1974, **7**(1), pp.347-349.
82. APARNA, M., M. RAGHAVENDER, G. PRASAD and G.S. KUMAR. ELECTROMECHANICAL CHARACTERIZATION OF LANTHANUM-DOPED SODIUM BISMUTH TITANATE CERAMICS. *Modern Physics Letters B*, 2006, **20**(09), pp.475-480.

83. HERABUT, A. and A. SAFARI. Processing and Electromechanical Properties of (Bi0.5Na0.5)(1−1.5x)LaxTiO3 Ceramics. *Journal of the American Ceramic Society*, 1997, **80**(11), p.5.
84. LI, Y., W. CHEN, J. ZHOU, Q. XU, H. SUN and R. XU. Dielectric and piezoelecrtic properties of lead-free (Na0.5Bi0.5)TiO3–NaNbO3 ceramics. *Materials Science and Engineering: B*, 2004, **112**(1), pp.5-9.
85. KOUNGA, A.B., S.-T. ZHANG, W. JO, T. GRANZOW and J. RÖDEL. Morphotropic phase boundary in (1−x)Bi0.5Na0.5TiO3–xK0.5Na0.5NbO3 lead-free piezoceramics. *Applied Physics Letters*, 2008, **92**(22), p.222902.
86. ZUO, R., X. FANG and C. YE. Phase structures and electrical properties of new lead-free (Na0.5K0.5)NbO3–(Bi0.5Na0.5)TiO3 ceramics. *Applied Physics Letters*, 2007, **90**(9), p.092904.
87. NAGATA, H., N. KOIZUMI and T. TAKENAKA. Lead-Free Piezoelectric Ceramics of (Bi1/2Na1/2)TiO3-BiFeO3 System. *Key Engineering Materials*, 1999, **169-170**, pp.37-40.
88. PENG, C., J.-F. LI and W. GONG. Preparation and properties of (Bi1/2Na1/2)TiO3–Ba(Ti,Zr)O3 lead-free piezoelectric ceramics. *Materials Letters*, 2005, **59**(12), pp.1576-1580.
89. LIN, D., D. XIAO, J. ZHU, P. YU, H. YAN and L. LI. Synthesis and piezoelectric properties of lead-free piezoelectric [Bi0.5(Na1−x−yKxLiy)0.5]TiO3 ceramics. *Materials Letters*, 2004, **58**(5), pp.615-618.
90. TAKENAKA, T., K.O. SAKATA and K.O. TODA. Piezoelectric properties of (Bi1/2Na1/2)TiO3-based ceramics. *Ferroelectrics*, 1990, **106**(1), pp.375-380.
91. CHU, B.-J., D.-R. CHEN, G.-R. LI and Q.-R. YIN. Electrical properties of Na1/2Bi1/2TiO3–BaTiO3 ceramics. *Journal of the European Ceramic Society*, 2002, **22**(13), pp.2115-2121.
92. LI, Y., W. CHEN, Q. XU, J. ZHOU and X. GU. Piezoelectric and ferroelectric properties of Na0.5Bi0.5TiO3–K0.5Bi0.5TiO3–BaTiO3 piezoelectric ceramics. *Materials Letters*, 2005, **59**(11), pp.1361-1364.
93. WANG, X., H.L.-W. CHAN and C.-L. CHOY. Piezoelectric and dielectric properties of CeO2-added (Bi0.5Na0.5)0.94Ba0.06TiO3 lead-free ceramics. *Solid State Communications*, 2003, **125**(7), pp.395-399.
94. WANG, X.X., H.L.W. CHAN and C.L. CHOY. (Bi0.5Na0.5)0.94Ba0.06TiO3 lead-free ceramics with simultaneous addition of CeO2 and La2O3. *Applied Physics A*, 2005, **80**(2), pp.333-336.
95. HALASYAMANI, P.S. and K. PEOEPPELMEIER, R. Noncentrosymmetric Oxides. *Chem. Mater.*, 1998, **10**, p.17.
96. ZHOU, X.Y., H.S. GU, Y. WANG, W.Y. LI and T.S. ZHOU. Piezoelectric properties of Mn-doped (Na0.5Bi0.5)0.92Ba0.08TiO3 ceramics. *Materials Letters*, 2005, **59**(13), pp.1649-1652.
97. HIRUMA, Y., H. NAGATA and T. TAKENAKA. Grain-Size Effect on Electrical Properties of (Bi1/2K1/2)TiO3Ceramics. *Japanese Journal of Applied Physics*, 2007, **46**(3A), pp.1081-1084.

98. NEMOTO, M., Y. HIRUMA, H. NAGATA and T. TAKENAKA. Fabrication and Piezoelectric Properties of Grain-Oriented (Bi1/2K1/2)TiO3–BaTiO3Ceramics. *Japanese Journal of Applied Physics*, 2008, **47**(5), pp.3829-3832.
99. ELKECHAI, O., M. MANIER and J.P. MERCURIO. Na0.5Bi0.5TiO3–K0.5Bi0.5TiO3 (NBT-KBT) system: A structural and electrical study. *physica status solidi (a)*, 1996, **157**(2), pp.499-506.
100. SASAKI, A., T. CHIBA, Y. MAMIYA and E. OTSUKI. Dielectric and Piezoelectric Properties of (Bi0.5Na0.5)TiO3–(Bi0.5K0.5)TiO3 Systems. *Japanese Journal of Applied Physics*, 1999, **36**, p.4.
101. OH, T. Dielectric Relaxor Properties in the System of (Na1-xKx)1/2Bi1/2TiO3Ceramics. *Japanese Journal of Applied Physics*, 2006, **45**(6A), pp.5138-5143.
102. ZHANG, Y.-R., J.-F. LI and B.-P. ZHANG. Enhancing Electrical Properties in NBT-KBT Lead-Free Piezoelectric Ceramics by Optimizing Sintering Temperature. *Journal of the American Ceramic Society*, 2008, **91**(8), pp.2716-2719.
103. LI, Y., W. CHEN, J. ZHOU, Q. XU, H. SUN and M. LIAO. Dielectric and ferroelectric properties of lead-free Na0.5Bi0.5TiO3–K0.5Bi0.5TiO3 ferroelectric ceramics. *Ceramics International*, 2005, **31**(1), pp.139-142.
104. LAM, K.H., X.X. WANG and H.L.W. CHAN. Lead-free piezoceramic cymbal actuator. *Sensors and Actuators A: Physical*, 2006, **125**(2), pp.393-397.
105. LIU, W. and X. REN. Large piezoelectric effect in Pb-free ceramics. *Phys Rev Lett*, 2009, **103**(25), p.257602.
106. PRAVEEN, J.P., T. KARTHIK, A.R. JAMES, E. CHANDRAKALA, S. ASTHANA and D. DAS. Effect of poling process on piezoelectric properties of sol–gel derived BZT–BCT ceramics. *Journal of the European Ceramic Society*, 2015, **35**(6), pp.1785-1798.
107. MATTHIAS, B.T. and J.P. REMEIKA. Dielectric Properties of Sodium and Potassium Niobates. *Physical Review*, 1951, **82**(5), pp.727-729.
108. HEWAT, A.W. Cubic-tetragonal-orthorhombic-rhombohedral ferroelectric transitions in perovskite potassium niobate: neutron powder profile refinement of the structures. *Journal of Physics C: Solid State Physics*, 1973, **6**, p.15.
109. NAKAMURA, K. and M. OSHIKI. Theoretical analysis of horizontal shear mode piezoelectric surface acoustic waves in potassium niobate. *Applied Physics Letters*, 1997, **71**(22), pp.3203-3205.
110. WOOD, E. Polymorphism in potassium niobate, sodium niobate, and other ABO3 compounds. *Acta Crystallographica*, 1951, **4**(4), pp.353-362.
111. TENNERY, V.J. and K.W. HANG. Thermal and X-Ray Diffraction Studies of the NaNbO3–KNbO3 System. *Journal of Applied Physics*, 1968, **39**(10), pp.4749-4753.
112. SHIRANE, G., R. NEWNHAM and R. PEPINSKY. Dielectric Properties and Phase Transitions of NaNbO3and (Na,K)NbO3. *Physical Review*, 1954, **96**(3), pp.581-588.
113. TELLIER, J., B. MALIC, B. DKHIL, D. JENKO, J. CILENSEK and M. KOSEC. Crystal structure and phase transitions of sodium potassium niobate perovskites. *Solid State Sciences*, 2009, **11**(2), pp.320-324.

114. SHIRATORI, Y., A. MAGREZ and C. PITHAN. Particle size effect on the crystal structure symmetry of K0.5Na0.5NbO3. *Journal of the European Ceramic Society*, 2005, **25**(12), pp.2075-2079.
115. KOSEC, M. and D. KOLAR. ON ACTIVATED SINTERING AND ELECTRICAL PROPERTIES OF NaKNbO. *Materials Research Bulletin*, 1975, **10**, p.5.
116. JAEGER, R.E. and L. EGERTON. Hot Pressing of Po tassiu m-Sodiu m Niobates. *Journal of the American Ceramic Society*, 1962, **45**(5), p.5.
117. SAITO, Y., H. TAKAO, T. TANI, T. NONOYAMA, K. TAKATORI, T. HOMMA, T. NAGAYA and M. NAKAMURA. Lead-free piezoceramics. *Nature*, 2004, **432**, p.84.
118. AKDOGAN, E.K., K. KERMAN, M. ABAZARI and A. SAFARI. Origin og high piezoelectric activity in ferroelectric (K0.44Na0.52Li0.04)-(Nb0.84Ta0.1Sb0.06)O3 ceramics. *Applied Physics Letters*, 2008, **92**, p.3.
119. KAWADA, S., M. KIMURA, Y. HIGUCHI and H. TAKAGI. (K,Na)NbO3-Based Multilayer Piezoelectric Ceramics with Nickel Inner Electrodes. *Applied Physics Express*, 2009, **2**(11), p.111401.
120. KOBAYASHI, K., Y. DOSHIDA, Y. MIZUNO, C.A. RANDALL and D. DAMJANOVIC. A Route Forwards to Narrow the Performance Gap between PZT and Lead-Free Piezoelectric Ceramic with Low Oxygen Partial Pressure Processed (Na0.5K0.5)NbO3. *Journal of the American Ceramic Society*, 2012, **95**(9), pp.2928-2933.
121. REISMAN, A. and F. HOLTZBERG. Phase Equilibria in the System K2CO3-Nb2O5 by the Method of Differential Thermal Analysis. *J Am Chem Soc*, 1955, **77**(8), pp.2115-2119.
122. KARI, N.M., T.A. RITTER, S.E. PARK, T.R. SHROUT and K.K. SHUNG. Investigation of potassium niobate as an ultrasonic transducer material. *In: 2000 IEEE Ultrasonics Symposium. Proceedings. An International Symposium (Cat. No.00CH37121)*, 22-25 Oct. 2000, 2000, pp.1065-1068 vol.2.
123. WIESENDANGER, E. Dielectric, mechanical and optical properties of orthorhombic KNbO3. *Ferroelectrics*, 1973, **6**(1), pp.263-281.
124. WANG, K. and J.-F. LI. Low-Temperature Sintering of Li-Modified (K, Na)NbO3 Lead-Free Ceramics: Sintering Behavior, Microstructure, and Electrical Properties. *Journal of the American Ceramic Society*, 2010, **93**(4), pp.1101-1107.
125. ---. Domain Engineering of Lead-Free Li-Modified (K,Na)NbO3 Polycrystals with Highly Enhanced Piezoelectricity. *Advanced Functional Materials*, 2010, **20**(12), pp.1924-1929.
126. ZHAO, P., B.-P. ZHANG and J.-F. LI. Enhanced dielectric and piezoelectric properties in LiTaO3-doped lead-free (K,Na)NbO3 ceramics by optimizing sintering temperature. *Scripta Materialia*, 2008, **58**(6), pp.429-432.
127. ZHANG, S., H.J. LEE, C. MA and X. TAN. Sintering Effect on Microstructure and Properties of (K,Na)NbO3 Ceramics. *Journal of the American Ceramic Society*, 2011, **94**(11), pp.3659-3665.
128. WU, J., D. XIAO and J. ZHU. Potassium–sodium niobate lead-free piezoelectric ceramics: recent advances and perspectives. *Journal of*

Materials Science: Materials in Electronics, 2015, **26**(12), pp.9297-9308.
129. ZHOU, J.-J., K. WANG, F. LI, J.-F. LI, X.-W. ZHANG and Q.-M. WANG. High and Frequency-Insensitive Converse Piezoelectric Coefficient Obtained in AgSbO3-Modified (Li, K, Na)(Nb,Ta)O3 Lead-Free Piezoceramics. *Journal of the American Ceramic Society*, 2013, **96**(2), pp.519-523.
130. KLEIN, N., E. HOLLENSTEIN, D. DAMJANOVIC, H.J. TRODAHL, N. SETTER and M. KUBALL. A study of the phase diagram of (K,Na,Li)NbO3 determined by dielectric and piezoelectric measurements, and Raman spectroscopy. *Applied Physics*, 2007, **102(1)**, pp.014112-1 - 014112-8.
131. KIM, M.-R., H.-C. SONG, J.-W. CHOI, Y.-S. CHO, H.-J. KIM and S.-J. YOON. Synthesis and piezoelectric properties of (1 − x)(Na0.5K0.5)NbO3–x(Ba0.95Sr0.05)TiO3 ceramics. *Journal of Electroceramics*, 2008, **23**(2), p.502.
132. GUO, Y., K.-I. KAKIMOTO and H. OHSATO. Phase transitional behavior and piezoelectric properties of (Na0.5K0.5)NbO3–LiNbO3 ceramics. *Applied Physics Letters*, 2004, **85**(18), pp.4121-4123.
133. WANG, K., J.-F. LI and N. LIU. Piezoelectric properties of low-temperature sintered Li-modified (Na,K)NbO3 lead-free ceramics. *Applied Physics Letters*, 2008, **93**(9), p.092904.
134. HOLLENSTEIN, E., D. DAMJANOVIC and N. SETTER. Temperature stability of the piezoelectric properties of Li-modified KNN ceramics. *Journal of the European Ceramic Society*, 2007, **27**(13), pp.4093-4097.
135. CHANG, Y., S. POTERALA, Z. YANG and G.L. MESSING. Enhanced Electromechanical Properties and Temperature Stability of Textured (K0.5Na0.5)NbO3-Based Piezoelectric Ceramics. *Journal of the American Ceramic Society*, 2011, **94**(8), pp.2494-2498.
136. ZHANG, S., R. XIA and T.R. SHROUT. Modified (K0.5Na0.5)NbO3 based lead-free piezoelectrics with broad temperature usage range. *Applied Physics Letters*, 2007, **91**(13), p.132913.
137. HOLLENSTEIN, E., M. DAVIS, D. DAMJANOVIC and N. SETTER. Piezoelectric properties of Li- and Ta-modified (K0.5Na0.5)NbO3 ceramics. *Applied Physics Letters*, 2005, **87**(18), p.182905.
138. GUO, Y., K.-I. KAKIMOTO and H. OHSATO. (Na0.5K0.5)NbO3–LiTaO3 lead-free piezoelectric ceramics. *Materials Letters*, 2005, **59**(2-3), pp.241-244.
139. WANG, Y., D. DAMJANOVIC, N. KLEIN, E. HOLLENSTEIN and N. SETTER. Compositional Inhomogeneity in Li- and Ta-Modified (K, Na)NbO3Ceramics. *Journal of the American Ceramic Society*, 2007, **90**(11), pp.3485-3489.
140. WANG, Y., J. WU, D. XIAO, W. WU, B. ZHANG, L. WU and J. ZHU. Microstructure and Electrical Properties of [(K0.50Na0.50)0.95−xLi0.05Agx](Nb0.95Ta0.05)O3 Lead-Free Ceramics. *Journal of the American Ceramic Society*, 2008, **91**(8), pp.2772-2775.
141. YANG, Z., Y. CHANG, B. LIU and L. WEI. Effects of composition on phase structure, microstructure and electrical properties of

(K0.5Na0.5)NbO3–LiSbO3 ceramics. *Materials Science and Engineering: A*, 2006, **432**(1-2), pp.292-298.
142. WU, J., T. PENG, Y. WANG, D. XIAO, J. ZHU, Y. JIN, J. ZHU, P. YU, L. WU and Y. JIANG. Phase Structure and Electrical Properties of (K0.48Na0.52)(Nb0.95Ta0.05)O3-LiSbO3 Lead-Free Piezoelectric Ceramics. *Journal of the American Ceramic Society*, 2008, **91**(1), pp.319-321.
143. ZHANG, S., R. XIA, T.R. SHROUT, G. ZANG and J. WANG. Piezoelectric properties in perovskite 0.948(K0.5Na0.5)NbO3–0.052LiSbO3 lead-free ceramics. *Journal of Applied Physics*, 2006, **100**(10), p.104108.
144. WU, J., Y. WANG, D. XIAO, J. ZHU, P. YU, L. WU and W. WU. Piezoelectric Properties of LiSbO3-Modified (K0.48Na0.52)NbO3Lead-Free Ceramics. *Japanese Journal of Applied Physics*, 2007, **46**(11), pp.7375-7377.
145. WU, J., D. XIAO, Y. WANG, J. ZHU and P. YU. Effects of K content on the dielectric, piezoelectric, and ferroelectric properties of 0.95(KxNa1−x)NbO3−0.05LiSbO3 lead-free ceramics. *Journal of Applied Physics*, 2008, **103**(2), p.024102.
146. ZHANG, S., R. XIA, H. HAO, H. LIU and T.R. SHROUT. Mitigation of thermal and fatigue behavior in K(0.5)Na(0.5)NbO(3)-based lead free piezoceramics. *Appl Phys Lett*, 2008, **92**(15), pp.152904-1529043.
147. WANG, R., R.J. XIE, K. HANADA, K. MATSUSAKI, H. KAWANAKA, H. BANDO, T. SEKIYA and M. ITOH. Enhanced piezoelectricity around the tetragonal/orthorhombic morphotropic phase boundary in (Na,K)NbO3–ATiO3 solid solutions. *Journal of Electroceramics*, 2007, **21**(1-4), pp.263-266.
148. PARK, H.-Y., K.-H. CHO, D.-S. PAIK, S. NAHM, H.-G. LEE and D.-H. KIM. Microstructure and piezoelectric properties of lead-free (1−x)(Na0.5K0.5)NbO3-xCaTiO3 ceramics. *Journal of Applied Physics*, 2007, **102**(12), p.124101.
149. LEI, C. and Z.-G. YE. Lead-free piezoelectric ceramics derived from the K0.5Na0.5NbO3–AgNbO3 solid solution system. *Applied Physics Letters*, 2008, **93**(4), p.042901.
150. WANG, R., H. BANDO, M. KIDATE, Y. NISHIHARA and M. ITOH. Effects of A-Site Ions on the Phase Transition Temperatures and Dielectric Properties of ($1-x$)(Na$_{0.5}$K$_{0.5}$)NbO$_{3}$–xAZrO$_{3}$ Solid Solutions. *Japanese Journal of Applied Physics*, 2011, **50**(9), p.09ND10.
151. CHANG, Y., Z. YANG, X. CHAO, R. ZHANG and X. LI. Dielectric and piezoelectric properties of alkaline-earth titanate doped (K0.5Na0.5)NbO3 ceramics. *Materials Letters*, 2007, **61**(3), pp.785-789.
152. KOSEC, M., V. BOBNAR, M. HROVAT, J. BERNARD, B. MALIC and J. HOLC. New lead-free relaxors based on the K0.5Na0.5NbO3–SrTiO3 solid solution. *Journal of Materials Research*, 2011, **19**(6), pp.1849-1854.
153. GUO, Y., K.-I. KAKIMOTO and H. OHSATO. Dielectric and piezoelectric properties of lead-free (Na0.5K0.5)NbO3–SrTiO3 ceramics. *Solid State Communications*, 2004, **129**(5), pp.279-284.

154. MALIC, B., J. BERNARD, J. HOLC, D. JENKO and M. KOSEC. Alkaline-earth doping in (K,Na)NbO3 based piezoceramics. *Journal of the European Ceramic Society*, 2005, **25**(12), pp.2707-2711.
155. CHANG, Y., Z. YANG, L. WEI and B. LIU. Effects of AETiO3 additions on phase structure, microstructure and electrical properties of (K0.5Na0.5)NbO3 ceramics. *Materials Science and Engineering: A*, 2006, **437**(2), pp.301-305.
156. MATSUMOTO, K., Y. HIRUMA, H. NAGATA and T. TAKENAKA. Piezoelectric Properties of Pure and Mn-doped Potassium Niobate Ferroelectric Ceramics. *Japanese Journal of Applied Physics*, 2006, **45**(5B), pp.4479-4483.
157. WATANABE, Y., K. SUMIDA, S. YAMADA, S. SAGO, S.-I. HIRANO and K. KIKUTA. Effect of Mn-Doping on the Piezoelectric Properties of (K0.5Na0.5)(Nb0.67Ta0.33)O3Lead-Free Ceramics. *Japanese Journal of Applied Physics*, 2008, **47**(5), pp.3556-3558.
158. ZHENG, T., J. WU, X. CHENG, X. WANG, B. ZHANG, D. XIAO, J. ZHU, X. LOU and X. WANG. New potassium–sodium niobate material system: a giant-d33 and high-TC lead-free piezoelectric. *Dalton Trans*, 2014, **43**(30), pp.11759-11766.
159. CHENG, X., J. WU, X. LOU, X. WANG, X. WANG, D. XIAO and J. ZHU. Achieving both giant d(33) and high T(c) in patassium-sodium niobate ternary system. *ACS Appl Mater Interfaces*, 2014, **6**(2), pp.750-6.
160. CHENG, X., J. WU, X. WANG, B. ZHANG, X. LOU, X. WANG, D. XIAO and J. ZHU. Mediating the Contradiction of d33 and TC in Potassium–Sodium Niobate Lead-Free Piezoceramics. *ACS Appl Mater Interfaces*, 2013, **5**(21), pp.10409-10417.
161. DEMARTIN MAEDER, M. and D. DAMJANOVIC. Lead free piezoelectric materials. *In*, 2002, p.389.
162. PARK, H.-Y., J.-Y. CHOI, M.-K. CHOI, K.-H. CHO, S. NAHM, H.-G. LEE and H.-W. KANG. Effect of CuO on the Sintering Temperature and Piezoelectric Properties of (Na0.5K0.5)NbO3Lead-Free Piezoelectric Ceramics. *Journal of the American Ceramic Society*, 2008, **91**(7), pp.2374-2377.
163. SEO, I.-T., K.-H. CHO, H.-Y. PARK, S.-J. PARK, M.-K. CHOI, S. NAHM, H.-G. LEE, H.-W. KANG and H.-J. LEE. Effect of CuO on the Sintering and Piezoelectric Properties of 0.95(Na0.5K0.5)NbO3-0.05SrTiO3Lead-Free Piezoelectric Ceramics. *Journal of the American Ceramic Society*, 2008, **91**(12), pp.3955-3960.
164. MATSUBARA, M., K. KIKUTA and S. HIRANO. Piezoelectric properties of (K0.5Na0.5)(Nb1−xTax)O3−K5.4CuTa10O29 ceramics. *Journal of Applied Physics*, 2005, **97**(11), p.114105.
165. BERNARD, J., A. BENČAN, T. ROJAC, J. HOLC, B. MALIČ and M. KOSEC. Low-Temperature Sintering of K0.5Na0.5NbO3Ceramics. *Journal of the American Ceramic Society*, 2008, **91**(7), pp.2409-2411.
166. MATSUBARA, M., T. YAMAGUCHI, K. KIKUTA and S.-I. HIRANO. Sinterability and Piezoelectric Properties of (K,Na)NbO3Ceramics with Novel Sintering Aid. *Japanese Journal of Applied Physics*, 2004, **43**(10), pp.7159-7163.
167. ---. Synthesis and Characterization of (K0.5Na0.5)(Nb0.7Ta0.3)O3Piezoelectric Ceramics Sintered with

Sintering Aid K5.4Cu1.3Ta10O29. *Japanese Journal of Applied Physics*, 2005, **44**(9A), pp.6618-6623.
168. PARK, S.-H., C.-W. AHN, S. NAHM and J.-S. SONG. Microstructure and Piezoelectric Properties of ZnO-added (Na0.5K0.5)NbO3Ceramics. *Japanese Journal of Applied Physics*, 2004, **43**(No. 8B), pp.L1072-L1074.
169. ZUO, R., J. RÖDEL, R. CHEN and L. LI. Sintering and Electrical Properties of Lead-Free Na0.5K0.5NbO3 Piezoelectric Ceramics. *Journal of the American Ceramic Society*, 2006, **89**(6), pp.2010-2015.
170. TAKAO, H., Y. SAITO, Y. AOKI and K. HORIBUCHI. Microstructural Evolution of Crystalline-Oriented (K0.5Na0.5)NbO3 Piezoelectric Ceramics with a Sintering Aid of CuO. *Journal of the American Ceramic Society*, 2006, **89**(6), pp.1951-1956.
171. HAERTLING, G.H. Properties of Hot-Pressed Ferroelectric Alkali Niobate Ceramics. *Journal of the American Ceramic Society*, 1967, **50**(6), p.2.
172. WU, J., D. XIAO, B. WU, W. WU, J. ZHU, Z. YANG and J. WANG. Sintering temperature-induced electrical properties of (Ba0.90Ca0.10)(Ti0.85Zr0.15)O3 lead-free ceramics. *Materials Research Bulletin*, 2012, **47**(5), pp.1281-1284.
173. STOICA, L. *Long Binder Burnout* 2018.
174. PAN WANG, Y.L., YIQING LU. Enhanced piezoelectric properties of (Ba0.85Ca0.15)(Ti0.9Zr0.1)O3 lead-free ceramics by optimizing calcination and sintering temperature. *Journal of the European Ceramic Society*, 2011, **31**, p.8.
175. TUNG, V.T., N.T. TINH, N.H. YEN and D.A. TUAN. Evaluation of Electromechanical Coupling Factor for Piezoelectric Materials Using Finite Element Modeling. *International Journal of Materials and Chemistry*, 2013, **3**(3), p.4.
176.
177. BOWEN, C. *Instructions for the d31 adaptor*, 2017.
178. STANSFIELD, D. and A. ELLIOTT. *Underwater Electroacoustic Transducers.* Peninsula Publishing, 2017.
179. SHERMAN, C.H. and J.L. BUTLER. *Tranducers and Arrays for Underwater Sound.* Underwater Acoustics. Springer, 2007.
180. SOZER, E.M. *Underwater Acoustics: A Brief Introduction*. Unpublished,
181. YIN, N., A. JALALIAN, L. ZHAO, Z. GAI, Z. CHENG and X. WANG. Correlation between crystal structures, Raman scattering and piezoelectric properties of lead-free Na0.5K0.5NbO3. *Journal of Alloys and Compounds*, 2015, **652**, pp.341-345.
182. SHUVAEVA, V.A. and M.Y. ANTIPIN. Structural disorder in K Nb O3 crystal from X-ray diffraction and EXAFS spectroscop. *Crystallography Reports*, 1995, **40**, p.5.
183. DU, H., F. TANG, D. LIU, D. ZHU, W. ZHOU and S. QU. The microstructure and ferroelectric properties of (K0.5Na0.5)NbO3–LiNbO3 lead-free piezoelectric ceramics. *Materials Science and Engineering: B*, 2007, **136**, p.5.